UNIVERSIDADE DA BEIRA INTERIOR
Faculdade de Engenharia

Modelling of Spray-Wall Impingement

Christian Michel Gomes Rodrigues

Tese para obtenção do Grau de Doutor em
Engenharia Aeronáutica
(3º ciclo de estudos)

Orientador: Prof. Doutor André Resende Rodrigues da Silva
Orientador: Prof. Doutor Jorge Manuel Martins Barata

Covilhã, Março de 2016

Acknowledgments

I would like to take this opportunity to express my sincere gratitude to Professor André Resende Rodrigues da Silva for his support, encouragement and guidance during the course of this study at the University of Beira Interior. I am also deeply indebted to Professor Jorge Manuel Martins Barata for his confidence and for giving me the unique opportunity to enter the world of multiphase flow modelling in an excellent scientific environment.

Many thanks to my colleagues at AeroG for all the help and suggestions provided along the way, and particularly to Carlos Velosa for the contributing support and interesting discussions.

Last but not least, I am grateful to my family and to Liliana for their encouragement and patience during the production of this thesis. I would also like to extend my acknowledgement to Teresa Vasconselos for the time invested in the lecture and revision of some sections of the manuscript.

The present work was performed under the scope of Laboratório Associado em Energia, Transportes e Aeronáutica (LAETA) activities. I gratefully acknowledge the financial support of the Fundação para a Ciência e Tecnologia (FCT) through the PhD grant SFRH/BD/77651/2011.

Abstract

When a drop collides with an interposed surface, three phases are usually involved: liquid (the drop), solid (the substrate) and gas (the surrounding environment). Such an event involves a number of parameters associated with the physical characteristics of the incident particles, the properties of the target surface, and the natural features of the air flow. Each occurrence leads to a singular outcome, since each particle experiences a different reality throughout the injection cycle. Therefore, the development of appropriate modelling strategies of this complex multi-phase flow requires a thorough understanding of the mechanisms underlying the spray impingement process.

Several computational models have been reported in the open literature, although not always successfully. From these, only a few have attempted to replicate the more intricate scenarios that include the formation and development of a liquid film over the surface due to the deposition of previously injected particles, the presence of a high velocity cross-flowing gas, and the thermal effects promoted by the existence of hot walls. Even though these elements are some of the more influential parameters affecting the final outcome of spray-wall impacts, most of the simulations still neglect some of them in their formulation.

Therefore, in order to capture the majority of the physical phenomena observed in experimental studies, CFD codes must be equipped with superior mathematical formulations. During the present doctoral research, three independent computational extensions have been devised and integrated into the model used by our research group to simulate spray-wall interactions. The upgrades — that have been proposed over the course of the study — have been denominated as the liquid film, evaporation and breakup sub-models. They are intended to complement the basic mathematical formulation adopted in the original simulation procedure. This approach has contributed to enhance the prediction capabilities of the model, since it is now capable of capturing some phenomena that were not considered previously. On the other hand, it has also extended the range of applicability of the CFD code to a new set of impact conditions (i.e., in hot environments and with a high velocity crossflow).

Furthermore, the present work provides a detailed analysis of the results obtained, with major emphasis given to the disintegration mechanisms and secondary droplet characteristics. Both quantitative and qualitative comparisons between computational and experimental results are presented. When pertinent, the impact of a particular sub-model onto the outcome predicted is also evaluated by comparing the versions of the model with and without the corresponding computational extension. Moreover, a systematic approach is adopted at each section to infer the influence of different parameters on the final outcome. This methodology has been decisive to better understand the factors affecting the phenomena occurring during impact.

Keywords

Spray impingement, spray-wall interactions, secondary droplet characteristics, heat transfer, liquid film, breakup, drop deformation, splash

Resumo

Quando uma gota colide com uma superfície interposta, estão normalmente envolvidas três fases: líquida (a gota), sólida (o substrato) e gasosa (o ambiente circundante). Este evento envolve um determinado número de parômetros associados com as características físicas das partículas incidentes, as propriedades da superfície alvo, e as características naturais do escoamento de ar. Cada ocorrência conduz a um desfecho singular, uma vez que cada partícula experimenta uma realidade diferente ao longo do ciclo de injeção. Por conseguinte, a elaboração de estratégias de modelação adequadas deste escoamento multifásico complexo requer um conhecimento profundo dos mecanismos subjacentes ao processo relativo ao impacto de spray.

Foram propostos vários modelos computacionais na literatura, embora nem sempre com sucesso. Destes, apenas alguns tentaram reproduzir os cenários mais intrincados que incluem a formação e desenvolvimento de um filme líquido sobre a superfície devido à acumulação de partículas anteriormente injetadas, a presença de um escoamento transversal com elevada velocidade, e os efeitos térmicos promovidos pela existência de paredes quentes. Embora estes sejam alguns dos parâmetros que mais influenciam o resultado final do impacto de sprays em paredes, a maioria dos modelos ainda negligenciam alguns deles na sua formulação.

Assim, de modo a capturar a maioria dos fenómenos físicos observados em estudos experimentais, os códigos de CFD devem ser equipados com uma formulação matemática mais desenvolvida. Durante esta investigação, foram concebidas três extensões computacionais independentes. Estes desenvolvimentos foram, posteriormente, integrados no modelo utilizado para simular as interações spray-parede. Estes sub-modelos — que foram propostos ao longo do estudo — foram denominados de filme líquido, evaporação e *breakup*, e eram destinados a complementar a formulação matemática de base adotada na simulação original. Esta abordagem contribuiu para aumentar a capacidade de previsão do modelo uma vez que este é agora capaz de capturar alguns fenómenos que não eram considerados anteriormente. Por outro lado, permitiu alargar a gama de aplicabilidade do código de CFD para um novo conjunto de condições de impacto (isto é, em ambientes quentes e com escoamentos cruzados de alta velocidade).

Além disso, este trabalho apresenta uma análise detalhada dos resultados obtidos, sendo que é atribuída grande ênfase aos mecanismos de desintegração e características de gotas secundárias. São recorrentemente apresentadas comparações entre os resultados computacionais e experimentais tanto de forma quantitativa como qualitativa. Quando pertinente, o impacto de um determinado sub-modelo para o resultado previsto na simulação é também avaliado através da comparação das versões do código de CFD com e sem o respetivo sub-modelo. Além disso, uma abordagem sistemática é adotada em cada secção para inferir acerca da influência de diferentes parâmetros sobre o resultado final. Esta metodologia revelou-se decisiva para compreender melhor os fatores que afetam os fenómenos decorrentes do impacto.

Palavras-chave

Impacto de gotas, interações entre spray e parede, características das gotas secundárias, transferência de calor, película líquida, *breakup*, deformação da gota, *splash*

Resumo alargado

Quando uma gota colide com uma superfície interposta, estão normalmente envolvidas três fases: líquida (a gota), sólida (o substrato) e gasosa (o ambiente circundante). Este evento envolve um determinado número de parâmetros associados com as características físicas das partículas incidentes, as propriedades da superfície alvo, e as características naturais do escoamento de ar. Cada ocorrência conduz a um desfecho singular, uma vez que cada partícula experimenta uma realidade diferente ao longo do ciclo de injeção. Por conseguinte, a elaboração de estratégias de modelação adequadas deste escoamento multifásico complexo requer um conhecimento profundo dos mecanismos subjacentes ao processo relativo ao impacto de spray.

Este trabalho de investigação visa estudar os fenómenos de interação spray-parede e aumentar a capacidade do código de CFD desenvolvido no nosso grupo de investigação em fornecer previsões adequadas. Embora pontualmente alguns modelos computacionais tenham sido propostos ao longo dos anos com o objetivo de prever o resultado de problemas de impacto de gotas em paredes sólidas, ainda é necessário percorrer um longo caminho de forma a ser possível reconhecer a formulação matemática que deve ser adotada para proporcionar a simulação mais correta possível. Fornecer um modelo de dispersão flexível — cuja formulação possa ser modificada através do uso de correlações empíricas mais adequadas (que tenham sido derivadas a partir de um determinado conjunto de dados experimentais) — com limitações mínimas no que refere ao tempo de simulação seria um grande trunfo para a indústria e academia. Tal objetivo motivou o presente trabalho, que começou com uma fase de avaliação do processo de simulação para identificar os aspetos que poderiam ser melhorados. Esta fase incluiu a análise da energia de dissipação durante o *splash*, bem como o estudo da malha na região próxima da parede.

Assim, o primeiro aspeto investigado foi o termo de dissipação de energia encontrado durante o regime *splash*. Foram introduzidas na simulação várias equações propostas em diferentes publicações e as previsões computacionais foram comparadas com dados experimentais. Os resultados mostraram que a expressão de dissipação de energia que é considerado no balanço de energia entre as gotas incidentes e secundárias tem uma influência importante sobre o resultado do mecanismo de impacto. A comparação das quatro expressões apresentadas evidencia que a relação original assumida no modelo de base é, nesta altura, a melhor aproximação disponível na literatura da energia dissipada durante o evento *splash*. Além disso, a discrepância entre os resultados obtidos com esta equação e as outras confirma o efeito não negligenciável deste parâmetro sobre o comportamento das gotas secundárias. A sobreavaliação do perfil de velocidade ao longo de todo o espetro de tamanho de gotas sugere que o termo de dissipação está subestimado nestes casos.

Quanto aos resultados obtidos no âmbito do método de rastreamento das gotas na região próxima da parede, a nova abordagem aqui proposta fornece uma forma alternativa de aumentar a precisão na fase dispersa nessa região. Esta alternativa pode ser considerada ao invés de um refinamento geral da malha, uma vez que este procedimento acarreta um aumento computacional extremamente dispendioso. No entanto, é importante referir que nenhuma das soluções irá alterar significativamente as previsões da fase contínua uma vez que foram realizados extensos estudos de independência de malha para este modelo. Por outro lado, as implicações reais deste refinamento da malha na fase dispersa nunca tinham sido avaliadas de forma adequada, em particular na região perto da parede, que é onde a camada limite pode ter uma repercussão importante sobre a trajetória das gotas antes do impacto. A análise dos resulta-

dos evidencia que o tratamento refinado da camada limite não fornece melhorias significativas que justifiquem os custos computacionais adicionais. Esta conclusão também sugere que a formulação matemática está livre de influências numéricas que se poderiam propagar durante o procedimento computacional seguido na simulação. No entanto, tendo em conta a importância que o escoamento paralelo à parede tem na dispersão da gota, esta abordagem poderá ser mais útil em outras aplicações específicas.

Por detrás de grande parte do esforço de investigação investido em estudos experimentais reside também a expectativa de encontrar uma expressão matemática — constituída por um (limitado) número de variáveis — capaz de reproduzir um conjunto de dados recolhidos nas medições efetuadas. Uma descoberta destas tornar-se-ia ainda mais importante se a concordância entre a equação proposta e os dados observados se estendesse a outras condições de fronteira e configurações. No entanto, a partir da revisão bibliográfica realizada no âmbito deste trabalho, foi possível perceber que, apesar de algumas correlações deduzidas experimentalmente terem sido propostas para intervalos semelhantes de condições de impacto, estas estão muitas vezes definidas em função de parâmetros distintos ou revelam diferentes pesos atribuídos a parcelas idênticas.

É neste contexto que emergem os modelos computacionais, uma vez que estes podem desempenhar um papel crítico nesta fase para determinar qual é a combinação de equações que fornece os resultados mais precisos. De facto, se, por um lado, é possível concluir a partir dos resultados apresentados neste documento que a integração do sub-modelo filme líquido no modelo básico melhora a concordância entre os resultados computacionais e experimentais, por outro, é também importante ajustar a estratégia de simulação com essa alteração. Assim, uma vez que a nova interface líquido/líquido está a ser considerada, o critério de transição proposto por Motzkus et al. (2011) foi utilizado para determinar o início do regime *splash* de modo a ter em conta a influência da espessura da camada de líquido nos mecanismos subjacentes aos eventos de impacto.

Os motivos que levam à modelação de fenómenos de impacto de sprays podem ser muito variados. Em alguns casos, apenas a quantidade de líquido depositado na superfície é objeto de interesse (por exemplo, pintura por pulverização), ao passo que em outros casos, os mecanismos de transferência de calor (por exemplo, sistemas de refrigeração) ou a desintegração das gotas incidentes antes do impacto (por exemplo, injeção em turbina a gás) são os mecanismos que pretendem ser capturados.

Por conseguinte, a complexidade dos modelos também pode variar consideravelmente, dependendo da aplicação para a qual estes estão a ser desenvolvidos. O cenário ideal — que é também o mais exigente — seria um código CFD capaz de simular com precisão um caso em que todos estes elementos pudessem ser considerados. Essa meta também tem impulsionado o decurso dos trabalhos realizados durante este projeto de doutoramento. Apesar de ainda existirem alguns aspetos do processo de simulação que foram simplificados/negligenciados, a versão final do modelo inclui agora uma base matemática que permite inferir que é capaz de simular fenómenos de impacto numa gama mais ampla de condições (que inclui ambientes quentes e escoamentos cruzados de alta velocidade) com resultados satisfatórios.

De facto, o sub-modelo de evaporação destina-se a alargar a gama de aplicabilidade do modelo a condições em que a transferência de calor não pode ser negligenciada. Foram avaliados duas temperaturas iniciais diferentes para inferir acerca da influência deste parâmetro nos resultados do impacto do spray. As conclusões seguintes podem ser retiradas: com o aumento da temperatura, (1) o número de gotas incidentes que se espera que se estabeleçam sobre a superfície aumenta, enquanto que a fração de massa de gotas que se depositam na mesma superfície

diminui; (2) as gotas devem estender-se sobre a superfície de forma mais uniforme uma vez que as partículas mais pequenas (parcialmente evaporadas) são mais propensas a serem afetadas pelo efeito de dispersão promovido pelo escoamento cruzado de ar (sendo que no ambiente mais frio, existe uma maior concentração de líquido em volta da zona de impacto).

Por outro lado, o sub-modelo de *breakup* foi construído com recurso a correlações disponíveis na literatura atual. Os resultados das previsões computacionais são comparados com dados experimentais para avaliar a precisão do modelo implementado. Com base nos resultados obtidos, é possível concluir que os resultados computacionais oferecem uma primeira aproximação razoável do fenómeno físico original. Foi proposto um critério de transição para o aparecimento de desintegração para experiências realizadas com jatos contínuos. Este provou ser adequado para as condições testadas e o comportamento geral dos fragmentos originados a partir do processo de *breakup* mostrou uma concordância geral aceitável com as medições.

Além disso, este trabalho oferece uma análise detalhada dos resultados obtidos, sendo que é atribuída uma grande ênfase aos mecanismos de desintegração e características de gotas secundárias. São apresentadas comparações entre os resultados computacionais e experimentais tanto de forma quantitativa como qualitativa. Quando pertinente, o impacto de um determinado sub-modelo para o resultado previsto na simulação é também avaliado através da comparação das versões do código de CFD com e sem o respetivo sub-modelo. Além disso, uma abordagem sistemática é adotada em cada secção para inferir acerca da influência de diferentes parâmetros sobre o resultado final. Esta metodologia revelou-se decisiva para compreender melhor os fatores que afetam os fenómenos decorrentes do impacto.

Contents

List of Figures

List of Tables

Nomenclature

A_i	Cell neighbouring coefficient	
B_M	Spalding mass transfer number	
B_T	Spalding heat transfer number	
C_d	Vapour/air binary diffusion coefficient	m^2/s
C_p	Specific heat capacity at constant pressure	$m^2/s^2/K$
$C_{D,S}$	Drag coefficient based on initial diameter	
C_D	Drag coefficient	
D	Drop diameter	m
d	Spreading diameter	m
D_k	Drop diameter in each parcel	m
D_p	Most Probable secondary droplet diameter	m
D_V	Volumetric mean diameter	m
D_{cs}	Deformed drop characteristic length in the cross-stream direction	m
$\bar{D}$	Number mean diameter	m
E	Drop aspect ratio	
E_D	Dissipative energy loss	$kg\ m^2/s^2$
E_K	Kinetic energy	$kg\ m^2/s^2$
E_S	Surface energy	$kg\ m^2/s^2$
E_{acc}	Accumulated energy	$kg\ m^2/s^2$
F	Convective mass flow per unit area	$kg/m^2/s$;
f	Frequency	Hz
F_D	Aerodynamic drag force	$kg\ m/s^2$
G	Turbulence energy production term	$kg/m/s^3$
g_i	External forces	$kg\ m/s^2$
H_C	Heat transfer coefficient	$kg/s^3/K$
h_d	Thickness of spreading drop	m
k	Turbulent kinetic energy	m^2/s^2
K_C	Mass transfer coefficient	m/s

K_G	Thermal conductivity	$kg\ m/s^3/K$
L	Latent heat of vaporization	m^2/s^2
l_e	Characteristic dimension of an eddy	m
l_r	Length scale of roughness	m
M	Molar mass	
m	Drop mass	kg
$\dot{m}$	Droplet vaporization rate	kg/s
N	Number of particles	
P	Ambient gas pressure	$kg/m/s^2$
p	Probability distribution function shape parameter	
P_0	Atmospheric pressure, 101000 Pa	$kg/m/s^2$
P_{Fs}	Saturated pressure of fuel vapour at the surface temperature	$kg/m/s^2$
q	Probability distribution function scale parameter	
Q_L	Rate of heat transfer to drop from surrounding	$kg\ m^2/s^3$
$\dot{q}_V$	Flux density	m/s
r_k	Radial position in measurement plane	m
r_s	Surface roughness	m
RN	Random Number (min;max)	
S	Source term	
T	Temperature	K
t	Time	s
t^*	Characteristic breakup time	s
t_{bin}	Breakup initiation time	s
t_c	Time taken for the drop height to go from its maximum value of D_0 to 0	s
t_{tot}	Total breakup time	s
U	Velocity	m/s
U^r	Relative velocity between drop and gas in the main flow direction	m/s
u'	Velocity fluctuations	m/s
V	Volume	m^3
x, y, z	Cartesian coordinates	m
Y_F	Fuel mass fraction	

Greek Symbols

α	Impact/Ejection angle	$[^\circ]$
δ_{ij}	Kronecker's delta function	
ε	Turbulence dissipation	m^2/s^3
η	Circumferential angle	$[^\circ]$
Γ	Effective diffusion coefficient	
μ	Dynamic viscosity	$kg/m/s$
ν	Kinematic viscosity	m^2/s
ω_n	Natural frequency of droplet oscillations	s^{-1}
Φ	Dissipation function	
ϕ	General variable property per unit mass	
ρ	Density	kg/m^3
σ	Surface tension	kg/s^2
τ_d	Damping time	s
τ_e	Eddy lifetime	s
τ_i	Eddy-droplet interaction time	s
τ_p	Relaxation time	s
τ_t	Eddy transit time	s
θ	Incident angle	$[^\circ]$
θ_a	Dynamic contact angle	$[^\circ]$
θ_w	Static contact angle	$[^\circ]$
θ_Y	Young contact angle	$[^\circ]$
Δt	Time step	s

Subscripts

∞	Far-field region, ambient conditions
( )	Drop property
0	Initial value (before impact)
bl	Boundary layer
bn	Normal boiling point
core	Core fragment after breakup
cr	Critical

cs	Cross-stream direction
frag	Fragments resulting from breakup
G	Gas/ambient property
Leid	Leidenfrost
LF	Liquid film
max	Maximum
N	Normal component
Ob	Oblique
p	Particle (Drop)
PA	Pure Adhesion
pa	Secondary parcel
PR	Pure Rebound
R	Rebound
ref	Reference
s	Secondary droplets (after impact)
sat	Saturation
sf	Drop surface
shear	Fragments resulting from shear breakup
SMD	Sauter Mean Diameter
sw	Stream-wise direction
T	Tangential component
t	Turbulent
w	Wall

Acronyms and abbreviations

CHF	Critical Heat Flux
DI	Direct Injection
DSF	Deterministic Separated Flow
LIF	Laser-Induced Fluorescence
MMD	Mass Median Diameter
PDA	Phase Doppler Anemometry
PDF	Probability Density Function

PFI	Port Fuel Injector
QUICK	Quadratic Upstream Interpolation for Convective Kinetics
SI	Spark Ignition
SIMPLE	Semi-Implicit Method for Pressure-Linked Equations
SMD	Sauter Mean Diameter
SSF	Stochastic Separated Flow
TAB	Taylor Analogy Breakup
TDMA	Tri-Diagonal Matrix Algorithm

Dimensionless Groups

β	Spreading ratio	d_{max}/D_0
δ	Dimensionless liquid film thickness	h_{LF}/D_0
Λ	Dimensionless time	$U_0 t/D_0$
f^*	Dimensionless frequency	$f/(U_0/D_0)$
h_c	Dimensionless thickness of the lamella at the impact axis	h_d/D_0
K	Splashing threshold parameter	$We\,Oh^{-0.4}$
r_m	Ratio of total splashing to incident mass	m_s/m_0
R_s	Dimensionless surface roughness	r_s/D_0
La	Laplace number	$\sigma\rho D/\mu^2$
Nu	Nusselt number	$H_C D/K_G$
Oh	Ohnesorge number	$\mu/\sqrt{\rho\sigma D}$
Pr	Prandtl number	$C_p\mu/K_G$
Re	Reynolds number	$\rho U D/\mu$
Sc	Schmidt number	$\mu/\rho C_d$
Sh	Sherwood number	$K_C D/C_d$
We	Weber number	$\rho U^2 D/\sigma$

Chapter 1

Introduction

The present thesis is devoted to the numerical study of the fluid dynamic phenomena occurring during the impact of liquid drops onto solid surfaces with the presence of a cross flowing air. Such sequence of events produces complex mechanisms of interaction between the three phases involved which are intended to be simulated by means of an in-house developed computational model.

This chapter enlightens the reader towards the main reasons behind the choice of such topic for the research undertaken (section 1.1), and exposes the main goals established (section 1.2) for the work. This doctoral project has given rise to several publications throughout the course of the study. They are identified and described in section 1.3. In the last section (1.4), the general outline of this document is summarized.

1.1 Motivation

In the context of fluid mechanics, multiphase flows may be considered simply as a fluid flow system consisting of more than one phase or component, having a certain level of separation at a scale well above the molecular level. This leaves a huge spectrum of distinct multiphase flows which can be classified according to the state of the different phases or components: gas-solid, liquid-solid or gas-liquid flow. In this thesis, only the latter combination is addressed since the basic configuration studied here refers to the motion of liquid drops in a moving gas.

Ever since the pioneering studies of Worthington (1876b,a), the impact of liquid drops onto solid surfaces have captured the interest of researchers in numerous fields due to the host of applications where this phenomenon can be found. This includes the ink-jet printing technology, rapid spray cooling of hot surfaces (turbine blades, rolls in rolling mills for steel production, lasers, semiconductor chips, and electronic devices), annealing, quenching of aluminium alloys and steel, fire suppression by sprinklers systems, internal combustion engines (such as intake ducts of gasoline engines and piston bowls in direct-injection diesel engines), incinerators, spray painting and coating, as well as plasma and crop spraying. For this reason, a major scientific effort has been invested in a comprehensive understanding of the phenomena underlying the spray impingement process, whether through experimental, numerical or theoretical analysis. This explains the large number of studies — from quite dissimilar areas — reported in the literature.

Nonetheless, in this recent global context in which increasingly stringent environmental regulations are imposed to the industry in the attempt of promoting sustainable energy policies, researchers have been incited to explore new concepts for energy savings and reduction of pollutant emissions. This concern is particularly relevant in internal combustion engines or gas turbines since the progress achieved in the technological development of such systems relies on the accurate description of the fluid dynamics occurring during spray-wall interactions. However, much of the physical mechanisms involved in such prominent engineering applications are still poorly understood.

Under this context, several questions arise with respect to the dynamic behaviour of the

drops before combustion when the spray injected through a quiescent surrounding onto a dry or wet surface is affected by external variables. In many situations (as, for example, upon intake valve opening in injections systems), a cross stream of air also enters the domain. This new element has a huge repercussion on the dispersion of the drops before and after impact. Moreover, if the air flow rate is high enough, deformation and breakup of the particles will occur before impact. On the other hand, another important concern occurs when the target is hot and thermal effects are significant.

Let us assume now that we are facing a scenario of cold start engine or early/late injections. In such situations, it is common that a significant amount of liquid persists on the piston surface through the compression stroke and, eventually, into the next cycle (Stevens and Steeper, 2001). According to Witze (1996), this fuel film strongly affects the mixing process, causes unstable burn and leads to a decrease in efficiency. However, the description of this mechanism is not trivial. For instance, even though the presence of this liquid layer is important to avoid in the case of the above examples, the emerging research topic related to cooling applications (such as in electronic devices) has shown that the presence of this liquid film is desired here. On the other hand, there are also other applications (such as in spray painting production lines) in which it is important to maintain a uniform layer of liquid over the solid surface.

Even though spray impact phenomena are difficult to analyse in operating engines — because of the problems of access — useful information can be obtained through photographic techniques in specially adapted engines (see e.g. Winterbone et al., 1994). However, the detail of the information that can be obtained with this approach is very limited, and the test conditions are difficult to alter. For this reason, most of the studies reported in the literature still consider simplified conditions in the attempt to better understand the fundamental mechanisms involved in such flows (Arcoumanis et al., 1997; Cossali et al., 1997). A usual assumption is to admit that the spray may be described as the superposition of numerous individual liquid particles. Even though the interaction between drops gives rise to distinct impact mechanisms than a set of non-interactive drops would (Roisman et al., 1999), the simplified approach still provides a precious contribution to the spray impingement comprehension. This is why numerous works can still be found in the literature under these circumstances.

On the other hand, advanced CFD codes are a valuable complement to experimental studies since they allow a detailed local analysis of the flow. Several spray-wall interaction models have been proposed over the past couple of decades. However, the agreement between numerical and experimental results has only been reasonable until this point in past simulations reported in the literature. This lack of accuracy could be somewhat expected since only a few of the proposed spray impingement models (Jafarmadar et al., 2009; Arienti et al., 2011) provide a sufficiently elaborate computational basis that is able to account for the general mechanisms found in the multi-phase flow addressed here. Furthermore, in none of the references cited above the authors contributed with a detailed analysis of the results obtained in terms of the impact outcome or with a quantitative characterization of secondary droplets. Such information is relevant to understand the phenomena occurring during impact, as well as to acquire more information regarding how the interaction between the different elements takes place. Therefore, it is important to try to continue improving the mathematical formulations adopted in computational models in order to replicate more accurately experimental results in a wider range of conditions.

1.2 Objectives

Distinct aspects of the simulation procedure have been targeted over the course of the work. In each case, specific computational extensions have been devised and integrated into the general spray impingement model. This procedure has enhanced the prediction capabilities obtained during the simulations and the model is now able to replicate more accurately some of the physical phenomena that were not captured originally (without the presence of the sub-model).

Therefore, on balance, the major goal of this study is to improve the accuracy of the computational model adopted by our research group to simulate the spray-wall interaction process. Even though punctual numerical models intended to predict the outcome of such multiphase flows have been proposed over the years in the scientific community, it still has to be reached a level of knowledge that allows one to identify the best numerical formulation to achieve the most accurate simulation possible.

The conventional approach used by modellers is to develop fully theoretical models. However, they are often disapproved because they fail to capture some of the mechanisms observed experimentally. This is not surprising given the fact that there are numerous gaps that still remain in the knowledge of the spray impingement topic, which hinders the development of more accurate theoretical models.

On the other hand, numerous simplified experimental studies are continuously being reported in the literature along with new correlations aimed at characterizing particular sets of measurement data. Each correlation is bound up with a vast number of observations — usually merged into one relationship — which are expected to capture the particularities of the flow (at least within the condition for which they have been proposed). This situation has been explored here by examining some of the mathematical expressions and by assessing their performances when they are integrated into a neutral macroscopic computational model.

Furthermore, it is often noticed that distinct expressions are derived by different authors from (partially) coincident boundary conditions. It becomes crucial to determine which of the solutions performs better within a specific interval of impact conditions. Only then one can declare without reserve that specific experimentally-derived correlations provide a sufficiently strong physical base for the formulation adopted in a particular simulation. Accordingly, in each section, the accuracy of the numerical predictions is evaluated by comparing them against experimental data. Once adequate results are achieved (and the model is assumed to be validated), a systematic approach is followed to infer about the influence of singular parameters on the final outcome.

For the sake of clarity, it is important to highlight that, at the end of this research project, it is not expected to have a comprehensive and precise computational model capable of replicating the spray impingement process under any circumstances. Such criterion is not reasonable considering the current understanding of the physical phenomena involved in these multiphase flows. Nevertheless, with the present work, an influential contribution shall be disposed to the permanent bibliography in the form of a computational research by devising new approaches to simulate specific mechanisms of interaction, evaluating experimentally-deduced correlations and analysing the influence of specific parameters on the outcome of spray-wall impacts.

1.3 Contribution

Under the framework of the work performed during the doctoral programme, several publications have been presented to the research community both in scientific journals and interna-

tional conferences.

The first contribution occurred before the beginning of the doctoral works. A bibliographic survey was conducted to identify the most relevant transition criteria for the onset of disintegration after impact of liquid drops onto solid surfaces. These equations have then been integrated separately into the computational model and their performances have been evaluated by comparing the results obtained in each case. Even though some of the equations were derived for coincident impact conditions, perceptible discrepancies could be identified between the correlations attributed by the different authors. For this reason, putting them into a fixed context has allowed us to determine the one that provided the best results in the configuration tested. The content of this study has been presented at international conferences (Silva et al., 2011a,b) and, later, in a scientific journal (Silva et al., 2013). Moreover, the publications also reinforced the importance of defining accurately the deposition/disintegration threshold on the outcome of the spray impingement process.

At this point, it also became clear that the post-impingement events were not accurately described in the literature. For instance, in the simulations performed, considerable discrepancies could be noticed between computational and experimental velocity profiles of secondary droplets. This suggested that the formulation adopted was not adequate. To calculate the velocity of secondary droplets, the methodology relied on the energy conservation concept, before and after impact. This means that kinetic and surface energies of incident drops should match the same energy terms of the fragments plus an additional parcel corresponding to the energy loss through viscous dissipation, which is referred as the dissipative energy loss.

If the estimation of the kinetic and surface energy terms is relatively straightforward and consensual, the same cannot be said for the dissipative energy loss. In fact, it is remarkable to note that there is little literature available related to this particular parameter, even though it plays a critical role in the energy transfer equation (considering that the other terms are fixed and well-established). Most of the dissipative energy loss relationships have been deduced for the spread regime. For this reason, it only accounts for the expansion of the lamella (until it reaches its maximum extent) but disregards the detachments of the secondary droplets from the rim — which characterizes the disintegration process — or the raising of the lamella in the particular case of a corona splash.

Besides considering the above mentioned spread-based equations to model the splashing mechanism, one can also adopt the alternative proposed by Bai et al. (2002), who derived an expression to account for the mechanisms that occur during the splash event. However, even in this approach the authors relied on the assumption that the transition to the disintegration stage — in which secondary droplet start to detach from the rim — is assumed to only take place at the maximum diameter point. This assumption is typical when one considers the deformation stage but lacks of physical support to extend the hypothesis to the onset of splash.

Again, the survey of the several options available in the literature has been accompanied with a detailed analysis of each approach. Then, they have been tested computationally and classified. This study has been carried out during the course of the present thesis and is the precursor of the line of research adopted in this doctoral project. Three papers have been published within the scope of this research subject: some preliminary results have been revealed in the first place at an international conference (Rodrigues et al., 2012a), and then the theme was further explored, giving rise to another participation at an international conference (Rodrigues et al., 2012d) and a publication in a scientific journal (Rodrigues et al., 2013c). In the latter two cases, the major subject addressed has been combined with an in-depth analysis of a near-wall mesh treatment, which corresponded to an alternative way of providing an increment of the

accuracy in the final results without a direct mesh refinement. It is also worth mentioning that the latter publication in the journal *Fuel Processing Technology* (Rodrigues et al., 2013c) has been identified as being of special interest to the energy sector by the Renewable Energy Global Innovations Series (which is a service that alerts the scientific community to breaking journal articles considered to be of importance to the progress in renewable energy technologies) in November 2014.

The subjects addressed in this thesis have not been chosen randomly. Instead, they are intended to bridge the gaps identified in the literature and answer to the requests raised by the scientific community. From those inputs, it has been decided that the next step would be the development of a computational extension that would account for the formation and evolution of the liquid film over the surface due to the deposition of previous liquid particles. The results of this work have shown a clear improvement, as shown in Rodrigues et al. (2012c). The study has later been published in the journal *Atomization and Sprays* (Rodrigues et al., 2012b). The model has been further ameliorated to include a more precise formulation of both the law of momentum conservation (for the evolution of the thin layer distribution over the impingement surface) and the temporal evolution of the liquid film distribution (Rodrigues et al., 2013a).

Even though acceptable results were obtained at this stage, it was also pointed out that due to the lack of comprehensive spray data available in the literature, some difficulties were encountered to replicate accurately the incident drops at the early stages after leaving the injector nozzle. For this reason, the initial conditions of the simulation were not ideal: not having this initial computational environment established with a certain level of precision (in relation to the original spray characteristics provided by the experiments) led to an important additional source of discrepancy that propagated to the ensuing results. Moreover, even though the results obtained were adequate for the conditions simulated, it would still not be possible to infer about the model capabilities in distinct scenarios since only one configuration was tested.

Therefore, at this stage, a different set of experimental data has begun to be employed, which provided both free spray measurements — which were used to determine the initial characteristics of the spray in the simulation procedure — and spray-wall impingement measurements (with crossflow) — which were used as a benchmark to evaluate the prediction results obtained in the simulations. This more comprehensive source of experimental data has also enabled us to test new boundary conditions and, consequently, a distinct flow dynamic. By way of illustration, the simulations revealed that the maximum Weber number of the impinging drops corresponded to nearly half the one obtained in the former circumstances and the viscous forces proved to be much less significant than before. Evidently, these modifications were expected to influence the post-impingement characteristics and, consequently, could cast doubts on the accuracy of the computational model.

However, the agreement between numerical and experimental data proved better than ever before (Rodrigues et al., 2013b). These conditions have been used ever since in our simulations. From this foundation, two recent projects have been successfully undertaken: 1) simulate the deformation and breakup stage, and 2) consider thermal effects during spray-wall impact simulations. Both sub-models should not be regarded as an approach to enhance the accuracy of the model by themselves for the configuration tested. Instead, they are computational extensions that have been attached to the main model and have allowed extending its applicability for a wider range conditions. Under this context, the scenario in which the injected drops are subjected to the influence of a high velocity air crossflow is covered by the former sub-model, whereas the latter may be applied when the surfaces are hot. The two works combined have given rise to three papers that have been presented at international con-

ferences (Rodrigues et al., 2014, 2015b,c). Furthermore, the study that deals with the heat transfer and evaporation of drops has been accepted recently for publication in the *Journal of Thermophysics and Heat Transfer* (Rodrigues et al., 2015a).

1.4 Overview

The present document is organized in six chapters, including this one which provides the context, expectation and corresponding profits of the research undertaken. Chapter 2 is dedicated to the review of the bibliography related to the subject addressed in this thesis. The review of the relevant background and central concepts required for the comprehension of the work is introduced in this chapter and the various phenomena are presented in the following sections.

Chapter 3 presents a detailed description of the methodology adopted in the mathematical formulation of the model. The continuous and dispersed phases are distinguished and their interaction is recognized. The boundary conditions are also identified at this stage.

The basic scenario analysed in this work is the injection of a spray through a crossflow and eventual impact onto a non-heated, dry surface. This simple yet effective configuration gives some important insight into the thermodynamic phenomena occurring during impact. This is explored in Chapter 4 where the initial conditions of the incident drops, the impact mechanisms, and post-impingement characteristics of secondary droplets are discussed. The simulations are based upon a mathematical formulation to which computational extensions may be integrated. This chapter also highlights the main characteristics of these computational extensions developed, which include the liquid film, evaporation and breakup sub-models.

In chapter 5, the results are examined and the practical implications of the study are also discussed. Besides the results obtained after considering each of the three computational extensions mentioned above, the outcome of the adaptive mesh refinement analysis and dissipative energy evaluation are also examined here.

Finally, the last chapter (Chapter 6) summarizes the most important conclusions of this research and presents future work suggestions.

Chapter 2

Literature review

This chapter presents a review of some of the papers dealing with spray-wall impingement. A huge number of contributions have been provided to the available literature over the recent decades. Of this collection of publications, one can distinguish a considerable amount of different research topics, as well as several distinct approaches to the problem. Therefore, it is opportune to establish some criteria defining how the current review is organized. Numerous combinations could be adopted and no perfect solution has necessarily to exist to scrutinize this subject.

Here, the first two sections address the two basic conditions that can be considered in spray-wall impingement: impact of liquid particles onto a dry or wet wall. In section 2.3, a heat load is added to the problem and the corresponding literature review focus on this particular aspect. The last section discusses the deformation and eventual breakup that may occur before impact in situations of high relative velocity between the liquid drops and the crossflow.

2.1 Drop impact onto non-heated, dry surfaces

When a drop collides with an interposed surface, three phases are usually involved: liquid (the drop), solid (the substrate) and gas (the surrounding environment), which may be described by a number of parameters or physical properties. Each injection corresponds to a new set of impact conditions, which leads to a singular outcome. The modelling of this complex multiphase flow, in order to be used in engineering systems, requires a thorough understanding and knowledge of the following research topics: 1) description of the initial conditions of the spray; 2) establishment of the map of impingement regimes and identification of the transition criteria; and 3) characterization of the secondary atomization. Additional complexities may also be considered, such as the existence of a cross flowing gas affecting the dispersion of the liquid particles, multiple drop interaction within the spray or heat transfer between the three phases.

In this chapter, the fluid dynamic mechanisms occurring when a single liquid drop impacts onto a non-heated, dry solid surface is reviewed. Furthermore, emphasis is also placed on the determination of the boundaries between impingement regimes and the characterization of secondary droplets resulting from splash.

2.1.1 Mechanisms of interaction

The characterization of the hydrodynamic phenomena occurring during the impact of drops onto a solid surface is very complex and involves numerous influencing parameters. The main mechanisms are generally classified according to the impact energy and based on the visible morphological characteristics of the impinging drop. The four basic outcomes generally attributed in the literature are stick, spread, rebound and splash. This categorization has been proposed by Bai and Gosman (1995) from the analysis of single drop impacts onto a wall.

The stick regime occurs at very low Weber number, when the impinging particle gently adheres to the wall and nearly maintains its spherical form. Increasing the initial velocity, the

drop may reach an impact energy that can lead it to spread out and form a liquid film over the surface (spread regime). This liquid layer takes the shape of a lamella with visible outer rim. Once the first drops spread, the wall can no longer be considered as being dry and distinct conditions should be applied. It is worth noting that these regimes are often considered as being a single one, denominated as the deposition (or coalescence) regime. Such terminology may also be used in the present document when convenient. When the Weber number is such that the drop bounces off the wall after impact, the rebound regime has been attained. For cold surface conditions, this only happens if the wall is wet, which is true if a spread event has occurred previously around the same location. For very high impact energy, the splash regime takes place with the emergence of a circular crown-like sheet — which forms following to the collision — and the production of secondary droplets from the unstable free rim.

Rioboo et al. (2001) identified new outcomes that were not considered in the approach of Bai and Gosman (1995). Besides the common deposition, rebound and splash regimes, they introduced the receding breakup regime as the result of the disintegration of a receding lamella from which secondary droplets would detach. The authors also divided the disintegration mechanism into prompt and corona splash according to the morphological features observed in their experiments: in the former — which only occurred in rough surfaces — the event was characterized by the generation of secondary droplets directly at the contact line, whereas the corona splash was consistent with the notion previously adopted by Bai and Gosman (1995) for the generic splash regime but was observed mainly in impacts onto wet surfaces. According to Roisman et al. (2006), the threshold condition for the occurrence of corona splash arrived at lower impact values than for the emergence of secondary droplets.

Furthermore, one can find in the literature some new occurrences reported at certain impact conditions: Rioboo et al. (2001) identified a fingering pattern during the spreading phases, whereas Moita and Moreira (2007) reported the existence of a finger breakup regime in highly non-wettable surfaces. This mechanism was observed at moderate impact velocities, being the early expression of instabilities at the fringe of the lamella during the spreading stage. Such fingers-like structures may grow ahead of the contact line and eventually break-up during the last stages of the spreading event. A detailed review of the fingering mechanisms is given by Yarin (2006) and a successful attempt to replicate computationally these structures has been reported by Bussmann et al. (2000). The rebound regime is also subjected to different interpretations: it is sometimes split into partial and total rebound to indicate that all or a portion of the liquid particles bounces off the wall (Rioboo et al., 2001; Šikalo and Ganić, 2006). However, even though this categorization may be more descriptive of the mechanisms occurring during the impact event, most of the investigators do not differentiate the cases (see e.g. Mao et al., 1997; Sommerfeld and Huber, 1999; Jafarmadar et al., 2010). For this reason, the term rebound is used herein to indicate whether there is a complete or partial detachment of the liquid from the wall after initial contact.

Rioboo et al. (2001) also raised some doubts about the validity of applying such explicit and rigid limits between impingement regimes as in Bai and Gosman (1995). Nevertheless, this system of classification based on the impact energy continued to be used across the scientific community. Numerous experimental studies were undertaken to analyse the mechanisms of interaction between liquid drops and solid surfaces. In the vast majority of them, deposition (or spread), rebound and splash were the regimes referred and the nomenclature adopted by the authors (Yarin, 2006; Moreira et al., 2010). Accordingly, Fig. 2.1 shows the corresponding outcomes and morphologies of the liquid drops upon impact onto non-heated, dry surfaces.

From the above, it becomes evident that the occurrence of a particular outcome from drop

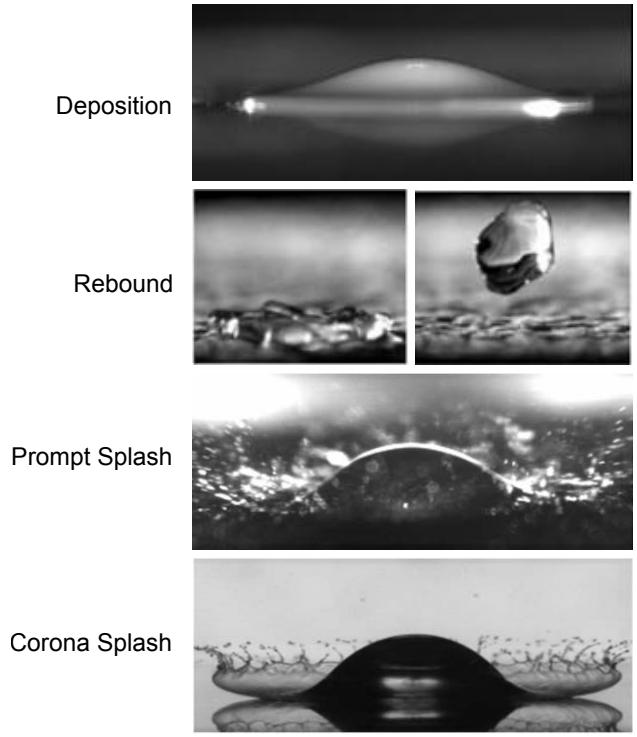

Figure 2.1: Morphology of single drop impacts onto non-heated, dry surfaces. Deposition and rebound images from Rioboo et al. (2001), and splash images from Xu (2007).

impact depends upon the boundary conditions adopted in each case. The spray-wall interactions are affected by a number of parameters, ranging from the characteristics of the incident drops (liquid properties, size, velocity and impact angle), topography of the target surface (roughness, wet/dry condition) and the setting of the gas phase environment (crossflow). Prediction of the exact mechanism involves accounting for the relative magnitude of the forces involved during impact, which are usually grouped in dimensionless numbers. The main dimensionless groups governing drop impact that have been employed in the present work are presented in Table 2.1, where D_0 and U_0 are the diameter and velocity of the incident drop, and ρ, μ and σ stand for the liquid density, viscosity, and surface tension, respectively.

Table 2.1: Main dimensionless groups governing drop impact.

Dimensionless Numbers	Physical Significance	Expression	Relation
Weber Number	Inertial Forces/Surface tension forces	$We = \frac{\rho U_0^2 D_0}{\sigma}$	
Reynolds Number	Inertial forces/Viscous forces	$Re = \frac{\rho U_0 D_0}{\mu}$	
Ohnesorge Number	Viscous forces/Surface tension forces	$Oh = \frac{\mu}{\sqrt{\rho \sigma D_0}}$	$Oh = \frac{\sqrt{We}}{Re}$
Laplace Number	Surface tension forces/ Momentum transport	$La = \frac{\rho \sigma D_0}{\mu^2}$	$La = \frac{Re^2}{We} = Oh^{-2}$

The impact angle, α_0, is formed by the angle between the absolute velocity vector of the incident drop and the surface of impact, as depicted in Fig. 2.2. Alternatively, the injected particles can also be characterized by the incident angle, θ_0, which is the angle between the

absolute vector and the normal to the surface. Upon impact, secondary droplets may be produced, with the ejection angle, α_s, being the angle between the absolute velocity vector of the secondary droplets and the targeted surface.

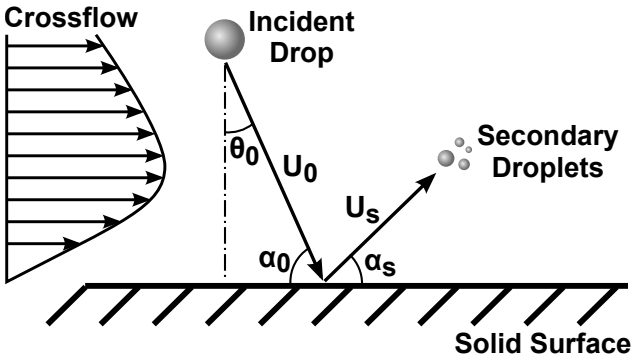

Figure 2.2: Schematic diagram of the angles involved in spray impingement situations.

In the present document, the fragments produced by the disintegration mechanisms that occur during the splash regime are designated as ”droplets”, whereas the incident liquid particles injected into the flow field are denominated as ”drops”. Such terminology enables us to implement a clearer distinction between the two collections of particles. The word ”particle” is also employed in some occasions instead of drop/droplet (depending on the context) for ease of reading. Furthermore, the subscripts ”0” and ”s” have been used to represent the state before impact and after the splash event, respectively. This nomenclature has been kept throughout the thesis. Note that in some occasions, more than one subscript may be attributed to a particular parameter. When such situation occurs, the subscripts are identified consecutively according to the states that are being referenced.

A good knowledge of the pre-impingement conditions is crucial to better control and understand the phenomena occurring during impact. This assertion has led investigators to study the influence of each parameter individually. Most of the researches reported in the literature still consider simplified conditions in the attempt to better understand the fundamental mechanisms involved in such flows. A usual assumption is to admit that the spray may be described as the superposition of numerous individual drops. Even though the interaction between the drops that construct the spray gives rise to distinct impact mechanisms than a set of non-interactive drops would (Roisman et al., 1999), it still provides a precious contribution to the spray impingement comprehension. For this reason, there are still numerous works under these circumstances (see e.g. Moita and Moreira, 2007; Hwang et al., 2010).

One of the first experimental studies with the aim of investigating the effect of a certain input variable on the products of impact has been undertaken by Stow and Stainer (1977). However, the work has only been completed when Stow and Hadfield (1981) examined, in a systematic manner, the influence of changes in both impact velocity and size of the incident drop on the dynamics of impact. Besides having reported the significance of both parameters in the results, the investigation provided also some insight into the importance of accurately describing the nature of the target surface. In fact, several authors attributed to the surface roughness a crucial role in the development of the impact dynamics (Levin and Hobbs, 1971; Mundo et al., 1995; Vander Wal et al., 2006b). However, such consequences are mainly reflected on the critical thresholds between impingement regimes and on the post-impingement stage, as discussed in Section 2.1.2 and 2.1.3, respectively. More recently, the research has been extended to drop collisions onto complex surfaces (Marengo et al., 2011; Unnikrishnan et al.,

2014) and geometrically distinct target structures (Shim et al., 2009; Liu et al., 2012).

At the same time, attention has been directed towards the concept of wettability of the surface. This thermodynamic property of the liquid-solid-vapour system quantifies the tendency of a fluid to spread on or adhere to a solid surface. It is usually characterized by the contact angle, θ_w, which can be defined $-$ in simplistic terms $-$ as the angle between the tangent to the liquid-vapour interface and the surface of the solid wall. Values of θ_w vary inversely with mutual attraction and ease of wetting, and can range from $0°$ to (theoretically) $180°$. Therefore, $\theta_w = 0°$ corresponds to a complete wetting system, whereas $\theta_w = 180°$ would mean that the liquid would not have any degree of bonding with the solid. Such condition has already been rejected by a host of early experiments whose conclusions stated that there is always some degree of adhesion of any liquid to any solid (Zisman, 1964).

The closest to this theoretical condition of complete non-wetting system may be achieved by employing liquid repellent surfaces. Recently, studies concerning surface with high hydrophobicity have been reported in the literature with contact angles that could go up to $175°$. According to Antonini et al. (2012), such superhydrophobic surfaces (SHS, which are usually characterized by having a contact angle greater than $150°$ and a contact angle hysteresis lower than $10°$) present different phases of drop spreading and reveal distinct time scales than surfaces with a lower degree of hydrophobicity. Rioboo et al. (2008) identified four outcomes from drop impact onto SHS: deposition, rebound, sticking and fragmentation. The authors also proposed a corresponding map of the outcomes, which revealed that while the onset of fragmentation is governed by the Weber number alone (being the threshold We value near 60), the deposition/rebound transition depends upon the Weber number and on two solid surface parameters: the average contact angle (which is the average between the advancing and receding contact angles) and the contact angle hysteresis, $\Delta\theta$.

Between the two extremes (complete wetting and non-wetting), partial wetting and non-wetting systems may be achieved for contact angles ranging from $0°$ to $90°$ and $90°$ to $180°$, respectively. Figure 2.3 illustrates the concept of contact angle for an ideal surface and the corresponding morphology of the drops in each of the four conditions exposed.

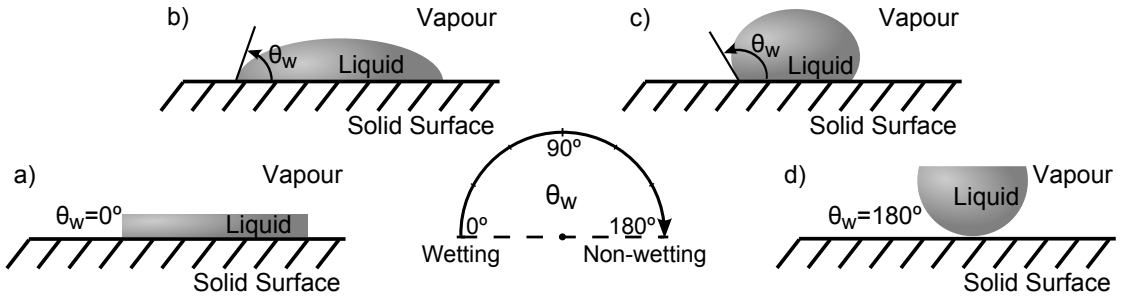

Figure 2.3: Possible contact angles of a drop impacting onto an ideal surface: a) complete wetting; b) partial wetting; c) partial non-wetting; d) complete non-wetting.

Other questions arise concerning the dynamic behaviour of the particles prior to impact. For instance, the role of the crossflow has been the subject of numerous studies. This cross stream of gas has been found to affect directly the dispersion (and eventual disruption) of the incident drops before impact (Opfer et al., 2011; Zhang et al., 2013), as well as the impact dynamics and the secondary atomization (Panão and Moreira, 2005a; Panão et al., 2013). Additional concerns are related to the film liquid that may form over the impingement wall (such conditions is then referred to as wet wall), the heat transfer occurring when the walls are hot, and the atomization process taking place when incident drops are injected with a high

relative velocity between drop and gas. However, each point is discussed more thoroughly in sections 2.2, 2.3 and 2.4 of the present chapter.

2.1.2 Transition criteria

The outcome of drop impacts onto a solid wall depends upon the impingement conditions under consideration. Extensive efforts have been directed towards providing experimental evidences that allow one to distinguish the different morphologies of the drops after impact. Accordingly, empirical correlations have been proposed to establish the transition criteria between impingement regimes. Such equations are used to define the boundaries that delimit the impact events.

The transition criteria include combinations of different dimensionless parameters characterizing the relative magnitude of the forces acting on the particle. The most popular are the Weber (We), the Reynolds (Re), the Ohnesorge (Oh) and the Laplace (La) numbers. Once a critical threshold has been exceeded, the following regime ensues with the corresponding mechanisms of interactions taking place. This numerical value depends upon parameters, such as the impingement conditions (size, velocity and impact angle of the incident drop), the fluid properties (density, viscosity and surface tension), and the surface topography (roughness, liquid film thickness, etc.).

Most of the existing transition criteria have been developed for the splash regime which, according to Stow and Hadfield (1981), depends upon the Ohnesorge and Weber numbers only. Therefore, the splash threshold is assumed to be governed by a single composite group called the "splashing parameter":

$$K_{cr} = WeOh^{-0.4} \tag{2.1}$$

This combination of Oh and We has been found to provide an appropriate measure for the deposition/splash threshold. Since then, most of the correlations proposed in the literature have been written in accordance with this parameter or with slight modifications to the original equation.

The earliest report of a critical threshold for a drop impacting onto a dry surface has been attributed to Stow and Hadfield (1981). A series of impacts were examined for a specified range of drop diameters and velocities. It was found that for the surface under consideration the splash threshold was invariant with both parameters. From the same collection of measurements, Bai and Gosman (1995) were able to derive a correlation for the deposition/splash limit, which can be expressed as follows:

$$WeOh^{-0.366} = A \tag{2.2}$$

where A is a coefficient that depends upon the surface roughness (in their study $A = 2630$). Note that Eq. 2.2 presents some modifications relative to the splashing parameter: although the weight given to the Ohnesorge group is slightly lower, the major difference has to do with the fact that the authors take into account the surface roughness as an influencing parameter in the splashing event (through the fitting constant A).

According to Vander Wal et al. (2006b), the effect of a rough surface upon the splash boundary is to dramatically lower the critical threshold of splash. Furthermore, differences in surface tension and viscosity become far less significant in determining both the splashing threshold and the subsequent dynamics which become very similar for all fluids. Therefore, it is expected that as the dimensionless surface roughness, R_s, increases, the fitting constant in

Eq. 2.2 decreases. This behaviour is in accordance with the typical values adopted by Bai and Gosman (1995).

Mundo et al. (1995) were able to notice a clear boundary between deposited and splashing droplets for both smooth and rough surface which could be correlated by $K_{cr} = 57.7$. A value of K greater than 57.7 resulted in splashing, whereas below that threshold complete deposition of the drops was detected. Meanwhile, this parameter has been used in several spray impingement models for the splashing threshold (such as in Lee and Ryou, 2000; Grover and Assanis, 2001; Yoon and DesJardin, 2006). Later, Vander Wal et al. (2006c) tested several combinations of Oh, Re and We numbers to obtain the most comprehensive collection of measurements possible for drops impacting upon a dry surface. The following power-law correlation was drawn from the data available:

$$WeOh^{1.285} = 0.577 \tag{2.3}$$

which proved effective in defining the boundary between splash/non-splash regimes within the impingement conditions tested ($0 < Re < 7500$). By taking advantage of the coefficients derived by Vander Wal et al. (2006c), Liu et al. (2010) proposed a semi-empirical splash threshold correlation:

$$WeOh^2 = 65.05\,(P/P_0)^{-1.68} \tag{2.4}$$

which is similar in form to the previous equations but extends the range of applicability to non-atmospheric air pressures.

Others proposals have also been reported contemplating only the variables included in the Weber number as influencing variables on the splash phenomenon. For instance, Park and Watkins (1996) used the experimental data of Wachters and Westerling (1966) to propose a splash threshold based solely on the Weber number ($We_{cr} = 80$). Even though the approach was based on a set of measurements obtained from drops impacting onto a hot surface, they were tested in cold impact conditions. Similarly, Gavaises et al. (1996) adapted the previous value to their own experimental data, giving rise to a critical Weber number of 100. However, more recently Roisman (2009) suggested that the Weber number would only be sufficiently rigorous to describe the phenomenon if viscous effects were negligible.

It is worth highlighting that in most of the critical Weber numbers adopted to represent the onset of splash, the velocity of the primary drops is given exclusively by the normal component of the variable. In fact, a number of studies reported that the splash mechanism was only influenced by the normal momentum component (Mundo et al., 1995; Senda et al., 1999). However, this finding was called into question by Okawa et al. (2008) who observed in their experiments a noticeable influence of the impingement angle on the outcome of single water drop impact. More recently, Liu et al. (2010) attributed the onset of splashing to the relative velocity between the spreading drop and the surrounding gas. Even though only a small minority of references conflicts with this consensus, care must be taken when adopting such assumption.

2.1.3 Post-impact characterization

Once the drop reaches the solid substrate, one of the above mentioned impingement regimes ensues. There is a great number of studies addressing the detailed description and analyses of both spread and splash regimes. In the former, once the drop impacts onto a solid surface, a lamella is formed which spreads out radially until the drop spreading diameter reaches a

maximum. During this stage, the drop evolves from a sphere to a cylinder-like shape. Its development is determined by the flow in the lamella and the propagation of the rim over the surface (Roisman et al., 2002). Rioboo et al. (2002) classified the different stages of spreading as the kinematic, spreading, relaxation and wetting/equilibrium phases. The authors revealed that the importance of the influencing parameters varied in each phase of the process.

The kinematic phase corresponds to the earliest stage of impact, when no noticeable lamella propagates radially from the base of the drop ($t^* < 0.1$). According to the authors, this phase has been found to be completely described by the impact velocity and initial diameter of the drop only.

Then follows the spreading phase in which a lamella is ejected from the base of the drop and forms a thin film bounded by a rim until it reaches its maximum extension. Here, inertial forces are still driving the flow, but now viscous dissipation and wettability effects are no longer negligible. It quickly became evident among researchers that the maximum spreading diameter (d_{max}) had a crucial role on the ensuing mechanisms upon impact. Mao et al. (1997) found out that the tendency to rebound correlated well with this parameter, whereas Chandra and Avedisian (1991) associated the maximum spreading diameter to the energy dissipated during the spreading phase and underlined the large implications of the parameter on the post-impingement occurrences.

Therefore, estimation of the maximum spreading diameter has been attempted by several researchers either by using numerical methods or energy conservation techniques. Regarding the second group, the approach is based on an energy conservation principle with consideration of the pre-impact conditions and final stages of deformation:

$$E_{K0} + E_{S0} = E_{Ks} + E_{Ss} + E_D \tag{2.5}$$

In this energy balance, kinetic (E_{K0}) and surface (E_{S0}) energies of the incident spherical parcels are equated to the kinetic (E_{Ks}) and surface (E_{Ss}) energies of the liquid after impact plus the energy dissipated (E_D) during the entire process. The initial kinetic and surface energy equations are given by:

$$\begin{aligned} E_{K0} &= \left(1/2\,\rho U_{0N}^2\right)\left(1/6\,\pi D_0^3\right) \\ E_{S0} &= \pi D_0^2 \sigma \end{aligned} \tag{2.6}$$

After impact, if one considers the instant immediately after the maximum spreading diameter has been attained, the kinetic energy is zero. On the other hand, the surface energy can be written as follows:

$$E_{Ss} = \left(1/4\,\pi d_{max}^2\right)\sigma\left(1 - \cos\theta_w\right) \tag{2.7}$$

Major differences in the models proposed in the literature have to do with the problem simplifications and assumptions adopted, as well as handling of the viscous energy dissipation term. As far as the former matter is concerned, Roisman et al. (2009) reported that most of the theoretical works consider that: 1) the flow in the disk can be described assuming the energy balance of the entire deforming drop; 2) the characteristic thickness of the disk is a function of the Weber and Reynolds number; and 3) the liquid film expands uniformly as a cylindrical disk with specific diameter and height (and, consequently, the drop shape is assumed to be a disk the moment the drop diameter reaches its maximum value). In view of the latter assessment, from mass balance — and at the time corresponding to the maximum spreading — the thickness

of the deformed drop (h_d) may be related to d_{max} in the form:

$$h_d = \frac{2}{3}\frac{D^3}{d_{max}^2} \tag{2.8}$$

However, the above relation has been proved to be inaccurate for certain conditions (Roisman et al., 2002, 2009). For this reason, Roisman et al. (2002) advanced with a new model in which a complex shape was assumed. Rather than a simplistic regular disk, the lamella presented a non-uniform thickness and was bounded by a thicker rim. As a result, an equation for the time evolution of the drop diameter and an approximate model for the maximum spreading diameter were derived. It was found that the theoretical predictions agreed well with available experimental data. Based on this more accurate shape of the deformed drop, Roisman et al. (2009) proposed a dimensionless thickness (h_c) of the lamella at the impact axis (scaled by the drop diameter D_0):

$$\begin{aligned} h_c &\approx 1 - \Lambda && at\ \Lambda < 0.4 \\ h_c &\approx \left(\frac{0.39}{0.25 + \Lambda}\right)^2 && at\ 0.7 < \Lambda < \Lambda_{viscous} \end{aligned} \tag{2.9}$$

instead of Eq. 2.8, which was found to provide a poor agreement over the entire time period in which the spreading and receding stages occur. Therefore, the authors used a set of experimental and numerical data available in the literature to establish correlations for h_c. As suggested by Eq. 2.9, two regimes are identified within the stage of deformation which, in its turn, is bounded by the limit $\Lambda = \Lambda_{viscous}$. In other words, in this stage, the authors considered that the viscous stresses are not very significant. Furthermore, in the initial phase of drop deformation the correlation proposed was a linear function of time, whereas during the second stage the drop height followed the inverse square dependence of time given by the remote asymptotic solution of Yarin and Weiss (1995). The combination of both equations was found to provide a good fit of the experimental and numerical data evaluated for the first and second non-viscous regime of the drop deformation stage.

The second source of major differences in the models has to do with the treatment of the energy dissipation term. It is the last equation in the energy balance that needs to be defined. Chandra and Avedisian (1991) reported that the dissipative energy loss is directly proportional to viscosity. The authors approximated this energy lost in deforming the drop against viscosity by using the following expression:

$$E_D = \int_0^{t_c} \int_V \Phi \, \mathrm{d}V \, \mathrm{d}t \approx \Phi \, V \, t_c \tag{2.10}$$

where the dissipation function Φ is given by:

$$\Phi = \mu \left(\frac{\partial U_i}{\partial x_j} + \frac{\partial U_j}{\partial x_i}\right)\frac{\partial U_i}{\partial x_j} \approx \mu \left(\frac{U}{h_d}\right)^2 \tag{2.11}$$

and t_c (period taken for the drop to spread out until reaching its maximum extension) is estimated as:

$$t_c \approx D_0/U \tag{2.12}$$

which is a time scale characteristic of convection. Note that the parameter h_d is the drop height during spreading. Combining Eqs. 2.10 to 2.12, and considering the volume of the liquid in the drop once it has flattened out in the shape of a disk, yields:

$$E_D = \frac{1}{4}\pi\mu\left(\frac{U}{h_d}\right)D_0 d_{max}^2 \tag{2.13}$$

Since then, several investigators took the assumptions of Chandra and Avedisian (1991) to estimate the energy dissipation and tried to improve the accuracy of the theoretical model. Pasandideh-Fard et al. (1996) assumed that the overestimation of the maximum spreading diameter was connected to incorrect assumptions associated with the viscous dissipation term. Therefore, the authors replaced the splat drop thickness in the dissipation function Φ by the boundary layer thickness h_{bl} at the solid-liquid interface, calculated as:

$$h_{bl} = \frac{2D_0}{\sqrt{Re}} \tag{2.14}$$

This new length scale allowed the authors to deal with the overestimation of d_{max}. Moreover, the authors adopted a new approach to determine t_c based on new considerations about the drop shape, resulting in:

$$t_c = \frac{8}{3}\frac{D_0}{U} \tag{2.15}$$

Introducing Eqs. 2.14 and 2.15 into Eq. 2.10 yields:

$$E_D \approx \frac{1}{3}\pi\rho U_0^2 D_0 d_{max}^2 \frac{1}{\sqrt{Re}} \tag{2.16}$$

d_{max} is often normalized by the original diameter of the incident drop, resulting in a maximum spreading ratio, β_{max}. Combining all the energy terms, Pasandideh-Fard et al. (1996) was able to propose an expression for β_{max}, as follows:

$$\beta_{max} = \sqrt{\frac{We + 12}{3\left(1 - \cos\theta_a\right) + 4\left(We/\sqrt{Re}\right)}} \tag{2.17}$$

where θ_a is the dynamic advancing contact angle at the maximum spread. Other contributions include the work of Madejski (1976) which has been one of the first analytical study for predicting β_{max}. The model accounted for the effect of viscous energy dissipation and surface tension in determining the spread of a liquid drop during the splat-quenching solidification process. Several years later, Bennett and Poulikakos (1993) referred to it as "the most advanced treatment of the drop deformation problem". The final relation for β_{max} when freezing is precluded from analysis (i.e., drop spread termination is dictated exclusively by surface tension and viscous energy dissipation) is given as:

$$\frac{3\left(\beta_{max}^2 - 4\right)}{We} + \frac{1}{Re}\left(\frac{\beta_{max}}{1.2941}\right)^5 = 1 \tag{2.18}$$

However, the equation performed badly when compared against experimental data. Bennett and Poulikakos (1993) pointed out that such deficiencies could be overcome by incorporating the surface energy terms (both before and after impact) as in the work of Chandra and Avedisian (1991).

Ukiwe and Kwok (2005) presented a comparative analysis of several models available in the literature (including the above mentioned models of Madejski (1976); Pasandideh-Fard et al. (1996); Roisman et al. (2002)) for the maximum spreading diameter of liquid drops upon impact onto solid surfaces. The results were compared against experimental data for a specific interval of boundary conditions. It was found that the model of Pasandideh-Fard et al. (1996) agreed

well with the data. However, the authors observed that drop impact dynamics were influenced by impact energy and physical properties of the liquid drops, as well as solid surface tensions. Modifying the expressions to account for the influence of such parameters, it was possible to obtain an even better agreement. The corresponding maximum spreading ratio was achieved with:

$$(We + 12)\,\beta_{max} = 8 + \beta_{max}^3 \left(3\,(1 - \cos\theta_Y) + 4\frac{We}{\sqrt{Re}}\right) \tag{2.19}$$

where θ_Y is the Young contact angle. More recently, Roisman et al. (2009) suggested that the energy balance approach could be applied to the description of the dynamics of drop spreading only if the edge effects were considered accurately. The same authors, in a different paper (Roisman, 2009), contributed with a new model in which the influence of the rim was included in their approach to estimate the maximum drop diameter. The authors proposed the following semi-empirical relation based on the simple fit of the experimental data available in the literature using a linear combination of the maximum spreading diameter and rim relative velocity equations:

$$d_{max}/D_0 \approx 0.87Re^{1/5} - 0.40Re^{2/5}We^{-1/2} \tag{2.20}$$

As the ratio of the viscous force to the surface tension was negligibly small in the considered measurements, the effect of the viscous stresses on the rim velocity was neglected in their analysis. Therefore, the proposed scaling relation was only valid for very viscous liquid or very small drops. Similarly, Eggers et al. (2010) considered two distinct regimes within the spreading phase: one where viscosity may be neglected so that surface tension is the only influencing parameter; whereas the other viscous dissipation dominates surface tension, and the maximal diameter appears as a balance between inertia and viscosity. Both relations are given as:

$$\begin{aligned} \beta_{max} &\approx (We/6)^{1/2} \qquad low\text{-}viscosity\ regime \\ \beta_{max} &\approx C_v Re^{1/5} \qquad high\text{-}viscosity\ regime \end{aligned} \tag{2.21}$$

where $C_v = 1.113$. This approach had already been followed several years before when Mao et al. (1997) proposed an empirical equation using the same principles as in Chandra and Avedisian (1991) except for the estimation of the dissipative energy loss, for which they considered two regimes: low and high viscosity regimes. Therefore, the authors were able to cover a large domain of We and Oh numbers, by using the following empirical equations:

$$\begin{aligned} \left(\frac{1}{4}\,(1 - \cos\theta_w) + 0.35\frac{We}{\sqrt{Re}}\right)\beta_{max}^3 - \left(\frac{We}{12} + 1\right)\beta_{max} = -\frac{2}{3} \qquad & low\text{-}viscosity\ regime \\ \left(\frac{1}{4}\,(1 - \cos\theta_w) + 0.20\frac{We^{0.83}}{Re^{0.33}}\right)\beta_{max}^3 - \left(\frac{We}{12} + 1\right)\beta_{max} = -\frac{2}{3} \qquad & high\text{-}viscosity\ regime \end{aligned} \tag{2.22}$$

After the spreading phase, the drop undergoes the relaxation phase, which may have different outcomes, depending mainly upon the magnitude of the receding contact angle. The excess of surface energy at the end of spreading leads to a receding movement of the liquid. The wettability effects are quite important at this stage because the recoiling velocity is much smaller than the spreading velocity (due to the viscous dissipation during the process). If the drop manages to dissipate its excess internal energy during both spreading and recoiling phases, the lamella decelerates continuously until it reaches a stable diameter (equilibrium phase). On

the other hand, if the energy dissipated is small, the system may remain at the end of the recoiling phase with a positive energy balance (excess of energy). The consequence is the occurrence of rebound, whose regime is characterized by taking place only in non-wetting systems (Mao et al., 1997). For highly wetting surfaces, the lamella continues slowly to wet the surface, giving rise to the wetting phase as identified by Rioboo et al. (2002).

For very high impact energy, the splash regime ensues. Splash is usually identified when at least one secondary droplet is created from the disintegration of the incident particle upon impact onto the surface. Different types of disintegration mechanisms have already been distinguished in the present work. Each of these regimes gives rise to a collection of secondary droplets with distinct characteristics (in terms of size and velocity), which has a crucial influence on the spray-wall interaction outcome. For this reason, it is of utmost importance to achieve a comprehensive knowledge of the phenomena occurring during splash. The relevance of this concern is also demonstrated by the number of studies published recently with the purpose of either identifying the transition criterion that define the onset of disintegration, describing the different stage of the referred regime, or characterizing the secondary droplets created from the impact.

One of the earliest reference to the splash phenomenon has been attributed to Worthington (1876b,a) back in the second half of the 19$^{\text{th}}$ century. The author is known for his extensive research on this particular area of fluid mechanics and his work has been compiled in a book (Worthington, 1908) with almost 200 sketches of drops.

Levin and Hobbs (1971) and Stow and Stainer (1977) also attempted to characterize the splash regime by means of experimental studies. In both cases, the authors reported that the size distribution function of secondary droplets obeyed the log-normal distribution, which is given by:

$$f(D) = \frac{1}{\sqrt{2\pi}\gamma D} \exp\left(-\frac{1}{2}\left(\frac{\ln D/D_p}{\gamma}\right)^2\right) \tag{2.23}$$

where D_p is the most probable value for the diameter of secondary droplets (or, alternatively, the logarithmic mean diameter) and γ is the standard coefficient in the log-normal distribution functions that characterizes the width of the distribution curve (can also be replaced by the variance instead).

A random variable is usually approximated with a log-normal distribution when it can be considered as the multiplicative product of many independent random variables. The fact that this distribution has been found to fit the experimental data in several studies suggests that the disintegration process has a multiplicative nature. This function is semi-empirical in nature and has been chosen because it matches the observed shape of the diameter distribution of secondary droplets. Samenfink et al. (1999) reached the same conclusion in their experiments with distilled water drops impacting onto a shear-driven liquid film deliberately created onto a surface. Wu (2003) went one step further and conducted physical and thermomechanical analyses to estimate the most probable diameter and width of the distribution: the two free parameters contained within the log-normal distribution. This approach prevents the need to rely on experiments to obtain both values. Applying the derived parameter to the log-normal distribution function, it yields

$$f(D) = \frac{\sqrt{3}}{\sqrt{\pi}D} \exp\left(-3\left(\ln\frac{D}{D_p} - \frac{1}{6}\right)^2\right) \tag{2.24}$$

which was found to compare reasonably well with known experimental data when gravitational force becomes negligible. It is worth highlighting that for $10 < We^2/Re < 50$, the fraction D_p/D_0 may be simplified by $19.86K_{cr}^{-0.5}$, which removes the variable D_p from the equation.

A second approach to describe secondary atomization is based on a purely empirical method in which the data is approximated by a "standard" empirical distribution. There is a sizeable collection of such functions (namely Rosin-Rammler, Chi-Square, and Nukyiama-Tanasawa) which gives the possibility to select the form that best fits the particular set of data in consideration. In this case, the general distribution function can be expressed as:

$$f(D) = \left[\frac{q}{\overline{D}}\left(\frac{D}{\overline{D}}\right)^{p}\right]\exp\left[-\left(\frac{D}{\overline{D}}\right)^{q}\right] \tag{2.25}$$

where p and q are adjustable parameter to fine-tune the shape and the scale, and $\overline{D}$ shifts the size distribution within its range (Moreira and Panão, 2011). In the case of the Rosin-Rammler (or Weibull) distribution, the parameter p is replaced by $q-1$, whereas in the Chi-Squared case p and q should be replaced by the values 0 and 1, respectively.

Bai et al. (2002) adopted the Chi-square distribution function to fit their data for the secondary droplet sizes. The authors identified the parameter $\overline{D}$ as the number mean diameter, which was defined as follows:

$$\overline{D} = \frac{D_V}{6^{1/3}} = \frac{D_0}{6^{1/3}}\left(\frac{r_m}{N_s}\right)^{1/3} \tag{2.26}$$

where D_V is the volumetric mean diameter and r_m is the ratio of the splashed to incident mass (m_s/m_0). The latter parameter is determined randomly according to a most-likely range of variation identified from experimental data. Accordingly, r_m, can be estimated as:

$$r_m = \frac{m_s}{m_0} = 0.2 + RN(0;C) \tag{2.27}$$

where RN corresponds to a random number between 0 and the value of the constant C, which is 0.6 for a dry wall and 0.9 for a wet wall. In the wet surface scenario, the ratio can take values greater than 1 since the liquid film can transfer liquid to the splashing particles (Panão and Moreira, 2005b).

As an alternative to the above mentioned empirical methods, two analytical approaches for predicting size distributions have been developed: the maximum entropy (ME) method, and the discrete probability function (DPF) method. The major difference between them is that whereas the ME method relies on a non-deterministic physical interpretation of the drop generation process, the DPF method divides the spray formation process into deterministic and non-deterministic portions. However, neither of the analytical approaches have been addressed in the present work, which focus instead on the more empirical method. Nevertheless, for those interested in the subject, the thorough review provided by Babinsky and Sojka (2002) is advised.

For the estimation of the total number of secondary droplets, Bai et al. (2002) obtained the following correlation by fitting the data of Stow and Stainer (1977):

$$N_s = a_0\left(\frac{We}{We_{cr}} - 1\right) \tag{2.28}$$

in which $a_0 = 5$ and We_{cr} is the critical Weber number for which disintegration occurs.

Many other important contributions have been advanced by different investigators for the estimation of the total number of secondary droplets resulting from splash, as identified in Table 2.2. Although both correlations of Park and Watkins (1996) and Lee and Ryou (2000) are

based on the experimental data of Naber and Farrel (1993), they still differ from each other by the value attributed to the intercept constant. In its turn, Mundo et al. (1997) established a correlation from their own measurements of drops impacting onto a dry surface.

The last piece of information regarding the characteristics of secondary droplets has to do with the determination of the velocity profile of the splashing droplet. According to Mundo et al. (1995), the velocity distribution of the ejected droplets has a remarkable strong dependence upon the impingement kinematics of the incident particles.

The most common way to calculate the velocity of the droplets is by applying the energy conservation law. As in the spreading phase, the kinetic and surface energy of the incident drop should balance the kinetic and surface energy of splashing droplets and the dissipative loss due to the action of viscosity. The splash kinetic energy is the unknown quantity (from which the velocity parameter will be calculated), whereas the remaining terms are easily determined with the exception of the energy dissipation parameter for which attention must be directed towards. As already discussed in this section, some recent effort has been applied in this field with the purpose of improving the accuracy of the approaches used to determine this parameter. However, most of the dissipative energy loss relationships have been deduced exclusively for the spread regime, which excludes any form of disintegration of the original drop.

Although there are no studies that confirm this issue, it should be fair to say that the energy loss in the splash regime is greater than in the spread regime as it should account for the energy lost during both the expansion of the lamella (and eventually the receding stage also) and the detachment of the secondary droplets from the rim (for corona splash, the crown emergence should also carry an additional amount of viscous loss). One of the few works that really addressed this subject has been provided by Bai et al. (2002), in which the dissipative energy loss parameter is expressed as:

$$E_D = \max\left(0.8E_{K0}; \frac{We_{cr}}{12}\pi\sigma D_0^2\right) \tag{2.29}$$

The authors deduced their own relationship for the dissipated energy in terms of the critical Weber number, but due to the under-estimation of the values in certain ranges of application, the parameter was then limited by a postulated value of 80% of the kinetic incident energy based on the normal incident velocity of the drops.

Similarly, Lee and Ryou (2000) determined the total velocity of droplets after impingement by using a dissipative energy correlation deduced from particular experimental data which is as follows:

$$E_D = \left(\frac{K_v C_w We_{0N}\beta_s^4}{r_m Re_{0N}} - \frac{12C_w}{r_m}\right) \tag{2.30}$$

where K_v is a constant (with value 4.5) and C_w is given by $(r_m/N_s)^{1/3}$. Here, the splash event is assumed to initiate at the moment the maximum spreading extension is reached and immediately before the disintegration process occurs (whether by prompt fragmentation of the rim or the emergence of the crown and formation of secondary droplets). For this scenario, Yarin and Weiss (1995) reported that the diameter of the drop when splash begins is twice the diameter of the original drop, which yields $D_s = 2D_0$.

By employing a collection of different experimental data, Roisman et al. (2006) also proposed an empirical model for the secondary spray, for which the energy lost due to viscosity is also estimated. The authors referred that the energy lost due to viscosity can influence the magnitude of the absolute velocity of secondary droplets. Therefore, the characteristic dissipative

Table 2.2: Post-impingement characteristics of secondary droplets adopted in dry wall impact models.

References	Velocity of Secondary Droplets	Size of Secondary Droplets	Number of Secondary Droplets	Observations
Park and Watkins (1996)	$U_{sT,1} = U_{0T} + \xi\, 0.835(3.096 - 2\chi)U_{0N}$ $U_{sT,2} = U_{0T} - \xi\, 0.835(3.096 - 2\chi)U_{0N}$ $U_{sN} = -\left(\frac{\sigma We}{\rho D_0}\right)^{0.5}$	$D_s = \frac{D_0}{N_s^{1/3}}$	$N_s = (0.187\, We - 14.0)\, N_0$	$K_{cr,mod} = We = 80$ $\chi \cong 1$ $\xi = RN(0;1)$
Mundo et al. (1997)	$U_{sT} = \left[1.337 - 1.318\frac{D_s}{D_0} + 2.339\left(\frac{D_s}{D_0}\right)^2\right] U_{0T}$ $U_{sN} = \left[0.249 + 2.959\frac{D_s}{D_0} - 7.794\left(\frac{D_s}{D_0}\right)^2\right] U_{0N}$	$D_s = \min\left[D_{ref}; 1.0\right] D_0$ $D_{ref} = 8.72 \exp^{-0.0281K}$	$N_s = \min\left[N_{ref}; 1000\right] N_0$ $N_{ref} = 1.676 \times 10^{-5} K^{2.539}$	$K_{cr} = 657.5$
Lee and Ryou (2000)	$U_s^2 = \frac{\sigma}{\rho D_s}(...)$ $\left[\left(\frac{r_m}{N_s}\right)^{1/3} \frac{1}{r_m}\left[We_0 - \left(72\frac{We_{0N}}{Re_{0N}} - 12\right)\right]\right]$ $U_{sT} = 0.452\, \xi Re_{0N}^{1/8} U_{0N}/\sqrt{\psi}$ $U_{sN} = \sqrt{U_s^2 - U_{sT}^2}$	$D_s = \left(\frac{r_m}{N_s}\right)^{1/3} D_0$	$N_s = 0.187\, We_{0N} - 4.45$	$r_m = m_s/m_0 = 0.2 + 0.9RN(0;1)$ $\psi = \begin{cases} 1.0 & if\ Re_{0N} \leq 577 \\ 0.204 Re_{0N}^{0.25} & if\ Re_{0N} > 577 \end{cases}$ $\xi = RN(0.81; 0.91)$
Grover and Assanis (2001)	$U_{sT,i} = U_{s,i} \sin(\alpha_s)$ $U_{sN,i} = U_{sT,i}/\tan(\alpha_s)$	$pdf(D) = \frac{3}{2}(...)$ $\frac{D^2}{D_m^3} \exp\left[-\left(\frac{D}{D_m}\right)^{3/2}\right]$	$N_{s,1} = \frac{6m_s}{\rho\pi}(...)$ $\frac{1}{\left(D_{s,1}^3 + f_{21} D_{s,2}^3 + f_{31} D_{s,3}^3\right)}$ $N_{s,2} = f_{21} N_{s,1}$ $N_{s,3} = f_{31} N_{s,1}$	$\alpha_s = 0.3155\alpha + 62.239$ $f_{21} = \frac{pdf(D_{s,2})}{pdf(D_{s,1})}$ $f_{31} = \frac{pdf(D_{s,3})}{pdf(D_{s,1})}$ $D_m = D_{SMD}/2.16$

(*continued on next page…*)

Table 2.2 – (*continued*)

References	Velocity of Secondary Droplets	Size of Secondary Droplets	Number of Secondary Droplets	Observations
Bai et al. (2002)	$U_s = U_{sN} + U_{sT} \quad with \;\; U_{sT} = C_f U_{0T}$ $\frac{1}{2}\frac{m_s}{p}\left[(U_{sN,1})^2 + ... + (U_{sN,p})\right] = E_{K_s}$ $E_{K_s} = E_{K0} + E_{S0} - E_{S_s} - E_D$ $E_D = \max\left(0.8E_{K0}; \frac{We_{cr}}{12}\pi\sigma D_0^2\right)$ $\frac{U_{sN,1}}{U_{sN,i}} \approx \frac{\ln(D_1/D_0)}{\ln(D_i/D_0)} \quad with\,(i = 2...p)$	$f(D) = \frac{1}{\bar{D}}\exp\left(\frac{D}{\bar{D}}\right)$ $\bar{D} = \frac{1}{6^{1/3}}\left(\frac{r_m}{N_s}\right)^{1/3} D_0$	$N_s = a_0\left(\frac{We}{We_{cr}} - 1\right)$ $with \;\; a_0 = 5$ $n_s D_s^3 = \frac{r_m D_0^3}{p}$	$Wet\;surface\;treated\;as\;rough\;surface$ $C_f = RN(0.6; 0.8)$ $r_m = \begin{cases} [0.2 - 0.8] & for\;dry\;walls \\ [0.2 - 1.1] & for\;wet\;walls \end{cases}$ $K_{cr,mod} = WeOh^{-0.366} = 2630$ $p = RN(1; 6)$

energy was expressed as:

$$E_D = \rho D_0 h_d U_0^3 t_s \tag{2.31}$$

The above procedure allows one to determine the velocity of the ejected particles by applying the energy conservation law. However, this is not the only approach that can be used. For example, Mao et al. (1997) approximated the flow field of a drop impinging on a surface by a stagnation point-flow, which led to a theoretical viscous dissipation model characterized by the liquid viscosity, impact velocity and maximum spread. Another alternative is to advance with a correlation based on experimental measurements, as accomplished by Park and Watkins (1996) and Mundo et al. (1997).

Studies of splash produced by the impact of drops are mainly focused on the estimation of the critical threshold defining the onset of disintegration and the description of the splash mechanism (and corresponding influencing parameters). The fact that there is no absolute consensus among studies regarding the exact parameters affecting the transition criterion between deposition and splash evidences that further research is required to better understand the phenomena underlying the disintegration mechanism.

Nevertheless, numerous papers may be found in the literature concerning this event: notably, Deegan et al. (2008) provided a detailed description of the sequence of events following to impact, whereas other investigators have attempted to characterize the crown formation (Trujillo and Lee, 2001) and corresponding instabilities of the rim at the edge of the liquid sheet (Roisman, 2010).

Mundo et al. (1995) reported that the secondary droplets are strongly affected by the incident angles: a small impingement angle of the primary drops induces a large ejection angle, whereas a large incident angle induces a small ejection angle. Moreover, it was also pointed out that the smaller the impingement angle, the larger the ratio of tangential to normal momentum of the primary drops. Experimental data also showed that the ratio between the tangential momentum of the ejected droplet and the primary incoming drop was greater than one. This indicates that the momentum in the normal direction is partially transformed into tangential momentum. Moreover, Bird et al. (2009) showed that the tangential component of impact can act to enhance or suppress splash.

Several authors (Engel, 1955; Levin and Hobbs, 1971; Xu, 2007) have observed a strong tendency of drops to splash with increasing surface roughness. This effect becomes as important as the droplets become small compared to the surface roughness. However, for a precise description of the splashing limit, Range and Feuillebois (1998) postulated that the substrate roughness has to be supplemented with information regarding the surface profile. In fact, for the same value of R_s, different occurrences were detected for different surface profiles. On the other hand, it has been found that increasing surface roughness alters the trajectory of secondary droplets (Mundo et al., 1995; Kalantari and Tropea, 2010) and decreases their mass (Mundo et al., 1998). An additional concern should be attributed to the pressure parameter, which was demonstrated both experimentally (Engel, 1955; Xu, 2007; Mishra et al., 2011) and numerically (Andreassi et al., 2007; Bang et al., 2011) to govern the occurrence of this event.

However, there are also some contradictions found in the available literature concerning particularly the viscosity parameter. In fact, according to Mundo et al. (1995) and Rioboo et al. (2001), an increase in the viscosity inhibits splashing, whereas Range and Feuillebois (1998) found out that an increase in the viscosity would not produce any change in the critical Weber number to reach splash. It is worth mentioning that both measurements were carried out under

similar ranges of liquids properties and drop characteristics. On the other hand, Vander Wal et al. (2006b) observed that increasing the viscosity promoted splashing. These contradictions seem to be the result of slight differences in the experimental conditions.

More recent studies are mostly concerned with the fundamental understanding and descriptions of the mechanisms underlying the splash event. For instance, Park et al. (2008) observed that the gas layer captured between the substrate and the drop (air entrapment) is instrumental in inducing splashing, Mandre et al. (2008) and Mani et al. (2010) concluded that air entrapment provides a dynamic pressure cushion that leads to instabilities inducing splash, and Driscoll et al. (2010) postulated that air entrapment is a characteristic of high-viscosity liquid. Furthermore, the experimental study of the impact of high-viscosity liquids onto a dry glass performed by Palacios et al. (2012) allowed the authors to shed lights on the distinctive features of the air entrainment phenomenon.

2.2 Drop impact onto liquid films

Advances in the investigation of the spray formation and impingement onto solid surfaces has been driven by the importance of this research topic in a multitude of technical disciplines. However, due to the host of parameters that influence the outcome, a comprehensive understanding of the underlying mechanisms has not been yet accomplished. In fact, one of those parameters — which is, curiously, often neglected in spray impingement models (Bai and Gosman, 1995; Bai et al., 2002; Mundo et al., 1997; Park and Watkins, 1996) — is the formation of a liquid film due to the deposition and accumulation of incident drops over the impingement surface.

The correct understanding of the film dynamic is of utmost importance for the accurate modelling of the spray impingement phenomenon. It is key in several specific applications: if, in situations of diesel engines cold-starting, the formation of a liquid layer over the surface should be avoided, in cooling systems the presence of this wall film should be promoted in order to achieve the highest cooling rates. Moreover, there are also other applications (such as in spray painting production lines) in which it is important to control the atomization process since a uniform liquid sheet onto the target surface is aspired to.

2.2.1 Mechanisms of interaction

With today's increasing concerns about hydrocarbon emissions, a major scientific effort has been devoted to investigate — through either experimental studies or numerical simulations — the formation of the liquid film deposited onto the surface. This situation has been motivated by the detection of fuel film formation on the walls of intake ports, valves and liner of internal combustion engines. As a consequence, unstable burn as well as decreased combustion efficiency could be expected (Witze, 1996; Adrian et al., 1997). Due to the low temperatures within the engine in cold-start situations, the deposited wall film developed over the surface during spray impingement does not have time to vaporize prior to the following intake stroke, which leads to serious repercussions on the mixture fraction. In fact, Stevens and Steeper (2001) investigated piston-wetting effects in optical direct injection (DI) spark ignition (SI) engines and observed through laser-induced fluorescence (LIF) imaging technique that even though fuel films were created on the pistons head at all injection timings, only early and late injections produced fuel film that could persist through the compression stroke and, eventually, into the next stroke.

Similar observations were also found in port fuel injection (PFI) systems (Shin et al., 1994; Takeda et al., 1995; Gold et al., 2000), with the fuel film after flowing past the inlet valve re-depositing onto the cylinder walls or pistons head.

Under this framework, some experimental studies were carried out with the purpose of satisfying this particular need for further research into the liquid film formation topic (Ko and Arai, 2002a,b). Senda et al. (1999) found out that as the distance between the injector and the wall increased, the adhered fuel ratio decreased while the area of the film remained constant. As a result, the average thickness of the liquid layer decreased. Consequently, it could be concluded that the adhesion process onto the wall was dependent upon the quality of the atomization which, in turn, was influenced by the distance between the injector nozzle and the target surface (i.e., spray penetration). With a greater impingement distance, the atomization was more effective, originating smaller incident drops which upon impact resulted in a lower adhesion ratio and a thinner liquid film. Under normal conditions, a spray impinging normally onto the surface produced a circular liquid film (Senda et al., 1999; Mathews et al., 2003). As the angle between the spray and the normal to the surface increased, the adhered film evolved gradually from a circular disk to an elliptical shape. This was due to the increasing transfer of the tangential momentum to the liquid film. Senda et al. (1999) observed that both deposited fuel ratio and film thickness had their maximum value under normal impingement conditions and decreased with oblique impingements.

On the other hand, the liquid film thickness has also been proved to be a key parameter on the spray impingement process. It may range from just a few microns to some millimetres depending upon the characteristics of the drop that constitute the spray and the condition of the target surface. The film thickness is often described as a dimensionless parameter, δ, calculated as the ratio between the thickness of the liquid layer, h_{LF}, and the drop initial size, D_0:

$$\delta = h_{LF}/D_0 \tag{2.32}$$

Despite the new boundary conditions promoted by the liquid/liquid interactions, the surface characteristics may still have significant influence upon the outcome depending upon the thickness of the film (Vander Wal et al., 2006c). In fact, given the topography of the target surface and the thickness of the liquid film, Tropea and Marengo (1999) classified the impacts into four categories, which have been portrayed by Moreira et al. (2010) as follows:

- very thin film ($l_r/D_0 < \delta < 3R_s^{0.16}$): drop behaviour depends upon the surface topography (where l_r is the length scale of roughness);
- thin film ($3R_s^{0.16} < \delta < 1.5$): the dependence of the drop behaviour upon surface topography becomes weaker;
- thick film ($1.5 < \delta < 4$): drop impact is no longer dependent upon the surface topography, but only on the film thickness;
- deep pool ($\delta > 4$): drop impact does not depend either upon the surface topography or on the film thickness.

Numerous works are reported in the literature addressing the impact of drops onto deep pools (Oguz and Prosperetti, 1990; Prosperetti and Oguz, 1997; Manzello and Yang, 2002). However, this subject will not be considered here as the conditions reported in this study are associated with drop impact onto films with dimensionless thickness smaller than unity.

Other evidences showing the effect of the liquid thickness on the impingement dynamics are available mainly for the particular case of the splashing regime (Hobbs and Osheroff, 1967; Stow and Stainer, 1977; Roisman and Tropea, 2002; Vander Wal et al., 2006b). Özdemir and Whitelaw (1993) described the occurrence of secondary atomization when a Diesel spray impinged onto a plate coated with a liquid film generated from previous injections. Arcoumanis et al. (1997) extended these experiments to a gasoline spray and observed that with a greater quantity of fuel injected, the film thickness increased and led to an increase in the secondary droplet diameters.

In the case of very thin liquid layers ($\delta < 0.1$) it has been found that the critical threshold in terms of Weber number to obtain secondary droplets is insensitive to the variation of the film thickness (Schmehl et al., 1999; Wang and Chen, 2000). When the film thickness is comparable to the incident drop diameter ($\delta \approx 1$), but is much greater than the surface roughness, it lies in the thin film regime and the surface morphology is not expected to influence significantly the splash event (Cossali et al., 1997). Between these two marks ($0.1 < \delta < 1$), Vander Wal et al. (2006a) reported the detection of two splashing modes: prompt and corona splash. For $1 < \delta < 10$, the same authors concluded that the liquid film acted to restrict the former mode and tended to inhibit the latter. According to Roisman and Tropea (2005), if the thickness of the film is much larger than the drop diameter, the impact of the particle creates a crater in the liquid layer. When this crater recedes, bubble entrapment may occur, as well as formation of an uprising central jet which ends up by breaking up and creating secondary droplets. Moreover, the liquid film can also influence the splashing process by transferring liquid from the layer to the elements of the splash regime (so the ratio of the splashed mass becomes greater than one). As a consequence, larger jets will be formed which give rise to larger droplets, yielding in some cases a secondary size distribution with double peaks (Özdemir, 1992).

Recently, new investigations were undertaken on the impact dynamic of drops onto moving liquid films (Alghoul et al., 2010, 2011). Although it was expected to have subtly different physics than in the quiescent situation, no distinctive impact outcomes could be inferred from the results. Samenfink et al. (1999) revealed also the results of an investigation related to the interaction between drops and a shear-driven liquid film. The work was particularly focused on the establishment of correlations for the deposited mass fraction and secondary droplet characteristics.

Alongside with the moving liquid film, also the presence of a cross-flowing gas alters the impact dynamic of the impinging spray. The presence of a crossflow results in the formation of a thinner liquid film over the surface (Arcoumanis et al., 1997; Rodrigues et al., 2012b; Panão et al., 2013). Arcoumanis et al. (1997) observed that the average size of secondary droplets decreased with the decrease in the film thickness or, alternatively, the increase in the number of droplets. Panão et al. (2013) completed the analysis by relating this increased production of particles resulting from the secondary atomization to the splash enhancement since thinner liquid films are known to promote splash (Cossali et al., 2004b; Vander Wal et al., 2006a).

At this point, advanced CFD codes are a valuable complement to experimental studies, since they facilitate a detailed local analysis of the flow (see e.g. publications of Nikolopoulos et al., 2005, 2007). Several spray-wall interaction models have been proposed over the past couple of decades, as already mentioned above. However, only a few of them (Arienti et al., 2011; Jafarmadar et al., 2009, 2010) take into account the formation of the liquid film as an influencing parameter. One pioneering contribution in this subject was given by Stanton and Rutland (1997) (and following companion papers: Stanton et al., 1998; Stanton and Rutland, 1998) who integrated into their spray impingement model a computational extension with the contribution

of the liquid film dynamic. This sub-model simulated the thin fuel film flow over a solid surface by solving the continuity, momentum, and energy equations for the two-dimensional film that flows over a three-dimensional surface. The major physical processes considered included mass and momentum contributions to the film due to spray drop impingement, splashing effects, various shear forces, piston acceleration, dynamic pressure effects, gravity driven flow, conduction, and convective heat and mass transfer. The model compared well with experimental data for fuel film thickness, percentage of fuel that adheres to the wall and the spreading of the film as well as global engine parameters, such as cylinder pressure. Similarly, Senda et al. (1999) simulated the fuel film formation in a spark ignition (SI) engine with a port injection system. In their sub-model, fuel film development due to the particle-particle interaction near the wall and drop-wall film interactions, fuel film transport and breakup, as well as the velocity and direction of splashing droplets were considered by taking into account correlations proposed in several experimental results. The agreement obtained with experimental results was reasonable.

Nonetheless, the major distinction between models has to do with the criteria used to define the boundaries between impingement regimes in wet wall conditions, which is discussed in the following section.

2.2.2 Transition criteria

The formation of a liquid film induces complex interactions between incident spray and liquid layer which takes effect on numerous properties involved during the spray impingement, such as the secondary droplet characteristics and the splash threshold. In fact, it is known that thin liquid films stimulate splash dynamics. In other words, under the same conditions, a drop would eventually splash upon impacting onto a thin film, whereas no splash would be observed if the target was a solid dry surface (Vander Wal et al., 2006a). This experience was also extended by other investigators to surfaces with different liquid film thicknesses. Cossali et al. (1997) stated that thicker liquid films inhibited splashing while Mundo et al. (1998) concluded that an increase in the film thickness led to an increase in the dissipation of kinetic energy during the deformation process. The latter observation means that with a thicker liquid layer the kinetic energy of the incoming drops must be greater to cause break up. Moreover, it has been observed that the additional fluid available gives rise to larger secondary droplets (Stow and Stainer, 1977; Mundo et al., 1998) but in smaller number (Hobbs and Osheroff, 1967).

Yarin and Weiss (1995) established the threshold for disintegration of drops impacting onto a thin liquid layer in a train of frequency f by means of a correlation expressed as follows:

$$U_{cr} >> 18(\sigma/\rho)^{1/4}(\upsilon)^{1/8}f^{3/8} \tag{2.33}$$

where υ is the kinematic viscosity. According to Eq. 2.33 the diameter of the drop has no effect on the splashing threshold. On the other hand, for single impacts the frequency f may be approximated by the relation U_0/D_0. Thus, at this point the drop size comes into action and the expression can then be rewritten as follows:

$$K_{cr} = WeOh^{-0.4} >> 1 \tag{2.34}$$

Therefore, it is assumed that a single composite dimensionless group governs the splashing threshold of single drops impacting onto pre-existing liquid film. Above a critical value of K_{cr}, splash is expected. This combination of Weber and Ohnesorge numbers has been used

successfully to quantify the disintegration threshold conditions of drops impacting onto wet surfaces. Cossali et al. (1997) established the criterion for drop splashing on a pre-existing liquid film in the form:

$$K_{cr} = 2100 + 5880\delta^{1.44} \tag{2.35}$$

with $0.1 < \delta < 1$, $Oh > 7 \times 10^{-3}$ and $R_s = 5 \times 10^{-5}$. Recently, Motzkus et al. (2011) modified this expression, by replacing the value of the coefficient 5880 by 2000, in order to obtain a better agreement with their experimental observations. Similarly, Rioboo et al. (2003) investigated splash initiation of liquid drops impacting onto wet solid substrates. All measurements were found to be dependent upon only two variables: the dimensionless film thickness, δ, and the K parameter. The proposed transition criterion for disintegration ($K_{cr} = 2100$) was in reasonable agreement with Eq. 2.35 for low-viscosity liquids. The data were obtained for $0 < \delta < 0.14$. This finding was corroborated years later by Okawa et al. (2006) for normal water drop impact onto a plane water surface. Yet, for Vander Wal et al. (2006b), the boundary delineating the splash and non-splash regions for drops impacting upon a thin fluid film covering a dry solid surface follows a power-law relation in terms of Oh and Re, as given by:

$$We^{0.585} Oh^{-0.17} = 63 \tag{2.36}$$

The authors noticed that the presence of a thin film caused a dramatic shift in the splashing threshold for all of the fluids studied. However, it is interesting to note that the splash/non-splash boundary proposed bears no relationship to the film thickness. On the other hand, Huang and Zhang (2008) conducted experimental observations of drops impacting onto oil and water liquid films. Both drop size and liquid film thickness were varied throughout the experiments ($0.3 < \delta < 1.3$). The authors argued that the expression advanced by Cossali et al. (1997) revealed significant differences with their measurements for all but the thinner liquid film studied. Based on these findings, the following transition criterion was proposed [Note that the correlation has been corrected due to a typographical error published in Huang and Zhang (2008)]:

$$We^{0.375} Oh^{-0.25} = 25 + 7\delta^{1.44} \tag{2.37}$$

A different approach has been proposed by Bai and Gosman (1995), who did not include the effect of the film thickness in the deposition-splash thresholds. Instead, the authors adopted the same criterion as in dry surfaces but updated the fitting constant A, by assuming the analogy of the liquid film as a very rough surface:

$$WeOh^{-0.366} = A \tag{2.38}$$

with $A = 1320$. This analogy must be carefully considered because the film thickness may have an opposite effect to that of augmenting roughness amplitude, depending upon the thickness of the liquid film, as discussed above.

Table 2.3 summarizes the transition criteria available in the literature for impacts onto wet surfaces. The table is divided into two parts: one highlights the equations that obey to the general K parameter, whereas the second shows the disintegration thresholds that assign different weighs — by means of the exponents a and b — to the We and Oh numbers. It is worth mentioning that the mathematical expressions have been arranged so the exponent over We (which is referred as a) is equal to one and the general aspect of the entries are as close as possible to the original K parameter.

Table 2.3: Transition criteria between impingement regimes for wet walls.

Splash Transition Criteria		
K Parameter $K_{cr} = WeOh^{-0.4}$	Cossali et al. (1997)	$K_{cr} = 2100 + 5880\delta^{1.44}$
	Motzkus et al. (2011)	$K_{cr} = 2100 + 2000\delta^{1.44}$
	Rioboo et al. (2003)	$K_{cr} = 2100$
	Okawa et al. (2006)	$K_{cr} = 2100$
Modified K Parameter $K^*_{cr} = We^a Oh^b$	Bai and Gosman (1995)	$WeOh^{-0.366} = 1320$
	Vander Wal et al. (2006a)	$WeOh^{-0.290} = 1190.7$
	Huang and Zhang (2008)	$WeOh^{-0.667} = (25 + 7\delta^{1.44})^{2.667}$

Nevertheless, such information should be used with caution since the experimental data behind the proposed correlations have been obtained under different circumstances. Each case is only valid within the boundary conditions and data ranges for which they have been proposed. Disregarding these facts (by, for example, using the equations outside their range of validity) precipitates erroneous or misleading results. On the other hand, table 2.3 also provides an objective tool to compare the diverse approaches.

For lower impact velocities, drops can either stick to the wall or rebound if they still possess an excess of energy at the end of the spreading phase. Transition criteria have been given by Bai and Gosman (1995) for both stick/rebound and rebound/spread boundaries as $We_{cr} \approx 2$ and $We_{cr} \approx 5$, respectively, based on the existing data on water drops. However, later, the authors corrected the critical Weber number for the transition between rebound and spread to 20 in order to properly account for interference effects of neighbouring previously-impacting drops. Stanton and Rutland (1997) adopted a similar approach but considered $We_{cr} \approx 5$ for the stick/rebound limit and $We_{cr} \approx 10$ for the rebound/spread limit.

Also concerning the rebound regime, Šikalo and Ganić (2006) reported that from the analysis of their own experimental data, they concluded that the K_{cr} parameter should not be used as the transition criterion between rebound and spread. The authors also noticed that the drops would rebound from the liquid film at larger angles than from a dry surface under the same condition. According to Rioboo et al. (2001), rebound is promoted by an increase in the surface tension of the liquid and in the receding contact angle, whereas Sommerfeld and Huber (1999) concluded that also wall roughness considerably alters the rebound behaviour of the particles. Nevertheless, on balance, it is important to note that this outcome only occurs for highly non-wettable liquid/solid systems for which the initial spreading phase is followed by a receding phase. Therefore, very singular conditions are required for this regime to take place, which has somewhat hindered the interest of investigators in such phenomena.

2.2.3 Post-impact characterization

Splashing occurs when the incident particles collide against an interposed surface with very high impact energy. This event gives rise to the formation of secondary droplets. Whether the surface is dry or wet influences the outcome of the drop impact. However, this perception has not been substantiated in a complete agreement about the importance of the liquid film influence on the transition criteria proposed for impingements onto wet walls. Not all the correlations proposed take into account the thickness of the liquid film as an influencing parameter. Obviously, these different perspectives regarding the parameters affecting the impingement

event has a direct effect on the formulation adopted for the post-impingement characteristics of secondary droplets.

To facilitate comparisons and enable a systematic understanding of the evolution of current available models for the post-impingement characteristics of droplets, they are listed in Table 2.4 along with detailed information regarding the approaches and equations considered. All entries refer to drop impact models or experimental studies proposed with the aim of being usable as input data for new empirical models. One can recognize that some of the cases used correlations taken from their own dedicated experiments (Samenfink et al., 1999; Kalantari and Tropea, 2007), whereas others (Senda et al., 1999; Bai et al., 2002) collected several empirical results from the literature, giving their models the theoretical advantage of performing in a wider set of conditions.

There are still further punctual relevant contributions that have not been considered in those works. These are still useful to be used in the modelling of such flows as well as to help enriching the knowledge about the topic and, therefore, they are described in the next paragraphs.

In the study of Senda et al. (1999), the drop-wall interaction process is classified into high and low impact cases and the transition between both regimes occurs when $We_{cr} = 300$. In the lower energy regime, three types of disintegration mechanisms are detected based on the dimensionless film thickness, δ: for $0.6 < \delta < 1.35$, cluster type disintegration occurs and the number of ejected particles is equal to 4, whereas for $\delta < 0.6$ and $\delta > 1.35$, rim and column type breakups take place, respectively, but the number of secondary droplets is defined as being only 1. On the other hand, when impact energy is above the threshold established, the total number of secondary droplets is expressed as:

$$N_s = r_m \frac{D_0^3}{D_s^3} \tag{2.39}$$

and r_m is given the value of 0.8 by reference to the experimental results of Yarin and Weiss (1995).

Similarly, Okawa et al. (2008) conducted an experimental study to investigate the effect of the impingement angle on the total mass of secondary droplets produced during the collision of single water drops onto a plane water surface. The authors fitted an empirical correlation for the number of secondary droplets, N_s, valid for normal impacts, to their own experimental data and to the one reported by Stow and Stainer (1977), yielding the following relationship:

$$N_s = \max[4.97 \times 10^{-6}; 7.84 \times 10^{-6}(\delta)^{-0.3}]K^{1.8} \tag{2.40}$$

However, analysing the results reported by Okawa et al. (2006), one may argue that this relation is better suited for impacts onto liquid films with $\delta < 2$. On the other hand, the authors could also establish a relation between the mass of secondary droplets and the mass of incident drops for both normal and oblique water drop impacts onto plane water surfaces as:

$$\begin{aligned} r_{mN} &= 1.56 \times 10^{-3} \exp^{4.86 \times 10^{-4} K} \quad &for\ normal\ impacts \\ r_{mOb} &= r_{mN} \exp^{0.115(\alpha - 10)} \quad &for\ oblique\ impacts \end{aligned} \tag{2.41}$$

which are dependent upon the impingement angle of the spray. Similarly, Kalantari and Tropea (2007) also concluded from their measurements that the incident angle was an important variable in the estimation of the splashing to incident mass ratio. The correlations were expressed as follows:

Table 2.4: Post-impingement characteristics of secondary droplets adopted in wet wall impact models.

References	Velocity of Secondary Droplets	Size of Secondary Droplets	Number of Secondary Droplets	Observations
Stanton and Rutland (1996)	$pdf_V\left(\frac{U_{s,i}}{U_0}\right) = (...)$ $\left[\frac{q_V}{\bar{D_V}}\left(\frac{U_{s,i}/U_0}{\bar{D_V}}\right)^{q_V-1}\right]\exp\left[-\left(\frac{U_{s,i}/U_0}{\bar{D_V}}\right)^{q_V}\right]$ $U_{sT,i} = \phi U_{sN,i}$ $U_{sN,i} = \sqrt{\kappa}U_{s,i} \quad with$ $\kappa = \frac{1/2(1+\phi^2)m_0U_0^2 + \pi\sigma D_0^2N_0 - 1/2 m_0U_{cr}^2}{1/2(1+\phi^2)\sum_{i=1}^{3} m_{s,i}U_{s,i}^2 + \pi\sigma\sum_{i=1}^{3} D_{s,i}^2N_{s,i}}$	$pdf_D\left(\frac{D_{s,i}}{D_0}\right) = (...)$ $\left[\frac{q_D}{\bar{D_D}}\left(\frac{D_{s,i}/D_0}{\bar{D_D}}\right)^{q_D-1}\right]$ $\exp\left[-\left(\frac{D_{s,i}/D_0}{\bar{D_D}}\right)^{q_D}\right]$	$N_s = (...)$ $\frac{r_m m_0}{\frac{\pi}{6}\rho\sum_{i=1}^{3} D_{s,i}^3\, pdf_D(D_{s,i})}$	$\bar{D_V} = 0.158\exp^{0.017\alpha}$ $q_V = \begin{cases} 2.1 & for\ \alpha \le 50^\circ \\ 1.1 + 0.02\alpha & for\ \alpha > 50^\circ \end{cases}$ $\bar{D_D} = 0.21 - 7.69\times10^{-5}We$ $q_D = 2.71 - 9.25\times10^{-4}We$ $\phi = 1/\tan(65.4 + 0.266\alpha)$ $r_m = -27.2 + 3.15\,U_{ref} - (...)$ $0.1164\,U_{ref}^2 + 1.4\times10^{-3}U_{ref}^3$ $U_{ref} = We^{5/16}Oh^{-1/8}f^{*-3/8}$
Senda et al. (1999)	$\frac{1}{2}m_sU_s^2 + \pi\sigma D_s^2N_s = \frac{1}{2}m_0U_0^2 - \frac{We_{cr}}{12}\pi\sigma D_0^2N_0$	$D_s/D_0 = 3.932\times10^2K_{cr,mod}^{-1.416}$	$N_s = r_m\frac{D_0^3}{D_s^3}$	$Wet\ surface\ treated\ as\ rough\ surface$ $r_m = 0.8$ $K_{cr,mod} = WeOh^{0.4} = 2164 + 7560\delta^{1.78}$ $with\ We > 300$
Samenfink et al. (1999)	$U_{s,N} = U_{ref}\sin(\alpha_s)$ $U_{s,T} = U_{ref}\cos(\alpha_s)$ $U_{ref} = (...)$ $\left(0.082K_{cr,mod}^{-0.338}\alpha^{0.294}\delta^{-0.0311}Oh^{-0.231}\right)U_0$	$D_s = (1 - 0.0345\ (...)$ $W_{cr,mod}^{0.175}\alpha^{0.124}Oh^{-0.53}\big)\,D_0$	$N_s = \frac{r_m/m_0}{\frac{\pi}{6}\rho D_s^3}$	$K_{cr,mod} = WeOh^{-0.324} = 576$ $\alpha_s = 2.154K_{cr,mod}^{1.095}\alpha^{0.034}\delta^{-0.159}$ $r_m = 0.087\,(W_{cr,mod} - 1)^{0.319}\ (...)$ $\alpha^{0.122}\delta^{-0.959}$

(*continued on next page…*)

Table 2.4 – (*continued*)

References	Velocity of Secondary Droplets	Size of Secondary Droplets	Number of Secondary Droplets	Observations
Bai et al. (2002)	$U_s = U_{sN} + V_{sT} \quad with \;\; U_{sT} = C_f U_{0T}$ $\frac{1}{2}\frac{m_s}{p}\left[(U_{sN,1})^2 + ... + (U_{sN,p})\right] = E_{K_s}$ $E_{K_s} = E_{K0} + E_{S0} - E_{S_s} - E_D$ $E_D = \max\left(0.8E_{K0}; \frac{We_{cr}}{12}\pi\sigma D_0^2\right)$ $\frac{U_{sN,1}}{U_{sN,i}} \approx \frac{\ln(D_1/D_0)}{\ln(D_i/D_0)} \quad with\,(i = 2...p)$	$f(D) = \frac{1}{\bar{D}}\exp\left(\frac{D}{\bar{D}}\right)$ $\bar{D} = \frac{1}{6^{1/3}}\left(\frac{r_m}{N_s}\right)^{1/3} D_0$	$N_s = a_0\left(\frac{We}{We_{cr}} - 1\right)$ $with \;\; a_0 = 5$ $n_s D_s^3 = \frac{r_m D_0^3}{p}$	$Wet\;surface\;treated\;as\;rough\;surface$ $C_f = RN(0.6; 0.8)$ $r_m = \begin{cases} [0.2 - 0.8] & for\;dry\;walls \\ [0.2 - 1.1] & for\;wet\;walls \end{cases}$ $K_{cr,mod} = WeOh^{-0.366} = 1320$ $p = RN(1; 6)$
Kalantari and Tropea (2007)	$U_{sN} = -1.1 U_{0N} We_{0N}^{-0.36}$ $U_{sT} = 0.862\, U_{0T} + 0.094$	$D_s = (...)$ $(-0.003 We_{0N} + 1.2)\, D_0$	$Normal\;impact:$ $N_{sN} = \left(2.16 \times 10^{-3}\;(...)\right.$ $\left. We_{0N} + 8.96 \times 10^{-2}\right) N_0$ $Oblique\;impact:$ $N_{s,Ob} = \left(7.1 We_{0N}^{-1.14}\right) N_0$	$r_{m,N} = 6.74 \times 10^{-3} We_{0N} - 0.204$ $r_{m,Ob} = 35\, We_{0N}^{-1.63}$

$$\begin{aligned} r_{mN} &= 6.74 \times 10^{-3} We_{0N} - 0.204 \quad for\ normal\ impacts \\ r_{mOb} &= 35 We_{0N}^{-1.63} \qquad\qquad\qquad for\ oblique\ impacts \end{aligned} \tag{2.42}$$

On the other hand, Stanton and Rutland (1996) determined the mass ratio r_m by curve fitting the experimental data of Yarin and Weiss (1995) as function of a non-dimensional velocity of reference:

$$r_m = -27.2 + 3.15 U_{ref} - 0.1164 U_{ref}^2 + 1.4 \times 10^{-3} U_{ref}^3 \tag{2.43}$$

in which $U_{ref} = U_0(\sigma/\rho)^{1/4}(\upsilon)^{1/8} f^{3/8}$.

Even though the previous examples have been proposed for a wet wall scenario, none of them has taken into account the film thickness as an influencing parameter. On the contrary, Samenfink et al. (1999) proposed the following correlation for r_m:

$$r_m = 0.087 \left(K_{cr,mod} - 1\right)^{0.319} \alpha^{0.122} \delta^{-0.959} \tag{2.44}$$

which depends upon the disintegration threshold, the impingement angle and the dimensionless film thickness.

Cossali et al. (2004a) completed the information regarding the characteristic of secondary droplets by fitting the time evolution of the mean droplet size ($\bar{D}$) with a power law:

$$\bar{D}/D_0 = C_{cm} \Lambda^{n_{cm}} \tag{2.45}$$

where C_{cm} and n_{cm} are fitting parameters, and Λ is the dimensionless time. Moreover, the authors also suggested that both the mean size and the number of the secondary droplets were not significantly influenced by the film thickness.

Besides the importance of characterizing the secondary droplet originated after impact, it is also crucial in wet wall environments to determine the thickness of the liquid film created right after the first impacts. Surprisingly, only a few studies have been undertaken concerning this subject.

Yarin and Weiss (1995) estimated that the dimensionless thickness of the liquid film was of the order of:

$$\delta \approx \left(\frac{\mu}{\rho D_0 U_0} \right)^{1/2} \tag{2.46}$$

This expression yielded reasonable agreement for the film thickness obtained in their experiments. In its turn, Pasandideh-Fard et al. (1996) concluded from volume conservation (assuming that the deposited drop attains a stable circular disk shape with uniform thickness and diameter) that the dimensionless film thickness could be written as:

$$\delta = \frac{2 D_0^2}{3 D_{max}^2} \tag{2.47}$$

Years later, Kalantari and Tropea (2007) derived a semi-empirical correlation for characterizing the average film thickness accumulated on the wall as follows:

$$\delta = \xi \frac{D_{V0}}{D_0} Re_{V0}^{-1/2} \left(\frac{\dot{q}_V}{U_{0N}} \right)^{\gamma} \tag{2.48}$$

where D_{V0} represents the volumetric mean diameter of incident drops, Re_{V0} is the Reynolds

number based on this mean diameter, $\dot{q}_V$ is the volume flux of impinging drops, and ξ and γ are constant values found to be 4 and -0.5, respectively, based on the measured data for normal impact conditions.

On the other hand, Roisman et al. (2006) aggregated a collection of experimental data for the film thickness at the time instant D_0/U_0. From the results, they could distinguish clearly two different trends according to the ranges of Reynolds number under consideration. At $Re > 2000$, the dimensionless film thickness could be scaled as $\delta \approx Re^{-1/2}$, whereas at $Re < 1000$, the film thickness was scaled in the form $\delta \approx Re^{-1/3}$.

2.3 Drop impact onto heated, dry surfaces

In the context of spray-wall interactions, considering a hot surface and the corresponding thermal effects associated to this condition carries a substantial influence on the hydrodynamic mechanisms that occur in this region. As a drop traverses a surrounding hotter gas, heat is transferred towards the drop interior, which causes it to heat up.

As the heat exchange occurs, the liquid mass is converted into vapour in the surrounding hot gas. This change in the characteristics of the incident particles is expected to have a critical repercussion on the general conditions of impact. If the liquid mass is not completely converted into vapour before reaching the hot target surface, further heat transfer mechanisms may occur between the liquid drop and the solid hot surface once they touch each other. Each process is usually treated independently but in the cases in which the evaporation effects are not severe enough to prevent the drop of impacting the wall, both mechanisms may happen in the same experiment. This will be the scenario adopted in the present study.

For this reason, the literature review advanced in Section 2.3.1 is implicitly divided into the following topics: 1) heat transfer occurring when a liquid particle gently deposits onto a hot solid surface, and 2) evaporation of drops dispersed in a hotter gas environment.

It is worth mentioning at this point that the present literature review is restricted to conditions where the temperatures considered are above the boiling point. Even though the cases with temperatures below the solidification point are of utmost interest and have numerous relevant applications, the subject will not be addressed in the present work.

Moreover, as several aspects of drop evaporation and heat transfer mechanisms have been studied for decades, the present review work cannot be considered exhaustive as there are exceptional detailed review articles that are of particular interest to both topic 1) (Law, 1982; Sirignano, 1983; Aggarwal, 1998; Sazhin, 2006) and topic 2) (Moita and Moreira, 2007; Moreira et al., 2010) identified above. Since this thesis aims most of the attention to spray-wall interactions, the remaining sections review some of the existing available literature related to that matter. Section 2.3.2 addresses the transition criteria between impingement regimes proposed by different investigators in hot condition experiments, whereas the post-impingement characteristics of secondary droplet are discussed in section 2.3.3.

2.3.1 Heat transfer mechanisms

The assumption of a heated target introduces an additional complexity to the analysis of the spray-wall interactions, making it more difficult to achieve an accurate description of the phenomena involved in such conditions. Depending upon the surface temperature (but not limited to), diverse heat transfer mechanisms between the target and the drop may occur.

According to the classical boiling theory (Dhir, 1991; Rein, 2002; Faghri and Zhang, 2006; Welty et al., 2008), there are four different regimes that can be recognized from the well-known pool boiling curve. Even though these regimes were originally identified in a hot wall covered by a continuous liquid layer, identical heat transfer regimes were found in the case of a drop gently depositing onto a horizontal hot solid surface. Therefore, as the value of the wall temperature, T_w, increases, the curve traverses four different regimes: 1) natural or free convection boiling, 2) nucleate boiling, 3) transition boiling, and 4) film boiling. Typical boiling and lifetime curves of a drop are sketched in Fig. 2.4.

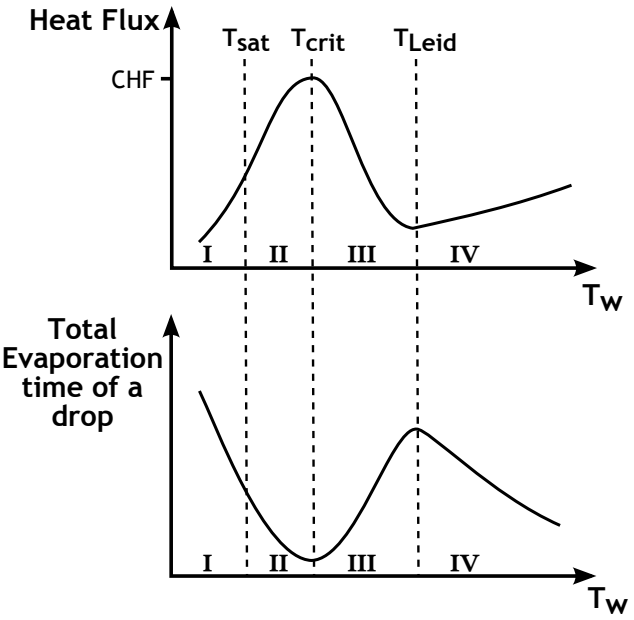

Figure 2.4: Boiling and lifetime curves of a drop.

In region I, the temperature is below the saturation temperature, T_{sat}, of the liquid and no bubbles form. Instead, the main heat transfer mechanism is natural convection, without phase change.

As the temperature of the surface is raised (above the saturation temperature), the system enters the nucleate boiling regime (region II). This is accompanied by the emergence of vapour bubbles at certain preferred locations (usually identified as nucleation sites) and the increase in the heat flux until the critical heat flux (CHF) point is reached.

Beyond the peak of the boiling curve, the transition boiling regime is entered (region III). From this point on, the rate of bubble generation exceeds the rate of bubble detachment from the hot surface. These bubbles — which are initially formed close to the wall and move up through the liquid by buoyancy — begin to merge and form a vapour film at the solid-liquid interface. This leads to a decrease in the contact area, which causes a thermal insulation that hinders the heat flux between both phases and precipitates the local minimum observed at the Leidenfrost temperature. As a consequence, the evaporation time increases while the heat flux decreases with increasing temperature values. Another feature of this regime that is worth highlighting is that the unstable behaviour of the vapour film leads, sometimes, to the abrupt detachment of the bubbles from the surface, bursting at the liquid-gas interface and eventually resulting in the ejection of small droplets.

When the temperature of the wall becomes high enough to sustain a stable vapour film, the drop becomes completely separated from the wall. This point — known as the Leidenfrost temperature — marks the onset of the film boiling regime (region IV) and is characterized by

having the local lower heat flux value. The heat transfer takes place mainly by conduction through the vapour film. Therefore, as the surface temperature increases, the heat flux is enhanced because of the higher gradients between liquid and surface.

To this theory, Bai and Gosman (1995) added two extra characteristic temperatures: pure adhesion temperature (below which impinging drops adhere at low impact energy), T_{PA}; and pure rebound temperature (above which impinging drops bounce at low impact energy), T_{PR}. On the other hand, a simplistic postulation has been advanced by Naber and Farrel (1993) by associating the heat transfer regimes to the corresponding hydrodynamic regimes. The first two regions with lower temperatures (i.e., natural convection and nucleate boiling regimes) were associated with a wetting regime, whereas the film boiling regime was associated with a non-wetting regime. In the transition regime, the contact between the drop and the surface was assumed to be intermittent.

Figure 2.4 gives a qualitative representation of boiling and lifetime curves of a drop, as well as an indication of the boundaries of the heat transfer regimes. However, the quantitative aspects (such as the exact values of T_{cr}, T_{sat}, T_{Leid}) depend mostly upon the nature of the impact process (Wachters and Westerling, 1966). If fuel drops were to be contemplated, auto-ignition should be considered at high wall temperatures (Rein, 2002).

The most sensitive of the critical points identified above is the Leidenfrost temperature, which is also the property for which most of the material is found in the literature. Contrary to the critical heat flux temperature, T_{Leid} is very sensitive to impact conditions, such as surface topography (Bernardin and Mudawar, 1999), liquid properties (Baumeister and Simon, 1973; Bertola, 2004), angle of impact (Kang and Lee, 2000) and ambient gas pressure (Emmerson, 1975). This may explain the large discrepancies found in the values proposed by different authors for this particular critical temperature. On the other hand, some investigators suggested that the Leidenfrost temperature was a dynamic property that could be obtained experimentally (Naber and Farrel, 1993; Wachters and Westerling, 1966). This concept has been introduced by Gottfried et al. (1966) but, even until today, no morphological feature can be indisputably attributed to a drop in the film boiling regime certifying that this dynamic critical value has been exceeded (Naber and Farrel, 1993).

The above review is intended to give some insight into the current state of knowledge regarding the heat transfer effects between a drop and a hot surface when they are in contact. Next is discussed the evaporation mechanisms occurring when the drops traverse a surrounding hot gas (still relatively far away from the target wall). Accordingly, when the walls of the domain in study have a certain temperature above the boiling point of the liquid, the evaporation process takes place with the fraction of mass of the particles starting to be converted into vapour.

Godsave (1953) and Spalding (1953) were the firsts to propose an evaporation model based on the D^2-law for an isolated single component drop. Since then, the existing theory has been largely reviewed by several authors (Law, 1982; Faeth, 1977; Lefebvre, 1989; Sirignano, 1983) but it has been mostly dedicated to study the dynamics of single drops. On the other hand, Abramzon and Sirignano (1989) extended the range of applications by proposing a drop vaporization model for a spray. The authors demonstrated that the convective effects were the most relevant parameters to consider.

Meanwhile, many papers have presented direct comparisons between computational results and experimental measurements with relative satisfactory results (Chen and Pereira, 1996; Karl et al., 1996; Sommerfeld, 1998). If special attention is given to evaporation of biofuels, the work undertaken by Barata (2008) is of particular interest. Nevertheless, most recent studies have been more concerned with issues related with transient heating (Sazhin et al., 2005) and

spatial distribution of temperature inside particles (Petsi and Burganos, 2011; Castanet et al., 2011) and along the surface (Zhang et al., 2014).

The above studies were performed with single component drops. However, most of the fuels used in engineering applications are complex multi-component fluids. In fact, both petroleum and bio-oil based fuels contain several hundreds of different chemical components. Tracking all the components would be a task too ambitious to achieve. However, it has been found (Long et al., 2014) that it is possible to replicate the values of heat and mass transfer observed during the evaporation process of a particular fuel by using an appropriate compound model composed of a relatively small number of components. As a result, multicomponent drop evaporation analysis has become a subject of major interest for researchers. For instance, Bhattacharya et al. (1996) carried out a theoretical study of a two-component hydrocarbon particle in high-temperature quiescent gaseous surroundings, whereas Maqua et al. (2008) measured the temperature distribution of two-component drops under different aero-thermal conditions. More recently, Strotos et al. (2011) proposed a numerical model of two-component hydrocarbon liquid drops and validated it against experimental data. Moreover, extensive parametric studies have been provided by the authors regarding the flow, temperature and concentration fields.

On the other hand, Sazhin and his group have managed to advance with evaporation models based on analytical solutions of heat conduction and species diffusion for two-component drops (Sazhin et al., 2010), as well as for an arbitrary number of species (Sazhin et al., 2011). More recently, this trend has been followed by several investigation groups whose research is contributing enormously to acquire a deeper knowledge on multicomponent evaporating drops (Saha et al., 2012; Banerjee, 2013; Brereton, 2013).

2.3.2 Transition criteria

Similarly to a cold impact scenario, the criteria proposed for the transition between impact regimes in a heated environment are based on the Weber number. In this case however, the critical thresholds should be addressed as function of the wall temperature and within the corresponding boiling regime.

Bai and Gosman (1995), Rein (2002) and Lee and Ryu (2006) proposed qualitative diagrams of the thresholds between regimes in convenient "We vs T_w" charts. However, each proposal — illustrated in Fig. 2.5 — reveals a distinct perspective of the way each parameter influences the occurrence of a particular impingement regime.

Figures 2.5(a) and 2.5(c) show evident similarities in terms of the general features observed in the representations proposed. Both authors consider fixed boundaries according to particular temperature values. This means that a fixed impact energy may lead to different impingement regimes depending upon the temperature of the surface. Such a conclusion has also been supported by Chandra and Avedisian (1991) in their experimental study. Moreover, Bai and Gosman (1995) and Lee and Ryu (2006) indicate two additional characteristic temperatures — beyond the three commonly adopted in the boiling theory (T_{sat}, T_{cr}, T_{Leid}) — which are recognized as important indicators to be used to determine the limits of certain impact regimes: pure adhesion temperature, T_{PA}, defines the maximum value for which adhesion is always observed for low impact energy; whereas pure rebound temperature, T_{PR}, corresponds to the lower temperature value for which the drop always bounces from the surface in a condition of low impact energy. According to the authors, the identification of the temperature thresholds could be done based on the observation of the drop morphology.

On the other hand, even though a fixed boundary is also defined to delimit the spreading

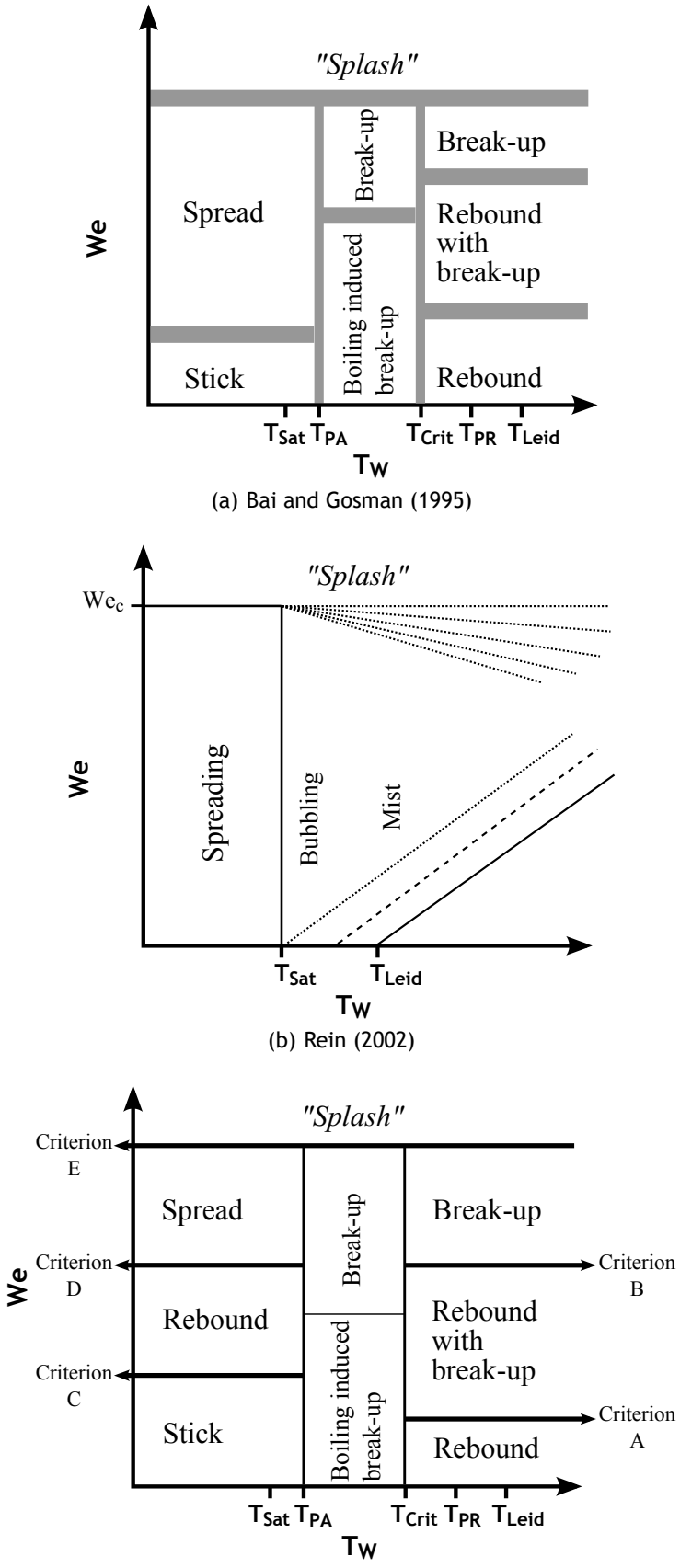

Figure 2.5: Global representations of impact regimes and transition conditions for heated surfaces.

regime at the saturated temperature, from this temperature mark Rein (2002) considers that the transition criteria between different regimes become dependent upon the surface temperature, i.e., the critical Weber number delimiting two different regimes increases by increasing the temperature values. This dynamic representation of certain impingement regimes contrasts with the completely rigid approaches illustrated in Fig. 2.5(a) and Fig. 2.5(c).

Nonetheless, it is evident that the splash regime is transversal to the three representations and occurs at high impact energy regardless of the wall temperature. This is the only regime that is not affected by passing from one boiling regime to another (according to the surface temperature).

Even though the above contributions are a valuable tool to gain some insight into the representation of the boundaries between impact regimes, no effective transition criterion is really proposed (e.g. to be used in computational models). Contrary to previous approaches, Wachters and Westerling (1966) advanced with explicit values for the boundaries after performing experimental measurements on surfaces with temperatures above 400 K. The authors concluded that rebound could be noticed for Weber numbers below 30, whereas disintegration occurred for Weber numbers above 80. Between those limits, rebound with breakup would be found.

Years later, Naber and Farrel (1993) carried out experiments with liquid drops depositing onto hot targets (with temperatures ranging from values below the saturation point up to values above the Leidenfrost temperature) and reported the existence of a single constant critical threshold — that would offer a simple correlation for the entire set of measurements performed — from which disintegration was always observed (except in the free convection boiling regime for which no disintegration was detected). Therefore, the authors concluded that the criterion for drop disintegration in a heated environment could be given by $We_N = 24$.

2.3.3 Post-impact characterization

Heat transfer between the liquid drop and the surface alters the dynamics involved during impact which means that the relations for the post-impingement characteristics devised for cold impact conditions may not be valid for heated targets. Given this scenario, it would be expectable that the dynamic behaviour of the secondary droplets within the different boiling regimes would have been scrutinized by the scientific community related to this topic. However, even though this interest has led to many research works in the past few years, there is still much to be done.

The basic approach has been to carry out parametric studies to examine the effect of particular variables on the outcome of spray-wall impact combined with the influence of heat transfer within each specific thermal regime. The transition regime has been object of very few investigations up to date because of the difficulty to recognize clearly the limits of this heat transfer regime. Investigators prefer to choose temperature ranges that will undoubtedly lead to nucleate or boiling conditions.

As far as the nucleate boiling regime is concerned, it has already been reported the influence of the liquid properties, surface roughness and impact angle on the disintegration mechanisms (Cossali et al., 2005; Moreira et al., 2007b; Moita and Moreira, 2007, 2009).

Nevertheless, most of the researches have been performed in the film boiling regime where the influence of each parameter has been more thoroughly studied than in the other boiling regimes. For instance, Cossali et al. (2005) reported a significant increase in the SMD of secondary droplets for larger fluid viscosities. Castanet et al. (2009) completed this observation by referring that the increase in temperatures led to the decrease in the viscosity of the fluid, and this phenomenon was responsible for the variation in the critical thresholds between im-

pingement regimes. Other influential parameters also reported in the literature are the impact angle (Kang and Lee, 2000; Karl and Frohn, 2000; Moreira et al., 2007b), the presence of cross-flow (Arcoumanis et al., 1998) and the nature of the target surface (Bernardin et al., 1996; Moita and Moreira, 2007). Even though the importance of the size and velocity distribution of secondary droplets has been analysed under the present boiling regime (Naber and Farrel, 1993; Arcoumanis and Chang, 1993; Cossali et al., 2005), no correlations have been proposed for this purpose, which hinders the modelling capabilities in situation where heat exchanges exist.

2.4 Drop deformation and secondary breakup

The development of a spray since the early stages of liquid injection is driven by a set of parameters, such as the pressure of injection, characteristics of the injector nozzle and properties of the surrounding environment (where the drops are inserted). The latter aspect — in which the presence of a cross-flowing gas may be considered — greatly influences the spray evolution without the need to directly interfere with the injection system. In fact, the pressure distribution around the drop due to the relative velocity between gas and particle is responsible for the emergence of instabilities that may lead to deformation and disintegration into smaller fragments. This process is referred to as secondary atomization.

Faeth et al. (1995) reported the existence of two stages of atomization: primary breakup and secondary breakup. During the former stage, the bulk fluid disintegrates into filaments and drops of different sizes close to the injection nozzle (Gorokhovski and Herrmann, 2008). This is usually followed by secondary atomization, which occurs further downstream, resulting in even smaller and more spherical droplets. The evolution from ligament-like elements — resulting from the primary atomization — to smaller spherical particles after secondary atomization highlights the importance of the breakup process in the development of the spray throughout the injection period. In practical applications, such as direct injection engines and gas turbines, the combustion efficiency is dictated by the vaporization rate which, in turn, is influenced by the fuel spray atomization (Kim et al., 2010). Therefore, the comprehensive understanding of the breakup mechanisms and the characteristics of the resulting elements is essential to make it possible to develop highly efficient systems that rely on the atomization process.

The main objective in the study of the deformation and breakup mechanisms is to determine the final droplet sizes in order to introduce them as initial conditions in the simulation procedure of spray impingement models. This goal has been proved very difficult to achieve due to the number of parameters that have a direct effect on the spray behaviour. Furthermore, besides the influence of the aerodynamic forces in the deformation response, the way those forces are applied to the particles also affects secondary atomization (Schmehl, 2002). Assuming the characteristic time t^* of deformation (which is given by $t^* = D_0(\rho/\rho_G)^{1/2}/U^r_{0,sw}$, where $U^r_{0,sw}$ is the relative velocity of the incident drops in the main flow direction), two types of aerodynamic loadings can be identified: sudden shock loading and slow gradual loading. The latter case aims at characterizing applications in which there is a gradual acceleration of the drop velocity in a condition of free fall. This experiment can be simulated by using the drop tower method. On the other hand, there are two distinct methods that can replicate the sudden shock loading concept: shock tubes provide an abrupt acceleration of the particles when subjected to large gas velocities (e.g. diesel injection); and continuous jets deliver a shearing effect as when a drop enters a stream of a moving gas (e.g. gas turbine injection) (Guildenbecher et al., 2009).

Regardless of the chosen method, the drops are always exposed to a spectrum of velocity

gradients that alters the aerodynamic forces acting on them. Once a critical threshold has been exceeded, a specific breakup type occurs. In this work, the categorization proposed by Hsiang and Faeth (1992) has been adopted, since it is the most recognized and accepted by researchers dedicated to the study of secondary breakup. The following three breakup regimes are identified: bag, multimode and shear breakups. Figure 2.6 illustrates the temporal evolution of the three breakup modes, from the deformation stage (left-hand side) until the state of complete drop disintegration (right-hand side).

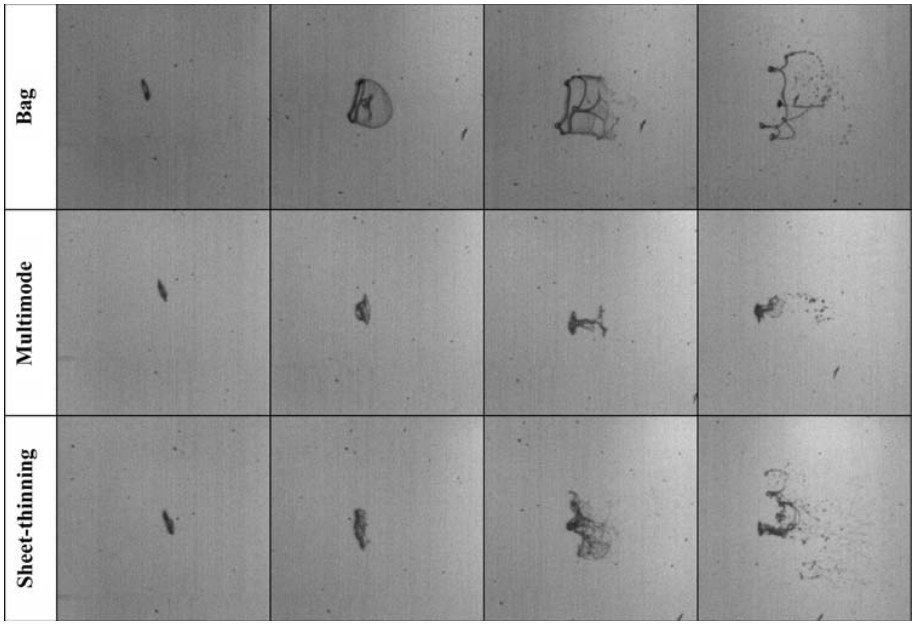

Figure 2.6: Shadowgraphs of secondary breakup of single liquid drops, from Guildenbecher et al. (2009). Time increases from left to right, and disruptive forces increase from top to bottom.

At low We, the unequal static pressure distribution over the drop surface leads to a deformation stage that modifies the particle shape. Assuming an inviscid fluid, the deformation of the drop is caused by the increased static pressures near the upstream and downstream stagnation points combined with the decreased static pressures near the drop periphery — due to the increased flow velocities in this region — which results in a compressive force in the gas flow directions that tends to originate a spheroid-like shape (Chou and Faeth, 1998). On the other hand, the surface tension acts as a restoring force that enables the particle to recover to its approximate spherical aspect. In consequence of this effect, oscillations occur and may give rise to a vibrational breakup regime observed by some authors (Pilch and Erdman, 1987). However, due to the distinctive characteristics of this breakup mode — which produces only a few fragments whose sizes are comparable to those of the parent drops and presents a breakup time that is much lower than that of the other modes — and the fact that it is not always observed during experiments, the first mode of secondary atomization considered in this investigation will henceforth be the bag breakup.

2.4.1 Mechanisms of deformation

Before the first secondary atomization regime arises, the drop experiences a deformation stage that affects its drag properties and, consequently, its trajectory before impact. During this phase, the drop evolves from a spherical to an oblate ellipsoidal shape, as illustrated in Fig. 2.7 with D_{cs} being the deformed drop characteristic length in the cross-stream direction. This

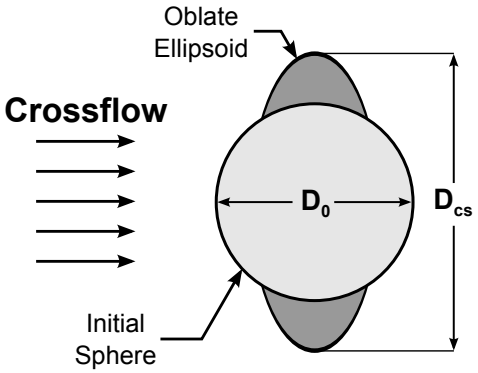

Figure 2.7: Sketch of drop deformation.

distortion should be reflected in the instantaneous drag coefficient (C_D) present in the drag force equation:

$$F_D = \frac{1}{2}\pi\rho_G(U^r_{0,sw})^2 C_D \frac{D^2_{cs}}{4} \tag{2.49}$$

The concern here is related to the quantification of the rate of deformation until secondary atomization takes place. Hsiang and Faeth (1992) reported that D_{cs} increased linearly as function of time until fragmentation began at the breakup initiation time (t_{bin}). The authors carried out an experimental study in which the properties of drop deformation and secondary breakup were observed for shock wave initiated disturbances in air at normal temperature and pressure. Their observations resulted in the following approximation for the maximum deformation, $(D_{cs})_{max}$, at t_{bin}:

$$\left({}^{D_{cs}}/_{D_0}\right)_{max} = 1 + 0.19We^{1/2} \qquad \text{for } We < 10^2,\ Oh < 0.1 \tag{2.50}$$

which was found to be necessary in the calculation of C_D defined as follows:

$$C_D = \frac{2\rho D_0^3 dx^2/dt^2}{3\rho_G D^2_{cs} U^r_{0,sw} - dx/dt)^2} \tag{2.51}$$

Liu and Reitz (1997) used the Taylor analogy breakup (TAB) model to estimate the deformation of drops, assuming that the drag coefficient of a distorting drop should lie between that of a rigid sphere and that of a disk. Relying on the assumption that for high Reynolds numbers the drag coefficient of a disk is about 3.6 times higher than that of a sphere, the authors proposed the following equation for C_D:

$$C_D = C_{D,S}(1 + 2.632y') \tag{2.52}$$

which is dependent upon the magnitude of the drop deformation through the y' parameter as follows:

$$y' = min\left(1, \frac{D_{cs}}{D_0} - 1\right) \tag{2.53}$$

Moreover, it is assumed that the drop is fully distorted when $D_{cs} = 2D_0$, which is close to the values considered for the drop maximum distortion before initiation of fragmentation in the study of Hsiang and Faeth (1992) ($D_{cs} \approx 1.8D_0$). The drag coefficient is given as a linear function of deformation, varying from the condition of no distortion ($y' = 0$) — with the drag coefficient being equal to that of a sphere ($C_D = C_{D,S}$) — to the condition of maximum deformation ($y' = 1$) — when the drag coefficient is approximated by that of a disk ($C_D = 3.632C_{D,S}$). Note that $C_{D,S}$

is the drag coefficient for a sphere, which can be expressed according to the following condition:

$$C_{D,S} = \begin{cases} {}^{24}/_{Re}\left(1 + {}^{1}/_{6}Re^{2/3}\right) & Re \leq 1000 \\ 0.424 & Re > 1000 \end{cases} \tag{2.54}$$

Up to this point, a linear interpolation between a sphere and a disk seemed to be sufficiently accurate for the modelling of drop deformation. However, O'Donnell and Helenbrook (2005) argued that, even though this approach delivered accurate results close to the end points (sphere and disk shape), at intermediate values it was not so adequate. Therefore, in an attempt to overcome this issue, the authors introduced a Lagrange interpolating polynomial for the drag coefficient as function of the aspect ratio of the drop, E (defined as the ratio of the length along the axis of symmetry to the maximum diameter normal to the axis):

$$C_D = 2(E-1)(E-0.5)C_{D,D} - 4E(E-1)C_{D,0.5} + 2E(E-0.5)C_{D,S} \tag{2.55}$$

where the drag on a disk, within the Reynolds number range of interest, is given by:

$$C_{D,D} = \begin{cases} {}^{64}/_{\pi Re}\left(1 + 0.1241Re^{0.8369}\right) & 0 \leq Re \leq 20 \\ {}^{64}/_{\pi Re}\left(1 + 10^{-1.1656+1.1885log_{10}Re-0.1223(log_{10}Re)^2}\right) & 20 \leq Re \leq 200 \end{cases} \tag{2.56}$$

and the drag on a sphere as well as on an ellipsoid of $E = 0.5$ are as follows:

$$C_{D,S} = \begin{cases} {}^{24}/_{Re}\left(1 + 0.1315Re^{0.82-0.05log_{10}Re}\right) & 0 \leq Re \leq 20 \\ {}^{24}/_{Re}\left(1 + 0.1935Re^{0.6305}\right) & 20 \leq Re \leq 200 \end{cases} \tag{2.57}$$

$$\frac{C_{D,0.5}}{C_{D,S}} = \begin{cases} 0.9053\left(1 + 10^{-2.957+1.201log_{10}Re-0.071(log_{10}Re)^2}\right) & 0 \leq Re \leq 20 \\ 0.9053\left(1 + 10^{-4.278+2.945log_{10}Re-0.616(log_{10}Re)^2}\right) & 20 \leq Re \leq 200 \end{cases} \tag{2.58}$$

With this new drag model, O'Donnell and Helenbrook (2005) could predict the data to within an error of 1.5% over the entire range of parameters, which was assumed as very satisfactory.

A different approach has been adopted by Chou and Faeth (1998), who investigated the temporal properties of bag breakup for shock-wave initiated disturbances in air at normal temperature and pressure. They were able to describe the temporal evolution of the characteristic diameter of the drop up to the moment of disintegration and, then, break it down into different stages. In fact, considering the dimensionless characteristic time (t/t^*), the authors concluded that the change in the drop diameter was not linear across the time window examined. Initially, the drop enters a deformation period ($0 \leq t/t^* \leq 2$); then, it undergoes a process of bag growth and breakup ($2 \leq t/t^* \leq 4$); and, finally, the bag breakup regime ends with the ring breakup period ($4 \leq t/t^* \leq 6$). During each of these stages, different empirical correlations were proposed to express the evolution of the drop diameters. In the particular case of the deformation stage, the correlation for the characteristic length of the deformed drop in the cross-stream direction (D_{cs}/D_0) has been defined as follows:

$$D_{cs}/D_0 = 1.0 + 0.5t/t^* \qquad 0 \leq t/t^* \leq 2 \tag{2.59}$$

During this period, the natural deformation of the particle towards a disk-like shape was found to be reasonably well expressed according to a linear equation. Once this threshold has

been reached, bag breakup regime ensues. This is the first breakup mode considered since it occurs at low We and minimal energy is needed to achieve the second stage of atomization. For this reason, this is perhaps the most widely investigated regime in the secondary atomization literature.

2.4.2 Breakup regimes

At relatively low air stream velocities, the drop becomes increasingly flattened, reaching a point where it is thin enough and the centre is blown out into the form of a thin hollow bag attached to a roughly circular rim. This bag is continuously stretched and swept off in the downstream direction until the moment the bag bursts into a set of small fragments (Lee and Reitz, 2000). Later, the toroidal ring to which the bag was attached also breaks up into fragments (fewer in number but bigger than in the previous fragmentation of the bag).

According to Chou and Faeth (1998), the development of the drop diameter varies depending upon the stage in which the drop is found. After the deformation stage, the growth and breakup period ensues within which the deformed drop characteristic length, D_{cs}, of the expanding toroidal ring could be correlated with the following expression:

$$D_{cs}/D_0 = 1.43 - 0.18t/t^* + 0.25(t/t^*)^2 \qquad 2 \leq t/t^* \leq 4 \tag{2.60}$$

Finally, the last stage of bag mode is characterized by the ring breakup, which occurs between the dimensionless characteristic time of 4 and 6, culminating in the fragmentation of the toroidal rim into a circular array of relatively large drops. The size of the parent drop is represented by the following correlation:

$$D_{cs}/D_0 = -2.51 + 1.79t/t^* \qquad 4 \leq t/t^* \leq 6 \tag{2.61}$$

According to the authors, taken together Eqs. 2.59, 2.60 and 2.61 provide a reasonable agreement with the results obtained for the drop characteristic diameter as function of the dimensionless characteristic time. Moreover, it was possible to conclude that the mean diameter of the fragments originated from the bag structure was approximately 4% of the initial drop diameter, whereas the mean diameter of the fragments of the basal ring was 30% the initial drop diameter.

Increasing considerably the relative velocities between the drop and the surrounding fluid, shear breakup occurs. However, it proceeds in a distinct fashion from the bag breakup regime. Instead of a bag being stretched in the main stream direction, a thin sheet is continuously stripped off of the rim by drag forces. The sheet then disintegrates into fine filaments or ligaments which later breakup into small droplets (Pilch and Erdman, 1987).

At values of We between those of bag and shear breakup occurs multimode breakup, which is a combination of both breakup modes. This mechanism is characterized by the formation of a bag accompanied by the presence of a core drop that evolves along the main stream direction. This results in the formation of a long ligament in the centre of the bag structure, which bursts first, followed by the rim and central column of liquid.

It is worth mentioning that even though the classification adopted in this investigation only incorporates three regimes, other mechanisms have been reported in the literature. At extremely high We, some researchers have observed the formation and growth of unstable surface waves on the leading edge of the deformed drop (Guildenbecher et al., 2011). This is referred to as catastrophic breakup. However, since such high velocities are not expected in

typical dense sprays — and, thus, practical applications of this breakup mode are limited — this will not be considered here.

The different morphologies and characteristic of the breakup modes considered in this study are illustrated with simplified renditions in Fig. 2.8. From top to bottom the modes are bag, multimode and shear breakup.

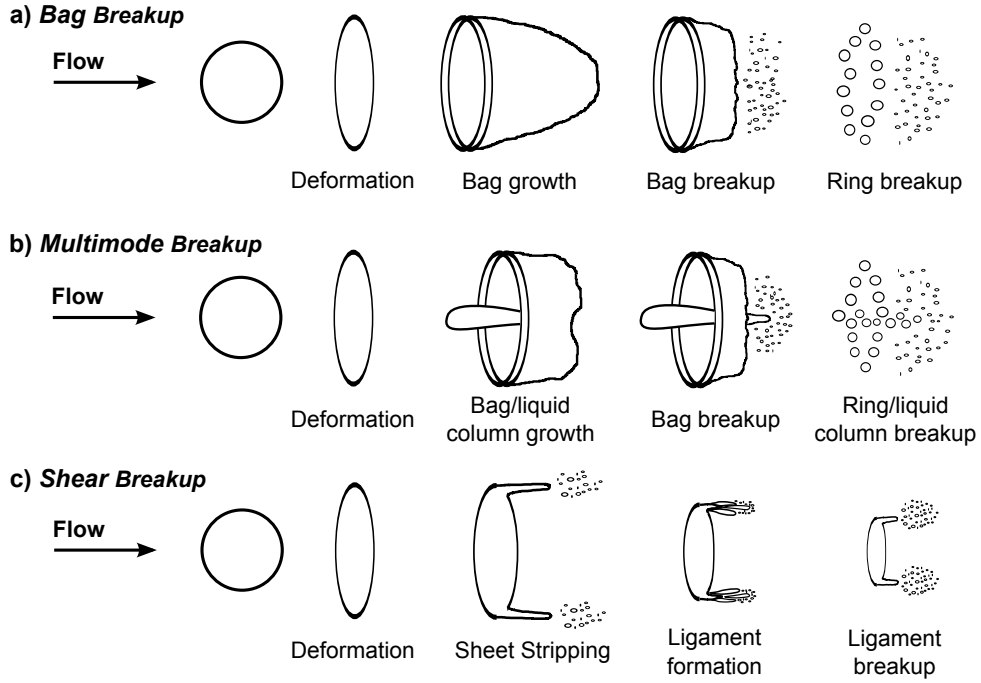

Figure 2.8: Breakup mechanisms. Adapted from Pilch and Erdman (1987).

2.4.3 Transition criteria between breakup modes

Even though the transition between breakup modes is a continuous process, the assumption of fixed values is widely accepted. In fact, the map of breakup regimes is usually defined in terms of the Weber number, being essentially constant for $Oh < 0.1$. However, the magnitude of each critical threshold is not uniform across the literature available.

The first investigations concerning the breakup of drops subjected to an intense air stream date back from the mid-twentieth century. At the time, Hinze (1955) could already identify various mechanisms of breakup depending upon the Weber number (with the velocity being the maximum velocity gradient in the flow field direction of the continuous phase). Moreover, the critical threshold from which secondary atomization occurred was identified as $We_{cr} = 13$ (which coincided with the onset of bag breakup).

Krzeczkowski (1980) implemented an experimental study for the disintegration mechanisms of liquid drops due to the presence of an air stream. Both breakup modes and time scales involved were found to be influenced by the Weber number, Laplace number and the ratio μ/μ_G. Considering the set of measurements carried out in their study, the transition between bag, multimode and shear regimes at low Oh were set with a We_{cr} of 10, 30 and 63, respectively.

A few years later, Pilch and Erdman (1987) presented a comprehensive review of liquid drops breakup. The experimental data were collected from several different sources available in the literature and were disposed in a consistent basis on their paper. The onset of bag, multi-

mode (here designated as bag-and-stamen breakup) and shear breakup regimes were attributed the critical We of 12, 50 and 100, respectively. Moreover, two additional regimes were also considered: vibrational breakup ($We \leq 12$) and catastrophic breakup ($We > 350$). In its turn, Hsiang and Faeth (1992) reported that the transition to the onset of bag, multimode and shear breakup regimes would occur at We of 13, 35 and 80, respectively.

In 1996, another exhaustive review was published by Gelfand (1996) and new breakup mode thresholds were proposed: $We_{cr} = 10 \pm 2$ for the onset of bag breakup, $We_{cr} = 40$ for the transition between bag and multimode regimes and $We_{cr} = 60$ for the critical threshold to reach shear breakup. More recently, Jenny et al. (2012) suggested that bag breakup occurred when the Weber number exceeded 11, whereas in the case of shear breakup the transition values was assumed to be 80.

Table 2.5 emphasizes the choices made by the different authors for the We_{cr} between bag, multimode and shear breakup regimes. It is noteworthy that while in the case of the first stage of breakup the critical thresholds proposed in the literature considered present similar values (around 12 ± 2), in the cases of both multimode and shear transition criteria the discrepancies are more noticeable.

Table 2.5: Summary of the various We_{cr} proposed in the literature for the transition between breakup regimes at $Oh < 0.1$.

Transition to:	Hinze (1955)	Krzeczkowski (1980)	Pilch and Erdman (1987)	Hsiang and Faeth (1992)	Gelfand (1996)	Jenny et al. (2012)
Bag breakup	13	10	12	13	10	11
Multimode breakup	-	30	50	35	40	-
Shear breakup	-	63	100	80	60	80

In all the cases aforementioned, constant Weber numbers are established to defined the transition between breakup modes (i.e., We_{cr} is independent of drop viscosity). This is valid for $Oh < 0.1$. For higher Ohnesorge numbers, the critical thresholds are dependent upon the value of Oh. In fact, as shown by Hsiang and Faeth (1995), at values of Oh greater than 0.1, the We required to reach each regime progressively increases by increasing Oh.

In this context, Brodkey (1969) $-$ and later confirmed by Pilch and Erdman (1987) $-$ proposed the following correlation to describe We_{cr} as function of the Oh:

$$We_{cr} = We_{cr,Oh\to 0}(1 + 1.077Oh^{1.6}) \tag{2.62}$$

Here, $We_{cr,Oh\to 0}$ is the critical Weber number at low Oh, as given in Table 2.5. In the case of the study presented by Pilch and Erdman (1987), $We_{cr,Oh\to 0} = 12$. Therefore, analysing Eq. 2.62, the critical Weber number is approximately 12 when the Ohnesorge number is small ($Oh < 0.1$), but becomes higher as the Ohnesorge number increases. A similar expression has been proposed by Gel'fand et al. (1973) for $Oh < 0.4$ which is as follows:

$$We_{cr} = We_{cr,Oh\to 0}(1 + 1.5Oh^{0.74}) \tag{2.63}$$

where, in the particular case of the liquid being water or kerosene, $We_{cr,Oh\to 0}$ is equal to 5.

Most of the contributions available in the literature regarding the breakup mechanisms refer to shock tube experiments in which the nature of the deformation is determined by an abrupt loading applied to the particles. Nevertheless, there are also papers that consider con-

tinuous jet experiments, such as those undertaken by Liu and Reitz (1997), Lee and Reitz (2000), Park et al. (2006) and Kim et al. (2010). However, no explicit transition criteria are given in these cases. In Lee and Reitz (2000), high velocity, gas-assisted liquid drop atomization processes were investigated. The Weber numbers studied were 72, 148, 270, and 532. The authors confirmed the existence of bag and catastrophic breakup regimes at low (72) and high (532) We, whereas for We between 148 and 270 shear breakup was observed. Similar experimental conditions were used in the investigation carried out by Liu and Reitz (1997) where the breakup mechanisms were analysed by using ultra-high magnification, short-exposure photography. Bag, shear and catastrophic breakup regimes were detected at Weber numbers of 56, 260 and 463, respectively. Previous conclusions are in line with observations of Park et al. (2006), whose measurements distinguished bag, shear and catastrophic breakup at We of 68, 153 and 383, respectively. It becomes clear that the values encountered for the regime thresholds are considerably greater than in the shock tube experiments. Therefore, it is possible to conclude that the nature of the disturbances applied to liquid drops proved to have a direct effect on the outcome of secondary atomization.

With respect to the drop tower concept — which represents slow gradual loadings applied to the drops — there is little work done in this area. The second stage of atomization of a free falling drop occurs when forces on the drop surface due to drag are too large to be stabilized by surface tension. Based on the drop acceleration, maximum deformation is obtained during the initial period of the fall. Hsiang and Faeth (1993) evaluated several experimental data on free falling drops and were able to come up with a criterion for the onset of disintegration for drops subjected to gradual disturbances. Instead of a singular value for the critical Weber number, the interval between 11 and 13 was defined as being the range in which the transition occurred. Similarly, in a theoretical investigation Tarnogrodzki (2001) defined the transition criterion We_{cr} as occurring within the interval of 10 to 15, for $Oh < 0.1$. Above this threshold the drop started to disintegrate according to the bag breakup mechanisms. In both cases, it is relevant to note that the values are close to the transition advanced in the literature for shock wave disturbances.

2.4.4 Fragment sizes and velocities

Regardless of the breakup mode, the outcome of secondary atomization is always a number of fragments with a specific distribution. This information is perhaps the most important property of the secondary atomization process, with a critical impact on the outcome of any breakup model. One major simplification provided by Ruff et al. (1992) in their work concerning the structure of dense sprays is the finding that local drop size distributions generally satisfy the universal root normal distribution function of Simmons (1977a,b), with $MMD/SMD = 1.2$.

Following the works of Simmons (1977a,b), Hsiang and Faeth (1992, 1993) found that for $Oh < 0.1$, drop size distributions after secondary breakup satisfied the root normal distribution function with $MMD/SMD = 1.2$ for both bag and multimode breakup regimes. Furthermore, after removal of the drop core, this same distribution was found to be applicable to shear breakup regime. The authors also found that drop sizes after secondary breakup decreased as We increased and a single correlation could express the SMD after bag, multimode and shear breakup. The data evaluated yielded the following empirical fit:

$$D_{SMD} = CD_0(\rho/\rho_G)^{1/4}\left[\frac{\mu}{\rho D_0 U_0^r}\right]^{1/2} \tag{2.64}$$

where C is a constant of proportionality which was assumed to be 6.2.

Wert (1995) also derived a correlation for the sauter mean diameter (SMD) of fragments produced by the bag breakup regime for incident drops having Ohnesorge numbers smaller than 0.1, which is as follows:

$$D_{SMD} = CD_0We^{-1/3}\frac{(t_{tot} - t_{bin})^{2/3}}{t^*} \tag{2.65}$$

where C is a constant of proportionality, which was suggested by the author to be 0.32. Even though the investigation was focused only on bag breakup, the resultant expression was shown to correlate reasonably well with data from multimode regime.

For the diameter of the core fragments resulting from the shear breakup, Hsiang and Faeth (1993) proposed the following equation:

$$We_{core} = (4Eo_{core}We/3\overline{C}_D)^{1/2}/(1 + C_v) \tag{2.66}$$

where

$$C_v = (3\overline{C}_D t_{tot}/4t^*)/(\rho/\rho_G)^{-1/2} \tag{2.67}$$

Earlier work has shown that $t_{tot}/t^* = 5$ for $10 < We < 10^6$ and $Oh < 0.1$ (Hsiang and Faeth, 1992). Assuming $\overline{C}_D = 5$ and $Eo_{core} = 16$, which are the values adopted by the authors, yields:

$$D_{core} = \frac{2.1D_0We^{-1/2}}{1 + 19(\rho/\rho_G)^{1/2}} \tag{2.68}$$

On the other hand, from their phenomenological analysis, Hsiang and Faeth (1993) could also relate the relative velocity of the core drop after breakup, U^r_{core}, to experimental conditions:

$$\frac{U^r_0 - U^r_{core}}{U^r_0}(\rho/\rho_G)^{1/2}(1 + 3C) = 3\overline{C}_D t_{tot}/4t^* \tag{2.69}$$

Using the above assumptions for t_{tot}/t^*, $\overline{C}_D$ and Eo_{core}, and simplifying the equation yields:

$$U^r_{core} = U^r_0\left(1 - \frac{19(\rho/\rho_G)^{-1/2}}{(1 + 57(\rho/\rho_G)^{-1/2}}\right) \tag{2.70}$$

It is noteworthy at this stage that according to the measurements carried out by Hsiang and Faeth (1993), the disintegration process occurring during the shear breakup leads to a relative velocity of the core drop at the end of the regime 30-40% lower than the initial relative velocity. This gives rise to a local Weber number of the core fragment generally greater than the critical threshold for the onset of bag breakup ($We = 13$). However, since no breakup was observed in these cases, it suggests that the criterion for breakup after first disintegration may differ from the criterion for initial breakup (Hsiang and Faeth, 1992).

The last piece of information refers to the relative velocity of the fragments resulting from the disintegration of drops during breakup. Chou et al. (1997) observed that the velocity of drops produced by shear breakup was related to the velocity of the gas. In addition, it was also found that the drop velocities were relatively independent of the drop size. Therefore, the following correlation was proposed for the mean relative velocity of the fragments as function of the velocity of the core drop for both stream-wise and cross-stream direction:

$$\begin{aligned} \overline{U}_{shear,sw} &= U_0 + 9.5(\rho/\rho_G)^{-1/2}(U_G - U_0) \\ \overline{U}_{shear,cs} &= 0 \end{aligned} \tag{2.71}$$

Regarding the velocity of the fragments originated from bag and multimode breakup regimes, Hsiang and Faeth (1993) proposed the following drop-size/velocity correlation at the completion of secondary atomization:

$$U_{frag}^{r} = U_{0}^{r}\left[1 + 2.7\left((\rho/\rho_G)^{-1/2} D_0/D\right)^{2/3}\right]^{-1} \tag{2.72}$$

2.4.5 Time scales

The breakup mechanisms do not take place instantaneously, but rather require a finite period of time. Therefore, knowledge of the time scales involved in such process is of paramount importance. Time, t_0, begins when the particle is introduced into the flow field (Guildenbecher et al., 2011). Then, there are two additional characteristic times of interest commonly reported in the literature: breakup initiation time and total breakup time. According to Pilch and Erdman (1987), the breakup initiation time (t_{bin}) is defined as the time when the first signs of the disintegration process appear, whereas the total breakup time (t_{tot}) is defined as the moment the drop and all corresponding fragments no longer undergo further breakup. This terminology is illustrated schematically in Fig. 2.9.

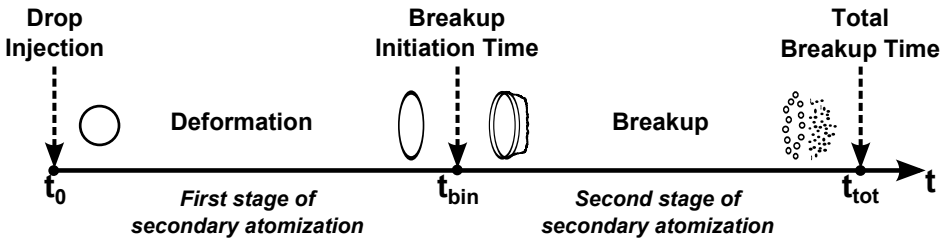

Figure 2.9: Time scales involved in secondary atomization.

The instant t_{bin} marks the beginning of the second stage of secondary atomization from which the models of deformation are no longer valid. For Pilch and Erdman (1987), the time required to initiate breakup decreases continuously by increasing the Weber number for both viscous and non-viscous drops. Based on this assumption, the authors proposed the following correlation:

$$t_{bin}/t^* = 1.9(We - 12)^{-0.25}(1 + 2.2Oh^{1.6}) \tag{2.73}$$

which represented adequately the data evaluated for $We < 10^5$ and $Oh < 1.5$.

Hsiang and Faeth (1992) studied the breakup initiation time by taking into analysis several sources of experimental data. At low Oh, drop distortion correlated reasonably well as a linear function of time, with the maximum distortion reached at roughly $t_{bin}/t^* = 1.6$. To extend the range of measurements to $Oh > 0.1$, the authors included a corrected parameter, which yielded the following expression for the breakup initiation time:

$$t_{bin}/t^* = 1.6/(1 - Oh/7) \tag{2.74}$$

which was applied to liquid drops with $We < 10^3$ and $Oh < 3.5$.

Similarly, Hsiang and Faeth (1992) proposed the following correlation for the total breakup time:

$$t_{tot}/t^* = 5/(1 - Oh/7) \tag{2.75}$$

which provided a reasonable fit of the data evaluated. Note that the approach is analogous to

the case of the breakup initiation time: an initial linear expression is provided ($t_{tot}/t^* = 5.0$) for the data including low viscosity drops and is then corrected to comprise the results with higher Oh.

In its turn, Pilch and Erdman (1987) presented correlations for the total breakup time at low Oh according to specific ranges of Weber numbers:

$$\begin{aligned}
t_{tot}/t^* &= 6/(We-12)^{-0.25} && 12 \leq t/t^* \leq 18 \\
t_{tot}/t^* &= 2.45/(We-12)^{0.25} && 18 \leq t/t^* \leq 45 \\
t_{tot}/t^* &= 14.1/(We-12)^{-0.25} && 45 \leq t/t^* \leq 351 \\
t_{tot}/t^* &= 0.766/(We-12)^{0.25} && 351 \leq t/t^* \leq 2670 \\
t_{tot}/t^* &= 5.5 && 2670 \leq t/t^* \leq 10^5
\end{aligned} \tag{2.76}$$

[Note that the third equation has been corrected due to a typographical error published in Pilch and Erdman (1987)].

Nevertheless, breakup time scales are still an on-going research area. Little research exists on the topic and there are an obstructing lack of validation results available on the literature which could attest the accuracy of the original findings.

Chapter 3

CFD methodology

As a basis for the model interpretation, the mathematical formulation is described in this chapter, which is divided between the two phases involved in the problem. In the fluid phase, an Eulerian reference frame is used to describe the effect of both inter-phase slip and turbulence on particle motion using random-sampling techniques (Monte Carlo). This is discussed in section 3.1. On the other hand, the dispersed phase is treated using a Lagrangian reference frame. As explained in section 3.2, the details of the flow around each of the particles are subsumed into assumed drag, lift and moment forces acting on and altering the trajectory of those particles. Section 3.3 is devoted to the description of both the measures used to account for the interaction between the two phases and the procedures adopted for the modelling of the flow considered. In the last section (section 3.4), the boundary conditions employed in the model are specified.

3.1 Continuous phase

The fluid will be regarded as a continuum. This is appropriate for flow analysis at a macroscopic length scale — as is the case of the present study — since at this level the molecular structure of matter and molecular motions may be ignored. Therefore, the continuum description of the gas neglects the fact that it is made up of discrete molecules. Macroscopic properties as density, pressure, temperature, and velocity are considered to be well-defined at infinitely small points, and are assumed to vary "continuously" from one point to another.

The governing equations for the gas phase represent the mathematical statements of the conservation laws of physics. Such laws state that the mass of a fluid is conserved, and the rate of change of momentum equals the sum of the forces on a fluid particle (Newton's second law). The resulting time-averaged partial differential equations are the continuity and momentum equations, which in index notation and for a steady, incompressible, viscous, Newtonian fluid can be expressed as:

$$\rho \frac{\partial \overline{U}_i}{\partial x_i} = S_m \tag{3.1}$$

and

$$\rho \overline{U}_j \frac{\partial \overline{U}_i}{\partial x_j} = -\frac{\partial \overline{P}}{\partial x_i} + \frac{\partial}{\partial x_j}\left(\mu \frac{\partial \overline{U}_i}{\partial x_j} - \rho \overline{u_i' u_j'}\right) + S_{U_i} \tag{3.2}$$

in which the over-bars represent time-averaged quantities and $\overline{u_i' u_j'}$ are additional turbulent stresses called the Reynolds stresses. This equation set comprising Eqs. 3.1 and 3.2 is called the Reynolds-averaged Navier-Stokes equations. The source terms (S_m and S_{U_i}) are used to account for the influence of the gas phase over the particles in the dispersed phase. Introducing a general variable property per unit mass, ϕ (which may stand for any of the scalar variables, velocity components, turbulent kinetic energy or dissipation properties), the resulting partial

differential equations for a steady incompressible flow can be reduced to a single convective-diffusive conservation equation of the form:

$$\frac{\partial(\rho\phi U_i)}{\partial x_i} = \frac{\partial}{\partial x_i}\left[\Gamma_\phi \frac{\partial \phi}{\partial x_i}\right] + S_\phi \tag{3.3}$$

in which Γ is the effective diffusion coefficient for quantity ϕ, and S_ϕ is the general source term, which can be divided into two parts: $S_{\phi G}$ specifies the source term of the gas and $S_{\phi p}$ specifies the source term of the particle. Equation 3.3 is the so-called transport equation for property ϕ. Such expression clearly highlights the various transport processes: the convective term is on the left side, whereas the diffusive and source terms are on the right side.

Turbulence is modelled with the "$k-\varepsilon$" turbulence model of Launder and Spalding (1974). It is one of the most frequently used and validated closure approaches for a wide range of applications. This two-equation model makes use of the Boussinesq hypothesis (Launder and Spalding, 1974) to compute the Reynolds stresses by relating it to the mean rates of deformation as follows:

$$\rho\overline{u_i' u_j'} = -\mu_t\left(\frac{\partial \overline{U_i}}{\partial x_j} + \frac{\partial \overline{U_j}}{\partial x_i}\right) + \frac{2}{3}\rho k \delta_{ij} \tag{3.4}$$

in which $k = (1/2)\left(\overline{u_i'^2} + \overline{v_i'^2} + \overline{w_i'^2}\right)$ is the turbulent kinetic energy per unit mass, δ_{ij} is the Kronecker delta ($\delta_{ij} = 1$ if $i = j$, and $\delta_{ij} = 0$ if $i \neq j$) and μ_t is the turbulent dynamic viscosity. This latter property is a space and time dependent quantity, the value of which depends entirely upon the local turbulent characteristics of the flow. It can be related to the turbulent kinetic energy, k, and dissipation rate, ε through dimensional analysis with the following expression:

$$\mu_t = C_\mu \rho \frac{k^2}{\varepsilon} \tag{3.5}$$

By replacing the property ϕ with the corresponding variable and selecting appropriate values for Γ and the source terms, one should get the special forms of the partial differential equations for the continuity, momentum, enthalpy, vapour mass fraction, turbulent kinetic energy, or dissipation, as expressed in Table 3.1, where G is the usual turbulence energy production term, which is defined as:

$$G = \mu_t\left[\frac{\partial \overline{U_i}}{\partial x_j} + \frac{\partial \overline{U_j}}{\partial x_i}\right]\frac{\partial \overline{U_i}}{\partial x_j} \tag{3.6}$$

Table 3.1: Terms in the general form of the differential equation.

ϕ	$S_{\phi,G}$	$S_{\phi,p}$	Γ_ϕ
1	$-$	$\overline{S_{m,p}}$	$-$
U_i	$-\frac{\partial}{\partial x_i}\left(P + \frac{2}{3}k\right) - \frac{\partial}{\partial x_j}\frac{2}{3}\mu_t\frac{\partial \overline{U_j}}{\partial x_i} + \rho g_i$	$\overline{S_{U_i,p}}$	$\mu + \mu_t$
T	0	$\overline{S_{T,p}}$	$\frac{\mu}{Pr} + \frac{\mu_t}{Pr_t}$
Y	0	$\overline{S_{Y,p}}$	$\frac{\mu}{Sc} + \frac{\mu_t}{Sc_t}$
k	$G - \rho\varepsilon$	$\overline{S_{k,p}}$	$\mu + \frac{\mu_t}{\sigma_k}$
ε	$C_{\varepsilon 1}\frac{\varepsilon}{k}G - C_{\varepsilon 2}\rho\frac{\varepsilon^2}{k}$	$\overline{S_{\varepsilon,p}}$	$\mu + \frac{\mu_t}{\sigma_\varepsilon}$

The empirical constant employed is the one that has been determined by Launder and Spalding (1974) based on the analysis of numerous turbulent free jets and mixing layer simulations. Additional constants — which are given in Table 3.2 — are determined by comprehensive data fitting for a wide range of turbulent flows. An obvious limitation of the "$k-\varepsilon$" model is that it is based on the underlying assumption that μ_t is isotropic, i.e., the ratio between Reynolds stress and mean rate of deformation is the same in all directions. Even so, it has been proven capable of predicting accurately a large number of complex flows.

Table 3.2: Coefficients of the "$k-\varepsilon$" turbulence model, from Launder and Spalding (1974).

$C_{\varepsilon 1}$	$C_{\varepsilon 2}$	σ_k	σ_ε	$C_{\varepsilon 3}$	Pr_t	Sc_t	Pr	Sc
1.44	1.92	1.0	1.3	1.1	0.6	0.85	$\mu C_p/K_G$	$\mu/\rho C_d$

The resolution of the differential equations for turbulent flows requires the use of a finite-difference method to obtain a system of algebraic equations that can be solved numerically. Those algebraic equations may be converted from the transport equation (Eq. 3.3) using a control-volume-based technique. The quadratic upstream interpolation for convective kinetics (QUICK) scheme of Leonard (1979) has been adopted for this purpose. Such high-order differencing scheme minimizes numerical diffusion errors by involving more neighbouring nodes: two upstream and one downstream nodal values. Therefore, the face value ϕ would be obtained from a quadratic function passing through two bracketing nodes (on each side of the face) and a node on the upstream side (see Fig. 3.1).

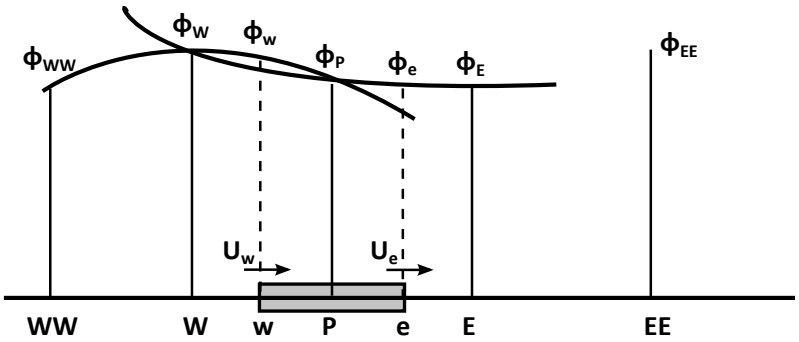

Figure 3.1: Quadratic profile used in QUICK scheme.

For instance, let the two bracketing nodes be *i* and *i-1*, and upstream node *i-2*. Then, for a uniform grid, the value of ϕ at the cell face between the three nodes is given by:

$$\phi_{face} = \frac{6}{8}\phi_{i-1} + \frac{3}{8}\phi_i - \frac{1}{8}\phi_{i-2} \tag{3.7}$$

Therefore, from Fig.3.1, when $U_w > 0$, the bracketing nodes for the west face w are P and W, the upstream node is WW and $\phi_w = \frac{6}{8}\phi_W + \frac{3}{8}\phi_P - \frac{1}{8}\phi_{WW}$. On the other hand, when $U_w < 0$, the bracketing nodes for w are W and P, the upstream node is E and, consequently, $\phi_w = \frac{6}{8}\phi_P + \frac{3}{8}\phi_W - \frac{1}{8}\phi_E$. Similarly, for the east face, one should get $\phi_e = \frac{6}{8}\phi_P + \frac{3}{8}\phi_E - \frac{1}{8}\phi_W$ or $\phi_e = \frac{6}{8}\phi_E + \frac{3}{8}\phi_P - \frac{1}{8}\phi_{EE}$ for positive or negative values of U_e, respectively. Furthermore, rearranging Eq. 3.7, it is possible to obtain:

$$\phi_{face} = \frac{1}{2}\left(\phi_i + \phi_{i-1}\right) - \frac{1}{8}\left(\phi_i - 2\phi_{i-1} + \phi_{i-2}\right) \tag{3.8}$$

in which the first term on the right hand side of the equation corresponds to the central differ-

ence formula, whereas the second term is the important stabilizing upstream-weighted normal curvature contribution.

It is worth mentioning at this stage that contrary to what could be expected, some of the variables are not stored at the nodes of an ordinary control volume, namely the scalar quantities (such as pressure, temperature, etc.). In fact, if velocities and pressures were to be defined at the nodal points, a highly non-uniform pressure field could act like a uniform field in the discretised momentum equations. Therefore, a staggered grid for the velocity components is used so they are defined at the (scalar) cell faces in between adjacent nodes. This is highlighted in Fig. 3.1 where the velocity components are estimated on the staggered grids centred around the cell faces and are identified by arrows, which indicate the direction of the flow.

Considering now a three-dimensional problem, a hexadron-shaped cell containing node P has now six neighbouring nodes (rather than the two considered in the one-dimensional form) as illustrated in Fig. 3.2.

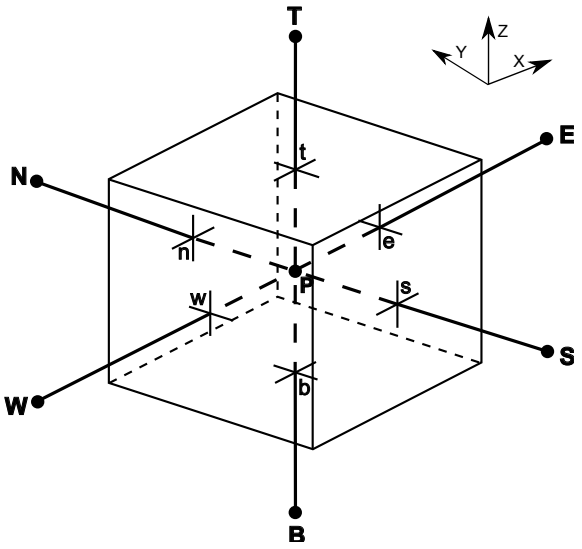

Figure 3.2: Nodal configuration for a control volume.

The notation w, e, t, b, n and s is used to refer to the west, east, top, bottom, north and south cell faces of the node P. Each face establishes the boundaries between the cell containing node P and the neighbouring nodes identified by W, E, T, B, N and S. It is possible to write the general form of the discretized equations for any dimensional problem as:

$$A_P^{\phi}\phi_P = \sum A_i^{\phi}\phi_i + S_U^{\phi} \tag{3.9}$$

where $\sum$ indicates summation over each neighbouring node i, A_i are the neighbouring coefficients (A_W and A_E in one dimension; A_W, A_E, A_S and A_N in two dimensions; and A_W, A_E, A_S, A_N, A_B and A_T in three dimensions), and ϕ_i are the values of the property ϕ at the neighbouring nodes. In Eq. 3.9, the coefficient at node P satisfies the following relation:

$$A_P^{\phi} = \sum A_i^{\phi} + (F_i - F_{i-1}) - S_P^{\phi} \tag{3.10}$$

in which the parameter F is the convective mass flux per unit area. Introducing Eq. 3.10 in 3.9 yields:

$$\sum A_i^{\phi}\left(\phi_P - \phi_i\right) + \left(F_i - F_{i-1}\right)\phi_P = S_U + S_P^{\phi}\phi_P \tag{3.11}$$

where $\left(S_U + S_P^{\phi}\phi_P\right)$ is the linearised source term.

The resolution of the set of equations for the complete field by the original QUICK method can lead to negative values of A_i^{ϕ}, which prevents a stable solution. In the present work, diagonal dominance of the coefficient matrix is ensured and enhanced by rearranging the difference equation for the cells in which the coefficients A_i^{ϕ} become negative. This rearrangement consists in subtracting $A_i^{\phi}\phi_P$ from both sides of Eq. 3.9, eliminating the negative contribution of A_i^{ϕ} and simultaneously enhancing the diagonal dominance of the coefficient matrix (Barata, 1989).

The solution procedure for the continuous phase is based on the semi-implicit method for pressure-linked equations (SIMPLE) algorithm, which has been widely used and reported in the literature (Patankar and Spalding, 1972). In this algorithm, the convective fluxes per unit area, F, through cell faces are evaluated from guessed velocity components. Furthermore, it is based on a guess-and-correct procedure in which a guessed pressure field is used to solve the momentum equations (and consequently determine guessed velocity components), whereas a pressure correction equation — which has been deduced from continuity equation — is solved to obtain a pressure correction field. This new set of values for the pressure is then used to update the velocity and pressure fields calculated in each iteration. As the algorithm proceeds, the aim is to progressively improve the guessed fields until convergence is reached. The tridiagonal matrix algorithm (TDMA) is then applied line-by-line to solve the set of equations.

3.2 Dispersed phase

Particle dispersion models can be classified based on their (Lagrangian or Eulerian) reference frame. Nonetheless, the Lagrangian representation is often referred to as the natural approach for treating particles because their motion is tracked as they move throughout the flow field. The path is created in each time step by reference to its origin and time elapsed after start of injection. The particle trajectory is determined by solving its momentum equation through the Eulerian fluid velocity field.

Eulerian models are very popular when particle loading is high (as for example in fluidized combustion systems) but have certain limitation in modelling simplified dilute flows. Since this chapter is limited to the dispersed phase of a dilute two-phase flow, the present section is dedicated only to the Lagrangian dispersion model.

In multiphase flows, it is usually convenient to use a Lagrangian-Eulerian framework. Therefore, the equations for the continuous phase remain expressed in the Eulerian form, whereas the conservation equations for the dispersed phase are written in the Lagrangian coordinate system in order to be able to move with each element.

The major difficulty in Lagrangian computations is to define the instantaneous gas field, as the time-averaged Eulerian equations only provide the gas mean properties (Chen and Pereira, 1995). Several models have been devised to account for the effect of the turbulence on the particle trajectory, such as the deterministic separated flow (DSF) and stochastic separated flow (SSF) models (Faeth, 1987). Among them the SSF model has been the most widely used.

In this model, the turbulent dispersion of a particle is considered based on the concept of energy containing eddies and their trajectories are obtained by solving the particle momentum equation through the Eulerian fluid velocity field. When the particles move through the turbulent flow field, they are assumed to interact with the local turbulent eddies, which are represented by an instantaneous property consisting of a mean quantity and a fluctuating quantity. The mean quantity can be obtained directly from the Reynolds averaged equations, whereas the

fluctuating quantity is selected from a Gaussian distribution with a standard deviation proportional to the locally predicted value of $\sqrt{k}$. Therefore, it can be said that this model introduces a stochastic effect by adding to the mean gas velocity a random component. Nevertheless, the key point in this stochastic treatment is to determine the length of time over which these random components exist, namely the interaction time of the particle and the turbulent eddy.

Note that the initial droplet size distribution of the spray is selected according to the given experimental probability density function (PDF). Also, since the number of drops in the real scenario is usually very large, it is common to employ a statistical approach in which a number of drops of identical size and properties are treated as a computational parcel. The number of parcels is chosen so the entire population is adequately represented in statistical terms. The trajectories of these representative samples are then determined in order to reduce the total number of trajectory computations to a reasonable figure.

The equations of motion of the particles can be deduced from Newton's Second Law of Motion if all the forces acting on a drop immersed in a turbulent flow are mathematically quantified. At first, one would probably assume that it should not be too difficult to obtain the trajectory of a particle in a fluid flow. However, the task has been found to be more intricate than expected, and numerous publications have been written about the subject. Fortunately, for dilute two-phase flows, it is possible to consider a simplified version of the problem by considering three major assumptions (Shirolkar et al., 1996): 1) the particle is assumed to be spherical; 2) particle-particle collision is neglected; and 3) the particle density is assumed to be much larger than the surrounding fluid density.

Most of the work relies on the application of these assumptions. In most practical dilute flow applications, assumption (1) is usually reasonable because the static pressure gradient is small and the drag in these particles should not be far from that on a sphere. Such simplified assumption becomes inapplicable when the air flow rate is high enough and the liquid drops enter a deformation stage. In this case, a proper treatment of the drops trajectory during this stage of atomization must be considered (see section 4.4.3 of the next chapter). In assumption (2), it is assumed that the particles are sufficiently dispersed so that the interaction between droplets is negligible, which is based on the observation reported by Faeth (1987) that in specific spray nozzles (such as the ones that create hollow-cone sprays) drop collisions are infrequent. For assumption (3), it is perfectly plausible to admit that most of the densities of liquid drops are much larger than that of water (typically, the droplet-to-fluid density ratio should be greater than 200 in order to consider this assumption valid). This simplifies the analysis because several fluid forces (such as Basset, virtual mass, Magnus, buoyancy and Saffman lift forces) become negligible. Consequently, it is considered that the steady-state drag term is the most important force acting on the particle. Under these conditions, the drop momentum equation can be greatly simplified, yielding:

$$\frac{\partial U_i}{\partial t} = \frac{1}{\tau_p}\left(U_{Gi} - U_i\right) + g_i \tag{3.12}$$

in which g_i corresponds to the external forces (i.e., gravity, centrifugal and Coriolis forces) and τ_p is the droplet relaxation time. In fact, if the drop is dense ($\rho >> \rho_G$), the inertial force at the gas-liquid interface will dampen the velocity fluctuations in relation to the fluctuations of the surrounding fluid. This reduction in its root mean square (rms) fluctuating velocity is known as inertia effect and is characterized by τ_p, which can be written as the mathematical expression (Shirolkar et al., 1996):

$$\tau_p = \frac{24\rho D^2}{18\mu C_D Re_p} \tag{3.13}$$

where Re_p is the particle Reynolds number, given by:

$$Re_p = \frac{\rho\,|U - U_G|\,D}{\mu} \tag{3.14}$$

and C_D is the drag coefficient which, according to the experimental data fitting reported by Crowe et al. (2012), may be expressed as:

$$C_D = \begin{cases} \left(\frac{24}{Re_p}\right)\left(1 + 0.15Re_p^{0.687}\right) & Re_p < 1000 \\ 0.44 & Re_p \geq 1000 \end{cases} \tag{3.15}$$

Substituting Eqs. 3.14 and 3.15 into Eq. 3.13, a new expression can be obtained for the droplet relaxation time:

$$\tau_p = \frac{m}{3\pi\mu D}\frac{1}{1 + 0.15Re_p^{0.687}} \tag{3.16}$$

Equations 3.12 and 3.16 are the most commonly used expressions in Lagrangian models to generate the particle trajectories. The particle momentum equation can be analytically solved over small time steps, Δt, in which the instantaneous fluid velocity and the droplet relaxation time are assumed to be constant. Therefore, by knowing the new drop velocity at the end of each time step, a drop trajectory can be constructed with the aid of the equations given below:

$$U_i^{NEW} = U_{Gi} + \left(U_i^{OLD} - U_{Gi}\right)e^{-\Delta t/\tau_p} + g_i\tau_p\left(1 - e^{-\Delta t/\tau_p}\right) \tag{3.17}$$

$$x_i^{NEW} = x_i^{OLD} + \frac{\Delta t}{2}\left(U_i^{NEW} + U_i^{OLD}\right) \tag{3.18}$$

Equations 3.17 and 3.18 should be applied to each of the components of the Cartesian coordinates system considered. Therefore, it is possible to obtain a three dimensional trajectory of the particles. Also, in the present case, it is worth highlighting that the external forces (namely, the gravity) are only found in the normal component calculations.

The critical issue is to determine the instantaneous fluid velocity as well as the duration of the particle interaction with a particular eddy. The time step is the eddy-droplet interaction time, τ_i, which is defined as the lower value between the eddy lifetime, τ_e, and the eddy transit time, τ_t:

$$\tau_i = \min\left(\tau_e, \tau_t\right) \tag{3.19}$$

Each eddy is characterized by a fluctuating velocity, a time scale (eddy lifetime), and a length scale (characteristic length of an eddy). The fluctuating velocity at the start of a eddy-droplet interaction is obtained by random sampling from an isotropic Gaussian probability density function (PDF) having a zero mean value and standard deviation of $\sqrt{2/3k}$.

The eddy lifetime can be estimated from the local turbulence properties (k and ε) along the particle trajectory:

$$\tau_e = A\frac{k}{\varepsilon} \approx 0.2\frac{k}{\varepsilon} \tag{3.20}$$

whereas the characteristic dimension of an eddy, l_e, has been expressed as:

$$l_e = B\frac{k^{3/2}}{\varepsilon} \approx C_\mu^{3/4}\frac{k^{3/2}}{\varepsilon} \tag{3.21}$$

where A and B are two dependent constants, which can be determined either by scaling analysis or from experimental data (Shirolkar et al., 1996). The transit time, τ_t, is the minimum time a particle would take to cross an eddy with characteristic dimension, l_e, and is given by:

$$\tau_t = \frac{l_e}{|U^r|} \tag{3.22}$$

in which U^r is the relative velocity between the particle and the fluid. A different expression for the transit time is also recommended in the literature (Shirolkar et al., 1996) and has been found to be more accurate for the present study:

$$\tau_t = -\tau_p \ln\left(1 - \frac{l_e}{\tau_p\,|U_{Gi} - U_i|}\right) \tag{3.23}$$

where the relative velocity is also estimated at the beginning of the new interaction. This equation has no solution when $l_e > \tau_p\,|U_{Gi} - U_i|$, i.e., when the linearized stopping distance of the particle is smaller than the eddy size. In such a case, the particle can be assumed to be trapped by the eddy and the interaction time is the eddy lifetime.

By knowing the interaction time and the randomly sampled fluctuating fluid velocity, it is possible to solve both Eqs. 3.17 and 3.18 for the drop trajectory. The time step is the eddy-droplet interaction time, over which the fluctuating velocity is assumed to be constant. At the end of each time step, a new fluctuating fluid velocity is sampled from a new PDF, which is generated using the local turbulence properties. The next interaction time is determined from the local properties at the new drop location.

This isotropic model has been extended in the present work to account for cross-correlations or anisotropy. To obtain the fluctuating velocities u'_f and v'_f at every time step, they may be correlated with two randomly sampled (independently) fluctuating velocities u'_1 and v'_2 and a correlation coefficient (R_{uv}) as follows:

$$\begin{cases} u'_f = u'_1 \\ v'_f = R_{uv}u'_1 + \sqrt{1 - R_{uv}^2}u'_2 \\ R_{uv} = \dfrac{\overline{u'_f v'_f}}{\sqrt{u'^2_f v'^2_f}} \end{cases} \tag{3.24}$$

in which R_{uv} varies from 0 to 1.

3.3 Interaction between phases & Implementation of the model

In dilute flows, the motion of each phase is influenced by the other via displacement of mass as well as momentum and energy transfer effects. Therefore, a two-way coupling method is favoured, and the interaction between the continuous and dispersed phase is introduced by treating particles as sources of mass, momentum and energy in the gaseous phase. The source terms due to the particles — which are summarized in Table 3.3 — are calculated for each Eulerian cell of the continuous phase and can be divided into two parts, as follows:

$$S_{\phi,p} = S_{\phi,i} + S_{\phi,m} \tag{3.25}$$

where $S_{\phi,i}$ specifies the source term due to inter-phase transport and $S_{\phi,m}$ deals with the transfer caused by evaporation.

Table 3.3: Source terms of the dispersed phase, from Sommerfeld (1998).

$S_{\phi,p}$	$S_{\phi,i}$	$S_{\phi,m}$
$\overline{S_{\rho,p}}$	0	$\sum_k \frac{\dot{m}_k N_k}{U_{i,j}}$
$\overline{S_{U,p}}$	$-\sum_k \frac{\dot{m}_k N_k}{U_{i,j}} \left[\left(U_k^{t+\Delta t} - U_k^t\right) g_i \Delta t\right]$	$\sum_k \frac{\dot{m}_k N_k U_{ia}}{U_{i,j}}$
$\overline{S_{T,p}}$	$-\sum_k \frac{N_k}{U_{i,j}} \left(L\,\dot{m}_k + Q_L\right)$	$\sum_k \frac{\dot{m}_k N_k}{U_{i,j}} C_{vap}\left(T_k\right) T_k$
$\overline{S_{Y_{air},p}}$	0	0
$\overline{S_{Y_{water},p}}$	0	$\sum_k \frac{\dot{m}_k N_k}{U_{i,j}}$
$\overline{S_{k,p}}$	$\overline{U_j S_{U_j i}} - \overline{U_j}\ \overline{S_{U_j i}}$	$\overline{U_j S_{U_j m}} - \overline{U_j}\ \overline{S_{U_j i}} + \frac{1}{26}\overline{U_j}\ \overline{U_j}\ \overline{S_m} - \frac{1}{2}\overline{U_j U_j S_m}$
$\overline{S_{\varepsilon,p}}$	$C_{\varepsilon 3}\frac{\varepsilon}{k}\overline{S_{ki}}$	$C_{\varepsilon 3}\frac{\varepsilon}{k}\overline{S_{km}}$

There are, of course, several ways to computationally implement the model. The concise numerical procedure implemented in this work to obtain a converged solution for both phases is as follows:

1. The initial conditions are established by defining both the staggered grid and the characteristics of the initial drops;
2. A converged solution of the gas flow field is calculated disregarding the source terms of the dispersed phase;
3. The discrete parcels are traced through the flow field in the dispersed phase and the values of the source terms are calculated;
4. The gas flow is recalculated considering now the source terms of the dispersed phase;
5. Steps 2 and 3 are repeated until convergence is reached;
6. Post-processing of the data occurs.

This iterative procedure is also represented in Fig. 3.3 with a flowchart in which the numbers 1 to 6 coincide with the numbers in the preceding list. Section 3.1 to 3.2 of the present chapter describe the continuous and dispersed phases and how they are connected. This corresponds to the solver module in the flowchart. The setup model in its turn refers to the initial conditions which are discussed in the following section (section 3.4). The post-processing module (or, in other words, the output of the model) is presented in Chapter 5 with the results obtained from the simulations performed.

3.4 Boundary conditions

Two sources of experimental data — with distinct solution domains and injection conditions — are employed to assess the accuracy of the predictions obtained in the simulations. In the first stage, the experimental rig of Arcoumanis et al. (1997) has been replicated (henceforth also denominated as *case 1*). The flow configuration is shown schematically in Fig. 3.4 and consists

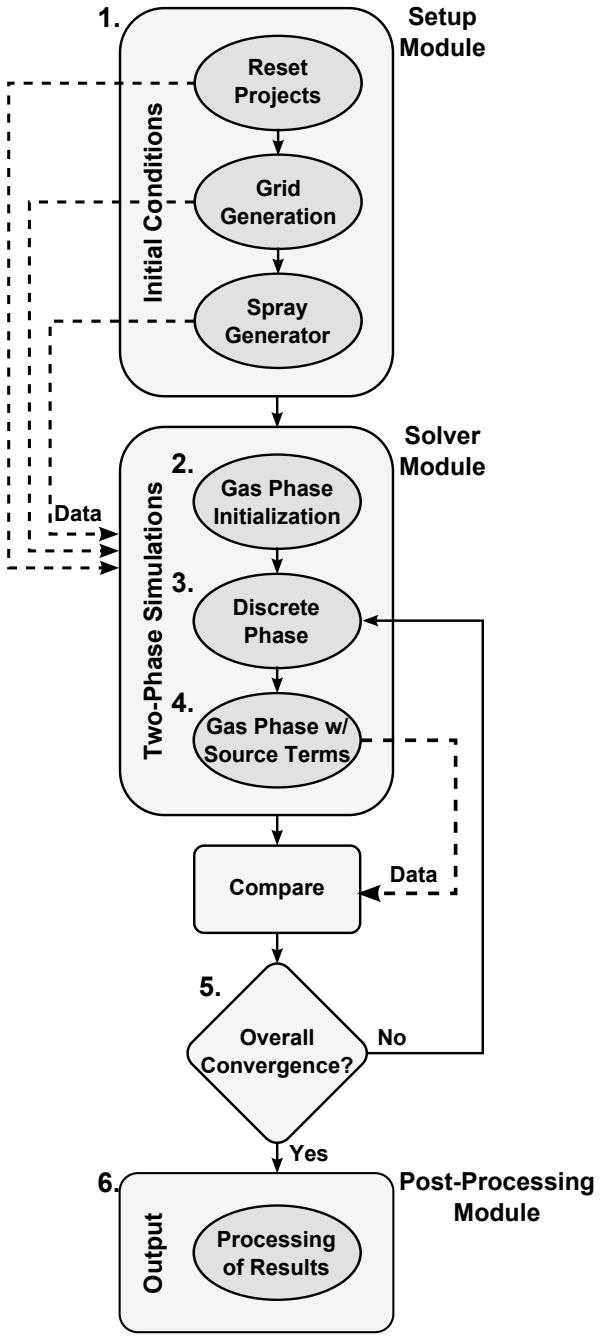

Figure 3.3: Flowchart illustrating the iterative procedure of the model.

of a spray stream of gasoline (density, ρ = 692 kg/m^3; viscosity, μ = 4.699$\times 10^{-4}$ kg/m/s; and surface tension, σ = 18.32 mN/m) injected through the upper wall of a rectangular channel with an inclination of 20° (in relation to the vertical plane) in the main flow direction. Both 5 m/s and 15 m/s crossflows are considered. The cross section of the solution domain is 32 mm $\times$ 86 mm and the channel length is 350 mm. The location of the injection point (Z_{in}) lies 50 mm downstream of the inlet plane along the centreline of the test section. The injection pressure, pulse duration and injection frequency has been set at 3 bar, 7 ms and 10 Hz, respectively and the air was at atmospheric pressure and room temperature.

The measurements were made using the PDA technique of ensemble-averaged drop sizes and velocities at four different positions (a, b, c, and d) as depicted in Fig. 3.5(a). The measurement points were located at 12, 15, 20 and 25 mm downstream of the injector location in

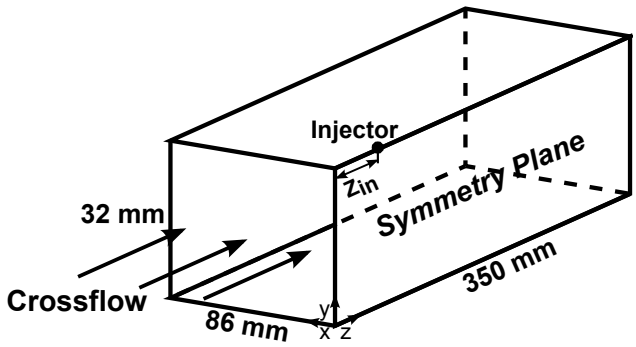

Figure 3.4: Schematic diagram of the flow geometry [Case 1].

a horizontal plane 5 mm above the impingement wall.

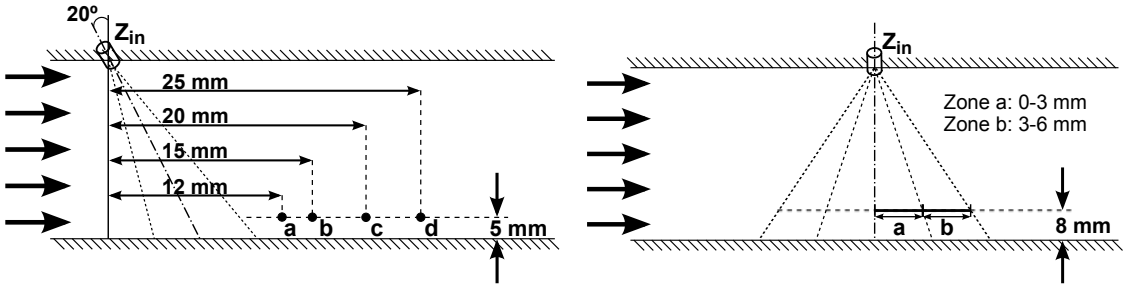

(a) Case 1 (b) Case 2

Figure 3.5: Illustration of the measurement locations.

The second source of measurements (*case 2*) has been provided by Panão et al. (2013) in a study aiming at replicating the conditions found in homogeneous charge combustion ignition (HCCI) engines. In these experiments, a port fuel injector — with a pintle diameter of 0.79 mm inserted in a cylindrical hole with 0.9 mm in diameter — has been used to spray gasoline (density, ρ = 749.6 kg/m^3; viscosity, μ = 4.2612$\times 10^{-4}$ kg/m/s; and surface tension, σ = 19.4 mN/m) perpendicularly to the wall, with the presence of a cross flowing air. The injection pressure, pulse duration and injection frequency were set at 3 bar, 10 ms and 10 Hz, respectively. The data were measured at a horizontal plane 8 mm above the surface with a two-component phase-Doppler system.

The corresponding setup reproduced in the computational procedure is shown in Fig. 3.6, and consists of a vertically-placed injector located at the top wall section of a rectangular channel (270 mm long, 150 mm wide and 50 mm high). The apparatus is facing down and sprays through a crossflow of air moving parallel to the impingement surface (11 m/s). The location of the injection point (Z_{in}) lies in the middle of the channel. A symmetry plane is assumed along the longitudinal axis, which gives rise to a cross-section of 270 mm by 75 mm.

Contrary to the first set of measurements evaluated, in these experiments the information is collected in two regions along the plane defined 8 mm above the impingement wall (Fig. 3.5(b)): the first region ranges from the location just below the injector position (r=0 mm) to 3 mm downstream (zone a), whereas the second region ranges from that position to 6 mm downstream of the injector location (zone b).

It is worth mentioning that even though gasoline is used as the liquid injected into the domain in both experiments, the properties of the fuels identified by the authors of the studies are different. The thermo-physical properties of both liquid fuels used in the simulations as

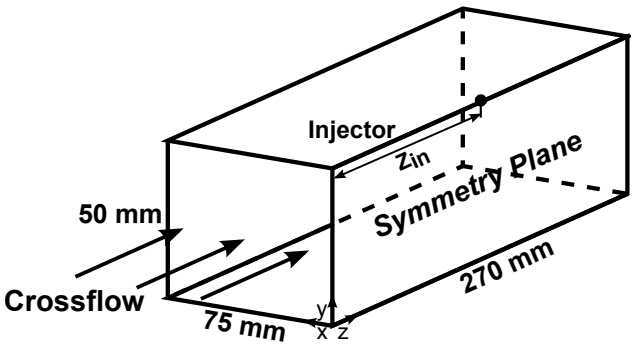

Figure 3.6: Schematic diagram of the flow geometry [Case 2].

well as that of air at 298 K are highlighted in Table 3.4.

Table 3.4: Thermo-physical properties of air and liquid fuels tested at 298 K.

Properties	Air	Gasoline [Case 1]	Gasoline [Case 2]
Density, ρ [kg/m^3]	1.211	692.0	749.6
Viscosity, μ [kg/m/s$\times 10^{-6}$]	18.2	469.9	426.1
Surface tension, σ [N/m$\times 10^{-3}$]	-	18.33	19.4

The model equations for k and ε are elliptic by virtue of the gradient diffusion term. Consequently, boundary conditions should be prescribed for each of the boundaries of the computational domain. In both cases evaluated the solution domain is constituted by six boundaries:

1. an inlet plane — the transported variables are specified on the boundary with uniform profiles;
2. an outlet plane — normal gradients for all dependent variables are set to zero ($\partial\phi/\partial n = 0$);
3. a symmetry plane — $\partial\phi/\partial n = 0$, except for the velocity component normal to the boundary, which is zero;
4. three non-slip walls — velocity components relative to the wall are zero; the wall function method (described in detail by Launder and Spalding, 1974) is used to prescribe the boundary conditions for the velocity and turbulence quantities, assuming that the turbulence is in state of local equilibrium.

Chapter 4

Spray impingement model

In this chapter, the spray impingement model is described. Key issues involved in the mathematical formulation are: 1) determination of the impingement regimes and corresponding transition criteria; and 2) derivation of the relations describing the post-impingement droplet characteristics for the different regimes. Each topic is addressed in section 4.2 and section 4.3, respectively. However, before impact it is crucial to determine the initial conditions of the array of liquid drops that are injected into the flow field. This subject is discussed in the first section of this chapter (section 4.1). In section 4.4, the additional computational sub-models that have been integrated into the general simulation procedure in order to account for particular thermo-dynamic mechanisms are explained. Each of these computational extensions give the model the capacity to replicate, with a certain level of accuracy, some phenomena that otherwise it would not be able to.

4.1 Atomization process

A key issue in simulating properly the spray impact process is to ensure that the initial characteristics of the incident drops in the near-nozzle region are estimated with adequate accuracy. However, there is a lack of reliable atomization models available in the literature for this type of injectors, which forces the use of an empirical procedure based on the methodology proposed by Bai et al. (2002) in order to estimate the characteristics of the spray at the injector exit from experimental data taken in downstream locations.

Therefore, the spray is assumed to consist of a collection of isolated incident drops. The input data required for invoking such methodology comprises both size and velocity of the liquid particles at some point relative to the impact surface. Hence, besides the spray impingement measurements which are used to evaluate the outcome of the spray-wall interaction problem, experimental data from free spray conditions in a downstream measurement plane are also used in the present work to determine the initial characteristics of the drops constituting the spray at the injector exit. Using free spray experiments grants access to the spray information without the influence of the presence of the crossflow or the impingement wall (which would have a huge repercussion on the behaviour of the drops). Thereby, these conditions may be applied to any spray-wall impact simulation that employs the same injection conditions.

In the first set of experimental data (case 1), the initial values have been estimated using the free spray measurements reported by Bai et al. (2002). In the experiments, the ensemble-averaged drop size and velocity characteristics of the spray were obtained at a horizontal measurement plane consisting of a circular region with 32 mm of radius and located 80 mm below the injector. The spray produced an external and an internal cone with impact angles of 20° and 10°, respectively.

On the other hand, the atomization in case 2 has been modelled with the experimental data provided by Panão et al. (2013). The fuel particles were injected into a quiescent surrounding air at 25°C and the data were acquired in a horizontal measurement plane located 10 mm

above the surface ($H_{meas} = 40mm$). Fig. 4.1 illustrates schematically the disposition of the injection system and the relative location of the horizontal plane in which the experimental data are acquired (with H_{meas} being the distance between the injector nozzle and the plane of measurement).

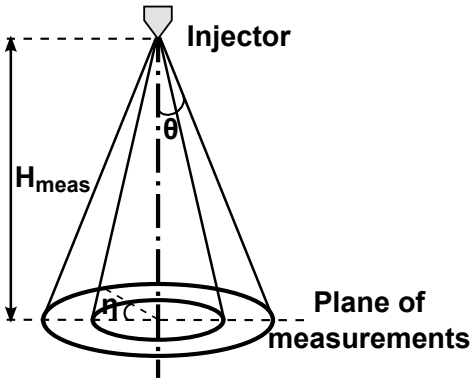

Figure 4.1: Illustration of the plane of measurements.

It is interesting to note that in both cases evaluated, the location of the plane of measurements in the free spray condition is different than in the spray impingement condition. This discrepancy is much more important in the simulations concerning case 1, in which the 27 mm of distance between the measurement plane and the injector nozzle in the spray impingement experiments contrasts with the 80 mm of distance in the free spray experiments. On the other hand, in the experimental data provided by Panão et al. (2013) this restriction of the procedure should have a minor effect on the outcome since the difference between the location of the measurement planes in both experiments is of just 2 mm.

The procedure for estimating the initial drop conditions consists of two steps: 1) estimation of the initial drop sizes, and 2) determination of the initial drop velocities. However, this methodology invokes two major simplifications. Firstly, the initial stage of atomization — characterized by unstable liquid sheets — must be represented by spherical particles. Secondly, drop aerodynamic breakup and particle-particle interactions are neglected. This may be justified by the fact that the critical drop Weber number (with the velocity being the one relative between the particle and the gas) never exceeds the maximum value generally attributed in the literature for the onset of breakup, which is around 12 (Faeth, 1987; Hsiang and Faeth, 1995; Guildenbecher et al., 2011; Jenny et al., 2012). On the other hand, no interaction between drops is justified by the fact that hollow cone sprays are normally well-dispersed, so the probability of collision is small. Nevertheless, this assumption implies that each injected drop parcel keeps the same size as assigned at the injector exit throughout the pulse duration. Consequently, the whole size range observed at the measured plane will correspond to that encountered in the near-nozzle region.

This is particularly useful for the determination of the initial size of the drops. A specified number of parcels evenly distributed over the spray cross-section are introduced from the nozzle at each computational step. For this purpose, the cross-sectional area is divided into a number of annular sections of equal area. Each section is penetrated by an equal number of parcels and the flux of liquid in each case is adjusted to coincide with the measured values. The size of the drops in each parcel, D_k, are sampled from the PDFs provided in the measurements according to the following equation:

$$D_k = D_{min} + \gamma_1 \left(D_{max} - D_{min} \right) \tag{4.1}$$

whereas the radial position in the measurement plane, r_k, is determined as:

$$r_k = r_{i-1} + \gamma_2 (r_i - r_{i-1}) \tag{4.2}$$

where γ_1 and γ_2 are uniformly distributed random numbers in the range $[0; 1]$, and D_{min} and D_{max} are experimentally-identified minimum and maximum sizes, respectively, in the annular region i: $r_{i-1} \leq r \leq r_i$. Therefore, the set of drop diameters can be recalculated at the injector exit by complying with the above conditions, whereas the number of droplets is estimated from mass conservation and by reference to the ensemble-average mass flux and measured PDF value associated with D_k.

Regarding the initial drop velocities, the approach is based on an iterative procedure in which the axial velocity profiles of the free spray at the downstream horizontal plane are approximated as best as possible by mathematical expressions that are a function of the incident angle (θ). For instance, to determine the normal component of the velocity, one commences with a guessed value and makes repeated corrections until close agreement is obtained with the measured drop size–velocity correlations. On the other hand, the radial component of the velocity is obtained by reference to the normal velocity profile and by assuming a random circumferential angle (η) with a value between 0 and 360 degrees. Therefore, this procedure creates a spray with a specific velocity magnitude taken from experimental data and a uniform circular ring of particles at the injector exit.

By simulating the two different experimental scenarios, it is possible to infer about the performance of the model with distinct conditions. By way of illustration, the maximum Weber number of the incident drops in case 2 corresponds to nearly half the one obtained in case 1. Moreover, in the second setup the viscous forces also proved to be less important than in the first one. This fact is expected to influence the post-impingement characteristics and, consequently, casts doubts on the capacity of the computational model to provide accurate results under such extended range of conditions. Table 4.1 highlights the main characteristics of the spray initial conditions used in both simulations.

Table 4.1: Spray characteristics at the injector exit.

	Case 1		Case 2	
Diameter	0 - 350	[μm]	0 - 170	[μm]
Axial Velocity	1.5 - 19	[m/s]	5 - 19.5	[m/s]
Radial Velocity	0 - 4.5	[m/s]	-1 - 2.5	[m/s]
We	0 - 4.8	$\times 10^3$	0 - 2.5	$\times 10^3$

4.2 Impact mechanisms

The basic scenario simulated by the original spray impingement model is represented schematically in Fig. 4.2: a spray constituted by liquid drops is injected through a crossflow and impact onto a solid wall. In each injection, a certain impact mechanism ensues which may result (or not) in the production of secondary droplets.

Therefore, each impingement regime states how the droplets will behave after impact and the existence of each one depends upon the properties of both incident particles and impingement surface. The phenomena can be characterized by the energy possessed by the drop at the time of impact as in Bai and Gosman (1995), where four different regimes have been identified,

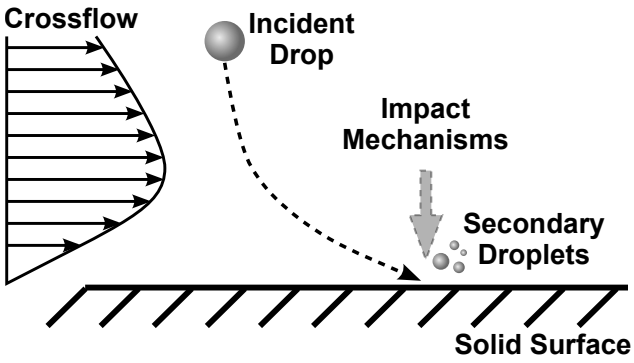

Figure 4.2: Schematic diagram of drop impacts onto a solid surface.

namely stick, rebound, spread and splash.

4.2.1 Impingement regimes

The first task is to predict the hydrodynamic regimes of impact occurring under given conditions. The description of each of the regimes has been made in Chapter 2. For this reason, at this stage, only important information concerning the mathematical formulation is reported.

Stick and spread events are usually combined into one more general regime, called deposition. In neither case there is formation of secondary droplets but the wall is considered to be wet at the impingement location. This will affect the subsequent impact events. Thus, even though it does not affect directly the atomization process, it still plays an important role in the dynamics of impact of the subsequent particles.

Rebound can be observed in both dry and wet walls, as stated before. The rebound velocity components are determined from the relationship developed for a particle bouncing on a solid wall (Matsumoto and Saito, 1970), which can be expressed as:

$$U_{RN} = -e\,U_{0N} \tag{4.3}$$

$$U_{RT} = 5/7\,U_{0T} \tag{4.4}$$

where U_{RN} and U_{RT} are the normal and tangential rebound velocity components, respectively. The quantity e is the "restitution coefficient", which has been derived by Grant and Tabakoff (1975) and is as follows:

$$e = 0.993 - 1.76\theta + 1.56\theta^2 - 0.49\theta^3 \tag{4.5}$$

Furthermore, it is important to refer that the rebounding droplets are assumed to have a negligible rotation effect, which according to Bai and Gosman (1995) is valid for the cases assumed here.

The last impingement regime mentioned is splash, which occurs when the incident particles collide against the solid surface with high impact energy giving rise to secondary droplets. Since the splash phenomenon is the regime with major repercussion onto the final outcome, it has been reserved a particular section to discuss it. Therefore, further details regarding the computational treatment of the secondary droplets are provided in section 4.3.

4.2.2 Transition criteria

The original version of the model used in our research group to simulate the spray-wall impact phenomenon employs the approach reported by Bai et al. (2002). In this study, the quantitative criteria for the regime transitions are derived from experimental data on single water drops impacting a wall. Even though both dry and wet surfaces are considered, the authors did not include the effect of the film thickness on the wall. Instead, they took the assumption that a wet surface behaves as a very rough dry wall and the effect of a liquid film is accounted in a fitting constant, which is derived from the data of Stow and Hadfield (1981) and depends upon the surface roughness.

Table 4.2 highlights the basic critical thresholds used in the spray impingement model to establish the boundaries between regimes. Spread-splash transition criteria for both dry- and wet-wall situations were derived from the Stow and Hadfield (1981) experimental data, giving rise to a Critical Weber number that is a function of the Laplace number. On the other hand, the stick-rebound and rebound-spread thresholds have been obtained from the measurements of Lee and Hanratty (1988) in wet wall experiments and were set with the critical Weber numbers of 2 and 20, respectively.

Table 4.2: Impingement regimes and corresponding transition criteria.

Wall Status	Transition State	Critical Weber Numbers
Dry	Deposition/Splash	We_{cr}=A.$La^{-0.183}$
Wet	Stick/Rebound	We_{cr}=2
	Rebound/Spread	We_{cr}=20
	Spread/Splash	We_{cr}=1320.$La^{-0.183}$

In the deposition/splash threshold for dry surfaces, the fitting constant, A, used to characterize the surface roughness has been chosen on the basis of the topography of the configuration simulated. Typical values of this coefficient were listed by Bai and Gosman (1995) as a function of the mean roughness of the impingement surface. From this information, a regression equation was constructed, which enabled us to determine fixed values for the fitting constant according to the corresponding mean surface roughness considered. In case 1, the original equation attributed to the onset of splash for dry surfaces (A=2630) is left unchanged because the topography of the surface (with $r_s = 0.84\ \mu m$) is similar to the one used in the study carried out by Bai and Gosman (1995). However, in case 2, the mean roughness value of the aluminium surface used in the experiments ($r_s = 2.5\ \mu m$) leads to a coefficient of 2050. Therefore, special care must be taken to ensure that both cases are treated properly throughout the simulation procedure.

Originally the set of transition criteria presented in table 4.2 was used in the entire spectrum of impact conditions simulated. However, it has been found that in some situations these thresholds were not the most accurate option. For instance, when a liquid film forms over the surface, the influence of its thickness should be accounted for in the transition criteria (which is not possible with the above options for wet walls). On the other hand, these expressions have been obtained from measurements in a non-heated environment. One should expect that when thermal effects are considered, the model provides transition criteria that have been derived under similar conditions. These two examples emphasize specific scenarios in which the original formulation is not equipped with adequate tools to enable the correct simulation.

However, it is important to point out that in the present work the set of transition criteria presented in table 4.2 has been completed with additional independent and more appropriate critical thresholds when convenient. These situations are analysed throughout the study. However, the adjustments performed are only explained at the corresponding section where they are required.

4.3 Post-impingement characteristics

The second task is to predict quantitatively the characteristics of secondary droplets (namely their velocity and trajectory) as well as their size distribution and fraction of mass.

Each splash event may produce hundreds of thousands of secondary droplets. Considering the large number of incident drops that constitute the spray which are likely to disintegrate into smaller fragments, the expense of tracking all such droplets would be computationally too high. A similar situation is found in the establishment of the initial conditions of the spray, which is circumvented by calculating only a statistical sample of the full population, with each computational parcel representing a set of real drops. The same practice is applied here for the secondary droplets. It is assumed that the fragments resulting from the splash regime are gathered in (up to) six parcels (p_a) that have equal proportion of mass but with different sizes and velocities.

After the successful deposition of an array of particles onto the surface, a liquid film starts to form. The interaction between this liquid layer and the impinging particles induces the exchange of mass between them, which will also influence the course of the simulation. The way this model accounts for this particular phenomenon is via the mass ratio parameter (which corresponds to the total splashing to incident drop mass ratio) and is treated as follows:

$$r_m = \frac{m_s}{m_0} = 0.2 + RN(0; C) \tag{4.6}$$

where RN corresponds to a random number between 0 and the value of the constant C, which is 0.6 for a dry wall and 0.9 for a wet wall. In the wet surface scenario, r_m can take a random value evenly distributed in the experimentally-observed range $[0.2; 1.1]$. The ratio can reach values greater than 1 to account for transfer of mass from the liquid film to the splashing droplets.

The ejection angle, α_s, of secondary droplets falls randomly $-$ but not uniformly $-$ into a cone with a specified range. According to Mutchler (1970), the limits of such ranges depend upon the surface roughness and liquid film thickness. Therefore, the authors claim that for a particular surface topography there are ranges in which there will be a greater probability to find droplets. For instance, in smooth hard walls, the ejection angle of secondary droplets has been found to vary in the range of $[5°; 50°]$, whereas in rough soil surfaces α_s falls in the range $[20°; 60°]$.

The three main characteristics that need to be determined are the size, number and velocity of secondary droplets. The size is determined with a Chi-squared distribution function given by:

$$f(D) = \frac{1}{\bar{D}} \exp\left(-\frac{D}{\bar{D}}\right) \tag{4.7}$$

where $\bar{D}$ denotes the number mean diameter which is related to the volumetric mean diameter D_V by:

$$\bar{D} = \frac{D_V}{6^{1/3}} = \frac{D_0}{6^{1/3}} \left(\frac{r_m}{N_s} \right)^{1/3} \tag{4.8}$$

Bai et al. (2002) have derived a correlation for the total number of secondary droplets, N_s, as:

$$N_s = a_0 \left(\frac{We}{We_{cr}} - 1 \right) \tag{4.9}$$

in which $a_0 = 5$. The number of droplets in each secondary parcel, N_{s,p_a}, is determined through mass conservation:

$$N_{s,p_a} D_{p_a}^3 = \frac{r_m D_0^3}{p_a} \tag{4.10}$$

The secondary droplets velocities resulting from oblique impingement are analysed as a superposition of those arising from normal impingement and a wall-tangential component. Thus, the splash velocity vector, U_s , is composed of two components resulting from the normal and tangential components of the velocity:

$$U_s = U_{sT} + U_{sN} \tag{4.11}$$

It is assumed that the tangential component of the velocity of secondary droplets is directly proportional to the tangential component of the velocity of incident drops as expressed in the following relationship:

$$U_{sT} = C_f U_{0T} \tag{4.12}$$

where the constant of proportionality C_f is the friction coefficient which has been estimated experimentally as being in the range $[0.6; 0.8]$ for a water drop splashing onto soil surfaces (Mutchler, 1970).

The other component of the velocity (U_{sN}) comes from the normal component of the incident velocity, which has been reported in numerous publications to be the component of the velocity responsible for the splashing event. In other words, the impact energy imparted to the disintegration phenomenon depends solely upon U_{sN}, whereas U_{sT} simply transfers a portion of the drop's tangential momentum to each secondary droplet. The normal component of the splashing droplets must then be estimated by considering the energy conservation law as follows:

$$\frac{1}{2} \frac{m_s}{p_a} \left[\left(U_{sN,1} \right) + ... + \left(U_{sN,p_a} \right) \right]^2 = E_{Ks} \tag{4.13}$$

where E_{Ks} is the splash kinetic energy due to U_{0N} only, and is given as:

$$E_{Ks} = E_{K0} + E_{S0} - E_{Ss} - E_D \tag{4.14}$$

in which $E_{K0} = 1/2 m_0 U_{0N}^2$ is the incident kinetic energy based on the normal velocity, $E_{S0} = \pi\sigma D_0^2$ is the incident drop surface energy, $E_{Ss} = \pi\sigma \sum_{i=1}^{p_a} N_{s,i} D_{s,i}^2$ is the total surface energy of splashing droplets, and E_D is the dissipative energy loss (which is discussed in section 5.3 of the next chapter).

After modelling the dissipative energy loss, it is possible to determine the splash kinetic energy and, consequently, the normal component of the secondary droplets. For only one sec-

ondary parcel ($p_a = 1$), the system of equation is closed and it is possible to determine all the variables. Otherwise ($1 < p_a \leq 6$), the following size-velocity correlation of secondary droplets is used as a supplementary equation:

$$\frac{U_{sN,1}}{U_{sN,p_a}} \approx \frac{\ln\left(D_{s,1}/D_0\right)}{\ln\left(D_{s,p_a}/D_0\right)} \tag{4.15}$$

4.4 Computational extensions

The spray impingement phenomenon is influenced by various parameters related with both the impact conditions and the liquid and surface properties. Depending on these parameters — as well as kinematic conditions — different outcomes are verified, giving rise to diverse secondary droplet characteristics. The simplified scenario shown in Fig. 4.2 provides a reasonable approximation of the outcome expected. However, several relevant mechanisms of interactions are disregarded. As a result, the development of accurate empirical sub-models is essential to enhance the capacity to replicate particular phenomena computationally.

4.4.1 Liquid film sub-model

The dynamic of drops impacting onto a dry or wet solid surface plays an important role in a wide variety of fields. However, even though a major scientific effort has been invested into the comprehensive knowledge of the mechanisms underlying the spray impingement process, there are still numerous open issues that still remain to be completely understood. One of those concerns refers to the formation and evolution of the liquid film accumulated on the wall due to the deposition of incident drops, which is schematically illustrated in Fig. 4.3.

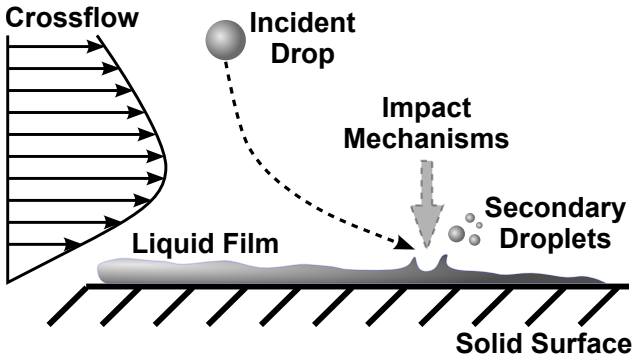

Figure 4.3: Schematic diagram of drop impacts onto a liquid film.

The correct understanding of the film dynamic is of utmost importance for the accurate modelling of the spray impingement phenomenon: on balance, the formation of a liquid film and its interaction with the incident spray strongly affects the impingement process. For this reason, it has been found imperative to develop this new feature for the main model. Furthermore, in previous simulations, it was reported that the post-impingement treatment needed to be enhanced, particularly regarding the conditions under which the velocity profile of the parcels resulting from the splash regime were obtained. In this sense, the introduction of the liquid film upgrade gives rise to a different impingement problematic environment which is expected to improve the general outcome of the simulation.

The liquid film formation sub-model has been formulated by considering the basic laws of conservation between incident and impacted particles. However, the closure of the system

has been completed by integrating an empirical correlation deduced from experimental data of Kalantari and Tropea (2007) for the average film thickness. Therefore, rather than considering a fully theoretical formulation, the approach pursued here aims at establishing a connection to the phenomenological experience — by means of experimentally-deduced correlations — which can easily be fitted and updated to specific settings (provided that a sufficient number of measurements have been carried out).

There are not many expressions that have been reported in the literature for the average film thickness that recognize both the incident drop characteristics and the topography of the target surface as influencing parameters, although these are two of the parameters that were defined as critical for the formation of the liquid film. One of the few correlations that comply with these requirements has been derived from dimensional analysis by Kalantari and Tropea (2007), which is as follows:

$$h_{LF} = \xi D_{V0} Re_{V0}^{-1/2} \left(\frac{\dot{q}_V}{U_{0N}} \right)^{\gamma} \tag{4.16}$$

where D_{V0} represents the volumetric mean diameter of incident drops, Re_{V0} is the Reynolds number based on this mean diameter, $\dot{q}_V$ is the volume flux of impinging drops, and ξ and γ are constant values found to be 4 and -0.5, respectively, based on the measured data for normal impact conditions. Despite the narrow application range in which the expression has been proposed (but still covering — until a certain extent — the conditions of the current numerical simulations), the prediction capabilities showed good consistency with the measurements provided by the authors.

The drop shape, after flattened out along the surface, is approximated by a regular disk as shown in Fig. 4.4. This simplification may be justified by the fact that the apex height is much smaller than the capillary length (Rioboo et al., 2003) and by neglecting the influence of previous film on the spreading formation of singular drops.

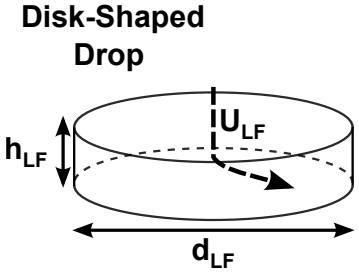

Figure 4.4: Illustration of the disk-shaped drop.

This circular form is considered when the particles spread to neighbouring nodes and interact with existing liquid. In fact, a mesh refinement procedure has been considered in order to determine more accurately the total area affected by the flattened drop. The procedure is based on a two-dimensional implicit grid which is generated over the target surface at the moment of impact, but is only used in cases in which it strictly improves the information allocated for the liquid film distribution. Fig. 4.5 shows an example of the nodes affected by the spreading of a liquid particle with the inclusion of the original mesh (with axis i and j) as well as with the auxiliary mesh (i_k and j_k).

It becomes evident that the addition of the second mesh allows one to achieve a drop shape that is much more similar to the intended circular form. Moreover, the number of nodes that become ”wet” (which means that they are assumed to have some liquid deposited onto the surface) is higher and, consequently, the interaction occurring between the incident drops and

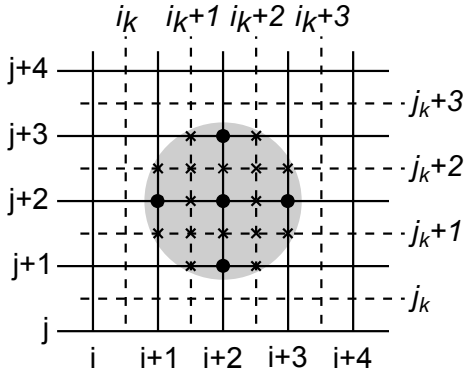

Figure 4.5: Mesh refinement procedure for the liquid film sub-model.

the liquid film occurs much more frequently.

In situations in which there are multiple drops impacting onto the same location (or a drop spreading to a node in which there is already liquid accumulated), the size of the corresponding liquid layer is the sum of the diameters of all the particles ($d_{LF} = \sum_i d_{LFi}$). On the other hand, the final thickness is defined as the mean value of each disk thickness ($h_{LF} = \sum_i h_{LFi}/i$) which are calculated according to Eq. 4.16. However, it is worth mentioning that this methodology lacks of physical observation basis for single consecutive particles impacting onto the same location because no fundamental studies were found on this particular matter. Nevertheless, this procedure satisfies the laws of conservation and, thus, produces consistent results.

After a significant amount of liquid accumulated onto the surface, the incident drop starts to impact onto a liquid film rather than a solid wall. If the splash phenomenon is considered, there will be transfer of mass between the elements involved. The quantity of mass assigned in each impact is defined with recourse to the mass ratio equation (Eq. 4.6). The percentage of liquid taken of or added to the deposited particle is determined, and then both diameter and thickness of the liquid film are recalculated with an increment or subtraction of the square root of that value.

There are several semi-empirical correlation available in the literature that describe the deposition/splash threshold according to different ranges of experimental conditions. It is important to assure that the simulations do not extend the data used in the empirical models outside the validity range in which the measurements were carried out, even though this is sometimes difficult to satisfy due to the limited experimental data available in the literature. In the study of Motzkus et al. (2011), where several transition criteria between deposition and splash were analysed for diverse impingement conditions, the authors suggested a particular correlation that excelled in relation to the others for a wide range of experimental conditions. This expression is based on the one proposed by Cossali et al. (1997) which may be expressed as:

$$We_{cr} = (2100 + 5880\delta^{1.44})/Oh^{-0.4} \tag{4.17}$$

but with the coefficient value of 5880 replaced by 2000. This change resulted in a better agreement with experimental data for a wider range of impingement conditions, including the range in which the present simulations are performed.

Comparing this equation to the spread/splash threshold for wet surfaces presented in Table 4.2, it is possible to conclude that besides the distinct dimensionless group used to identify the boundary between the deposition and splash regimes — which by itself corresponds to a dissimilar view of the properties affecting the disintegration process of the particles — the tran-

sition criterion proposed by Cossali et al. (1997) and latter modified by Motzkus et al. (2011) considers the film thickness as an influencing parameter on the accurate evaluation of the critical threshold. Considering the formulation of the liquid film model, one would expect the use of a relationship describing the threshold between deposition and splash regimes that would take into account the film thickness as an influencing parameter. Only this way, it is possible to take maximum advantage of these two factors in the final outcome. Therefore, in this section, the modified correlation of Cossali et al. (1997) has been used in the spray impingement model to define the critical splash threshold instead of the one proposed by Bai et al. (2002).

4.4.2 Evaporation sub-model

Several questions arise regarding the dynamic behaviour of the particles before combustion when the spray impingement process is affected by external variables. An important concern occurs when the target is hot and thermal effects are taken into account, as depicted in Fig. 4.6. Godsave (1953) and Spalding (1953) were the first to propose an evaporation model for an isolated single component drop using the D^2-law. Since then, this model has been extensively reviewed and enhanced by several authors (see e.g. Law, 1982; Sirignano, 1983) but the existing theory was mostly dedicated to the dynamics of single drops. Years later, Abramzon and Sirignano (1989) extended the range of application to sprays and demonstrated that the convective effects were the most influential parameters.

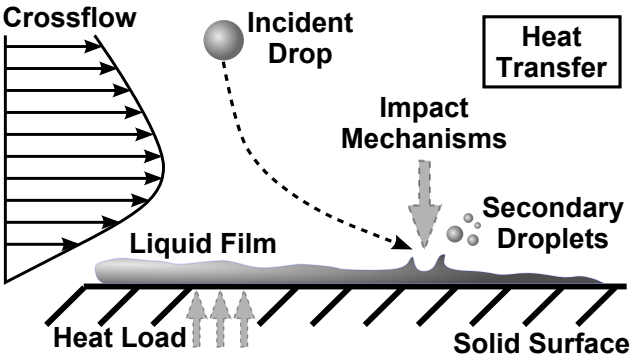

Figure 4.6: Schematic diagram of spray impacts onto a hot surface.

Meanwhile, many papers have reported direct comparisons between computational results and experimental measurements with relative satisfactory results (Chen and Pereira, 1996; Sommerfeld, 1998). However, published works on the direct influence of the thermal effects on the outcome of spray-wall interactions are very scarce in the literature (Moreira et al., 2010). The most relevant experimental study can be found in Arcoumanis and Chang (1993) who concluded that the wall heat transfer rates are governed by the spray characteristics prior to impingement. According to the authors, the higher the impact velocity of the incident drop, the higher the heat transfer. On the other hand, if attention is concentrated on the modelling component, then no relevant work can be found.

When the simulations are performed in a heated environment, adequate transition criteria should be assumed to make sure the model is performing within the range of conditions for which it has been formulated. All the previous regime limits have been proposed under cold impact conditions. Therefore, the set of transition criteria integrated into the model has been updated to include a new expression for hot conditions. Accordingly, the critical threshold reported by Naber and Farrel (1993) has been used as the criterion for drop disintegration in

a heated environment. The authors concluded that $We_N = 24$ was the single constant critical threshold obtained for the entire set of measurements that they carried out, which ranged from temperatures below the saturation point to temperatures above the Leidenfrost temperature.

The vaporization phenomena are described by using the model proposed by Barata (2005), which is based on the Abramzon and Sirignano (1989) approach. The convection effects are taken into account by introducing empirical correlation laws. With the inclusion of this sub-model, the simplifying assumption of ignoring evaporation is no longer required. The main assumptions considered in here are: spherical symmetry; quasi-steady gas film around the drop; uniform physical properties of the surrounding fluid; uniform pressure around the drop; and liquid/vapour thermal equilibrium on the drop surface.

The effect of the convective transport caused by the drop motion relative to the gas was accounted for by the so-called "film theory", which results in modified correlations for the Nusselt ($Nu = H_C D/K_G$) and Sherwood ($Sh = K_C D/C_d$) numbers. For rapid evaporation (i.e. boiling effects) additional corrections were applied. The infinite drop conductivity model was used to describe the liquid side heat transfer taking into account particle heat-up. Hence, two differential equations for the temporal changes of drop size and temperature have to be solved:

$$\frac{dD}{dt} = -\frac{2\dot{m}}{\pi\rho D^2} \tag{4.18}$$

$$\frac{dT}{dt} = \frac{6Q_L}{\pi C_p D^3} \tag{4.19}$$

Under the assumption of steady-state conditions in the gas film and considering a spherical control surface around the drop, the total mass flow through this surface is equal to the evaporation rate $\dot{m}$:

$$\dot{m} = \pi\overline{\rho_G}\,\overline{C_d} D\, Sh^* \ln\left(1 + B_M\right) \tag{4.20}$$

and

$$\dot{m} = \pi\frac{\overline{K_G}}{\overline{C_{pG}}} D\, Nu^* \ln\left(1 + B_T\right) \tag{4.21}$$

These two equations for $\dot{m}$ are similar to the expressions for the drop vaporization rate predicted by the classical model with the values of the non-dimensional parameters Nu_0 and Sh_0 being substituted by the "modified" Nusselt (Nu^*) and Sherwood (Sh^*) numbers, which can be expressed as:

$$Sh^* = 2 + \left(Sh_0 - 2\right)/F_M \tag{4.22}$$

and

$$Nu^* = 2 + \left(Nu_0 - 2\right)/F_T \tag{4.23}$$

According to these two equations, Nu^* and Sh^* tend to Nu_0 and Sh_0 as F_T and F_M tend to the unity. Nu_0 and Sh_0 are evaluated by employing the well-known Frossling correlations:

$$Nu_0 = 2 + 0.552 Re^{1/2} Pr^{1/3} \tag{4.24}$$

$$Sh_0 = 2 + 0.552 Re^{1/2} Sc^{1/3} \tag{4.25}$$

In the case of an isothermal surface and constant physical properties of the fluid, the

problem has a self-similar solution and the correction factors F_M and F_T do not depend upon the local Reynolds number. It was found that both values are practically insensitive to the Schmidt and Prandtl numbers, as well as the wedge angle variations, so that they can be approximated by:

$$F_M = F\left(B_M\right) \tag{4.26}$$

and

$$F_T = F\left(B_T\right) \tag{4.27}$$

in which $F(B)$ is the universal function given by:

$$F(B) = (1+B)^{0.7\dfrac{\ln(1+B)}{B}} \tag{4.28}$$

The evaporation rate $\dot{m}$ with convection is:

$$\dot{m} = \pi\overline{\rho_G}\overline{C_d}D\ln\left(1+B_M\right)\left(2+\frac{0.552Re^{1/2}Sc^{1/3}}{F_M}\right) \tag{4.29}$$

and

$$\dot{m} = \pi\frac{\overline{K_G}}{\overline{C_{pG}}}D\ln\left(1+B_T\right)\left(2+\frac{0.552Re^{1/2}Pr^{1/3}}{F_T}\right) \tag{4.30}$$

The Schmidt number and the Prandtl number are equal assuming a Lewis number of unity. Eq. 4.29 has the advantage that it applies under all conditions, including the transient state of drop heat-up, whereas Eq. 4.30 can only be used for steady-state evaporation.

Finally, the evaporation rate $\dot{m}$ is:

$$\dot{m} = \pi\frac{\overline{K_G}}{\overline{C_{pG}}}D\ln\left(1+B_M\right)\left(2+\frac{0.522Re^{1/2}Pr^{1/3}}{F_M}\right) \tag{4.31}$$

and the equations for the temporal changes of drop size and temperature are:

$$\frac{dD}{dt} = -\frac{4\overline{K_G}\ln\left(1+B_M\right)}{\overline{C_{pG}}\rho D}\left(1+\frac{0.276Re^{1/2}Pr^{1/3}}{F_M}\right) \tag{4.32}$$

$$\frac{dT}{dt} = \frac{12K_G\ln\left(1+B_M\right)}{C_{pG}\rho DC_p}\left(1+\frac{0.276Re^{1/2}Pr^{1/3}}{F_M}\right)\left(\frac{C_{pG}\left(T_\infty - T_{sf}\right)}{B_M} - L\left(T_{sf}\right)\right) \tag{4.33}$$

The quantity $\overline{\rho_G}\overline{C_d}$ can be replaced by $\overline{K_G}/\overline{C_{pG}}$ by assuming a Lewis number of unity. The heat penetrating into the drop can be expressed as:

$$Q_L = \dot{m}\left(\frac{\overline{C_{pG}}\left(T_\infty - T_{sf}\right)}{B_M} - L\left(T_{sf}\right)\right) \tag{4.34}$$

where the subscripts sf and ∞ refer to drop surface and ambient conditions, respectively.

The Spalding mass (B_M) and heat transfer (B_T) numbers are calculated as:

$$B_M = \frac{Y_{Fsf} - Y_{F\infty}}{1 - Y_{Fsf}} \tag{4.35}$$

$$B_T = \frac{\overline{C_{pG}}\left(T_\infty - T_{sf}\right)}{L\left(T_{sf}\right) + Q_L/\dot{m}} \tag{4.36}$$

in which Y_{Fsf} is the fuel mass fraction on the drop surface, which can be expressed as:

$$Y_{Fsf} = \left[1 + \left(\frac{P}{P_{Fs}} - 1\right)\frac{M_A}{M_F}\right] \tag{4.37}$$

where M_A and M_F are the molar masses of air and fuel, respectively, and $L\left(T_{sf}\right)$ is the latent heat of vaporization at temperature T_{sf}, which according to Watson (1931) may be given by the following equation:

$$L\left(T_{sf}\right) = L\left(T_{bn}\right)\left(\frac{T_{cr} - T_{sf}}{T_{cr} - T_{bn}}\right)^{-0.38} \tag{4.38}$$

For any given value of surface temperature, the vapour pressure is readily estimated from the Clausius-Claperyon equation:

$$P_{Fs} = \exp\left(a - \frac{b}{T_{sf} - 43}\right) \tag{4.39}$$

where a and b are constants of the fuel.

Of the air/vapour mixture in the boundary layer near the drop surface, the best results are obtained using the one-third rule of Sparrow and Gregg (1958), in which average properties are evaluated at the following reference temperature and composition:

$$T_{ref} = T_{sf} + \frac{T_\infty - T_{sf}}{3} \tag{4.40}$$

$$Y_{Fref} = Y_{Fsf} + \frac{Y_{F\infty} - Y_{Fsf}}{3} \tag{4.41}$$

From these reference values, it is possible to determine the specific heat at constant pressure as:

$$C_{p_G} = Y_{Aref}C_{p_{air}}\left(T_{ref}\right) + Y_{Fref}C_p\left(T_{ref}\right) \tag{4.42}$$

where $Y_{Aref} = 1 - Y_{Fref}$.

4.4.3 Breakup sub-model

One of the assumptions considered earlier was that the incident drops maintained their spherical shape until they reached the wall. Such assumption may be valid in situations in which the air flow rate is not very high. However, as the velocity of the crossflow increases, a deformation stage arises, which can lead to the disintegration of the incident liquid particles. This scenario is schematically illustrated in Fig. 4.7.

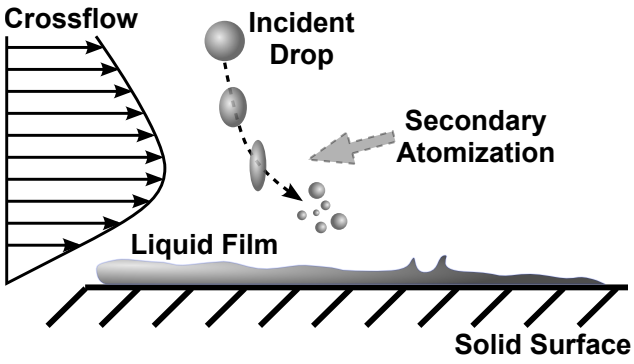

Figure 4.7: Schematic diagram of secondary atomization of incident drops.

Numerous experimental studies have been carried out with the purpose of describing the mechanisms of deformation (Hsiang and Faeth, 1992; Liu and Reitz, 1997; Chou and Faeth, 1998), characterizing the fragments resulting from each breakup regime (Hsiang and Faeth, 1992, 1993; Chou et al., 1997), determining the time scales involved in the atomization process (Pilch and Erdman, 1987; Hsiang and Faeth, 1992) and identifying the parameters affecting the criteria used to define the boundaries between the breakup regimes (Hinze, 1955; Krzeczkowski, 1980).

These findings have enabled investigators to devise computational models in the attempt to replicate the secondary atomization phenomenon. Liu and Reitz (1997) have developed a local deformation model to evaluate the performance of the correlations that the authors had derived from their experimental data concerning that particular stage of secondary atomization. The model predictions were found to be in good agreement with the measurements. Similarly, Helenbrook and Edwards (2002) performed a thorough computational analysis of the deformation response of a non-evaporating, isolated liquid drop in a uniform gaseous stream by means of fully resolved numerical simulations. That same year, Schmehl (2002) presented an analytical approach to simulate drop deformation and breakup by aerodynamic pressure forces. The numerical model was based on linear normal mode analysis combined with the use of correlations for the pressure boundary conditions on the drop surface. However, the results obtained were not satisfactory.

More recently, Bartz et al. (2011) and Kim et al. (2010) reported numerical studies of the macroscopic atomization of liquid drops in which they employed both the original and a modified version of the Taylor analogy breakup (TAB) model for describing the drop deformation and breakup in sprays. In both stages of atomization, the improved version provided better prediction results than the original one. However, the authors reported that the discrepancies found between numerical and experimental results were due to the fact that some of the mechanisms occurring during the secondary atomization process could not be captured by the formulation adopted.

For this reason, in the methodology proposed in the present work, a purely empirical model is devised to simulate the deformation and breakup phenomena. This method relies on experimentally-derived correlations available in the literature that describe the different stages of the atomization process. With this approach, the simulation becomes phenomenologically connected to the fundamental physical mechanisms observed in the experiments. Therefore, it should offer a better insight into the physics of the phenomena examined than the theoretical models used in TAB-based approaches, which are often fine-tuned to match specific experimental data. Furthermore, it is evident that the rigour of the simulation is bounded by the precision of the equations considered. As a result, the present approach allows one to assess if the correlations are comprehensive and accurate enough to be used by modellers in computational simulations. Such an analysis may thus serve as a mean to evaluate the advances operated in measurement techniques and instruments of analysis of the secondary atomization process.

The proposed model is then evaluated by comparing the computational results against experimental data available in the literature. In this case, the experimental data provided by Kim et al. (2010) have been used as benchmark to validate the computational results. The configuration tested is shown schematically in Fig. 4.8. It consists of an air flow crossing perpendicularly the path of the injected stream of drops. Table 4.3 lists the properties of the fuels tested, whose values have been taken from the paper of Kim et al. (2010). The ambient pressure and temperature were held constant at 0.1 MPa and 293 K, respectively.

Depending on the flow rate, the interactions between both gas and liquid lead to different breakup mechanisms. To create conditions to detect bag breakup, an air flow rate of 16 L/min

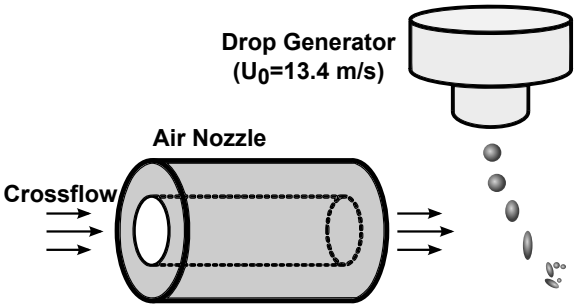

Figure 4.8: Schematic representation of the experimental configuration replicated.

Table 4.3: Diesel and bio-diesel fuel properties

Properties	Diesel	Bio-diesel
Density, ρ [kg/m^3]	830	880
Surface Tension, σ [kg/s^2]	0.02689	0.02833
Viscosity, μ [$kg/(m.s)$]	0.002233	0.00389

(84.9 m/s) was set, which corresponds to a Weber number of 68 and 62.4 for diesel and bio-diesel fuel cases, respectively.

Figure 4.9 illustrates the corresponding domain of solution of the computational simulations which is constituted by a rectangular channel with the following dimensions: 32 x 18 x 20 mm^3. The injector nozzle is located 2 mm downstream of the inlet plane. This distance is set to minimize the gas boundary layer. The flow enters the solution domain through a small inlet plane (2 $\times$ 2 mm^2). A symmetry plane is assumed along the longitudinal axis and the remaining boundaries are set with solid walls. The chosen mesh (20 in the vertical direction, 18 in the transverse direction and 30 points in the longitudinal direction, with the longitudinal axis corresponding to the crossflow direction) proved to deliver an adequate mesh refinement in the present simulations.

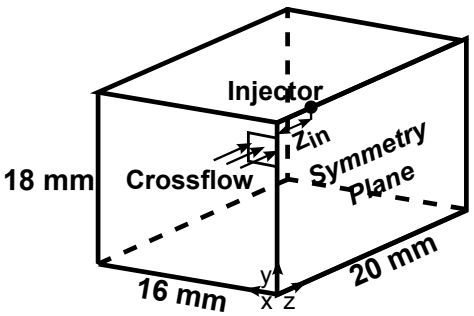

Figure 4.9: Schematic diagram of the flow geometry with breakup.

However, it is important to note that such measurements have been obtained under continuous jet experiments. Even though most of the papers reported in the literature regarding the breakup mechanisms refer to shock tube experiments (in which the nature of the deformation is determined by an abrupt loading applied to the particles), no systematic accessible contribution has been found to be convenient to validate computational models. Hence, it has been necessary to resort to continuous jet studies to find valuable experimental data that allowed us to assess the prediction results obtained in the simulations. In the present work, the

measurements provided by Kim et al. (2010) have been used as benchmark. However, some features of the setup analysed have been established to ensure that the flow produces similar results as the shock tube concept would in the same circumstances.

In fact, according to Guildenbecher et al. (2009), it is possible to guarantee that the results obtained from continuous jet experiments closely match those from shock tube experiments by ensuring that the distortion and breakup of the drops occur almost entirely when the particles are within the jet's uniform velocity region. The authors expressed this statement as follows:

$$U^r_{0,sw}\frac{(1+h_{bl}/D_0)}{t_{bin}\left(\rho/\rho_G\right)^{0.5}} < U^r_{0,cs} < U^r_{0,sw}\sqrt{\frac{We_{cr}}{We}} \tag{4.43}$$

where h_{bl} is the boundary layer thickness and We_{cr} is the critical Weber number. Considering the conditions adopted in the present work (and assuming that the nozzle is well designed, $h_{bl} \approx 0$), the previous equation yields: $2 < U_0 < 34$ m/s. The initial velocity of the injected drops is 13.4 m/s, so according to Guildenbecher et al. (2009), the continuous jet studied here operates in a manner that produces results that are very similar to shock tube ones.

Regardless of the chosen method, the drops are exposed to a spectrum of velocity gradients that alters the aerodynamic forces acting on them. Even though the transition between breakup modes is a continuous process, the assumption of fixed values is widely accepted. In fact, the map of breakup regimes is usually defined in terms of Weber numbers, being essentially constant for $Oh< 0.1$.

Once a critical threshold has been exceeded, a specific breakup type occurs. However, the magnitude of each critical threshold is not uniform across the literature available. In this study, the widely used categorization proposed by Hsiang and Faeth (1992) has been adopted. The following three breakup regimes are identified: bag, multimode and shear breakups. Nevertheless, the transition criteria established by the authors were developed for the case of shock tube experiments. In continuous jet situations, the critical Weber numbers limiting each breakup regime are much higher than in the abrupt acceleration concept. Yet, such thresholds have not been yet defined with accuracy in the literature.

Therefore, no critical limits between each breakup regime can be used in the present work based on experimental data. Rather, the simulations are performed for each set of experimental results available and an approximate value is proposed. For instance, if one particular measurement has been obtained under certain conditions (i.e. within a specified range of Weber numbers and air flow rates), this information is used to constrain the values of the corresponding critical We in our mathematical formulation. Then, the approach is based on an iterative procedure for which the initial information helps to minimize the number of simulations. The chosen critical We is the one that reflects the best fit with experimental data, particularly concerning the time scales involved for the onset of the second stage of secondary atomization. Even though these values are mere approximations based on the information available, they may be indicative of the scales involved in continuous jet experiments.

Before the secondary atomization regime arises, the drop experiences a deformation stage that affects its drag properties and, consequently, its trajectory before impact. During this phase, the drop evolves from a spherical to an oblate ellipsoidal shape. This distortion is reflected in the instantaneous drag coefficient (C_D) according to the following equation:

$$C_D = C_{D,S}\left(1 + 2.632y'\right) \tag{4.44}$$

which is dependent upon the magnitude of the particle deformation through the y' parameter

as follows:

$$y' = min\left(1, \frac{D_{cs}}{D_0} - 1\right) \tag{4.45}$$

Moreover, it is assumed that the drop is fully distorted when $D_{cs} = 2D_0$, which is close to the values considered for the drop maximum distortion before initiation of fragmentation in the study of Hsiang and Faeth (1992) ($D_{cs} \approx 1.8D_0$). Note that $C_{D,S}$ is the coefficient of drag for a sphere at the same Reynolds number which may be estimated as follows:

$$C_{D,S} = \begin{cases} \frac{24}{Re}\left(1 + \frac{1}{6}Re^{\frac{2}{3}}\right) & Re \leq 1000 \quad \text{(4.46a)} \\ 0.424 & Re > 1000 \quad \text{(4.46b)} \end{cases}$$

The natural deformation of the particle towards a disk-like shape was found to be reasonably well expressed according to a linear equation by Chou and Faeth (1998). The authors were able to describe the temporal evolution of the characteristic diameter of the drop up to the moment of disintegration. The deformation stage was defined by the following expression:

$$D_{cs}/D_0 = 1.0 + 0.5t/t^* \tag{4.47}$$

Once the deformation threshold has been reached, bag breakup regime ensues. This is the first breakup mode considered since it occurs at low We and for which minimal energy is needed to achieve the second stage of atomization. Hsiang and Faeth (1992, 1993) found that for $Oh < 0.1$, droplet size distributions after secondary breakup satisfied the root normal distribution function with $MMD/SMD = 1.2$ for both bag and multimode breakup regimes. Furthermore, after removal of the droplet core, this same distribution was found to be applicable to shear breakup regime. The authors also found that droplet sizes after secondary breakup decreased as We increased and a single correlation could express the SMD after bag, multimode and shear breakup. In fact, the data evaluated yielded the following empirical fit:

$$D_{SMD} = CD_0\left(\frac{\rho}{\rho_G}\right)^{1/4}\left[\frac{\mu}{\rho D_0 U_0^r}\right]^{1/2} \tag{4.48}$$

where C is a constant of proportionality which was estimated to be 6.2.

Similarly to the practices employed in previous sections, for each drop disintegrated, up to six child droplet samples are created. A mean diameter is calculated with Eq. 4.48 and the fragment sizes follow a normal distribution centred at the value given by the mean diameter of the fragments in each breakup event, with the variance being equal to 10 μm. The latter parameter has been attributed according to the size distributions of the fragments resulting from the experimental data of Kim et al. (2010).

The same authors (Hsiang and Faeth, 1992) studied the breakup initiation time by taking into analysis several sources of experimental data. They concluded that at low Oh, drop distortion correlated reasonably well as a linear function of time, with the maximum distortion reached at roughly $t_{bin}/t^* = 1.6$.

The last piece of information refers to the relative velocity of the fragments resulting from the disintegration of drops during breakup. The mean relative velocity of the fragments ($\overline{U}_{frag}$) as a function of the velocity of the core droplet for both stream-wise and cross-stream (cs) directions has been defined as:

$$\begin{aligned} \overline{U}_{shear,sw} &= U_0 + 9.5(\rho/\rho_G)^{-1/2}(U_G - U_0) \\ \overline{U}_{shear,cs} &= 0 \end{aligned} \tag{4.49}$$

whereas the velocity of fragments originated from bag and multimode breakup regimes can be determined as follows:

$$U^r_{frag} = U^r_0 \left[1 + 2.7\left((\rho/\rho_G)^{-1/2} D_0/D\right)^{2/3}\right]^{-1} \tag{4.50}$$

Equations 4.44 to 4.50 are used as a foundation for the deformation and breakup models proposed here. The integration of the different aspects of the first and second stage of secondary atomization — expressed through the referred equations — allows one to achieve the computational results expected according to the physical phenomena observed experimentally.

Finally, it is worth mentioning that this breakup sub-model cannot be used in conjunction with the empirical approach used to establish the initial characteristics of the spray at the injector exit (but rather instead), since this empirical approach can only be used if the crossflow velocity is low and the spherical drops maintain their size from the moment they leave the injector until the moment they impact the interposed surface. If these assumptions could be considered valid in the scenarios described until this section, the same cannot be said here. The deformation and breakup sub-model aims at bridging the gaps identified previously for when such assumptions were not valid, such as in situations in which the crossflow velocity is very high and results in secondary atomization of the incident drops before impact. Therefore, one should employ the selected procedure to establish the initial conditions of the drops according to whether the assumptions are valid or not.

4.4.3.1 TAB-based model (Kim et al., 2010)

In order to compare the present approach with a TAB-based methodology, the computational results reported by Kim et al. (2010) are also presented in this work. The authors proposed some improvements to the TAB model which were found to contribute to a better agreement with experimental data than the original version. Presenting such information in this thesis should be valuable to evaluate the performance of the approach adopted in this work, particularly when it is compared against the fine-tuned computational results obtained by Kim et al. (2010). Therefore, the next paragraphs are used to describe the TAB model as well as the modifications introduced by the authors.

The TAB model (O'Rourke and Amsden, 1987) is based on the analogy between the forces acting on an oscillating drop exposed to an air flow and the forces in an oscillating spring-mass system. The resulting equation for the equator displacement can be calculated by solving the referred system, which yields:

$$\ddot{y} + \frac{2}{\tau_d}\dot{y} + \omega_n^2 y = \frac{C_F \rho_G U^2}{C_b \rho r^2} \tag{4.51}$$

where y is the dimensionless displacement of the drop equator given by $y = (D_{cs} - D_0)\,/\,(C_b r)$, ω_n is the natural frequency of drop oscillations, τ_d is the damping time, and C_b and C_F are model constants (0.5 and 1/3, respectively). The differential equation is solved until critical deformation is reached (at $y = 1.5$) and then, the drops break up into smaller fragments. The size of these fragments is determined by means of an energy conservation analysis between the parent and child particles. O'Rourke and Amsden (1987) derived an expression for the ratio

between the size of the parent drop (D_0) and the mean size of the fragments ($\overline{D}_{frag}$) as:

$$\frac{D_0}{\overline{D}_{frag}} = 1 + \frac{\xi}{5} C_k C_b^2 + \frac{\rho D^3}{\sigma} C_b^2 \dot{y}^2 \left(\frac{6K - 5}{30} \right) \tag{4.52}$$

in which the model constants are $\xi = 10/3$ and $C_k = 8$. Once the size of the child droplets is determined (according to a χ-square distribution based on the values of $\overline{D}_{frag}$), the number of fragments can easily be calculated by mass conservation.

As far as the velocity is concerned, the TAB model attributes to the child droplets a velocity normal to the path of the parent drops, as follows:

$$U_{frag,N} = C_b r \dot{y} \tag{4.53}$$

However, Kim et al. (2010) developed a modified version of the model to enhance the accuracy of the drop deformation and breakup simulations. This version improved the droplet drag model by considering the effect of the frontal area in the drag estimation, in addition to the drop shape (which was the only variable assumed in the original approach). This modification aimed at better representing the physics of the drag effect which were found to be significantly underestimated. On the other hand, the model constants were also replaced by optimized empirical constants obtained from the experimental results of the drop motion. With the present modifications, the calculated drop deformation ratio was found to closely match the measured deformation ratio.

Furthermore, Kim et al. (2010) observed in their experiments that the atomization characteristics were strongly dominated by the frictional flow inside the drops, rather than only the kinetic and surface energies. The resulting equation for the ratio of the parent drop size to the mean child droplet size becomes:

$$\frac{D_0}{\overline{D}_{frag}} = \left[1 + \frac{E_{acc} - \pi D^3/4 \, \rho U_{frag,N}^2/3}{\pi D^2 \sigma} \right]^{1/(3n-2)} \tag{4.54}$$

where the model constant n has been chosen to be 1.2 and the total energy accumulated in the droplet surface during the first breakup stage, E_{acc}, has been estimated from the energy balance equation ($E_{acc} = E_{S\,frag} + E_{K\,frag} - E_{S0}$), yielding:

$$E_{acc} = \left(\frac{D_0}{\overline{D}_{frag}} \right)^{3n} \pi \sigma \overline{D}_{frag}^2 + \left(\frac{D_0}{\overline{D}_{frag}} \right)^{3n} \frac{3}{8} \pi \rho U_{frag,N}^2 \overline{D}_{frag}^3 / 8 - \pi D^2 \sigma \tag{4.55}$$

in which the first two terms on the right hand side of the equation ($E_{S\,frag}$ and $E_{K\,frag}$) are the surface and kinetic energy of the child droplets after breakup, and the last term (E_{S0}) is the surface energy of the parent drops.

As mentioned above, this version of the TAB model optimized for this specific flow configuration is also presented in the results reported in the next section. This comparison enables one to evaluate the approach used in this work as well as to infer about the adequacy of the fundamental knowledge (in terms of experimentally-deduced correlations) accessible in the literature.

Chapter 5

Results & Discussion

The results of the computational simulations — whose mathematical formulations have been described in Chapters 3 and 4 — are presented and discussed in the present chapter. Section 5.1 presents the results of the spray initialization procedures and compares the predicted and measured initial drop characteristics. This is the first step required for the spray impingement simulation procedure. The remaining five sections can be divided into two categories: 1) the results obtained under the evaluation stage of the computational model, and 2) the results obtained under the attempt to enhance certain aspects of the simulation.

In the first stage (evaluation phase), the original model has been examined with the purpose of identifying eventual shortcomings and diagnose more accurately what could effectively be improved in the simulation procedure. A key question about the spray-wall impact is whether or not the trajectory of the drops is sufficiently accurate in the near-wall region. Section 5.2 is devoted to this particular question and compares the base model results against an enhanced near-wall drop tracking method. Furthermore, in previous simulations, it was detected that the velocity profiles of secondary droplets resulting from the splash event did not provide as good an agreement as the probability density functions. The analysis of the dissipative energy loss — discussed in Section 5.3 — has been an attempt to verify how accurate the approach used in our model was.

It is worth mentioning that this evaluation phase could be extended to works that have been carried out before the beginning of this doctoral research. Here, efforts have been directed towards the evaluation of the transition criteria used for the onset of disintegration. There are numerous expressions available in the literature for the critical splash threshold, each of which has been advocated as the most accurate transition criteria. In some cases, different equations are intended to cover the same range of impact conditions, whereas in other cases, critical thresholds — which have been proposed for the same boundary between impingement regimes — are function of different variables. Such inconsistency has motivated the realization of a comprehensive review of the transition criteria for the onset of splash in order to identify in a systematic manner the alternatives available in the literature. The analysis has been completed by integrating each equation into the model and comparing the outcome obtained. It was found that the transition criterion for the onset of splash proposed by Bai et al. (2002) provided the best results for the range of impact conditions under study.

In the second stage of the work, specific instruments have been developed to respond to the needs determined previously. In fact, at this point, computational extensions have been devised to equip the general model with a specific mathematical formulation intended to capture some physical phenomena that would not be considered in the original model. Such approach is expected to improve the outcome of the simulation.

Accordingly, in section 5.4, the simulation results obtained with the application of the liquid film sub-model in combination with the splash threshold specially adopted for this situation (which takes into account the film thickness as an influencing parameter) are presented. The prediction results are compared against experimental data as well as the results obtained with an identical simulation but without the presence of the liquid film sub-model nor the liquid

film-adapted transition criterion (referred as ”present work w/o LF”).

A complete simulation of the spray-wall interaction is complex and requires the understanding of a host of different topics. In previous versions of the model, the evaporation process was disregarded so it could be postulated that the incident drops would keep their spherical shape until impact. Such hypothesis may not be valid when the surfaces are heated and thermal effects are significant. For this reason, it is important to be able to consider this aspect in the simulation procedure, which is only possible by developing a computational extension that takes into account this evaporation process when such conditions appear. This scenario is established in Section 5.5 where the evaporation sub-model is presented. The main objective is to address the evaporation process and investigate its influence on the phenomena resulting from the impact of drops onto solid surfaces. Distinct initial wall temperatures are considered and the results are compared to assess the influence of this parameter in the final outcome.

The last element that has been addressed is the crossflow, which is discussed in Section 5.6. In the original spray impingement model, it was assumed that the crossflow would be such that it would not induce deformation and breakup of the incident drops. Otherwise, the model would not be able to provide adequate results, as the secondary atomization stage is not accounted for by the corresponding mathematical formulation. With the breakup sub-model, such constraint has been resolved and the requirement of limited crossflow velocity is no longer necessary.

Before addressing the results obtained it is worth mentioning that two different populations of particles are distinguished in the data collected: one set consists of the drops moving towards the wall, whilst the other comprises the droplets moving in the opposite direction. Each set is usually represented by a line connecting delta (secondary droplets moving upward) or gradient (mainly incident drops) symbol shapes, respectively. On the other hand, experimental data is always represented with black circles with no line between the symbols. Furthermore, the predictions obtained under the base model simulations (without any of the sub-models reported in this work) can be distinguished from the results obtained with the improved versions of the model: while the former results are defined by black filled symbols, the latter are represented with white ones. This structured presentation of the plots is expected to facilitate the interpretation of the data reported here. The results presented in the following section contain both size distributions and size–velocity correlations of particles as well as other qualitative analyses.

5.1 Spray initialization

Experimental data from free spray conditions are employed to evaluate the accuracy of the procedure used to initialize the spray. Therefore, the drops are injected into the flow field without being influenced by the dragging effect of the crossflow. The initial drop sizes and velocities at the nozzle location are estimated by the procedure described earlier. The measurements are provided at horizontal planes located below the injector nozzle, namely at 80 mm and 40 mm in cases 1 and 2, respectively. The results are presented in this section.

Figures 5.1 compares the predicted and measured time-averaged drop size distributions at four different annular regions. It is worth highlighting that contrary to the practices employed in the measurement of the spray impingement data in case 1, in which experimental data are collected in fixed singular points, in the free spray condition, the measurements have been obtained in annular regions instead (located 80 mm below the injector nozzle). The different

zones are identified in the heading of the corresponding plot represented. The results reveal that the predicted PDFs capture reasonably well the general behaviour of the measured PDFs, with the exception of the central region (0 mm < r < 5 mm) where the occurrence probability of drops with sizes in the 50-100 μm range is substantially underestimated in the calculations.

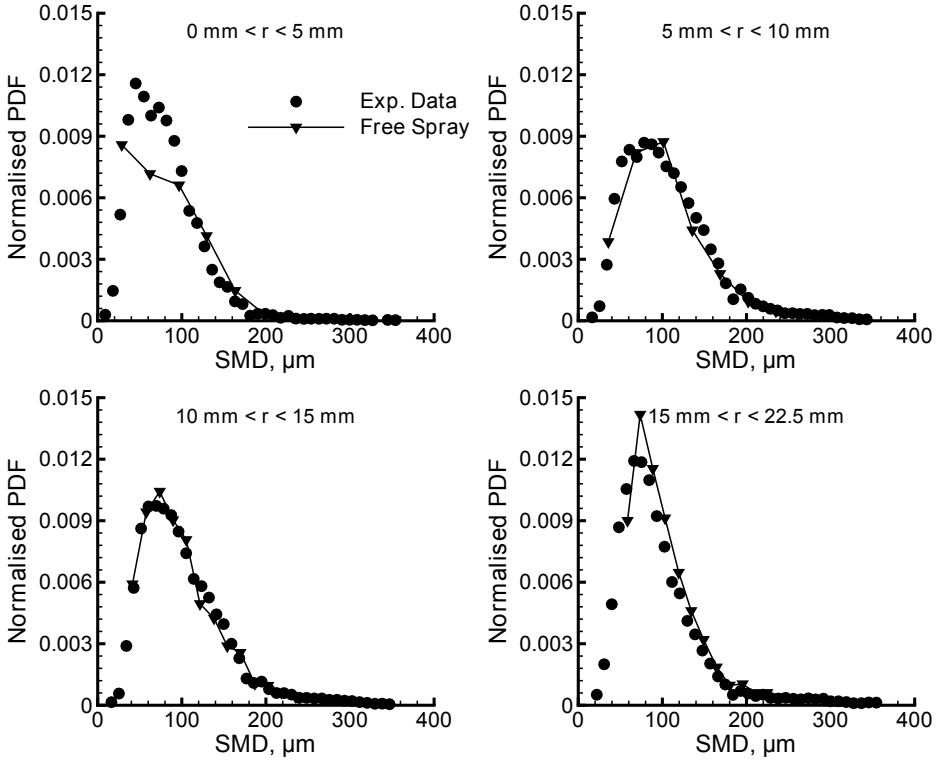

Figure 5.1: Drop size distributions for free spray experiments [case 1].

On the other hand, the predicted correlations defined for the drop size–axial velocity shown in Fig. 5.2 evidence a quite close agreement with experimental data.

The above results indicate that the suggested procedure for the estimation of the initial drop sizes and velocities can reproduce fairly well the measured spray characteristics at the measurement plane where the free spray data has been collected. However, it is important to note that this does not guarantee that a similar agreement will apply near the nozzle or just before impact onto an interposed surface. Nonetheless, in the absence of a better alternative, one should look for free spray data collected in a measurement plane located at around the same distance to the injector nozzle as the distance between the injection apparatus and the surface in the spray impingement experiments. This will minimize eventual source of discrepancies between experimental and computational results.

Such proposition is supported in the second configuration tested where the difference between the location of the measurement planes in the spray impingement (H_{meas}=42 mm) and free spray (H_{meas}=40 mm) experiments is of only 2 mm. This fact is expected to contribute to a more accurate prediction of the incident drop characteristics before impact. The corresponding results for the free spray comparison are presented in Figures 5.3 to 5.5. In the case of the drop size distributions illustrated in Fig. 5.3, the assumptions defined previously provide an almost perfect match between both numerical and experimental results in the two regions of the free spray analysed (0 mm $\leq$ r $\leq$ 3 mm and 3 mm $\leq$ r $\leq$ 6 mm). In a scenario in which breakup of the spray does not take place, the agreement comes down to choosing the same equal-sized bins, with a similar number of particles constituting the spray, and computing the data at the exact

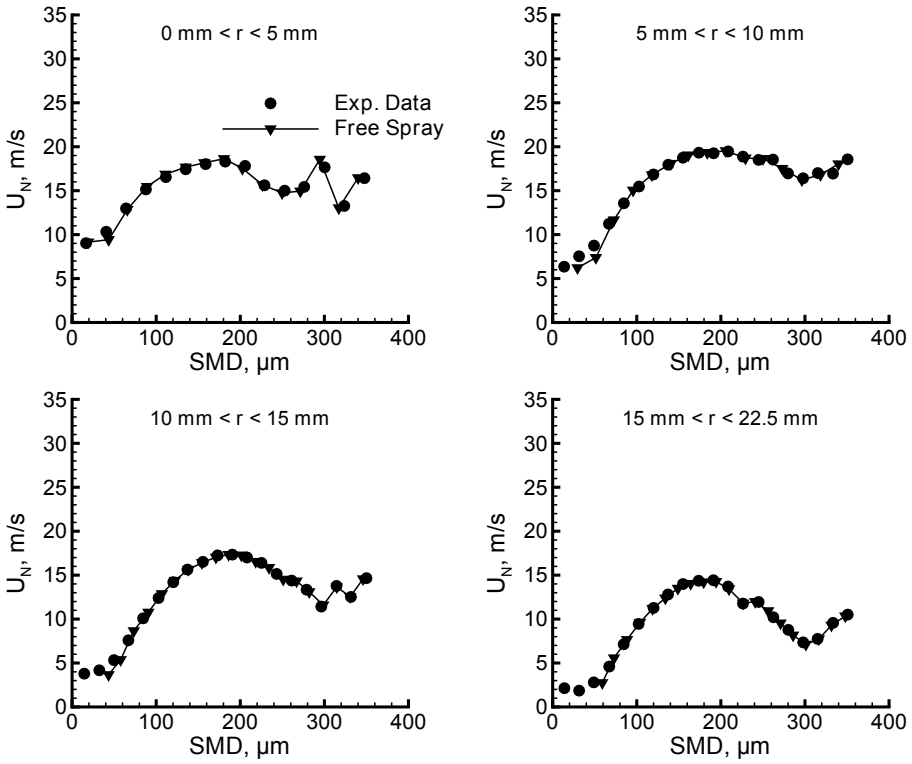

Figure 5.2: Drop size–axial velocity correlations for free spray experiments [case 1].

same location as in the experiments (here the difference is marginal and, thus, the discrepancy is imperceptible).

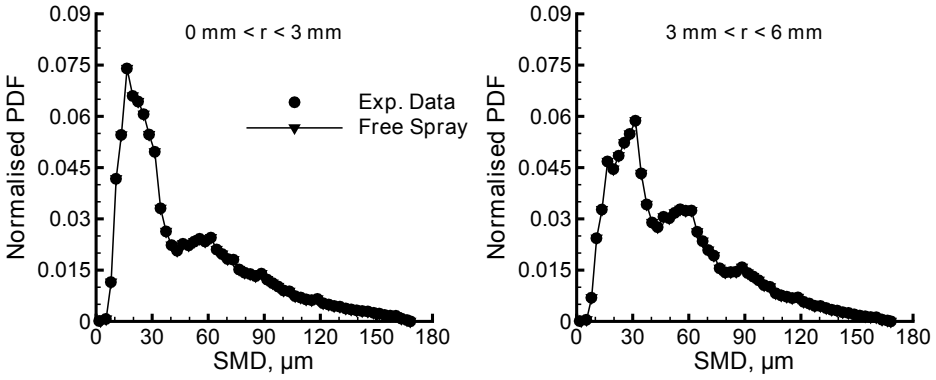

Figure 5.3: Drop size distributions for free spray experiments [case 2].

Regarding the velocity-size correlations in Fig. 5.4, it can be seen that the equations used to represent the velocity profile provide a good agreement between measurements and predictions. This fact is of utmost importance to establish accurately the initial environment of the incident drops. The radial component of the velocity is presented in Fig. 5.5 and, even though its estimation relies fundamentally on the assignment of random values for the circumferential angle (η), reasonable results are still obtained. In fact, although the agreement between computational and experimental results is not as good as in the normal component of the velocity, the trend evidenced in the computational predictions is similar to the experimental data. In this respect, it is interesting to note that the discrepancy between both results is more noticeable in the inner annular region than in the outer. Nevertheless, as it will be shown later, the

present radial velocity profile is considered to perform well enough for the remaining simulation procedure.

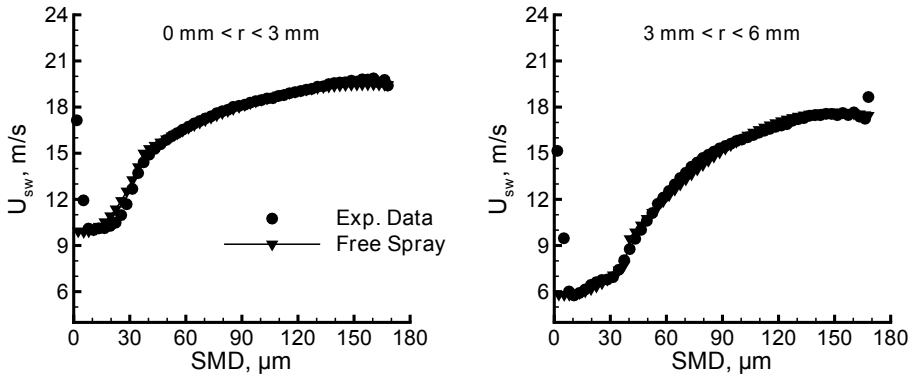

Figure 5.4: Drop size–axial velocity correlations for free spray experiments [case 2].

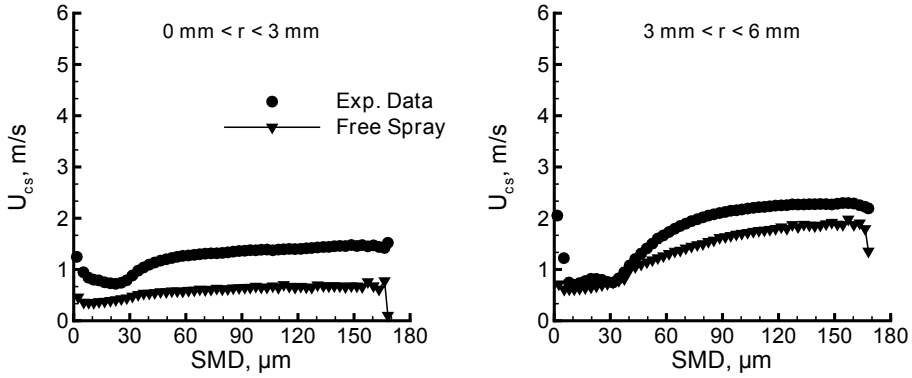

Figure 5.5: Drop size–radial velocity correlations for free spray experiments [case 2].

Therefore, it can be concluded that the present methodology replicates well the characteristics of the spray (i.e., mean drop size and velocity) at the measurement plane that lies 10 mm above the impingement wall (case 2). This allows one to achieve adequate initial conditions that contribute to minimize the source of discrepancies between numerical and experimental results in the remaining simulation procedure.

5.2 Adaptive mesh refinement

The existence of solid walls alters significantly the general behaviour of turbulent flows. At the solid boundary, the relative velocity between the fluid and the wall is zero. This is called the ”no-slip condition”. Consequently, the existence of a turbulent gas phase flowing parallel to the impingement surface leads to the emergence of a boundary layer in the immediate vicinity of the surface. The successful prediction of wall-bounded turbulent flows is determined by the accurate representation of the flow within this layer, particularly in the near-wall region where the effects of shear stresses are significant and large normal gradients can be found.

In multiphase flows, besides the turbulent gas flow, there is also a dispersed phase that must be considered. Once a drop enters the gas boundary layer, the aerodynamic forces exerted by the crossflow induces the deflection of the particle from its natural course (Arcoumanis and Cutter, 1995). The inability to produce accurate predictions of the flow field will result in an

unreliable estimation of the drop motion. Moreover, the difference between the air velocity in contact with the top and bottom of the particle provokes a rotation effect which leads to an additional force applied to the drop. Some authors (Panão and Moreira, 2002) reported that in the near-wall region — where the shear rate is higher — the magnitude of this transverse lift force becomes as important as the drag force. These phenomena influence the trajectory of the drops and, consequently, the general conditions of impact.

The modelling of such multiphase flow requires the accurate description of the boundary layer in the near-wall region. This resolution is usually determined by the construction of the mesh which, although it may be virtually free from numerical errors, can still lead to an erroneous prediction of the drop behaviour if not sufficiently accurate. Therefore, the key question that remains is: can the drops tracking procedure be enhanced by a more refined mesh in the near-wall region?

The analysis has been performed only with the configuration tested in case 1. The mesh is composed by 30x20x16 nodes along the three general axes. In order to use a wall function approach with confidence, it is imperative to ensure that the non-dimensional distance (based on the local cell fluid velocity) from the wall to the first mesh node (known as y^+) is within a certain range. In the mesh considered, the y^+ values of the first node outside the wall are around 35 for the crossflow of 15 m/s and 12 for the crossflow of 5 m/s. Therefore, in both situations the mesh lies in the fully turbulent layer and, thus, wall functions have been correctly applied to bridge the viscosity-affected region between the wall and the outer layer.

The corresponding computational and experimental velocity profiles of the gas phase for the air flow rate of 5 m/s is presented in Fig. 5.6 (measurements of Arcoumanis et al., 1997). The variable U_{sw} is the velocity of the gas in the stream direction, U_{swmax} is the value of the crossflow velocity that enters the solution domain (i.e. 5 m/s in Fig. 5.6), y is the distance to the surface and H is the height of the vertical wall (32 mm). The velocity profile has been taken at the vertical axis constituted by the intersection of $x/H = 0.05$ and $z/H = 1.3$ (which is located upstream of the injector position). The horizontal velocity component and the vertical length scale have been made dimensionless by the maximum crossflow velocity and the height of the solution domain, respectively.

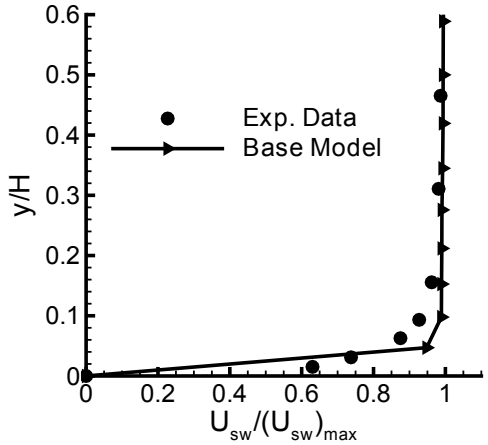

Figure 5.6: Velocity profile of the 5 m/s crossflow [case 1].

Figure 5.6 reveals that the numerical results are in good agreement with the Laser Doppler measurements of the air flow, particularly towards the outer part of the near-wall region. Near the wall, the discrepancy is slightly more expressive. This indication may affect the accuracy

of the drop tracking just before impact.

Mesh independence has already been performed in previous studies for the present conditions. It has been found that the improvements obtained with more refined grids are insignificant and do not justify the increment of the processing time required for the simulations. For this reason, this approach was not an option to improve the numerical solution of the problem in the near-wall region. Instead, an attempt has been made to enhance the methodology applied to the dispersed phase — via a more refined drop tracking method — which has been devised by decreasing the Lagrangian space and time steps between successive position of the particle under analysis. This methodology is expected to provide a more accurate computation of the drop position during the simulation, decreasing the number of iterations and improving the estimation of the drop final trajectory. The improved tracking procedure is only applied to the near-wall region, starting at the surface and going up to the second node above the solid boundary. A refinement of up to 5 times the original model has been applied in the referred region. The nodes above this point lie in the inviscid region of the boundary layer.

To evaluate this approach, the computational results of the downward-moving drops just before impact from the original simulation have been compared against the prediction results of the enhanced near-wall tracking method at the same locations. The corresponding plots are presented in Figs. 5.7 and 5.8 (only for location a and b for ease of analysis) which reveal that the outcome is marginally influenced by the improved drop tracking method.

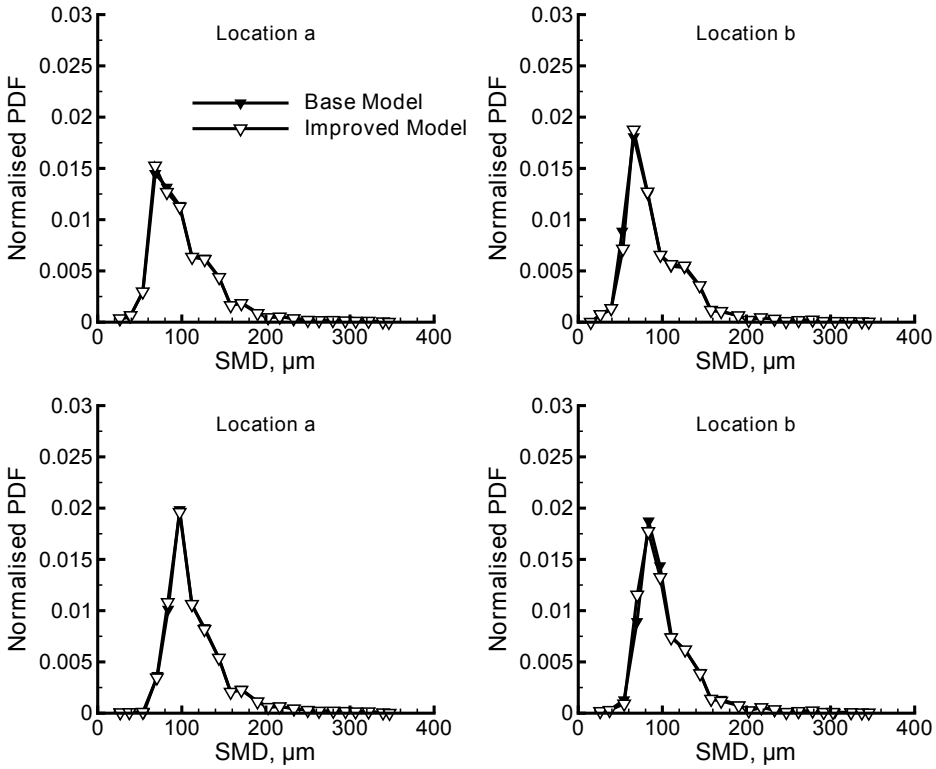

Figure 5.7: Drop size distributions at locations a and b for crossflow velocities of 5 m/s (top row) and 15 m/s (bottom row).

This conclusion — in combination with the mesh independence analysis — clearly indicates that the solution is independent of numerical influences and the original tracking approach is adequate for the purpose of the present work.

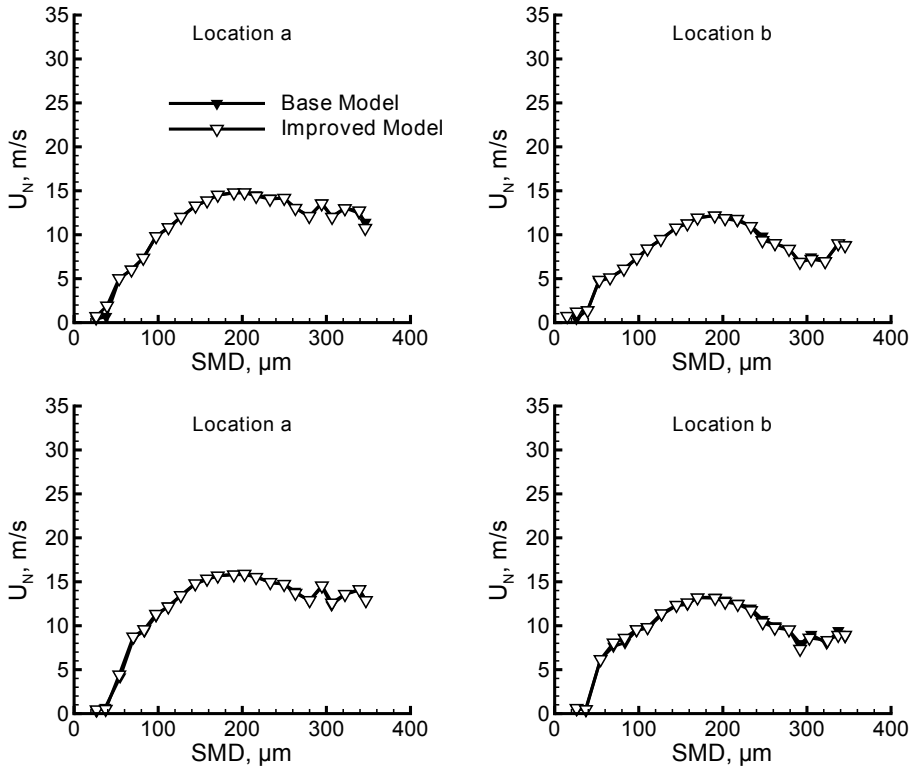

Figure 5.8: Drop size–axial velocity correlations at locations a and b for crossflow velocities of 5 m/s (top row) and 15 m/s (bottom row).

5.3 Dissipative energy loss

From a researcher's point of view, the study of the impact of drops and eventual splashing offers very interesting challenges. While the occurrence of rebound or spread plays a small role in defining the overall spray characteristics, splashing can substantially alter the size distribution of secondary droplets. However, much of the physical phenomena involved in this event are poorly understood and the modelling capabilities are still far from being fully reliable. Such evidence calls for further research on fundamental properties related to the impingement process.

In previous simulations, it was reported that the post-impingement treatment needed to be enhanced, particularly regarding the conditions under which the velocity profiles of the parcels resulting from the splash regime were obtained. As a result, in this section, attention is given to the dissipative energy loss relationship due to its influence on the post-impingement characteristics of splashing particles.

This parameter is, perhaps, the most critical quantity in the estimation of the velocity of secondary droplets. In fact, as discussed before, the other terms in the conservation of energy equation are well-defined in the literature. It is therefore interesting to note that so little attention has been directed towards the evaluation of E_D, particularly in the scenario in which splash occurs. In such a case, the kinetic and surface energy of the incident drop must equate the kinetic and surface energies of the splashing parcels plus the energy dissipated by viscous effects during the process. In most of the approaches adopted so far, authors took advantage of the bibliography available about the subject for a spreading drop (including both very cold and very hot impact conditions) and applied the same correlations to the splash event. Such simplification does not take into account the energy dissipated during the raising of the lamella — in the case of a corona splash — nor the detachment of secondary droplets from the rim.

Therefore, it is likely that E_D might be underestimated and, consequently, the velocity profile overestimated in those cases.

To overcome this issue, Bai and Gosman (1995) proposed an equation for the dissipative energy loss in splash events, which can be expressed as follows:

$$E_D = \frac{We_{cr}}{12}\pi\sigma D_0^2 \tag{5.1}$$

which was found to also underestimate the energy dissipation for high size and velocity of impinging drops. This band of the impact conditions spectrum (i.e. high impact energy) means that the splashing events occur much more often than in low impact energy situations. Therefore, the observation described by the authors (i.e. underestimation of the energy dissipation) in such range may be explained by the fact that E_D did not include the splashing mechanisms mentioned above. However, in their second attempt (Bai et al., 2002), the authors updated the approach and bound the parameter by a postulated value of 80$\%$ the kinetic energy, yielding the following relation:

$$E_D = \max\left(0.8E_{K0}, \frac{We_{cr}}{12}\pi\sigma D_0^2\right) \tag{5.2}$$

With Eq.5.2, the dissipative energy loss is defined, in most of the time, by the first term rather than the second. Therefore, this adjustment has an important repercussion on the results obtained.

To put this approach into perspective, in the present section, other correlations for the dissipative energy loss available in the literature are integrated into the simulation procedure independently, and the results are compared to identify the best option.

As mentioned before, there is little literature available related to this particular parameter for the splash event. However, important contributions have been provided to the spread related literature. The most relevant study on the subject has been conducted by Chandra and Avedisian (1991) who concluded that the energy dissipation was directly proportional to viscosity. Later, Pasandideh-Fard et al. (1996) claimed that they could improve the accuracy of the theoretical model by replacing the splat film thickness (h_{LF}) in the dissipation function (Φ) by the boundary layer thickness (h_{bl}) at the solid interface. In fact, the authors argued that the use of the splat film thickness term led to an overestimation of the maximum extension of the film, which could be overcome by using the boundary layer thickness instead. Moreover, a new time scale (for the drop to spread out until maximum extension) was adopted (being defined as $t_p = 8D_0/(3U)$). The above mentioned relationships are listed in Table 5.1 with some observations about the approaches adopted by the authors.

It is worth highlighting again that the bottom two equations have been the most consistently used relationships throughout the bibliography considered for the energy dissipation term, although they have been devised for the spread regime only. In order to apply these equations to splash, however, one must assume that this regime only occurs at the moment the detachment of secondary droplets from the rim occur or, ultimately, at the moment the crown emerges in the case of a corona splash. With this simplification, it is possible to attribute a value to d_{max} according to the findings of Yarin and Weiss (1995) who reported that the maximum diameter of the flattened particle, just before the occurrence of splash, is twice the incident drop diameter ($d_{max} = 2D_0$). However, the energy consumed by viscous effects during this stage of disintegration is ignored in such equations.

The last unknown variable that needs to be determined from Table 5.1 is h_{LF} in the re-

Table 5.1: Dissipative energy loss relationships and corresponding observations.

	Dissipative Energy Loss Relationships	Observations
Bai et al. (2002)	$E_D = \max\left(0.8E_{K0}, \frac{We_{cr}}{12}\pi\sigma D_0^2\right)$	Defined as the critical kinetic energy below which no splashing occurs. The incident kinetic energy based on the normal incident velocity is: $E_{K0} = \frac{1}{2}m_0U_{0N}$
Chandra and Avedisian (1991)	$E_D \approx \frac{1}{4}\pi\mu\frac{U}{h_{LF}}D_0d_{max}^2$	Estimated from $E_D = \int_0^{t_p}\int_V \Phi dV dt \approx \Phi V t_p$ where the dissipation function is given by $\Phi = \mu\left(\frac{\partial U_i}{\partial x_j} + \frac{\partial U_j}{\partial x_i}\right)\frac{\partial U_i}{\partial x_j} \approx \mu\left(\frac{U}{h_{LF}}\right)$ and $V \approx \frac{1}{4}\pi d_{max}^2 h_{LF}$ and $t_p = D_0/U$
Pasandideh-Fard et al. (1996)	$E_D \approx \frac{\pi}{3}\rho U^2 D_0 d_{max}^2 \frac{1}{\sqrt{Re}}$	Improvement of the Chandra and Avedisian (1991) theoretical model by replacing h_{LF} by $h_{bl} = \frac{2D_0}{\sqrt{Re}}$ and assuming $t_p = \frac{8}{3}\frac{D_0}{U}$

lationship proposed by Chandra and Avedisian (1991). The thickness parameter is estimated assuming that the incident drop immediately before impact keeps the same volume as the flattened drops at the last instant of the spreading phase (i.e., there is no detachment of secondary particles). Therefore, from volume conservation and considering the above hypothesis ($d_{max} = 2D_0$), the equation defining the thickness of the disk may be written as follows:

$$h = \frac{D_0}{6} \tag{5.3}$$

However, in the paper published by Roisman et al. (2009) a different expression has been derived from an eventual mass balance, as follows:

$$h = \frac{2}{3d_{max}^2} \tag{5.4}$$

which, admitting the previous value for the maximum spreading diameter, yields the following disk thickness:

$$h = \frac{1}{6D_0^2} \tag{5.5}$$

Eqs. 5.4 and 5.5 do not satisfy mass/volume conservation. The chances are that a typographical error is behind the expression reported. However, such contrasting equations enable us to establish an interesting exercise to determine the influence of the incident drop diameter on the dissipative energy loss relationship by comparing the final results obtained in both equations.

Therefore, both Eqs. 5.3 and 5.5 for the disk thickness have been introduced into the relationship deduced by Chandra and Avedisian (1991) (denominated as Model C and Model B, respectively) which in addition to the correlations of Bai et al. (2002) (Model A) and Pasandideh-Fard et al. (1996) (Model D) constitute the four energy dissipation relationships analysed in this section (see Table 5.2).

The four models are then integrated into the simulation procedure and the final outcomes are compared. As discussed above, the energy dissipation term significantly influences the estimation of the normal component of the secondary droplet velocities. Therefore, in this

Table 5.2: The four energy dissipation relationships tested.

Dissipative Energy Loss Relationships	Model A (Bai et al., 2002) $E_D = \max\left(0.8E_{K0}, \frac{We_{cr}}{12}\pi\sigma D_0^2\right)$	Model B $E_D \approx 6\pi\mu U_{0N} D_0^5$
	Model C $E_D \approx 6\pi\mu U_{0N} D_0^2$	Model D $E_D \approx \frac{4}{3}\pi\rho {U_{0N}}^2 D_0^3 \frac{1}{\sqrt{Re}}$

section, attention is directed towards the velocity profiles of the secondary droplets (resulting from splash) after impacting onto the wall. The numerical predictions presented in this section are compared against experimental data of Arcoumanis et al. (1997) for both 5 m/s and 15 m/s crossflow velocities.

Figure 5.9 shows the normal velocity-size correlations of upward-moving droplets. Both experimental data and computational results are presented, with the four models listed in the legend being the ones previously identified. It can be seen that the energy dissipation relationship established in Model A is the one that produces the best results as far as the velocity profile is concerned for an air flow rate of 5 m/s. The remaining options exhibit a reasonable agreement between them but over-predict the velocity along the entire spectrum of droplet diameters at the four locations evaluated.

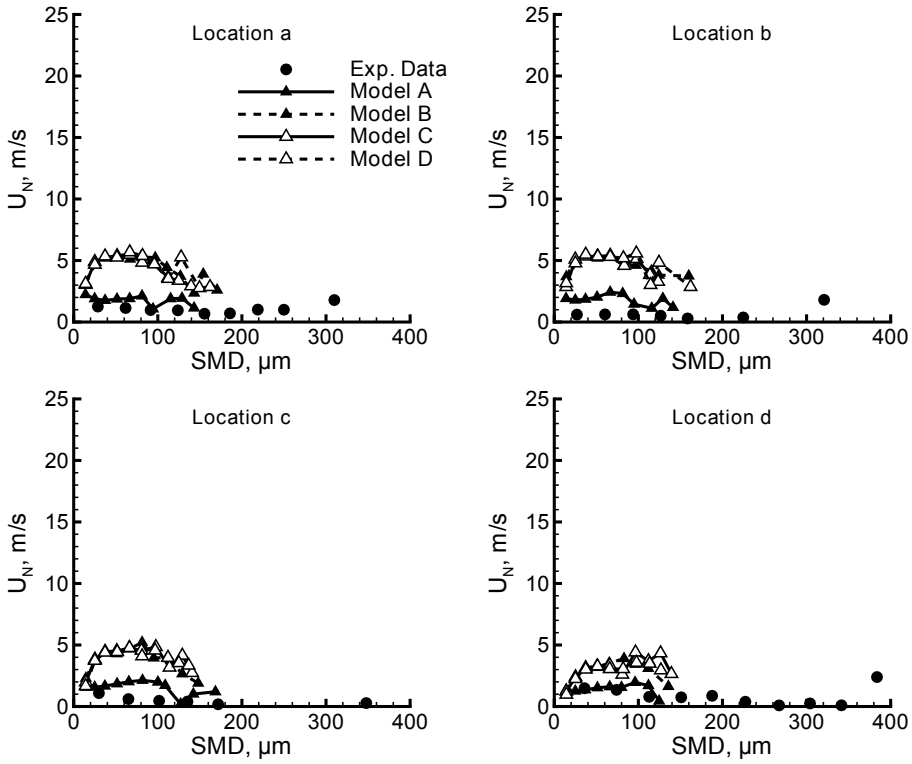

Figure 5.9: Droplet size–axial velocity correlations at four locations for crossflow velocity of 5 m/s.

With respect to the higher air flow rate (depicted in Fig. 5.10), as for the previous figure, the relationship given by Bai et al. (2002) is the model that provides the best approximation to the experimental data, whereas Model B, C and D reveal a relevant overestimation of the velocity profile.

It is curious to note, however, that the computational results reveal similar droplet di-

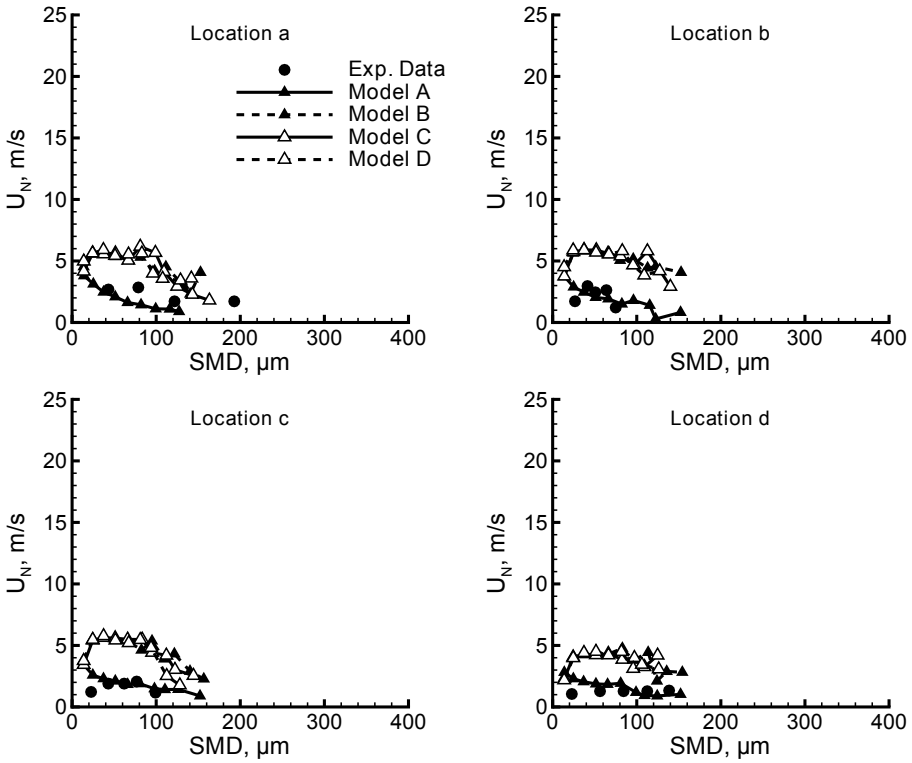

Figure 5.10: Droplet size–axial velocity correlations at four locations for crossflow velocity of 15 m/s.

ameter spectra regardless of the crossflow velocity, impact location or even energy dissipation relationship considered. In all the cases, the droplet sizes range from around 0 μm to almost 180 μm. Considering the fact that the expressions defined for Model B and Model C differ from each other by a factor of proportionality that is the incident drop diameter raised to the third power, it should be fair to conclude that D_0 does not play an important role on the final outcome.

On the other hand, even though the maximum size classes predicted in the simulations are similar to the ones found in the experiments for the higher velocity crossflow (around 180 μm), for the 5 m/s crossflow, the measurements extend up to 400 μm, which is more than twice the maximum size class value predicted computationally. This suggests that the transport of mass during the impact mechanisms is not accurately accounted for in the slower crossflow environment.

5.4 Liquid film

This section presents the more important results obtained under the framework of the liquid film sub-model application. The prediction results obtained with and without the inclusion of the liquid film sub-model are compared against experimental data. Particular attention is directed towards the droplet size–axial velocity correlations of the upward-moving particles, because the application of the computational extension is more prone to influence this type of graphs.

The liquid film sub-model provides a predictive tool for examination of wall wetting and associated mechanisms. This has been the first computational extension developed in this research with the aim of enhancing the results obtained in the simulations. Keeping in mind the goal of maintaining a flexible dispersion model — which could be adjusted to specific boundary conditions through the use of suitable experimental correlations — the liquid film sub-model has

been formulated considering the basic principles of volume and mass conservation. However, the closure equation has been determined by establishing a connection to the experimental data, given by a correlation for the dimensionless film thickness.

It is worth remembering that the transition criterion proposed by Motzkus et al. (2011) has been used as the critical threshold for the onset of splash ($We_{cr} = (2100 + 2000\delta^{1.44})/Oh^{-0.4}$). This equation was found to be suitable to apply at this stage (when the liquid film sub-model is considered) as it is dependent upon the dimensionless film thickness.

Figures 5.11 to 5.13 illustrate the mean velocities in the direction normal to the wall of the secondary droplets. In case 1, two different air flow rates (5 m/s and 15 m/s) are analysed and the measurements are taken at four locations. On the other hand, case 2 refers to the results obtained under the configuration employed by Panão et al. (2013) where only a 11 m/s crossflow has been considered. Rather than particular points (as in the former experiments), the experimental data are provided at horizontal annular regions (0-3 mm, 3-6 mm, and -5-14 mm) as explained before. This information is highlighted in the heading of each figure in order to distinguish the diverse results presented.

Regarding the results obtained in case 1 with the 5 m/s crossflow (Fig. 5.11), there is an evident improvement on the agreement between the simulation that includes the liquid film sub-model and the experimental data, rather than with the predictions obtained in the original simulation. However, despite the improvements, there is still some difficulty to predict the larger droplets that are found in the measurements.

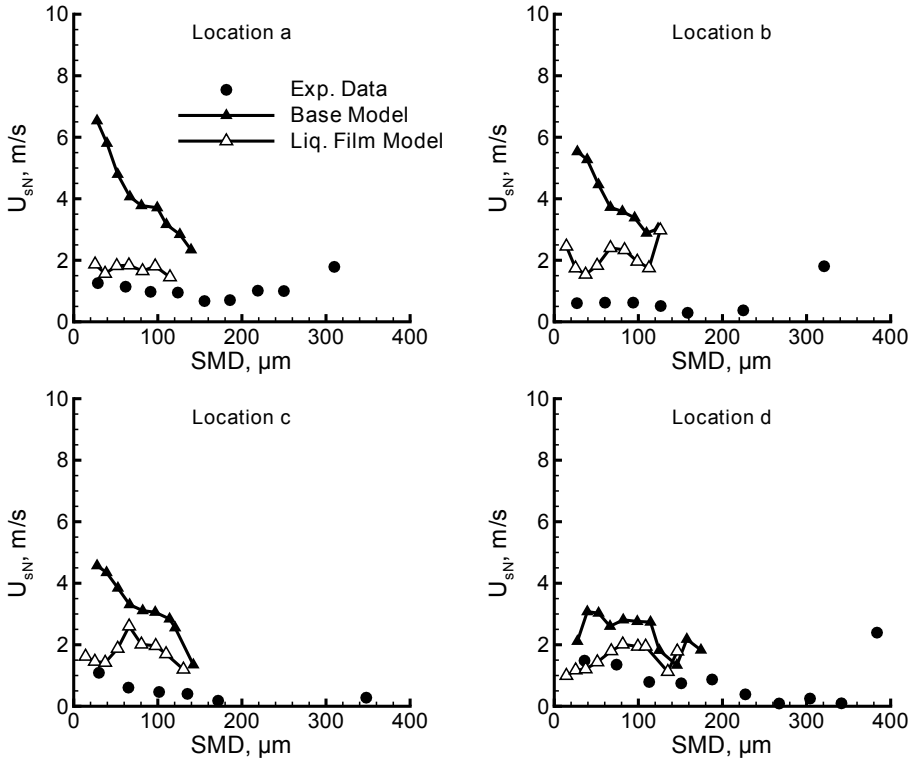

Figure 5.11: Droplet size–axial velocity correlations for crossflow velocity of 5 m/s [case 1].

Figure 5.12 refers to the higher crossflow velocity (15 m/s) and shows that, as in the previous figure, the integration of the liquid film into the model gives rise to more accurate predictions of the experimental data than the original model. However, contrary to the slower crossflow velocity, the drop diameter spectra identified in this case are similar in both experimental and computational results.

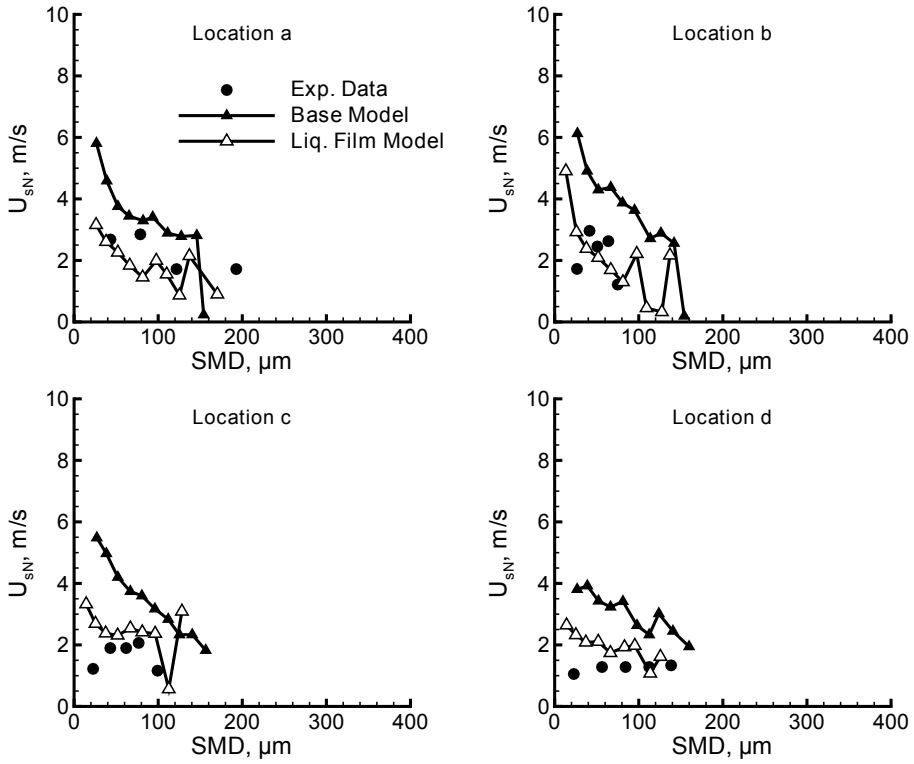

Figure 5.12: Droplet size–axial velocity correlations for crossflow velocity of 15 m/s [case 1].

As for the secondary droplet size–axial velocity correlations obtained in the second configuration mentioned in this document — which are presented in Fig. 5.13 — the version of the model with the liquid film sub-model provides more accurate and stable results than the one without it. This is more evident in the figure that shows the extended range of analysis (-5 mm $\leq$ r $\leq$ 14 mm), where a fairly good agreement is obtained between the computational and experimental results.

It should be noted that, even though the plots refer to splashing (and also rebounding) droplets, the values of the velocity in Fig. 5.13 are made positive (as in the incident drop plots) for easy of analysis. Nevertheless, it is important to keep in mind that, in general, incident drops move downward (towards the wall) and secondary droplets move upward (away from the wall).

Furthermore, it is worth highlighting that the maximum size class obtained in the simulations does not exceed 75 μm, which is less than the 175 μm detected in the measurements. This situation is in line with the results of the size distributions illustrated in Fig. 5.14 in which similar droplet size spectra were found in the three regions evaluated. In fact, it can be seen in the measurements that the droplet sizes extend up to 175 μm but from the 100 μm size class, the number of samples becomes considerably low. This fact is reflected on the non-uniform and scatter plot of the velocity profile in this range of values of the droplet diameter, which is evidenced in Figure 5.13.

The examination of Fig. 5.13 leads to the conclusion that even though the value of the velocity within the range of drop diameters in which more particles are expected (30 μm < SMD < 60 μm) are in reasonably good agreement with the measurements, it becomes also obvious that the general trend obtained in the computational results is different from the practically constant velocity value observed in the experiments. In fact, the negative slope identified in the velocity profiles of the secondary droplets illustrated in Fig. 5.13 suggests that an inverse trend

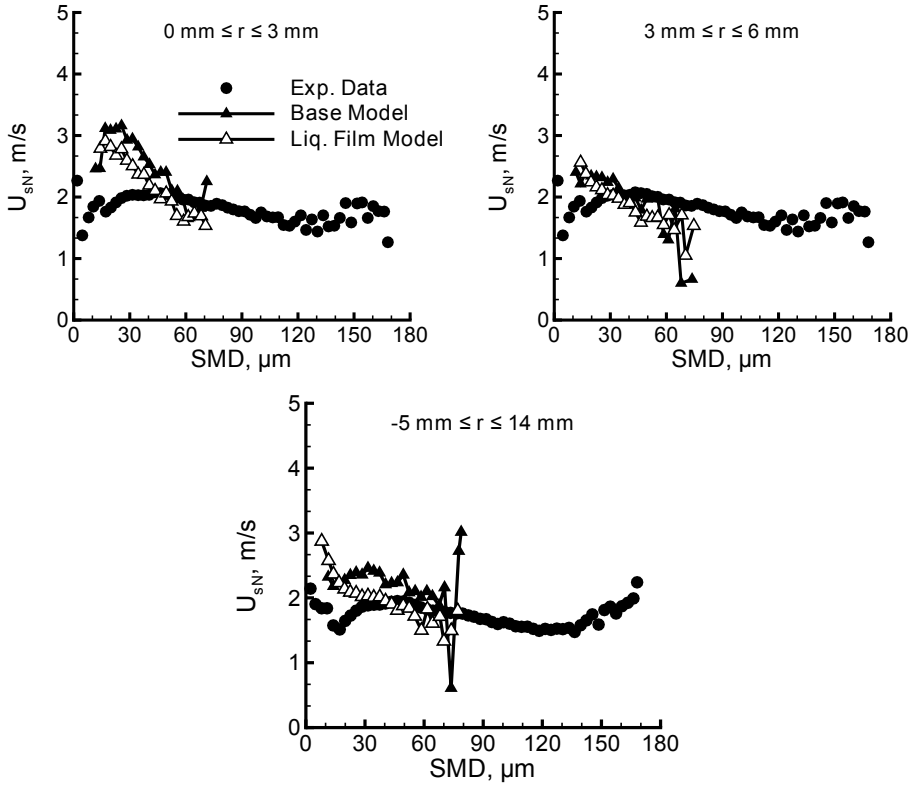

Figure 5.13: Droplet size–axial velocity correlations for crossflow velocity of 11 m/s [case 2].

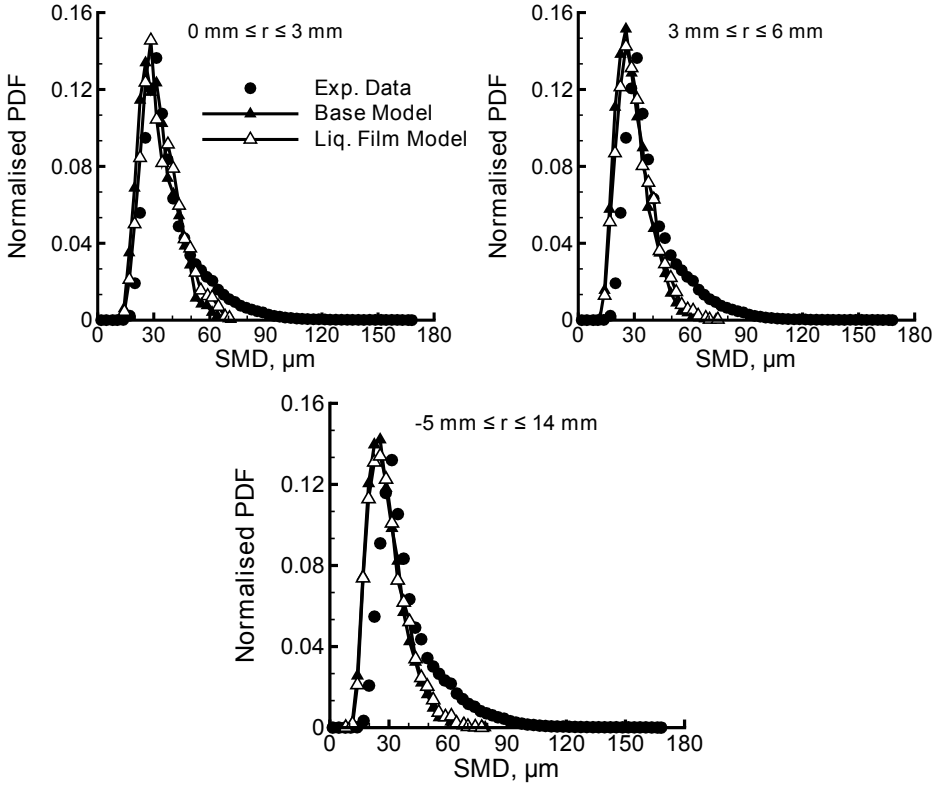

Figure 5.14: Droplet size distributions for crossflow velocity of 11 m/s [case 2].

may be governing another influential parameter on the final outcome. For each particle sample splashing, up to six child droplet samples are created. In each event, the energy is transferred

from kinetic and surface energy of incident droplets to kinetic and surface energy of secondary droplets plus an additional term corresponding to the dissipative energy loss. It has been shown in Section 5.3 that the latter additional term plays an important role on the final outcome, particularly on the estimation of the velocity profiles of secondary droplets. Therefore, the decrease in the axial velocity component of the secondary droplets indicates that, although the velocity of the incident particles increases with size, there is another source of energy loss in the impact mechanism of splash that acts against this effect.

This behaviour may be confirmed in Fig. 5.15 where the axial velocity of secondary droplets and the dissipative energy loss are depicted as function of the particle characteristic diameter. It becomes clear that E_D increases with an increase in the droplet sizes, whereas the opposite occurs in the case of the velocity profiles. It is worth highlighting that the size spectra of both parameters are distinct because the velocity profile refers to secondary droplets, whereas the energy dissipation replicates the incident liquid particles. Nevertheless, Fig. 5.15 demonstrates that a more accurate value for the energy loss during the splash regime could originate a velocity profile with a trend similar to the one found in the measurements. However, further studies are still mandatory in this field to explore these results and provide more insight into this matter.

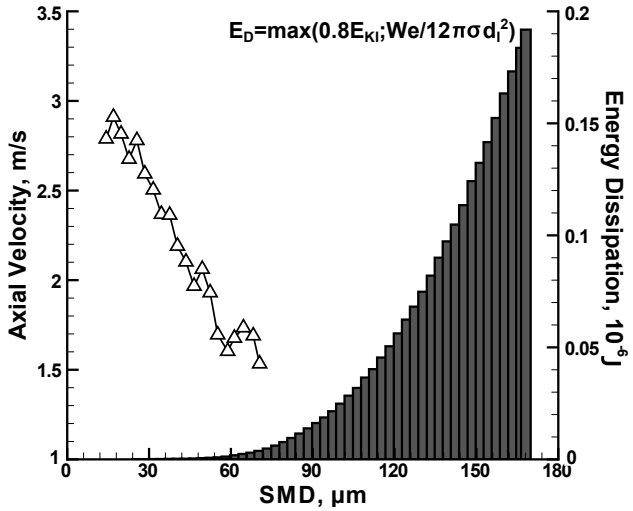

Figure 5.15: Relation between energy dissipation and axial velocity of secondary droplets [case 2].

The formation of a liquid film over the surface induces complex interactions between the incident spray and the liquid layer that is created over the wall after successive impingements. The development of the liquid film alters the circumstances of impact not only along the domain of simulations but also over time which ends up influencing other parameters, such as the chosen transition criterion and the post-impingement characteristics.

Measuring the liquid film over a surface is a difficult task to achieve experimentally. However, computational simulations may play an important role in assessing the behaviour and characteristics of the dynamic layer. In this context, the following figures present the evolution of the liquid film distribution over the impingement surface and the behaviour of the layer is evaluated by comparing the results against evidences that have been reported in the literature. The film thickness (h_{LF}) is made dimensionless with the sauter mean diameter (SMD) — as illustrated in the headers of the legends — yielding the dimensionless film thickness.

The impact of liquid particles — either the incident or the one resulting from the splash regime — with low Weber number may lead them to deposit and form a liquid layer over the solid surface that influences the dispersion of the subsequent impacting particles. Figure 5.16 illus-

trates the distribution of the relative liquid film thickness over the impingement wall obtained with crossflow rates of 5 and 15 m/s, respectively. The contour legends are specified to possess the same number of levels and colour distribution in both cases. This allows the reader to make a direct comparison between both distributions and identify the differences more easily. The maximum dimensionless film thickness with the slower air flow velocity is around 0.04, whereas in the case of the higher air flow velocity the maximum value is 0.027. Therefore, the latter value of 0.027 for the relative dimensionless film thickness has been used as upper limit of the legend in the two representations.

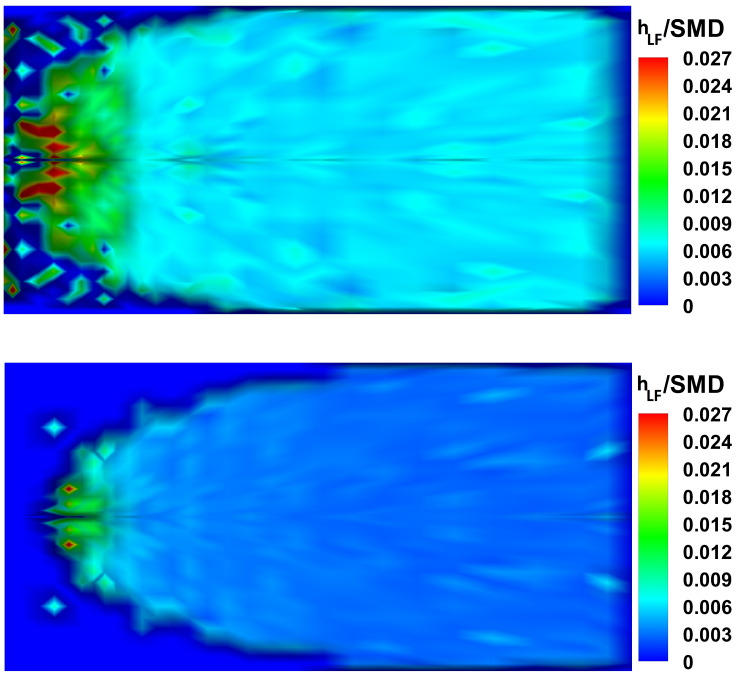

Figure 5.16: Distributions of the relative liquid film thickness for crossflow velocities of 5 m/s (top row) and 15 m/s (bottom row) [case 1].

A thin liquid film is formed along the surface but has a particular incidence in the region below the nozzle, which is where the maximum thickness is found. The mixing process is also associated with the interaction between the particles and the surrounding environment. The presence of a moving gas phase induces drag forces that promotes dispersion of particles as well as the appearance of a boundary layer that influences the spray-wall interactions. Arcoumanis et al. (1997) reported that with the increase in the shearing air velocity, the thickness of the liquid layer decreased and secondary droplets became smaller.

Comparing both representations in Fig. 5.16, it becomes clear that the reduction of the air flow rate induces the thickening of the liquid film. Moreover, more deposited particles are found upstream of the injector location, since the lower crossflow velocity prevents the dragging of the particles downstream. These observations are consistent with the results described by Alghoul et al. (2010), Panão et al. (2013) and Vander Wal et al. (2006a). The decrease of the number of secondary droplets with the increase of the film thickness — which has been verified in the simulations performed — agrees with the observations of Hobbs and Osheroff (1967). It can also be seen that the slower air flow rate reveals a mean relative thickness of 0.007 downstream of the zone of major interactions, whereas in the case of 15 m/s crossflow the mean relative thickness value lies around 0.004. Furthermore, the latter case presents a more tapered profile

due to the higher effect of the crossflow.

It is also of particular interest to assess the temporal evolution of the liquid film over the surface. The analysis has been made with the 15 m/s crossflow, as depicted in Fig. 5.17. The time starts counting from the moment the spray exit the injector and the simulation ends 100 ms after. It can be seen in the first frames that the liquid film begins to grow and reaches the outlet plane 25 ms after start of injection. From this moment on, the thickness of the layer becomes more uniform downstream of the impingement location, with the moving film being now fed by the secondary droplets that are still depositing onto the surface.

It is worth mentioning that the crossflow may be responsible for a special phenomenon at the impingement local described by Silva (2007). A recirculation pattern created by the trajectories of the particles upstream of the area of impact has been found and attributed to the complex interactions between the droplets and the existing crossflow. This may results in a larger amount of liquid upstream of the impingement point, as illustrated in Fig. 5.17. Zhang et al. (2013) reported the presence of large-scale vortices upon impact which could contribute to the preferential concentration of particles in certain locations. This situation may eventually lead the droplets to disperse along the direction against the crossflow, ending up by depositing slightly upstream due to the dragging forces exerted by the crossflow. Such phenomenon will be discussed in more detail in Section 5.5.

In case 2 (shown in Fig. 5.18), it can be seen that after the impact of the spray, a liquid film grows over the surface and develops towards the outlet plane. The incident drops reach the surface 3 ms after start of injection (ASOI) and, thenceforth, the particles keep feeding the moving layer over time. It is important to refer, however, that at this instant, the spray in the original experimental study has not yet reached the wall: from the Mie scattering images available in the paper of Panão et al. (2013) (that are not reproduced here) at 3 ms ASOI, the spray is nearly halfway towards the impact but at 7 ms a cloud of particles hangs over the surface due to the dispersion of secondary droplets. This evidence suggests that the first impacts occurred between those two instants. Therefore, it should be reasonable to admit — since in the case of the experiments the impacts happen shortly after — that this discrepancy may be due to the latency of the injector, which usually is in the order of the milliseconds. Nevertheless, it is important to reinforce that no information is given about this by the authors and a simple hypothesis is advanced in the attempt to justify the discrepancy found in the results observed.

At 7 ms ASOI, the results present a well-defined structure which almost reaches the outlet plane. A greater concentration of liquid is found upstream of the impact area (around z = 0.12 m, with the impingement point being around z = 0.14 m) which are due to the interactions between the drops and the existing crossflow. Figure 5.18 further suggests that the secondary droplets — resulting from previous impacts of early incident drops — are beginning to deposit onto the surface as small amounts of liquid are found in scattered positions. This dispersion feature of the child particles is also verified at 11 ms ASOI in further upstream locations. Moreover, the main liquid film structure reaches the outlet plane. At instant 25 ms ASOI, the distribution of the liquid film is completely established over the wall, being the crossflow responsible for the dragging of the structure downstream and creating a more uniform liquid layer.

Experimental data on the liquid film characteristics are very scarce in the literature due to the difficulty to come up with accurate and reliable measurements. In this sense, simulations by means of computer models may be an important alternative to explore since it is possible to obtain data without much effort. The simulations of the liquid film distribution are intended to go one step further towards that goal. The present results have evidenced that the general behaviour of the liquid film is in line with the observations that have been reported in the

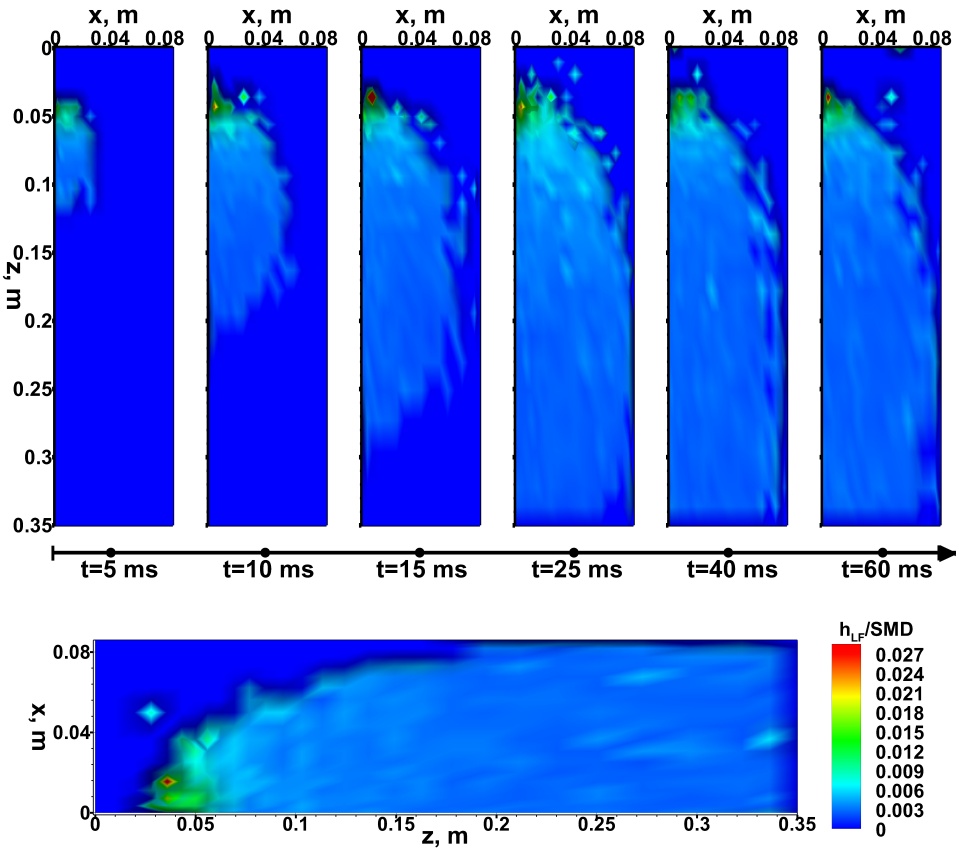

Figure 5.17: Temporal evolution (top row) and final stage (bottom row) of the distribution of the relative liquid film thickness for crossflow velocity of 15 m/s [case 1].

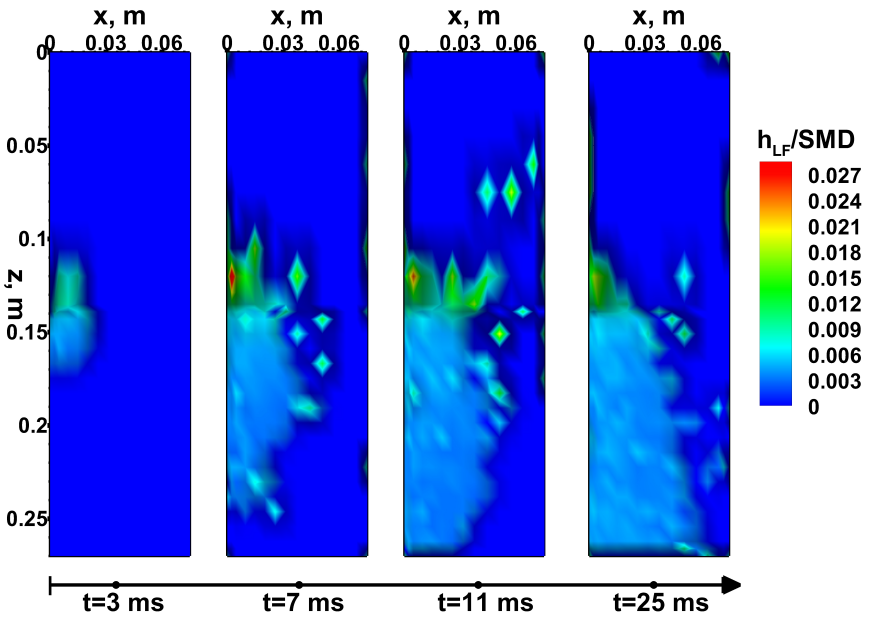

Figure 5.18: Temporal evolution of the distribution of the relative liquid film thickness for crossflow velocity of 11 m/s [case 2].

literature. Although this gives some reliability to the numerical results, further investigation is mandatory to validate the liquid film sub-model in quantitative terms.

5.5 Evaporation

A complete simulation of spray-wall interactions is complex and requires the understanding of a host of different topics. Nevertheless, the present computational model proved to deliver reasonable results in the prediction of the probability density functions and droplet size–velocity correlations under distinct impact conditions as discussed in previous sections. In this section, such analysis is not made. Instead, the work is now focused on the evaporating drop characteristics and their effect on the spray impingement phenomena. Therefore, distinct initial wall temperatures are considered and the results are compared in order to evaluate the influence of this parameter on the final outcome.

Figure 5.19 illustrates the D^2 variation with time for a selection of wall temperatures ranging from 300 to 750 K in Case 2. The temperature of both the vapour environment (in the near-wall region) and the solid surface is assumed to be in thermal equilibrium. The plot quantitatively depicts how the increase in the ambient temperature affects the rate of evaporation. As expected, an elementary deduction can be drawn: the higher the temperature of the walls, the higher the rate of evaporation of the drops.

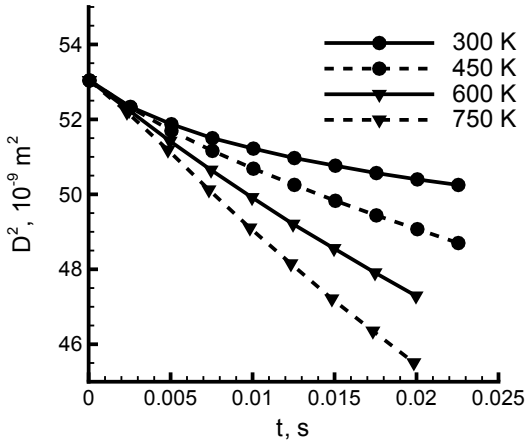

Figure 5.19: D^2 variation over time.

The initial environment is assumed to be suitable enough to allow a linear D^2 evaporation stage of the incident drops. This means that it is assumed that the heat transfer inside the particles occurs much faster than the evaporation process (and, then, it is possible to admit that the temperature inside it is spatially uniform). As a consequence, no condensation stage is considered before the common classical evaporation stage.

Extending the analysis to the whole spray, Fig. 5.20 shows the evolution of the drops under different thermal conditions and evidences the importance of the heat load on the dynamics of impact. Only the colder (300 K, top row) and hotter (750 K, bottom row) environments are considered. However, since the data was originally too dense, the index skip feature of the post-processing software adopted (which skips some data, with a defined frequency) has been used with a value of 20. Therefore, it is possible to get a clearer perspective of the behaviour of the droplets without affecting the final outcome. The comparison is performed at two specific points in the simulation time interval: the images in the first column are taken 3 ms after start of injection (which is about the time at which the incident drops are reaching the surface); whereas the images in column b refer to 5 ms after start of injection. Furthermore, downward and upward moving particles are depicted with black and grey circles, respectively. Under the

colder environment, the spray reaches the wall sooner than in the hot environment. Moreover, the colder secondary droplets seem to carry more momentum after impact since the cloud of upward-moving droplets extends to positions further above the surface. This suggests that the impacting liquid particles are bigger and, consequently, they may reach the disintegration regime more often.

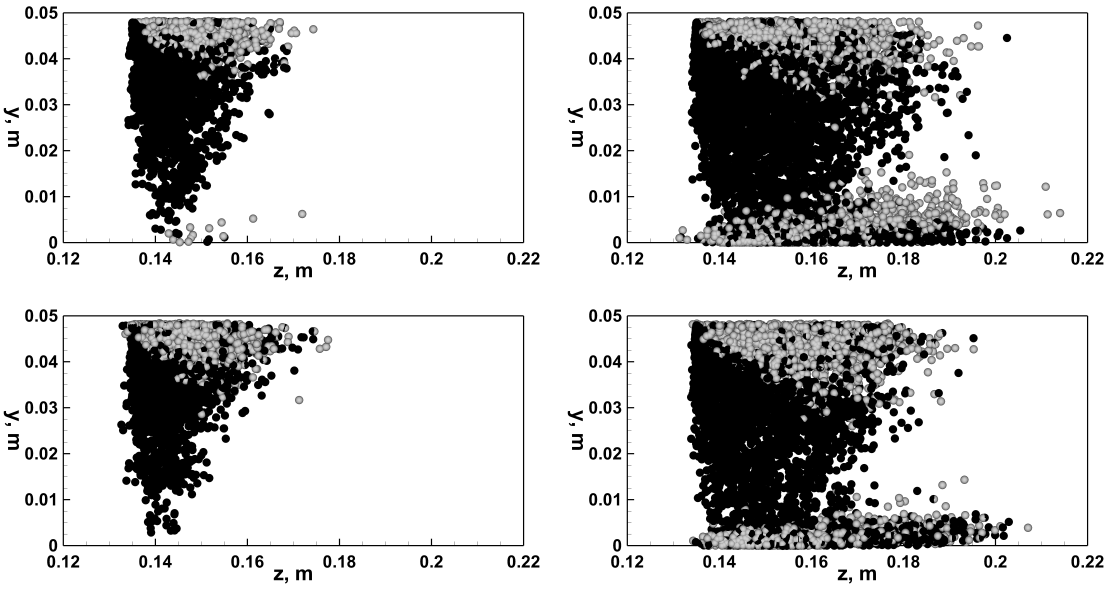

(a) t=3 ms. (b) t=5 ms.

Figure 5.20: Evolution of the spray under distinct thermal conditions: T= 300 K (top row) and T=750 K (bottom row). Grey circles are upward-moving droplets, whereas black circles are downward-moving droplets.

As far as the post-impingement effects are concerned, Fig. 5.21 evaluates the influence of temperature in the deposition of liquid over the surface. Note that the parameter defining the number of depositing drops (N_{dep}) is normalized by the total number of particles that constitutes the spray (N_{tot}). As the temperature increases, a larger number of particles settle on the interposed surface during the first 5 ms (which corresponds to the time required for all the incident drops to reach the wall). During this stage, this trend is more evident in the 750 K case evaluated as the curve reaches $N_{dep}/N_{tot} = 0.11$, whereas the 300 K case only goes up to 0.08 at 4 ms. After this moment, the liquid film is mostly fed by the deposition of secondary droplets resulting from earlier impacts. The number of depositing drops in the hotter scenario decreases and practically matches the curve obtained in the colder environment until the end of the simulation.

Consequently, the fraction of mass of drops expected to stick or spread over the surface to the mass of all the drops that constitute the spray (m_{dep}/m_{tot}) grows rapidly in the first 4 ms — corresponding to the period in which all the primary incident drops reach the wall — and, then, it stabilises. In this region (after 4 ms), even though more drops are found to deposit onto the surface in the 750 K case, the mass of drops expected to contribute to the liquid film is lower than in the 300 K case. In fact, the hotter environment presents a fraction of drop mass expected to deposit onto the surface to the total mass of the spray that only reaches $0.12 \times 10^{-7}\%$, whereas in the colder environment the curve becomes constant at $m_{dep}/m_{tot} \approx 0.15 \times 10^{-9}$. Such findings support the observations of Habchi et al. (1999) who reported that increasing the temperature

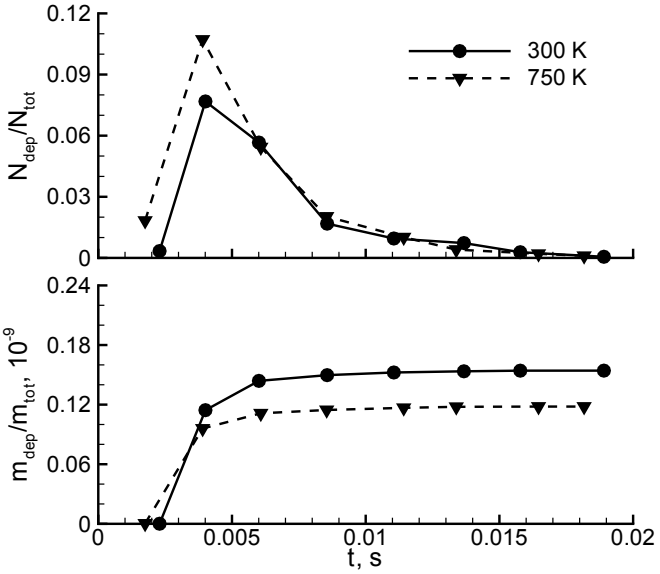

Figure 5.21: Normalized number and fraction of mass of depositing drops.

of the piston decreased the fuel unburned amount. On the other hand, they also give some insight about the important transport of mass at 300 K, which corresponds to larger impacting drops that deposit onto the surface throughout the injection cycle.

The impact of drops with low Weber number gives rise to the formation of a thin liquid film over the surface that influences the subsequent dispersion of droplets. The correct understanding of the film dynamic is of utmost importance for accurate modelling of the spray impingement phenomenon. In fact, it is a key influencing parameter in several specific applications: if, on the one hand it is important to avoid as far as possible the liquid layer over the surface in situation of cold-starting engines, on the other hand the presence of this liquid film is desired in cooling systems applications. Concerned about the latter application, some investigators reported that the thin film flow under spray impingement has a major influence on the heat transfer performances (Pautsch and Shedd, 2006; Moreira et al., 2007a) but more recently Xie et al. (2012) advocated that the applied heat load did not affect the film thickness originated from the spray impact on the surface.

In any case, adding a heat load to the initial environment becomes an extra source of influence that must be considered. Varying the temperature of the walls affects the evaporation rate of the incident particles, which gives rise to a completely new set of impacting drops and alters the final outcome of the spray-wall interactions (Mashayek and Ashgriz, 2011). Therefore, contrary to many authors (see e.g. Habchi, 2010), in the present work, the fraction of mass evaporated during the injection phase is taken into account in the simulation procedure.

Figure 5.22 illustrates the liquid film distribution over the impingement surface for both temperatures evaluated: 300 K (top row) and 750 K (bottom row). In the image on top, the liquid film exhibits a higher concentration of depositing particles in the region of impact, whereas the second image presents a liquid layer that extends much further downstream than in the 300 K case. Moreover, the distribution of liquid seems to be more balanced over the domain of the surface affected. This behaviour is in agreement with what has been described above: the greater number of droplets — but smaller in size — in the hotter scenario contributes to a more even distribution of the particles over the wall, whereas the colder scenario presents larger drops that are less influenced by the dispersion effect of the crossflow and, consequently, lead

to a larger concentration of liquid in the region of impact.

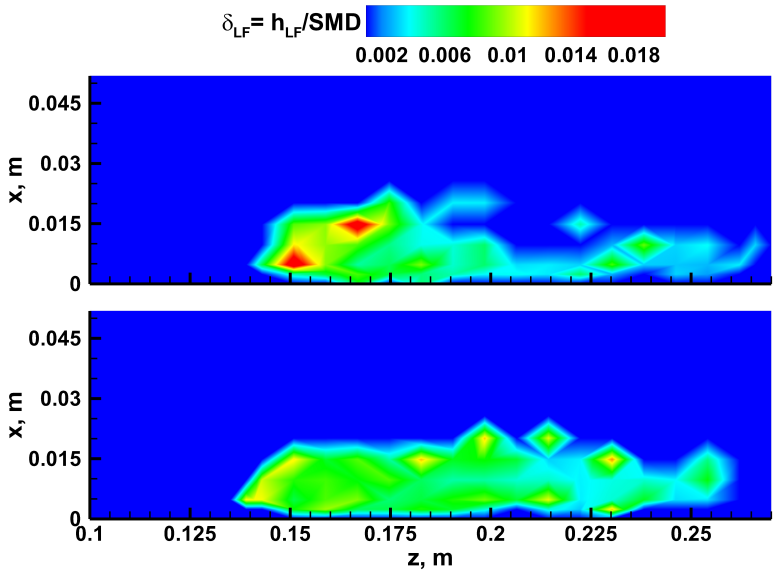

Figure 5.22: Distributions of the relative liquid film thickness at T=300 K (top row) and T=750 K (bottom row).

It is also worth highlighting that the maximum liquid thickness is seen to lie upstream of the region of impact. In fact, the impact zone lies approximately at z=0.155 m (i.e., z=1.15z_{in}). However, the thicker film thickness location in the 750 K case is found at z=0.145 m. This may be due to the complex interactions between the droplets and the existing crossflow, which are evaluated as follows with the aid of Fig. 5.23. Here, the total number of samples is reduced to 25 and the image illustrated is zoomed in to the area under analysis to obtain a clearer perspective and exhibit more details of the studied phenomena. The black spheres represent downward-moving drops, whereas the grey ones correspond to upward-moving droplets.

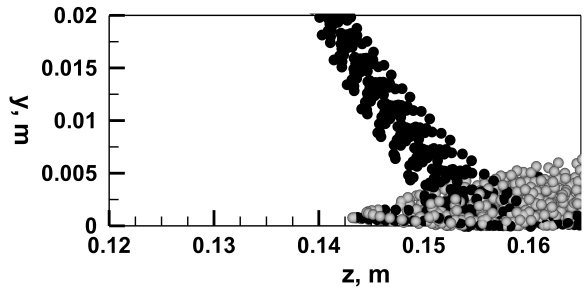

Figure 5.23: Detailed view of the droplet trajectories in the vertical plane of symmetry. Grey circles are upward-moving droplets, whereas black circles are downward-moving droplets.

The interactions between the droplets and the crossflow give rise to small vortices that contribute to the preferential concentration of particles. This situation may eventually induce the droplets to disperse along the direction against the air stream, ending up by depositing slightly upstream due to the dragging forces exerted by the crossflow. This behaviour is clearly perceived in the simulation performed and illustrated by Fig. 5.23. Even though the impact location of most of the incident particles is observed to be near z=0.155, the recirculation

pattern provokes some upstream movement which results in a higher concentration of liquid in that region.

5.6 Breakup

The breakup sub-model is employed once a critical Weber number is exceeded. The initiation and breakup times are calculated using the criteria derived from experiments. Depending on the stage of atomization, either deformation or breakup occurs and both are described by means of experimental correlations. In the first stage, the drag of the drop is linearly interpolated between the values of a spherical drop and a disk shape, whereas in the second stage, the fragments are generated using a root-normal distribution. The corresponding simulation procedure gives rise to the results presented in this section.

5.6.1 First stage of atomization

At low We, the crossflow velocity is not high enough to initiate the disintegration process, but the unequal static pressure distribution over the drop surface leads to a deformation stage that modifies the particle shape. In fact, the deformation of the drop is caused by the increased static pressures near the upstream and downstream stagnation points combined with the decreased static pressures near the drop periphery — due to increased flow velocities in this region — which results in a compressive force in the gas flow direction that tends to flatten the particle towards a spheroid-like shape (Chou and Faeth, 1998). The first stage of atomization is completed once the maximum distortion condition is reached. Figures 5.24(a) and 5.24(b) illustrate the evolution of the drop deformation ratio with the elapsed time for the air flow rates of 10 L/min (53.1 m/s) and 8 L/min (42.4 m/s). The measurements were taken from the experimental data carried out by Kim et al. (2010) and both diesel and bio-diesel fuels are evaluated. The results show that the maximum deformation ratio is higher with the higher crossflow velocity.

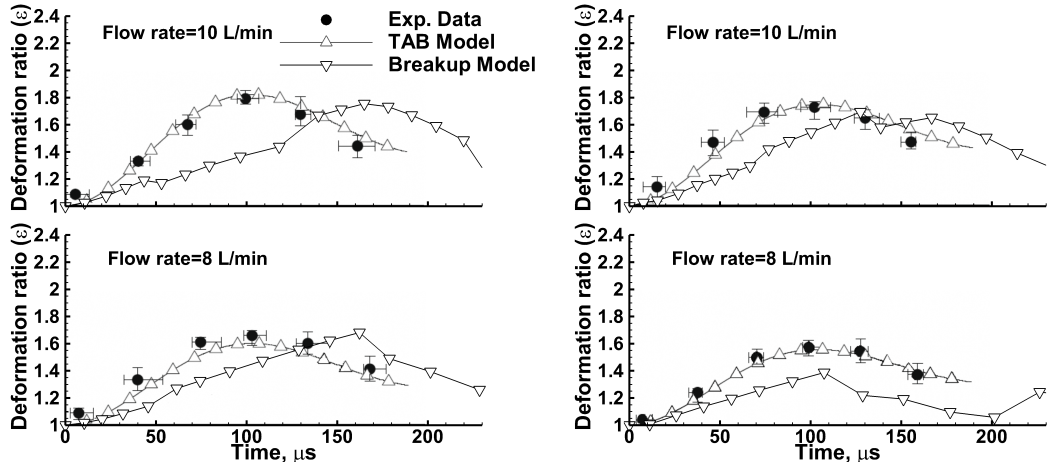

(a) Diesel fuel.

(b) Bio-diesel fuel.

Figure 5.24: Drop deformation ratio of diesel and bio-diesel fuels for flow rates of 10 L/min (top row) and 8 L/min (bottom row).

In the literature review, it was found that the natural deformation of the particle towards a disk-like shape correlated well with a linear function of time (Hsiang and Faeth, 1992). It be-

comes clear by analysing Fig. 5.24 that this conclusion is not applicable here since the pattern of the measured drop deformation ratio is a parabola curve. Even though the maximum value for the deformation ratio is approximately the same in computational and experimental results, the time at which they occur are different, with the computational results taking longer to reach that stage. Therefore, more comprehensive experimentally-deduced correlations should be devised for the deformation process in order to replicate more accurately the experimental data. Nevertheless, these discrepancies do not appear to have a major impact in the disintegration results, as discussed in the following section. On the other hand, by adjusting the model constants, the enhanced version of the TAB model formulated by Kim et al. (2010) is able to achieve a good agreement with experimental data.

5.6.2 Second stage of atomization

Unlike the current state of knowledge regarding the transition criteria between breakup modes in shock tube experiments (in which it is widely accepted the assumption of fixed values, with the thresholds between breakup modes being well defined in the literature), with respect to the continuous jet experiments, a criterion for the onset of disintegration is still to be attributed. Moreover, comprehensive information is still not accessible for this method which makes it difficult to replicate computationally the experimental data with accuracy. However, the mechanisms of deformation and breakup have been found to be similar to the shock tube concept (Guildenbecher et al., 2009; Bartz et al., 2011). Therefore, the model formulation presented in the previous section — which was intended to shock tube experiments — may be used as the approach to model the breakup mechanisms resulting from continuous jet operation. The key adjustment refers to the values adopted for the onset of disintegration, which, in the continuous jet case, is considerably greater than in the sudden shock loading concept.

In this respect, a transition criterion has been proposed in the present work by taking as reference the experimental results available. The objective was to attempt the best possible agreement with measurements. Therefore, to ensure that the breakup stage initiated around the same time in both approaches, the critical Weber number for the onset of disintegration was set at 35. This value has been set to match the experimental data considered. Furthermore, the criterion also respects the Weber number intervals reported in other papers available in the literature for which bag breakup was observed (Liu and Reitz, 1997; Lee and Reitz, 2000; Park et al., 2006). On the other hand, as expected, it is much higher than the critical threshold in shock tube experiments (which is around 12). It is also worth mentioning that secondary atomization only occurs once both critical We and the assumed breakup initiation time are exceeded. In this work, the maximum distortion is reached at $t_{bin} = 1.6t^*$.

Figures 5.25 and 5.26 illustrate the bag breakup formation observed by Kim et al. (2010) (background image) as well as the predicted trajectories obtained in the simulations carried out in the present work (black circles). Both simulations have been obtained with a critical We of 35, as discussed above. As far as the diesel fuel case is concerned (Fig. 5.25), very acceptable results are observed here. The time scales involved, as well as the trajectories of the major secondary droplets predicted by the model are in good agreement with the experimental results. On the other hand, it is evident — at least in the domain examined — that besides the core drops replicated, there is also a set of very small droplets that are not expected by the model implemented, which — influenced by the presence of the crossflow — are rapidly found in downstream locations. Furthermore, at the moment the breakup mechanism occurs, there is a clearance of several millimetres of the fragments which has not been yet effectively

addressed by researchers. These situations are not provided for by the actual mathematical formulation, which reveals the prevailing lack of knowledge regarding the characteristics of the breakup fragments.

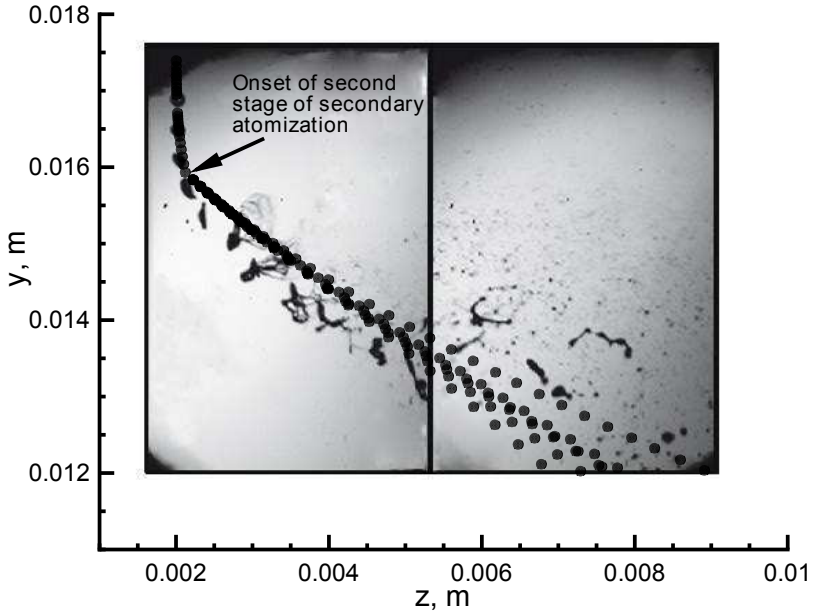

Figure 5.25: Macroscopic comparison of the breakup process of a diesel drop (We=68). Background image adapted from Kim et al. (2010).

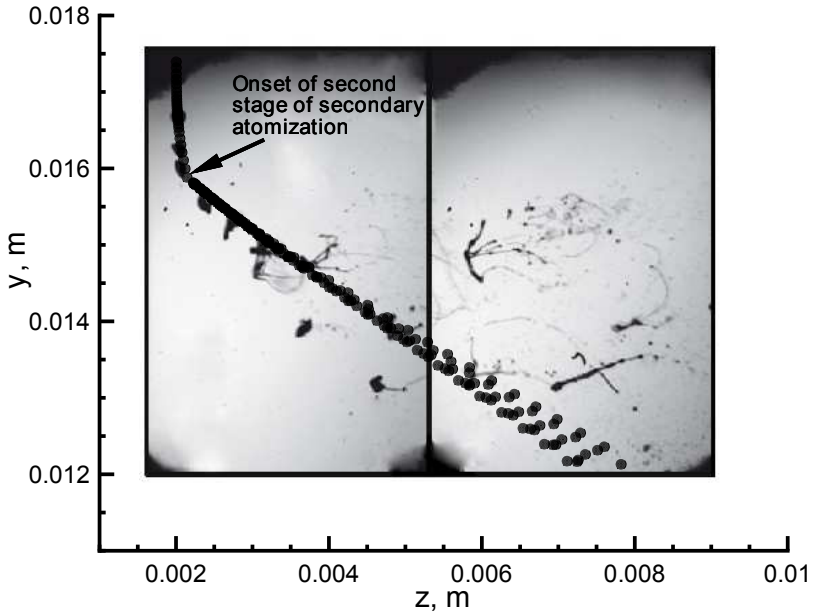

Figure 5.26: Macroscopic comparison of the breakup process of a bio-diesel drop (We=62.4). Background image adapted from Kim et al. (2010).

With respect to the bio-diesel fuel case (Fig. 5.26), two distinct paths are clearly perceived from the background image. It is possible to identify a particle with a trajectory more directed to the surface, which corresponds to a core fragment that has not burst into smaller droplets. This core particle possesses greater momentum and, so, is less prone to be influenced by the

crossflow. The remaining droplets follow a “standard” path, and are well replicated by the computational results. Even though the first stage of atomization begins approximately at the same time, the disintegration process (after bag formation) occurs later than in Fig. 5.25. Despite this fact, the time scales involved are still in good agreement with what has been predicted. However, as in the previous case, the smaller fragments (which appear to be the result of ring breakup) that are noticed in downstream locations have not been anticipated by the simulations. These evidences suggest that a bimodal size distribution would fit more adequately the outcome of bag breakup (as also reported by Opfer et al. (2012)).

The previous images illustrate the result of the breakup process of a single drop when subjected to an 84.9 m/s crossflow. Some discrepancies can be identified from the characteristics exhibited by the two fuels. This distinct behaviour is depicted in Fig. 5.27 which shows the shape of an array of 1000 drops of both diesel and bio-diesel fuels. This macroscopic qualitative result gives some insight about the effect of the liquid properties on the outcome of the secondary atomization process. One can notice that the fuel with lower viscosity (Fig. 5.27(a)) gives rise to a broader spray and a bigger coverage area (the relative span for diesel and bio-diesel sprays at z=8 mm are 0.50 and 0.62, respectively). Furthermore, the droplets are more affected by the presence of the crossflow, since the profile is more directed towards the outlet plane (in contrast with the bio-diesel spray, which is pointing towards the impingement surface). This observation suggests that the sizes of the diesel breakup fragments are smaller than in the bio-diesel case.

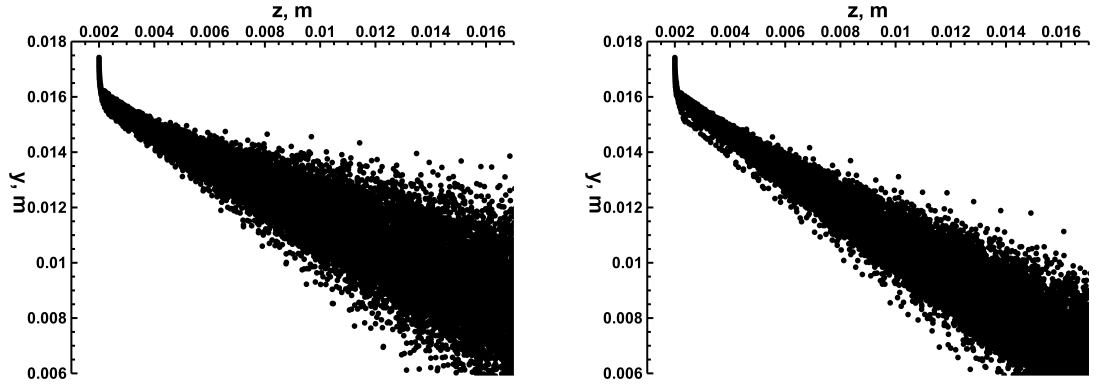

(a) Diesel fuel.

(b) Bio-diesel fuel.

Figure 5.27: General behaviour of (a) diesel and (b) bio-diesel sprays (constituted by 1000 drops).

The latter statement is analysed in Fig. 5.28, which compares the probability density function (PDF) of both fuels. Moreover, the diameter of the droplets are also evaluated at two distinct positions along the longitudinal axis (z=5 mm and z=8 mm), as illustrated in Fig 5.28(a). Two main conclusions can be drawn on the back of Fig. 5.28(b): 1) the diameter of the diesel fragments resulting from breakup is in general smaller than that of bio-diesel fuel droplets; 2) at downstream locations, the size distribution shifts slightly to the left which means a higher occurrence probability of smaller droplets. This conclusion is more evident with diesel fuel because the lower surface tension and viscosity of this liquid tend to offer less resistance to the variation of the particle shape.

Figure 5.29 depicts the distribution of the SMD at z=10 mm for an air flow rate of 16 L/min. Both experimental data of Kim et al. (2010) and the results of numerical predictions are

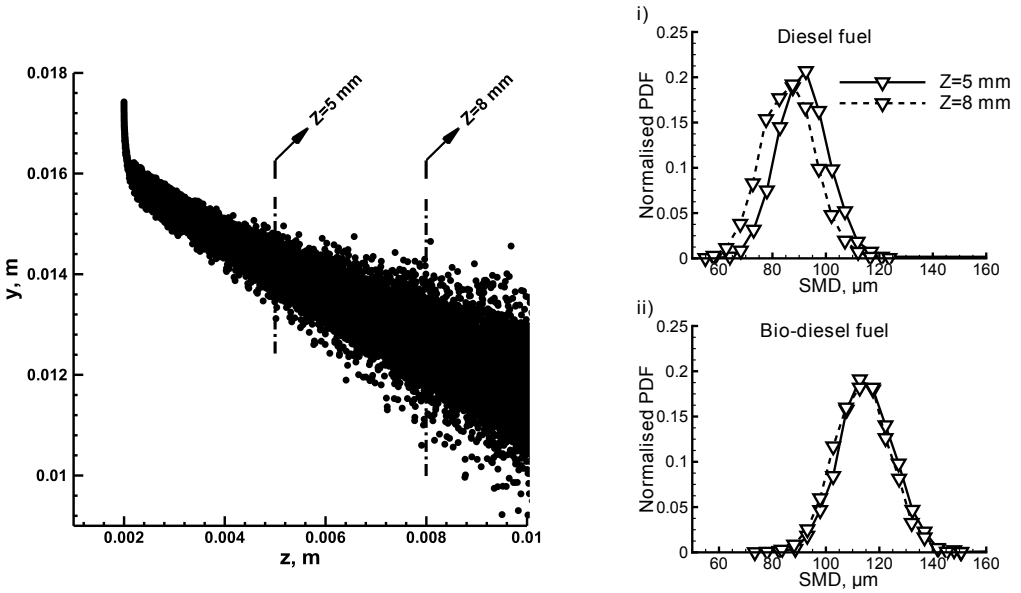

(a) Locations evaluated. (b) PDF of droplet sizes.

Figure 5.28: Diesel and bio-diesel drop size distributions for an air flow rate of 16 L/min.

presented, which allows one to evaluate the accuracy of the model in a quantitative perspective. As expected, the use of bio-diesel fuel leads to larger fragment sizes. This trend is accompanied by the computational results. However, the droplets are predicted in a more restricted area (y=0.014 m to y=0.010 m). Within this interval, Fig. 5.29(a) shows a good agreement between computational and experimental results. In the case of the higher viscosity and surface tension fuel (Fig. 5.29(b)), while in the experiments a approximately constant value of 140 μm for the SMD can be found from y=14 mm, the predicted results presented a similar trend as in Fig. 5.29(a): the droplet size increases as the distance to the injector increases.

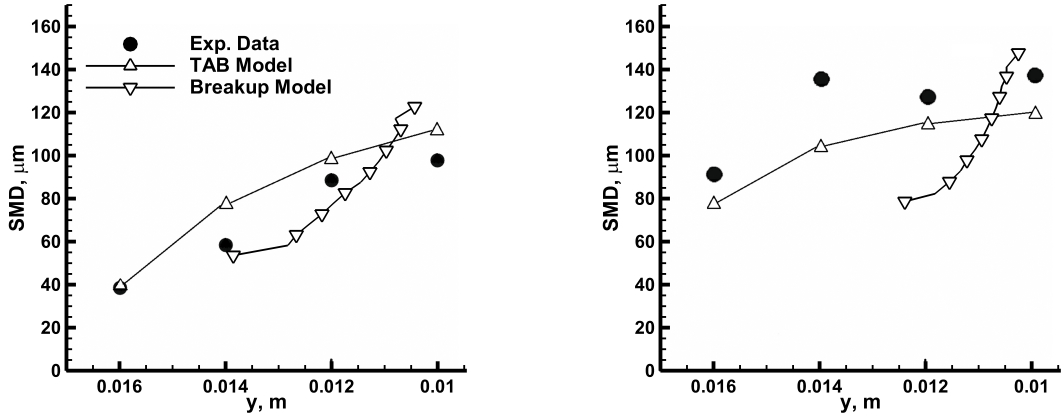

(a) Diesel fuel. (b) Bio-diesel fuel.

Figure 5.29: SMD distributions of diesel and bio-diesel along the axial axis for an air flow rate of 16 L/min.

Such a discrepancy in the behaviour of the referred plots evidences that the correlations adopted in the mathematical formulation may be disregarding the influence of certain parameters on the breakup mechanisms. In fact, it is worth highlighting that the trend of the fragment

size between the two fuels are distinct, which suggests an important effect of the fuel properties on the post-breakup fragment characteristics.

As for the computational results reported by Kim et al. (2010), the general behaviour observed in their predictions is similar to the one noticed in the measurements. In fact, in general, they provide an overall better replication of the physical phenomena detected experimentally than the predictions obtained with the simulation procedure described here. However, it is important to mention that the enhanced TAB model has been fine-tuned to provide the best approximation possible to the experimental data considered. On the other hand, the breakup model presented in this study makes use of correlations available in a number of publications in the literature to construct an integrated simulation procedure which may be applied to a wide range of breakup conditions. The accuracy of this method is bounded by the precision of the correlations adopted. Figure 5.29 suggests that the equations used in the formulation of the breakup model described in this study may be disregarding the influence of certain parameters on the phenomena analysed. This fact should alert researchers and incite them to come up with new correlations for the different aspects of the atomization process.

Chapter 6

Conclusions

This chapter presents the final conclusions of the research devoted to the study of spray-wall interaction phenomena and the enhancement of the capacity of the in-house developed CFD code to provide adequate prediction results. Even though punctual computational models have been proposed over the years to predict the outcome of spray-wall impact problems, a level of knowledge that allows one to identify the more suitable mathematical formulation which should be adopted to deliver the most accurate simulation possible still has to be reached. Providing a flexible dispersion model — that could be adjusted by employing more suitable empirical correlations fitting a particular set of experimental data — with minimal time constraints would be a great asset for both industry and academia. Such objective has motivated the present work which started with an evaluation phase of the simulation procedure to identify the aspects that could be improved. This stage included the near-wall mesh refinement study, as well as the dissipative energy loss analysis, which is described below.

The first aspect of the simulation procedure investigated was the energy dissipation term found in the splash event. Several equations proposed in different publications were introduced in the simulation procedure and the predictions were compared against experimental data. The results show that the dissipative energy loss considered in the energy balance between incident and secondary droplets has an important influence on the outcome of the impact mechanisms. The comparison of the four expressions presented here evidenced that the original relationship assumed in the base model is, by now, the best approximation available in the literature of the energy dissipated during the splash event. Furthermore, the discrepancy between the results obtained with the latter equation and the other ones confirmed the non-negligible effect of this parameter on the behaviour of secondary droplets. The over-estimation of the velocity profile along the entire drop size spectrum suggested that the dissipative term was being under-estimated in these cases.

Concerning the results under the analysis of the near-wall droplet tracking method, the new approach proposed here provides an alternative way to improve the accuracy in the dispersed phase, in the region close to the impinging surface. Such an alternative can be considered instead of a computationally-expensive general mesh refinement. Neither solution is expected to alter significantly the results obtained in the continuous phase since extensive mesh independence studies have been performed for this model. However, the real implications of this grid refinement in the dispersed phase had never been adequately evaluated, particularly in the near wall region, which is where the boundary layer may have an important repercussion on the trajectory of the drops before impact. The analysis of the results evidenced that the refined treatment of the boundary layer did not provide noticeable improvements that would justify the additional computational costs. Such a conclusion also suggested that the mathematical formulation was free from numerical influences that could propagate during the simulation procedure. Nonetheless, bearing in mind the importance that the shearing air flow has on drop dispersion (Arcoumanis et al., 1997), this approach might be more useful in other specific applications.

Behind much of the research effort invested in experimental studies lies also the expec-

tation of finding a mathematical expression — constituted by a (limited) number of variables — that is capable of replicating a collection of measurement data. Such a discovery becomes even more substantial if the agreement between the derived equation and the observed data extends to other boundary conditions and configurations. However, from the literature review carried out within the scope of this work, it was possible to realize that although some experimentally-deduced correlations were proposed for similar ranges of impact conditions, they were often a function of distinct parameters or revealed that contrasting weights were attributed to identical parcels.

Under this context computational models emerge which may play a critical role at this stage in determining which is the combination of equations that provides the most accurate results. Within this framework, and from the results presented in this document, it was possible to conclude that the integration of the liquid film extension to the base model improved the agreement between computational and experimental results. Furthermore, since the new liquid/liquid interface was being considered at this stage, the transition criteria proposed by Motzkus et al. (2011) was employed to determine the onset of splash regime under wet condition in order to account for the influence of the liquid film thickness in the mechanisms underlying the impact events.

On the other hand, the purpose of modelling spray impingement phenomena can be quite varied. In some cases, only the quantity of liquid deposited onto the surface is of interest (e.g. spray painting), whereas in other cases, the heat transfer mechanisms (e.g. cooling systems) or the disintegration of incident drops before impact (e.g. gas turbine injection) are the mechanisms that are intended to be captured.

Therefore, the complexity of the models may also vary considerably depending on the application for which it is being developed. The ideal scenario — which is also the most demanding — would be a CFD code capable of simulating with accuracy a case in which all those elements would be considered. This goal has also driven the course of the work carried out during this doctoral project. Even though there are still numerous aspects of the simulation procedure that have been simplified, the final version of the model now includes a mathematical basis that allows one to infer that it is more capable of simulating spray impingement phenomena in a wider range of impact conditions, which includes hot environments and with high velocity crossflow.

In fact, the evaporation sub-model was designed to extend the range of applicability of the spray impingement model to conditions in which heat transfer could not be disregarded. Two distinct initial temperatures were evaluated to assess the influence of this parameter on the outcome of spray impingement. The following conclusions were drawn: as the temperature increased, (1) the number of incident drops expected to settle on the surface increased, whereas the fraction of mass of depositing droplets decreased; (2) the droplets were expected to deposit onto the surface more uniformly as the smaller (partially-evaporated) particles were more prone to be influenced by the dispersion effect of the crossflow, and, consequently, they distributed more evenly over the surface, rather than in a reduced region as it happened in the colder environment (which presented a greater concentration of liquid around the impingement location).

The breakup sub-model was constructed with recourse to correlations available in the current literature. Therefore, specific mathematical equations were assigned to every aspect of the secondary atomization process. This approach allows one to judge: 1) how do the correlations reported in the literature behave when they are integrated into a computational simulation, and 2) are the correlations comprehensive and (at the same time) accurate enough to be used by modellers in computational simulations. To evaluate the performance of the model,

the prediction results were compared against experimental data as well as a fine-tuned version of the TAB model which has been proposed by Kim et al. (2010). On the basis of the results obtained, it was possible to conclude that the computational results offered a reasonable approximation of the main outcome expected. The transition criterion proposed for the onset of disintegration (35) was proven adequate in the conditions tested and the general behaviour of the fragments originated from the breakup process presented a general acceptable agreement with the measurements.

Nevertheless, further research should be considered, particularly regarding experiments considering the continuous jet concept. There is still a lack of detailed fundamental studies available — with well-defined operating conditions and relevant criteria derived from measurements — which prevents the development of more accurate mathematical formulations.

Bibliography

Abramzon, B. and Sirignano, W. A. (1989). Droplet Vaporization Model for Spray Combustion Calculations. *International Journal of Heat and Mass Transfer*, 32(9):1605–1618. 36, 73, 74

Adrian, R., Durão, D., Durst, F., Heitor, M., Maeda, M., and Whitelaw, J. (1997). *Developments in Laser Techniques and Fluid Mechanics: Selected Papers from the 8th International Symposium, Lisbon, Portugal 8-11 July, 1996*. Springer-Verlag, Heidelberg, Berlin. 24

Aggarwal, S. K. (1998). A Review of Spray Ignition Phenomena: Present Status and Future Research. *Progress in Energy and Combustion Science*, 24(6):565–600. 34

Alghoul, S. K., Eastwick, C. N., and Hann, D. B. (2010). Experimental investigation of a Single Droplet Interaction with Shear Driven Film. In *ILASS - Europe 2010, 23rd Annual Conference on Liquid Atomization and Spray Systems*, pages 1–10, Brno. 26, 99

Alghoul, S. K., Eastwick, C. N., and Hann, D. B. (2011). Normal Droplet Impact on Horizontal Moving Films: an Investigation of Impact Behaviour and Regimes. *Experiments in Fluids*, 50(5):1305–1316. 26

Andreassi, L., Ubertini, S., and Allocca, L. (2007). Experimental and Numerical Analysis of High Pressure Diesel Spray-Wall Interaction. *International Journal of Multiphase Flow*, 33(7):742–765. 23

Antonini, C., Amirfazli, A., and Marengo, M. (2012). Drop Impact and Wettability: From Hydrophilic to Superhydrophobic Surfaces. *Physics of Fluids*, 24(10):102104–13. 11

Arcoumanis, C. and Chang, J. C. (1993). Heat Transfer Between a Heated Plate and an Impinging Transient Diesel Spray. *Experiments in Fluids*, 16(2):105–119. 40, 73

Arcoumanis, C. and Cutter, P. (1995). Flow and Heat Transfer Characteristics of Impinging Diesel Sprays Under Cross-Flow Conditions. In *SAE Technical Paper 950448*. 87

Arcoumanis, C., Cutter, P., and Whitelaw, D. S. (1998). Heat Transfer Processes in Diesel Engines. *Chemical Engineering Research and Design*, 76(2):124–132. 40

Arcoumanis, C., Whitelaw, D. S., and Whitelaw, J. H. (1997). Gasoline Injection Against Surfaces and Films. *Atomization and Sprays*, 7(4):437–456. 2, 26, 59, 88, 93, 99, 113

Arienti, M., Wang, L., Corn, M., Li, X., Soteriou, M. C., Shedd, T. A., and Herrmann, M. (2011). Modeling Wall Film Formation and Breakup Using an Integrated Interface-Tracking/Discrete-Phase Approach. *Journal of Engineering for Gas Turbines and Power*, 133(3):1–7. 2, 26

Babinsky, E. and Sojka, P. E. (2002). Modeling Drop Size Distributions. *Progress in Energy and Combustion Science*, 28(4):303–329. 19

Bai, C. X. and Gosman, A. D. (1995). Development of Methodology for Spray Impingement Simulation. In *SAE Technical Paper 950283*, pages 550–568. 7, 8, 12, 13, 24, 28, 29, 36, 37, 38, 65, 66, 67, 91

Bai, C. X., Rusche, H., and Gosman, A. D. (2002). Modeling of Gasoline Spray Impingement. *Atomization and Sprays*, 12(1-3):1–27. 4, 19, 20, 24, 30, 63, 67, 69, 73, 83, 91, 92, 93

Banerjee, R. (2013). Numerical Investigation of Evaporation of a Single Ethanol/Iso-Octane Droplet. *Fuel*, 107:724–739. 37

Bang, B. H., Yoon, S. S., Kim, H. Y., Heister, S. D., Park, H., and James, S. C. (2011). Assessment of Gas and Liquid Velocities Induced by an Impacting Liquid Drop. *International Journal of Multiphase Flow*, 37(1):55–66. 23

Barata, J. (1989). *Estudo Numérico e Experimental de Jactos Incidentes Sobre Placas Planas Através de um Escoamento Cruzado*. PhD thesis, Intituto Superior Técnico. 55

Barata, J. (2005). On the Modelling of Droplet Transport, Dispersion and Evaporation in Turbulent Flows. *Silniki Spanilowe - Combustion Engines*, 3(122):42–55. 74

Barata, J. (2008). Modelling of Biofuel Droplets Dispersion and Evaporation. *Renewable Energy*, 33(4):769–779. 36

Bartz, F., Guildenbecher, D. R., Schmehl, R., Koch, R., Bauer, H.-J., and Sojka, P. E. (2011). Model Comparison for Single Droplet Fragmentation Under Varying Accelerations. In *ILASS - Europe 2011, 24th European Conference on Liquid Atomization and Spray Systems*, pages 1–11, Estoril. 77, 107

Baumeister, K. J. and Simon, F. F. (1973). Leidenfrost Temperature - Its Correlation for Liquid Metals, Cryogens, Hydrocarbons, and Water. *Journal of Heat Transfer*, 95(2):8. 36

Bennett, T. and Poulikakos, D. (1993). Splat-Quench Solidification: Estimating the Maximum Spreading of a Droplet Impacting a Solid Surface. *Journal of Material Science*, 28(4):963–970. 16

Bernardin, J. D. and Mudawar, I. (1999). The Leidenfrost Point: Experimental Study and Assessment of Existing Models. *Journal of Heat Transfer*, 121(4):894–903. 36

Bernardin, J. D., Stebbins, C. J., and Mudawar, I. (1996). Effects of Surface Roughness on Water Droplet Impact History and Heat Transfer Regimes. *International Journal of Heat and Mass Transfer*, 40(1):73–88. 40

Bertola, V. (2004). Drop Impact on a Hot Surface: Effect of a Polymer Additive. *Experiments in Fluids*, 37(5):653–664. 36

Bhattacharya, P., Ghosal, S., and Som, S. K. (1996). Evaporation of Multicomponent Liquid Fuel Droplets. *International Journal of Energy Research*, 20(5):385–398. 37

Bird, J. C., Tsai, S. S. H., and Stone, H. A. (2009). Inclined to Splash: Triggering and Inhibiting a Splash With Tangential Velocity. *New Journal of Physics*, 11(6):1–10. 23

Brereton, G. J. (2013). A Discrete Multicomponent Temperature-Dependent Model for the Evaporation of Spherical Droplets. *International Journal of Heat and Mass Transfer*, 60:512–522. 37

Brodkey, R. S. (1969). *The Phenomena of Fluid Motions*. Addison-Wesley Publishing Co., Reading, Massachusetts. 46

Bussmann, M., Chandra, S., and Mostaghimi, J. (2000). Modeling the Splash of a Droplet Impacting a Solid Surface. *Physics of Fluids*, 12(12):1–12. 8

Castanet, G., Labergue, A., and Lemoine, F. (2011). Internal Temperature Distributions of Interacting and Vaporizing Droplets. *International Journal of Thermal Sciences*, 50(7):1181–1190. 37

Castanet, G., Liénart, T., and Lemoine, F. (2009). Dynamics and Temperature of Droplets Impacting Onto a Heated Wall. *International Journal of Heat and Mass Transfer*, 52(3-4):670–679. 39

Chandra, S. and Avedisian, C. T. (1991). On the Collision of a Droplet With a Solid Surface. *Proceedings: Mathematical and Physical Sciences*, 432(1884):13–41. 14, 15, 16, 17, 37, 91, 92

Chen, X. Q. and Pereira, J. C. F. (1995). Prediction of Evaporating Spray in Anisotropically Turbulent Gas Flow. *Numerical Heat Transfer*, 27(2):143–162. 55

Chen, X. Q. and Pereira, J. C. F. (1996). Computation of Turbulent Evaporating Sprays With Well-Specified Measurements: A Sensitivity Study on Droplet Properties. *International Journal of Heat and Mass Transfer*, 39(3):441–454. 36, 73

Chou, W.-H. and Faeth, G. M. (1998). Temporal Properties of Secondary Drop Breakup in the Bag Breakup Regime. *International Journal of Multiphase Flow*, 24(6):889–912. 41, 43, 44, 77, 80, 106

Chou, W.-H., Hsiang, L.-P., and Faeth, G. M. (1997). Temporal Properties of Drop Breakup in the Shear Breakup Regime. *International Journal of Multiphase Flow*, 23(4):651–669. 48, 77

Cossali, G. E., Coghe, A., and Marengo, M. (1997). The Impact of a Single Drop on a Wetted Solid Surface. *Experiments in Fluids*, 22(6):463–472. 2, 26, 27, 28, 29, 72, 73

Cossali, G. E., Marengo, M., Coghe, A., and Zhdanov, S. (2004a). The Role of Time in Single Drop Splash on Thin Film. *Experiments in Fluids*, 36(6):888–900. 33

Cossali, G. E., Marengo, M., and Santini, M. (2004b). Impact of a Single and Multiple Drop Array on a Liquid Film. In *ILASS - Europe 2004, 19th Annual Conference on Liquid Atomization and Spray Systems*, pages 493–500, Nottingham. 26

Cossali, G. E., Marengo, M., and Santini, M. (2005). Secondary Atomisation Produced by Single Drop Vertical Impacts Onto Heated Surfaces. *Experimental Thermal and Fluid Science*, 29(8):937–946. 39, 40

Crowe, C. T., Schwarzkopf, J. D., Sommerfeld, M., and Tsuji, Y. (2012). *Multiphase Flows with Droplets and Particles*. CRC Press, Boca Raton, FL, second edition. 57

Deegan, R. D., Brunet, P., and Eggers, J. (2008). Complexities of Splashing. *Nonlinearity*, 21(1):C1–C11. 23

Dhir, V. K. (1991). Nucleate and Transition Boiling Heat Transfer Under Pool and External Flow Conditions. *International Journal of Heat and Fluid Flow*, 12(4):290–314. 35

Driscoll, M. M., Stevens, C. S., and Nagel, S. R. (2010). Thin Film Formation During Splashing of Viscous Liquids. *Physical Review E*, 82(3):1–7. 24

Eggers, J., Fontelos, M. A., Josserand, C., and Zaleski, S. (2010). Drop Dynamics After Impact on a Solid Wall: Theory and Simulations. *Physics of Fluids*, 22(6):1–13. 17

Emmerson, G. S. (1975). The Effect of Pressure and Surface Material on the Leidenfrost Point of Discrete Drops of Water. *International Journal of Heat and Mass Transfer*, 18(3):381–386. 36

Engel, O. G. (1955). Waterdrop Collisions With Solid Surfaces. *Journal of Research of the National Bureau of Standards*, 54(5):281–298. 23

Faeth, G. M. (1977). Current Status of Droplet and Liquid Combustion. *Progress in Energy and Combustion Science*, 3(4):191–224. 36

Faeth, G. M. (1987). Mixing, Transport and Combustion in Sprays. *Progress in Energy and Combustion Science*, 13(4):293–345. 55, 56, 64

Faeth, G. M., Hsiang, L.-P., and Wu, P.-K. (1995). Structure and Breakup Properties of Sprays. *International Journal of Multiphase Flow*, 21:99–127. 40

Faghri, A. and Zhang, Y. (2006). *Transport Phenomena in Multiphase Systems*. Elsevier. 35

Gavaises, M., Theodorakakos, A., and Bergeles, G. (1996). Modeling Wall Impaction of Diesel Sprays. *International Journal of Heat and Fluid Flow*, 17(2):130–138. 13

Gelfand, B. E. (1996). Droplet Breakup Phenomena in Flows with Velocity Lag. *Progress in Energy and Combustion Science*, 22(96):201–265. 46

Gel'fand, B. E., Gubin, S. A., Kogarko, S. M., and Komar, S. P. (1973). Singularities of the Breakup of Viscous Liquid Droplets in Shock Waves. *Journal of Engineering Physics*, 25(3):1140–1142. 46

Godsave, G. A. E. (1953). Studies of the Combustion of Drops in a Fuel Spray - the Burning of Single Drops of Fuel. *Symposium (International) on Combustion*, 4(1):818–830. 36, 73

Gold, M., Arcoumanis, C., Whitelaw, J., Gaade, J., and Wallace, S. (2000). Mixture Preparation Strategies in an Optical Four-Valve Port-Injected Gasoline Engine. *International Journal of Engine Research*, 1(1):41–56. 25

Gorokhovski, M. and Herrmann, M. (2008). Modeling Primary Atomization. *Annual Review of Fluid Mechanics*, 40(1):343–366. 40

Gottfried, B. S., Lee, C. J., and Bell, K. J. (1966). The Leidenfrost Phenomenon: Film Boiling of Liquid Droplets on a Flat Plate. *International Journal of Heat and Mass Transfer*, 9(11):1167–1188. 36

Grant, G. and Tabakoff, W. (1975). Erosion Prediction in Turbomachinery Resulting from Environmental Solid Particles. *Journal of Aircraft*, 12(5):471–478. 66

Grover, R. O. and Assanis, D. N. (2001). A Spray Wall Impingement Model Based Upon Conservation Principles. In *Proceedings of the Fifth International Symposium on Diagnostics and modeling of combustion in internal combustion engines (COMODIA 2001)*, pages 1–10, Nagoya. 13

Guildenbecher, D. R., López-Rivera, C., and Sojka, P. E. (2009). Secondary atomization. *Experiments in Fluids*, 46(3):371–402. xv, 40, 41, 79, 107

Guildenbecher, D. R., López-Rivera, C., and Sojka, P. E. (2011). Droplet Deformation and Breakup. In Ashgriz, N., editor, *Handbook of Atomization and Sprays: Theory and Applications*, chapter 6, pages 145–156. Springer US. 44, 49, 64

Habchi, C. (2010). New Correlations for Leidenfrost and Nukiyama Temperatures with Gas Pressure - Application to Liquid Film Boiling Simulation. In *ILASS - Europe 2010, 23rd Annual Conference on Liquid Atomization and Spray Systems*, pages 1–7, Brno. 104

Habchi, C., Foucart, H., and Baritaud, T. (1999). Influence of the Wall Temperature on the Mixture Preparation in Di Gasoline Engines. *Oil & Gas Science and Technology*, 54(2):211–222. 103

Helenbrook, B. T. and Edwards, C. F. (2002). Quasi-Steady Deformation and Drag of Uncontaminated Liquid Drops. *International Journal of Multiphase Flow*, 28(10):1631–1657. 77

Hinze, J. (1955). Fundamentals of the Hydrodynamic Mechanism of Splitting in Dispersion Processes. *AIChE Journal*, 1(3):289–295. 45, 46, 77

Hobbs, P. V. and Osheroff, T. (1967). Splashing of Drops on Shallow Liquids. *Science*, 158(3805):1184–1186. 26, 27, 99

Hsiang, L.-P. and Faeth, G. M. (1992). Near-Limit Drop Deformation and Secondary Breakup. *International Journal of Multiphase Flow*, 18(5):635–652. 41, 42, 46, 47, 48, 49, 77, 79, 80, 106

Hsiang, L.-P. and Faeth, G. M. (1993). Drop Properties After Secondary Breakup. *International Journal of Multiphase Flow*, 19(5):721–735. 47, 48, 49, 77, 80

Hsiang, L.-P. and Faeth, G. M. (1995). Drop Deformation and Breakup due to Shock Wave and Steady Disturbances. *International Journal of Multiphase Flow*, 21(4):545–560. 46, 64

Huang, Q. and Zhang, H. (2008). A Study of Different Fluid Droplets Impacting on a Liquid Film. *Petroleum Science*, 5(1):62–66. 28, 29

Hwang, I. H., Lee, D. J., Yoon, S. S., Kim, H. Y., and James, S. C. (2010). Splashing Characteristics of Monodisperse Sprays with Significant Viscosity Differences Impacting a Flat Surface. *Drying Technology*, 28(12):1321–1330. 10

Jafarmadar, S., Khalilarya, S., Shafee, S., and Barzegar, R. (2009). Modeling the Effect of Spray/Wall Impingement on Combustion Process and Emission of DI Diesel Engine. *Thermal Science*, 13(3):23–33. 2, 26

Jafarmadar, S., Shafee, S., and Barzegar, R. (2010). Numerical Investigation of the Effect of Fuel Injection Mode On Spray/Wall Interaction and Emission Formation in a Direct Injection Diesel Engine at Full Load State. *Thermal Science*, 14(4):1039–1049. 8, 26

Jenny, P., Roekaerts, D., and Beishuizen, N. (2012). Modeling of Turbulent Dilute Spray Combustion. *Progress in Energy and Combustion Science*, 38(6):846–887. 46, 64

Kalantari, D. and Tropea, C. (2007). Spray Impact Onto Flat and Rigid Walls: Empirical Characterization and Modelling. *International Journal of Multiphase Flow*, 33(5):525–544. 30, 33, 71

Kalantari, D. and Tropea, C. (2010). Influence of Surface Roughness in Spray/Wall Interaction Phenomena. In *ILASS - Europe 2010, 23rd Annual Conference on Liquid Atomization and Spray Systems*, pages 1–6, Brno. 23

Kang, B. S. and Lee, D. H. (2000). On the Dynamic Behavior of a Liquid Droplet Impacting Upon an Inclined Heated Surface. *Experiments in*, 29(4):380–387. 36, 40

Karl, A., Anders, K., Rieber, M., and Frohn, A. (1996). Deformation of Liquid Droplets During Collisions With Hot Walls: Experimental and Numerical Results. *Particle & Particle Systems Characterization*, 13(3):186–191. 36

Karl, A. and Frohn, A. (2000). Experimental Investigation of Interaction Processes Between Droplets and Hot Walls. *Physics of Fluids*, 12(4):785–796. 40

Kim, S., Hwang, J. W., and Lee, C. S. (2010). Experiments and Modeling on Droplet Motion and Atomization of Diesel and Bio-Diesel Fuels in a Cross-Flowed Air Stream. *International Journal of Heat and Fluid Flow*, 31(4):667–679. xvi, 40, 47, 77, 79, 80, 81, 82, 106, 107, 108, 109, 111, 115

Ko, K. and Arai, M. (2002a). Diesel Spray Impinging on a Flat Wall, Part I: Characteristics of Adhered Fuel Film in an Impingement Diesel Spray. *Atomization and Sprays*, 12(5-6):737–751. 25

Ko, K. and Arai, M. (2002b). Diesel Spray Impinging on a Flat Wall, Part II: Volume and Average Air-Fuel Ratio of an Impingement Diesel Spray. *Atomization and Sprays*, 12(5-6):753–768. 25

Krzeczkowski, S. A. (1980). Measurement of Liquid Droplet Disintegration Mechanisms. *International Journal of Multiphase Flow*, 6(1958):227–239. 45, 46, 77

Launder, B. E. and Spalding, D. B. (1974). The Numerical Computation of Turbulent Flows. *Computer Methods in Applied Mechanics and Engineering*, 3(2):269–289. xvii, 52, 53, 62

Law, C. K. (1982). Recent Advances in Droplet Vaporization and Combustion. *Progress in Energy and Combustion Science*, 8(3):171–201. 34, 36, 73

Lee, C. H. and Reitz, R. D. (2000). An Experimental Study of the Effect of Gas Density on the Distortion and Breakup Mechanism of Drops in High Speed Gas Stream. *International Journal of Multiphase Flow*, 26(2):229–244. 44, 47, 107

Lee, M. M. and Hanratty, T. J. (1988). The Inhibition of Droplet Deposition by the Presence of a Liquid Wall Film. *International Journal of Multiphase Flow*, 14(2):129–140. 67

Lee, S. H. and Ryou, H. S. (2000). Development of a New Spray/Wall Interaction Model. *International Journal of Multiphase Flow*, 26(7):1209–1234. 13, 19, 20

Lee, S. Y. and Ryu, S. U. (2006). Recent Progress of Spray-Wall Interaction Research. *Journal of Mechanical Science and Technology*, 20(8):1101–1117. 37, 38

Lefebvre, A. H. (1989). *Atomization and Sprays*. Taylor & Francis, New York. 36

Leonard, B. P. (1979). A Stable and Accurate Convective Modeling Procedure Based on Quadratic Upstream Interpolation. *Computer Methods in Applied Mechanics and Engineering*, 19(1):59–98. 53

Levin, Z. and Hobbs, P. V. (1971). Splashing of Water Drops on Solid and Wetted Surfaces: Hydrodynamics and Charge Separation. *Philosophical Transactions of the Royal Society of London A: Mathematical, Physical and Engineering Sciences*, 269(1200):555–585. 10, 18, 23

Liu, J., Vu, H., Yoon, S. S., Jepsen, R. A., and Aguilar, G. (2010). Splashing Phenomena During Liquid Droplet Impact. *Atomization and Sprays*, 20(4):297–310. 13

Liu, Y., Yeom, J. K., and Chung, S. S. (2012). An Experimental Study on the Effects of Impingement-Walls on the Spray and Combustion Characteristics of SIDI CNG. *Journal of Mechanical Science and Technology*, 26(8):2239–2246. 11

Liu, Z. and Reitz, R. D. (1997). An Analysis of the Distortion and Breakup Mechianisms of High Speed Liquid Drops. *International Journal of Multiphase Flow*, 23(4):631–650. 42, 47, 77, 107

Long, T., Li, M., Chen, Y., and Zhu, X. (2014). Study on Evaporation Characteristics of Bio-oil and its Compound Models. *Bioresources*, 9(2011):4242–4252. 37

Madejski, J. (1976). Solidification of Droplets on a Cold Surface. *International Journal of Heat and Mass Transfer*, 19(9):1009–1013. 16

Mandre, S., Mani, M., and Brenner, M. P. (2008). Precursors to Droplet Splashing on a Solid Surface. *Physical Review Letters*, 102(13):1–5. 24

Mani, M., Mandre, S., and Brenner, M. P. (2010). Events Before Droplet Splashing on a Solid Surface. *Journal of Fluid Mechanics*, 647:163–185. 24

Manzello, S. L. and Yang, J. C. (2002). An Experimental Study of a Water Droplet Impinging on a Liquid Surface. *Experiments in Fluids*, 32(5):580–589. 25

Mao, T., Kuhn, D. C. S., and Tran, H. (1997). Spread and Rebound of Liquid Droplets Upon Impact on Flat Surfaces. *AIChE Journal*, 43(9):2169–2179. 8, 14, 17, 18, 23

Maqua, C., Castanet, G., and Lemoine, F. (2008). Bicomponent Droplets Evaporation: Temperature Measurements and Modelling. *Fuel*, 87(13-14):2932–2942. 37

Marengo, M., Antonini, C., Roisman, I. V., and Tropea, C. (2011). Drop Collisions With Simple and Complex Surfaces. *Current Opinion in Colloid & Interface Science*, 16(4):292–302. 10

Mashayek, A. and Ashgriz, N. (2011). Dynamics of Liquid Droplets. In Ashgriz, N., editor, *Handbook of Atomization and Sprays: Theory and Applications*, chapter 4, pages 97–123. Springer US. 104

Mathews, W. S., Lee, C. F., and Peters, J. E. (2003). Experimental Investigations of Spray/Wall Impingement. *Atomization and Sprays*, 13(2-3):223–242. 25

Matsumoto, S. and Saito, S. (1970). On the Mechanism of Suspension of Paticels in Horizontal Conveying: Monte Carlo Simulation Based on the Irregular Bouncing Model. *Journal of Chemical Engineering*, 3(1):83–92. 66

Mishra, N. K., Zhang, Y., and Ratner, A. (2011). Effect of Chamber Pressure on Spreading and Splashing of Liquid Drops Upon Impact on a Dry Smooth Stationary Surface. *Experiments in Fluids*, 51(2):483–491. 23

Moita, A. S. and Moreira, A. L. N. (2007). Drop Impacts Onto Cold and Heated Rigid Surfaces: Morphological Comparisons, Disintegration Limits and Secondary Atomization. *International Journal of Heat and Fluid Flow*, 28(4):735–752. 8, 10, 34, 39, 40

Moita, A. S. and Moreira, A. L. N. (2009). Development of Empirical Correlations to Predict the Secondary Droplet Size of Impacting Droplets Onto Heated Surfaces. *Experiments in Fluids*, 47(4-5):755–768. 39

Moreira, A. L. N., Carvalho, J., and Panão, M. R. O. (2007a). An Experimental Methodology to Quantify the Spray Cooling Event at Intermittent Spray Impact. *International Journal of Heat and Fluid Flow*, 28(2):191–202. 104

Moreira, A. L. N., Moita, A. S., Cossali, G. E., Marengo, M., and Santini, M. (2007b). Secondary Atomization of Water and Isooctane Drops Impinging on Tilted Heated Surfaces. *Experiments in Fluids*, 43(2-3):297–313. 39, 40

Moreira, A. L. N., Moita, A. S., and Panão, M. R. O. (2010). Advances and Challenges in Explaining Fuel Spray Impingement: How Much of Single Droplet Impact Research Is Useful? *Progress in Energy and Combustion Science*, 36(5):554–580. 8, 25, 34, 73

Moreira, A. L. N. and Panão, M. R. O. (2011). Spray-Wall Impact. In Ashgriz, N., editor, *Handbook of Atomization and Sprays: Theory and Applications*, chapter 21, pages 441–455. Srpringer US. 19

Motzkus, C., Gensdarmes, F., and Géhin, E. (2011). Study of the Coalescence/Splash Threshold of Droplet Impact on Liquid Films and its Relevance in Assessing Airborne Particle Release. *Journal of colloid and interface science*, 362(2):540–52. x, 28, 29, 72, 73, 95, 114

Mundo, C., Sommerfeld, M., and Tropea, C. (1995). Droplet-Wall Collisions: Experimental Studies of the Deformation and Breakup Process. *International Journal of Multiphase Flow*, 21(2):151–173. 10, 13, 20, 23

Mundo, C., Sommerfeld, M., and Tropea, C. (1998). On the Modelling of Liquid Sprays Impinging on Surfaces. *Atomization and Sprays*, 8(6):625–652. 23, 27

Mundo, C., Tropea, C., and Sommerfeld, M. (1997). Numerical and Experimental Investigation of Spray Characteristics in the Vicinity of a Rigid Wall. *Experimental Thermal and Fluid Science*, 15(3):228–237. 20, 23, 24

Mutchler, C. K. (1970). *The Size, Travel and Composition of Droplets Formed by Waterdrop Splash in Thin Water Layers*. Phd thesis, University of Minnesota, St. Paul. 68, 69

Naber, J. D. and Farrel, P. (1993). Hydrodynamics of Droplet Impingement on a Heated Surface. In *SAE Paper 930919*. 20, 36, 39, 40, 73

Nikolopoulos, N., Theodorakakos, A., and Bergeles, G. (2005). Normal Impingement of a Droplet Onto a Wall Film: a Numerical Investigation. *International Journal of Heat and Fluid Flow*, 26(1):119–132. 26

Nikolopoulos, N., Theodorakakos, A., and Bergeles, G. (2007). Three-Dimensional Numerical Investigation of a Droplet Impinging Normally Onto a Wall Film. *Journal of Computational Physics*, 225(1):322–341. 26

O'Donnell, B. J. and Helenbrook, B. T. (2005). Drag on Ellipsoids At Finite Reynolds Numbers. *Atomization and Sprays*, 15(4):363–376. 43

Oguz, H. N. and Prosperetti, A. (1990). Bubble Entrainment by the Impact of Drops on Liquid Surfaces. *Journal of Fluid Mechanics*, 219:143–179. 25

Okawa, T., Shiraishi, T., and Mori, T. (2006). Production of Secondary Drops During the Single Water Drop Impact Onto a Plane Water Surface. *Experiments in Fluids*, 41(6):965–974. 28, 29, 30

Okawa, T., Shiraishi, T., and Mori, T. (2008). Effect of Impingement Angle on the Outcome of Single Water Drop Impact Onto a Plane Water Surface. *Experiments in Fluids*, 44(2):331–339. 13, 30

Opfer, L., Roisman, I. V., and Tropea, C. (2011). Effect of Crossflow on Spray-Wall Interaction: Experiments and Modeling. In *ILASS - Europe 2011, 24th European Conference on Liquid Atomization and Spray Systems*, pages 1–9, Estoril. 11

Opfer, L., Roisman, I. V., and Tropea, C. (2012). Aerodynamic Fragmentation of Drops : Dynamics of the Liquid Bag. In *ICLASS 2012, 12th Triennial International Conference on Liquid Atomization and Spray Systems*, pages 1–8, Heidelberg. 109

O'Rourke, P. J. and Amsden, A. A. (1987). The Tab Method for Numerical Calculation of Spray Droplet Breakup. In *SAE Technical Paper 872089*. 81

Özdemir, I. B. (1992). *Impingement of Single and Two-Phase Jets on Unheated and Heated Flat Plates*. Phd thesis, Imperial College. 26

Özdemir, I. B. and Whitelaw, J. H. (1993). Impingement of an Unsteady Two-Phase Jet on Unheated and Heated Flat Plates. *Journal of Fluid Mechanics*, 252:499–523. 26

Palacios, J., Hernández, J., Gómez, P., Zanzi, C., and López, J. (2012). On the Impact of Viscous Drops Onto Dry Smooth Surfaces. *Experiments in Fluids*, 52(6):1449–1463. 24

Panão, M. R. O. and Moreira, A. L. N. (2002). Visualization and Analysis of Spray Impingement Under Cross-Flow Conditions. In *SAE Technical Paper 2002-01-2664*, pages 1–12. 88

Panão, M. R. O. and Moreira, A. L. N. (2005a). Experimental Characterization of an Intermittent Gasoline Spray Impinging Under Cross-Flow Conditions. *Atomization and Sprays*, 15(2):201–222. 11

Panão, M. R. O. and Moreira, A. L. N. (2005b). Thermo- and Fluid Dynamics Characterization of Spray Cooling With Pulsed Sprays. *Experimental Thermal and Fluid Science*, 30(2):79–96. 19

Panão, M. R. O., Moreira, A. L. N., and Durão, D. F. (2013). Effect of a Cross-Flow on Spray Impingement with Port Fuel Injection Systems for HCCI Engines. *Fuel*, 106:249–257. 11, 26, 61, 63, 64, 95, 99, 100

Park, H., Yoon, S. S., Jepsen, R. A., Heister, S. D., and Kim, H. Y. (2008). Droplet Bounce Simulations and Air Pressure Effects on the Deformation of Pre-Impact Droplets, Using a Boundary Element Method. *Engineering Analysis with Boundary Elements*, 32(1):21–31. 24

Park, K. and Watkins, A. P. (1996). Comparison of Wall Spray Impaction Models with Experimental Data on Drop Velocities and Sizes. *International Journal of Heat and Fluid Flow*, 17(4):424–438. 13, 19, 23, 24

Park, S. W., Kim, S., and Lee, C. S. (2006). Breakup and Atomization Characteristics of Mono-Dispersed Diesel Droplets in a Cross-Flow Air Stream. *International Journal of Multiphase Flow*, 32(7):807–822. 47, 107

Pasandideh-Fard, M., Qiao, Y. M., Chandra, S., and Mostaghimi, J. (1996). Capillary Effects During Droplet Impact on a Solid Surface. *Physics of Fluids*, 8(3):650–659. 16, 33, 91, 92

Patankar, S. V. and Spalding, D. B. (1972). A Calculation Procedure for Heat, Mass and Momentum Transfer in Three-Dimensional Parabolic Flows. *International Journal of Heat and Mass Transfer*, 15(10):1787–1806. 55

Pautsch, A. G. and Shedd, T. A. (2006). Adiabatic and Diabatic Measurements of the Liquid Film Thickness During Spray Cooling with FC-72. *International Journal of Heat and Mass Transfer*, 49(15-16):2610–2618. 104

Petsi, A. J. and Burganos, V. N. (2011). Temperature Distribution Inside an Evaporating Two-Dimensional Droplet Lying on Curved or Flat Substrates. *Physical Review E*, 84(1):011201. 37

Pilch, M. and Erdman, C. A. (1987). Use of Breakup Time Data and Velocity History Data to Predict the Maximum Size of Stable Fragments for Acceleration-Induced Breakup of a Liquid Drop. *International Journal of Multiphase Flow*, 13(6):741–757. xv, 41, 44, 45, 46, 49, 50, 77

Prosperetti, A. and Oguz, H. N. (1997). Air Entrainment Upon Liquid Impact. *Philosophical Transactions of the Royal Society of London A: Mathematical, Physical and Engineering Sciences*, 355(1724):491–506. 25

Range, K. and Feuillebois, F. (1998). Influence of Surface Roughness on Liquid Drop Impact. *Journal of Colloid and Interface Science*, 203(1):16–30. 23

Rein, M. (2002). *Drop-Surface Interactions*. Springer-Verlag Wien GmbH, Wien. 35, 36, 37, 38, 39

Rioboo, R., Bauthier, C., Conti, J., Voué, M., and De Coninck, J. (2003). Experimental Investigation of Splash and Crown Formation During Single Drop Impact on Wetted Surfaces. *Experiments in Fluids*, 35(6):648–652. 28, 29, 71

Rioboo, R., Marengo, M., and Tropea, C. (2002). Time Evolution of Liquid Drop Impact Onto Solid, Dry Surfaces. *Experiments in Fluids*, 33(1):112–124. 14, 18

Rioboo, R., Tropea, C., and Marengo, M. (2001). Outcomes From a Drop Impact on Solid Surfaces. *Atomization and Sprays*, 11(2):155–166. xv, 8, 9, 23, 29

Rioboo, R., Voué, M., Vaillant, A., and De Coninck, J. (2008). Drop Impact on Porous Superhydrophobic Polymer Surfaces. *Langmuir*, 24(24):14074–14077. 11

Rodrigues, C., Barata, J., and Silva, A. (2012a). Influence of the Energy Dissipation in the Spray Impingement Modeling. In *50th AIAA Aerospace Sciences Meeting*, pages 1–11, Nashville, Tennessee. 4

Rodrigues, C., Barata, J., and Silva, A. (2012b). Liquid Film Dynamic on the Spray Impingement Modeling. *Atomization and Sprays*, 22(9):757–775. 5, 26

Rodrigues, C., Barata, J., and Silva, A. (2012c). Liquid Film Dynamic on the Spray Impingement Modelling. In *ICLASS 2012, 12th Triennial International Conference on Liquid Atomization and Spray Systems*, pages 1–8, Heidelberg. 5

Rodrigues, C., Barata, J., and Silva, A. (2012d). Spray Impingement Modelling: Evaluation of The Dissipative Energy Loss and Influence of an Enhanced Near-Wall Treatment. In *ICCEU 2012, 11th International Conference on Combustion and Energy Utilization*, pages 1–16, Coimbra. 4

Rodrigues, C., Barata, J., and Silva, A. (2013a). Development of a Dynamic Liquid Film Extension and Integration into a Spray Impingement Model. In *51st AIAA Aerospace Sciences Meeting*, pages 1–11, Grapevine, Texas. 5

Rodrigues, C., Barata, J., and Silva, A. (2013b). On the Modeling of Spray/Wall Impingement Under Crossflow Conditions. In *21st AIAA Computational Fluid Dynamics Conference*, pages 1–11, San Diego, California. 5

Rodrigues, C., Barata, J., and Silva, A. (2013c). Spray Impingement Modelling: Evaluation of the Dissipative Energy Loss and Influence of an Enhanced Near-Wall Treatment. *Fuel Processing Technology*, 107:71–80. 4, 5

Rodrigues, C., Barata, J., and Silva, A. (2014). A Comprehensive Numerical Study on the Modelling of Spray Impingement. In *SPEIC14 - Towards Sustainable Combustion*, pages 1–7, Lisbon. 6

Rodrigues, C., Barata, J., and Silva, A. (2015a). Modeling of Evaporating Sprays Impinging onto Solid Surfaces. *Journal of Thermophysics and Heat Transfer*, Accepted September 21. 6

Rodrigues, C., Barata, J., and Silva, A. (2015b). Modelling of Droplet Deformation and Breakup. In *53rd AIAA Aerospace Sciences Meeting*, pages 1–10, Kissimmee, Florida. 6

Rodrigues, C., Barata, J., and Silva, A. (2015c). On the Modelling of Evaporating Sprays Impinging onto Solid Surfaces. In *53rd AIAA Aerospace Sciences Meeting*, pages 1–10, Kissimmee, Florida. 6

Roisman, I. V. (2009). Inertia Dominated Drop Collisions. II. An Analytical Solution of the Navier-Stokes Equations for a Spreading Viscous Film. *Physics of Fluids*, 21(5):1–11. 13, 17

Roisman, I. V. (2010). On the Instability of a Free Viscous Rim. *Journal of Fluid Mechanics*, 661:206–228. 23

Roisman, I. V., Araneo, L., Marengo, M., and Tropea, C. (1999). Evaluation of Drop Impingement Models: Experimental and Numerical Analysis of a Spray Impact. In *ILASS - Europe 1999, 15th European Conference on Liquid Atomization and Spray Systems*, pages 1–6, Toulouse. 2, 10

Roisman, I. V., Berberović, E., and Tropea, C. (2009). Inertia Dominated Drop Collisions. I. On the Universal Flow in the Lamella. *Physics of Fluids*, 21(5):1–10. 14, 15, 17, 92

Roisman, I. V., Horvat, K., and Tropea, C. (2006). Spray Impact: Rim Transverse Instability Initiating Fingering and Splash, and Description of a Secondary Spray. *Physics of Fluids*, 18(10):1–19. 8, 20, 34

Roisman, I. V., Rioboo, R., and Tropea, C. (2002). Normal Impact of a Liquid Drop on a Dry Surface: Model for Spreading and Receding. *Proceedings of the Royal Society of London A: Mathematical, Physical and Engineering Sciences*, 458(2022):1411–1430. 14, 15, 16

Roisman, I. V. and Tropea, C. (2002). Impact of a Drop Onto a Wetted Wall: Description of Crown Formation and Propagation. *Journal of Fluid Mechanics*, 472:373–397. 26

Roisman, I. V. and Tropea, C. (2005). Fluctuating Flow in a Liquid Layer and Secondary Spray Created by an Impacting Spray. *International Journal of Multiphase Flow*, 31(2):179–200. 26

Ruff, G. A., Wu, P.-K., Bernal, L. P., and Faeth, G. M. (1992). Continuous- and Dispersed-Phase Structure of Dense Nonevaporating Pressure-Atomized Sprays. *Journal of Propulsion and Power*, 8(2):280–289. 47

Saha, K., Abu-Ramadan, E., and Li, X. (2012). Multicomponent Evaporation Model for Pure and Blended Biodiesel Droplets in High Temperature Convective Environment. *Applied Energy*, 93:71–79. 37

Samenfink, W., Elsaber, A., Dullenkopf, K., and Wittig, S. (1999). Droplet Interaction with Shear-Driven Liquid Films: Analysis of Deposition and Secondary Droplet Characteristics. *International Journal of Heat and Fluid Flow*, 20(5):462–469. 18, 26, 30, 33

Sazhin, S. S. (2006). Advanced Models of Fuel Droplet Heating and Evaporation. *Progress in Energy and Combustion Science*, 32(2):162–214. 34

Sazhin, S. S., Abdelghaffar, W. A., Krutitskii, P. A., Sazhina, E. M., and Heikal, M. R. (2005). New Approaches to Numerical Modelling of Droplet Transient Heating and Evaporation. *International Journal of Heat and Mass Transfer*, 48(19-20):4215–4228. 36

Sazhin, S. S., Elwardany, A., Krutitskii, P. A., Castanet, G., Lemoine, F., Sazhina, E. M., and Heikal, M. R. (2010). A Simplified Model for Bi-Component Droplet Heating and Evaporation. *International Journal of Heat and Mass Transfer*, 53(21-22):4495–4505. 37

Sazhin, S. S., Elwardany, A. E., Krutitskii, P. A., Deprédurand, V., Castanet, G., Lemoine, F., Sazhina, E. M., and Heikal, M. R. (2011). Multi-Component Droplet Heating and Evaporation: Numerical Simulation Versus Experimental Data. *International Journal of Thermal Sciences*, 50(7):1164–1180. 37

Schmehl, R. (2002). Advanced Modeling of Droplet Deformation and Breakup for CFD Analysis of Mixture Preparation. In *ILASS - Europe 2002, 18th Annual Conference on Liquid Atomization and Spray Systems*, pages 1–10, Zaragoza. 40, 77

Schmehl, R., Rosskamp, H., Willmann, M., and Wittig, S. (1999). CFD Analysis of Spray Propagation and Evaporation Including Wall Film Formation and Spray/Film Interactions. *International Journal of Heat and Mass Transfer*, 20(5):520–529. 26

Senda, J., Ohnishi, M., Takahashi, T., Fujimoto, H., Utsunomiya, A., and Wakatabe, M. (1999). Measurement and Modeling on Wall-Wetted Fuel Film Profile and Mixture Preparation in Intake Port of SI Engine. In *SAE Technical Paper 1999-01-0798*, pages 1–16. 13, 25, 27, 30

Shim, Y.-S., Choi, G.-M., and Kim, D.-J. (2009). Numerical and Experimental Study on Effect of Wall Geometry on Wall Impingement Process of Hollow-Cone Fuel Spray Under Various Ambient Conditions. *International Journal of Multiphase Flow*, 35(10):885–895. 11

Shin, Y., Cheng, W., and Heywood, J. (1994). Liquid Gasoline Behavior in the Engine Cylinder of a SI Engine. In *SAE Technical Paper 941872*. 25

Shirolkar, J. S., Coimbra, C. F. M., and McQuay, M. Q. (1996). Fundamental Aspects of Modeling Turbulent Particle Dispersion in Dilute Flows. *Progress in Energy and Combustion Science*, 22(4):363–399. 56, 58

Silva, A. (2007). *Experimental and Numerical Study of Physical Aspects of Fuel Processes*. PhD thesis, University of Beira Interior. 100

Silva, A., Barata, J., and Rodrigues, C. (2011a). Evaluation of Spread/splash Transition Criteria on the Spray Impingement Modelling. In *6th ERCOFTAC 2011*, pages 1–10, Vigo. 4

Silva, A., Barata, J., and Rodrigues, C. (2011b). Influence of Spread/Splash Transition Criteria on the Spray Impingement Modelling. In *ILASS - Europe 2011, 24th European Conference on Liquid Atomization and Spray Systems*, pages 1–10, Estoril. 4

Silva, A., Barata, J., and Rodrigues, C. (2013). Influence of Spread/Splash Transition Criteria on the Spray Impingement Modelling. *Journal of Energy and Power Engineering*, 7:290–300. 4

Simmons, H. C. (1977a). The Correlation of Drop-Size Distributions in Fuel Nozzle Sprays-Part I: The Drop-Size/Volume-Fraction Distribution. *Journal for Engineering for Power*, 99(3):309–314. 47

Simmons, H. C. (1977b). The Correlation of Drop-Size Distributions in Fuel Nozzle Sprays-Part II: The Drop-Size/Number Distribution. *Journal for Engineering for Power*, 99(3):315–319. 47

Sirignano, W. A. (1983). Fuel Droplet Vaporization and Spray Combustion Theory. *Progress in Energy and Combustion Science*, 9(4):291–322. 34, 36, 73

Sommerfeld, M. (1998). Analysis of Isothermal and Evaporating Turbulent Sprays by Phase-Doppler Anemometry and Numerical Calculations. *International Journal of Heat and Fluid Flow*, 19(2):173–186. xvii, 36, 59, 73

Sommerfeld, M. and Huber, N. (1999). Experimental Analysis and Modelling of Particle-Wall Collisions. *International Journal of Multiphase Flow*, 25(6-7):1457–1489. 8, 29

Spalding, D. B. (1953). The Combustion of Liquid Fuels. *Symposium (International) on Combustion*, 4(1):847–864. 36, 73

Sparrow, E. M. and Gregg, J. L. (1958). The Variable Fluid-Property Problem in Free Convection. *Transactions of the American Society of Mechanical Engineers*, 80(4):879–886. 76

Stanton, D. W., Lippert, A. M., Reitz, R. D., and Rutland, C. J. (1998). Influence of Spray-Wall Interaction and Fuel Films on Cold Starting in Direct Injection Diesel Engines. In *SAE Technical Paper 982584*, pages 1–22. 26

Stanton, D. W. and Rutland, C. J. (1996). Modeling Fuel Film Formation and Wall Interaction in Diesel Engines. In *SAE Technical Paper 960628*. 33

Stanton, D. W. and Rutland, C. J. (1997). Multi-dimensional modeling of fuel films in direct injection diesel engines. In *The American Society of Mechanical Engineers*, pages 1–9, Madison, WI. 26, 29

Stanton, D. W. and Rutland, C. J. (1998). Multi-Dimensional Modeling of Thin Liquid Films and Spray-Wall Interactions Resulting From Impinging Sprays. *International Journal of Heat and Mass Transfer*, 41(20):3037–3054. 26

Stevens, E. and Steeper, R. (2001). Piston Wetting in an Optical DISI Engine: Fuel Films, Pool Fires, and Soot Generation. In *SAE Technical Paper 2001-01-1203*. 2, 24

Stow, C. D. and Hadfield, M. G. (1981). An Experimental Investigation of Fluids-Flow Resulting from the Impact of a Water Drop with an Unyielding Dry Surface. *Proceedings of the Royal Society of London A: Mathematical, Physical and Engineering Sciences*, 373(1755):419–441. 10, 12, 67

Stow, C. D. and Stainer, R. (1977). The Physical Products of a Splashing Water Drop. *Journal of the Meteorological Society of Japan*, 55(5):518–531. 10, 18, 26, 27, 30

Strotos, G., Gavaises, M., Theodorakakos, A., and Bergeles, G. (2011). Numerical Investigation of the Evaporation of Two-Component Droplets. *Fuel*, 90(4):1492–1507. 37

Takeda, K., Yaegashi, T., Sekiquchi, K., Saito, K., and Imatake, N. (1995). Mixture Preparation and HC Emissions of a 4-Valve Engine with Port Fuel Injection During Cold Starting and Warm-up. In *SAE Technical Paper 950074*. 25

Tarnogrodzki, A. (2001). Theory of Free Fall Breakup of Large Drops. *International Journal of Mechanical Sciences*, 43(4):883–893. 47

Tropea, C. and Marengo, M. (1999). The Impact of Drops on Walls and Films. *Multiphase Science and Technology*, 11(1):19–36. 25

Trujillo, M. F. and Lee, C. F. (2001). Modeling Crown Formation Due to the Splashing of a Droplet. *Physics of Fluids*, 13(9):2503–2516. 23

Ukiwe, C. and Kwok, D. Y. (2005). On the Maximum Spreading Diameter of Impacting Droplets on Well-Prepared Solid Surfaces. *Langmuir*, 21(2):666–673. 16

Unnikrishnan, P. K., Vaikuntanathan, V., and Sivakumar, D. (2014). Impact Dynamics of High Weber Number Drops on Chemically Modified Metallic Surfaces. *Colloids and Surfaces A: Physicochemical and Engineering Aspects*, 459:109–119. 10

Vander Wal, R. L., Berger, G. M., and Mozes, S. D. (2006a). Droplets Splashing Upon Films of the Same Fluid of Various Depths. *Experiments in Fluids*, 40(1):33–52. 26, 27, 29, 99

Vander Wal, R. L., Berger, G. M., and Mozes, S. D. (2006b). The Combined Influence of a Rough Surface and Thin Fluid Film Upon the Splashing Threshold and Splash Dynamics of a Droplet Impacting Onto Them. *Experiments in Fluids*, 40(1):23–32. 10, 12, 24, 26, 28

Vander Wal, R. L., Berger, G. M., and Mozes, S. D. (2006c). The Splash/Non-Splash Boundary Upon a Dry Surface and Thin Fluid Film. *Experiments in Fluids*, 40(1):53–59. 13, 25

Šikalo, v. and Ganić, E. N. (2006). Phenomena of Droplet-Surface Interactions. *Experimental Thermal and Fluid Science*, 31(2):97–110. 8, 29

Wachters, L. H. and Westerling, N. A. J. (1966). Heat Transfer from a Hot Wall to Impinging Water Drops in Spheroidal State. *Chemical Engineering Science*, 21(11):1047–1056. 13, 36, 39

Wang, A.-B. and Chen, C.-C. (2000). Splashing Impact of a Single Drop Onto Very Thin Liquid Films. *Physics of Fluids*, 12(9):2155. 26

Watson, K. M. (1931). Prediction of Critical Temperatures and Heats of Vaporization. *Industrial & Engineering Chemistry*, 23(4):360–364. 76

Welty, J. R., Wicks, C. E., Wilson, R. E., and Rorrer, G. L. (2008). *Fundamentals of Momentum, Heat, and Mass Transfer*. John Wiley & Sons, Inc., 5th edition. 35

Wert, K. L. (1995). A Rationally-Based Correlation of Mean Fragment Size for Drop Secondary Breakup. *International Journal of Multiphase Flow*, 21(6):1063–1071. 48

Winterbone, D. E., Yates, D. A., Clough, E., Rao, K., Gomes, P. O., and Sun, J. H. (1994). Combustion in High-Speed Direct-Injection Diesel Engines - A Comparative Study. *Proceedings of the Institution of Mechanical Engineers*, 208(Part C):223–2240. 2

Witze, P. O. (1996). LIF Visualization of Liquid Fuel in the Cylinder of a Spark Ignition Engine. In *8th International Symposium on Applications of Laser Techniques to Fluid Mechanics*, Lisbon. 2, 24

Worthington, A. M. (1876a). A Second Paper on the Forms Assumed by Drops of Liquids Falling Vertically on a Horizontal Plate. *Proceedings of the Royal Society of London*, 25(171-178):498–503. 1, 18

Worthington, A. M. (1876b). On the Forms Assumed by Drops of Liquids Falling Vertically on a Horizontal Plate. *Proceedings of the Royal Society of London*, 25(171-178):261–272. 1, 18

Worthington, A. M. (1908). *A Study of Splashes*. Longmans, Green, and Co. 18

Wu, Z. (2003). Prediction of the Size Distribution of Secondary Ejected Droplets by Crown Splashing of Droplets Impinging on a Solid Wall. *Probabilistic Engineering Mechanics*, 18(3):241–249. 18

Xie, J. L., Zhao, R., Duan, F., and Wong, T. N. (2012). Thin Liquid Film Flow and Heat Transfer Under Spray Impingement. *Applied Thermal Engineering*, 48:342–348. 104

Xu, L. (2007). Liquid Drop Splashing on Smooth, Rough, and Textured Surfaces. *Physical Review E*, 75(5):1–8. xv, 9, 23

Yarin, A. L. (2006). Drop Impact Dynamics: Splashing, Spreading, Receding, Bouncing... *Annual Review of Fluid Mechanics*, 38(1):159–192. 8

Yarin, A. L. and Weiss, D. A. (1995). Impact of Drops on Solid Surfaces: Self-Similar Capillary Waves, and Splashing as a New Type of Kinematic Discontinuity. *Journal of Fluid Mechanics*, 283:141–173. 15, 20, 27, 30, 33, 91

Yoon, S. S. and DesJardin, P. E. (2006). Modelling Spray Impingement Using Linear Stability Theories for Droplet Shattering. *International Journal for Numerical Methods in Fluids*, 50(4):469–489. 13

Zhang, H., Bai, B., Liu, L., Sun, H., and Yan, J. (2013). Droplet Dispersion Characteristics of the Hollow Cone Sprays in Crossflow. *Experimental Thermal and Fluid Science*, 45:25–33. 11, 100

Zhang, K., Ma, L., Xu, X., Luo, J., and Guo, D. (2014). Temperature Distribution Along the Surface of Evaporating Droplets. *Physical Review E*, 89(3):032404. 37

Zisman, W. A. (1964). Relation of the Equilibrium Contact Angle to Liquid and Solid Constitution. In *Contact Angle, Wettability, and Adhesion*, chapter 2, pages 1–51. American Chemical Society, Washington, D.C. 11